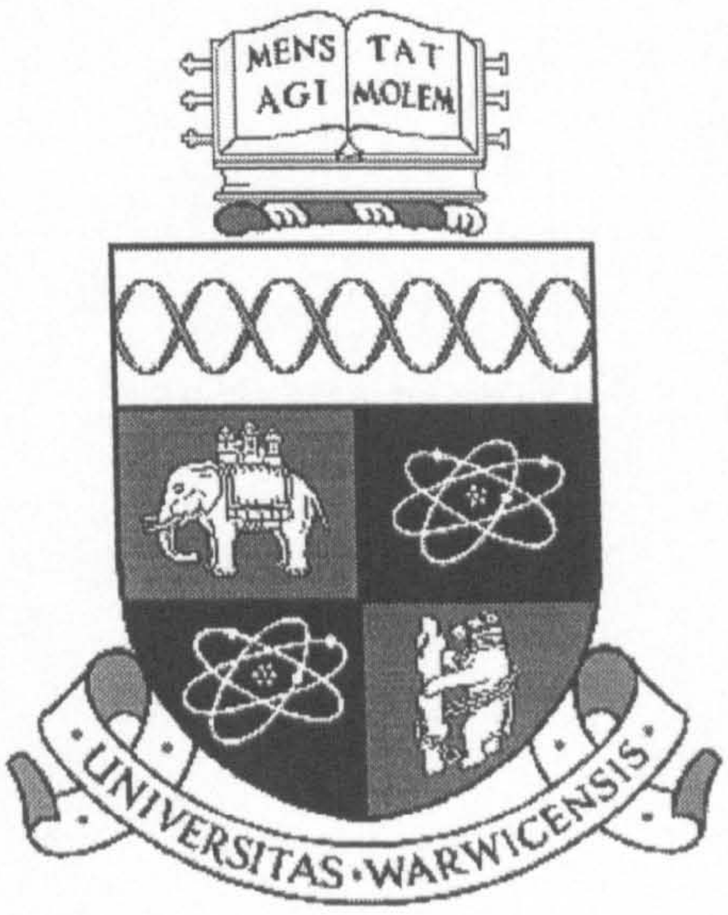

An Experimental and Numerical Investigation into Compact Heat Exchangers

Martin Fisher

Thesis submitted to the University of Warwick
for the degree of Doctor of Philosophy

Department of Engineering
University of Warwick
May 2000

Dedication

This thesis is dedicated to the memory of:

Professor N. K. Mitra (1939-1999)

Our small community is a much smaller and
poorer place without you. I hope we have the
opportunity to meet again.

Contents

List of Figures

List of Tables

Acknowledgements

This is probably the section of a thesis that is first thought about, thought about most often, changed most often and finally the last to write. It has undergone many revisions over my time at Warwick, but here at last are my final thoughts on the matter.

Firstly I would like to acknowledge both of my supervisors Dr Bob Critoph and Dr Chris Shaw. Their two very different styles of management allowed me to explore my own crazy ideas and pulled me back into line when I had gone too far. Without their help and encouragement this work would never have been completed.

Over my time at Warwick I have met quite a few people, the majority who I now consider as friends. Mark Burnet has always been overly helpful and gone out of his way many a time in a time of crises. We have shared a lot of good conversations and arguments over many pints of Kronenberg at numerous Top Banana's, and even managed to save the world many times over under a conservative government! The CFD boys, Rai, Jason, Reza and Alex have always been a good starting point for either a good argument over disk space and CPU time or a night out and in many cases both. In both cases I felt worse for wear the morning after. Roger and Zackary have always been very forthcoming with bright ideas and help during our afternoon tea breaks. One day just for you I might even drink a cup of coffee.

The technicians at Warwick have always been helpful and patient with my demands for things to be done by yesterday. John Matteri has put up with the brunt of it in his normal cheery way. Still on the work front but outside Warwick I am indebted to two organisations. Firstly, the people at Bochum University. Professor Leiner and Ender Tandogan have always been very helpful with my quests for information and guidance. My stay in Germany was made very pleasurable by meeting you. Secondly Britannia Heat Transfer have always been very helpful in providing information and

support. David Pierce and Andrew Davies have always encouraged me in my work and I am sure are looking forward to the results.

Outside the bubble of work and university, house mates have always been around to help me get over the days work. Neil who along with being a landlord is also a friend has seen me at my best and worst. Patsy is now only beginning to realise wheat Neil had to put up with.

I would like to acknowledge the Engineering and Physical Sciences Research Council (EPSRC) for funding me over the past three years under a PhD quota scholarship award. Likewise I would like to acknowledge the European Union for funding me since through contract JOE3-CT97-0056 under the JOULE III scheme.

Finally, Michelle, thank you. Thank you for walking into my life when you did. The final few months have been so much easier with your support and love.

Meanwhile back at the ranch...

Declaration

I hereby declare that the work contained in this thesis is the authors own work. Papers that have been published from the work contained in this thesis are attached to the end of the thesis in Appendix F. This thesis has not been submitted for a degree at any other university.

Summary

Experimental and numerical experiments were carried out on different heat exchanger section types to determine the performance of vortex generators. The heat exchanger sections investigated were plain channel fin types with delta and rectangular winglet pairs, rectangular wings and embossed vortex generators. Fin-tube heat exchangers were also investigated in both in-line and staggered arrangements with and without vortex generators over the Reynolds number range 65 - 653 and angle of attack of vortex generators 15° – 60°.

With the need for improved heat exchanger performance fin modifications are normally used to enhance the gas side heat transfer coefficient. However, with many of these fin modifications a significant pressure drop penalty can result. Vortex generators enhance heat transfer with a minimal increase in pressure drop. The effect of vortex generators in heat exchanger sections at low Reynolds numbers need to be assessed so that optimal positioning can be determined. To do this local heat transfer coefficients need to be measured.

Steady steady state physical tests with a constant heat flux boundary condition were used to measure local and average heat transfer values and thereby measure the effect of vortex generators on heat transfer and pressure drop. Numerical modelling allows a detailed picture of the flow field and local heat transfer to be seen. Such numerical modelling by Computational Fluid Dynamics (CFD) is still in its infancy and comparisons against detailed experimental data are still needed before simulations can be used without physical testing. The advantage of CFD is that a large number of simulations can be completed in a short time span when compared to full size physical tests.

At low Reynolds numbers, it was found that the inclusion of vortex generators in all heat exchanger types had the effect of increasing the average heat transfer coefficient and pressure drop. In all but one of the cases investigated, the in increase average heat transfer coefficient was larger than the increase in pressure drop. For the case of a staggered tube arrangement, with vortex generators at 60°, there was a reduction in pressure drop when compared to the case without vortex generators. This was due to delayed separation and reduced wake region behind the tube. This specific vortex generator position is considered to be near optimal.

It is shown that CFD can successfully reproduce data from physical tests on heat exchanger sections with and without vortex generators. The procedures given can be generalised to optimise further geometries. The benefits of including vortex generators in heat exchangers will enable smaller heat exchangers to be utilised or an increase in effectiveness for the user.

Nomenclature

Symbol	Definition	Units
A	Area	m^2
c_p	Specific heat capacity at constant pressure	kJ/KgK
c_v	Specific heat capacity at constant volume	kJ/KgK
D, d	Diameter	m
D_h	Hydraulic diameter	m
e	Internal energy	kJ/Kg
H	Channel height	m
h	Heat transfer coefficient	W/m^2K
k	Thermal conductivity	W/mK
L	Length	m
$\dot{m}$	Mass flow rate	kg/s
p	Pressure	Pa
Q	Energy	W
q	Heat flux by conduction or convection	W/m^2
$\dot{q}$	Heat flux input	W/m^2
S_m	Source terms	-
T	Temperature	K,° C
t	Time	s
u	Velocity component in the x direction	m/s
V	Volume	m^3
v	Velocity component in the y direction	m/s
w	Velocity component in the z direction	m/s
x	Spatial co-ordinates	m
y	Spatial co-ordinates	m
z	Spatial co-ordinates	m

Subscripts	Definition	Units
a	Air	-
CV	Control volume	-
g	Glass	-
lc	Liquid crystal	-
rad	Radiation	W
s	Solid	-

Greek symbols	Definition	Units
Γ	Diffusion coefficient	-
α	Thermal diffusivity	m^2/s
β	Angle of attack of vortex generators	$^\circ$
δ	Thickness of fin	m
ϵ	Emissivity or turbulent dissipation	-
λ	Second viscosity	m^2/s
μ	Dynamic viscosity	m^2/s
ρ	Density	kg/m^3
σ	Stefan-Boltzmann constant	W/m^2K^4
ϕ	Variable	-

Dimensionless groups	Definition
Biot number	$Bi = h(V/A)/k$
Colburn j factor	$j = StPr^{2/3}$
Friction factor	$f = \Delta P D_h/(1/2\rho u^2 L)$
Grashof number	$Gr = g\beta(T_s - T_a)x^3/\nu^2$
Goodness factor	$G = (Nu/Nu_0)/(f_{app}/f_{app\,0})$
Nusselt number	$Nu = hx/k$
Prandtl number	$Pr = c_p\mu/k$
Performance factor	$R_p = (j/j_0)/(f/f_0)$
Reynolds number	$Re = \rho x u/\mu$
Stanton number	$St = h/\rho c_p u$

Chapter 1

Introduction

1.1 Background

1.1.1 Improving heat exchanger performance

In any thermodynamic cycle heat has to be rejected at some stage, some form of heat exchanger has to be used to return the working fluid back to ambient temperature. In many cases the volume in which this can happen is limited necessitating a heat exchanger that has a large heat transfer rate per unit volume. Compact heat exchangers have been widely used for this task in applications that range from air conditioning systems to turbo inter coolers; their ratios of heat duty to volume usually exceed 700 kW/m^3, Fiebig (1993). To transfer more heat from a compact heat exchanger the solution has conventionally been to add more secondary surface (fins) to increase the overall area. However the total fin area is limited by the fin efficiency, which reduces significantly when the fin area is increased above a certain level and thus reduces the performance of the heat exchanger.

It is clear, therefore, that to transfer more heat from a compact heat exchanger in a particular process or thermodynamic cycle, the heat transfer coefficient of the heat

exchanger must be improved. This could lead to smaller heat exchangers, which in turn reduce the manufacturing costs because of a reduction in raw material used, or a reduction in the operating costs to the user through lower energy losses, Tiggelbeck et al. (1993). This increase in performance is especially important in liquid/gas heat exchangers because the gas side heat transfer resistance ($1/h_{air}$) is typically 10 - 50 times larger than the liquid side, Kays and London (1955), due to the lower density and thermal conductivity. To compensate for the lower heat transfer performance the gas side area is usually greater than the liquid side area resulting in gas side heat transfer surface per unit volume of between 700 and 1000 m^2/m^3. Despite the larger secondary surface area the higher heat transfer resistance still lies on the gas side dictating that if any performance increase can be achieved the gas side thermal resistance still needs to be further reduced. This is normally achieved by modifications to the fin.

1.1.2 Experimental methods

Before any analysis can be carried out on fin modifications it is important to be able to identify local as opposed to average heat transfer coefficients and thus find any areas of poor heat transfer on the fin. The traditional method of evaluating alternative designs has been to build prototype sections of a heat exchanger and then test these in a specialist facility. Unfortunately, in such cases, only the overall heat transfer coefficient can be measured, Holland et al. (1997), and so any changes in the air side performance cannot be measured directly. Further, the high cost of

tooling often limits the number of tests that can be completed with different designs and alternative geometries. Consequently engineers have been forced during the design stage to rely on standard texts such as that by Kays and London (1955) where empirical data for heat exchangers is given.

By identifying local heat transfer coefficients steps can be made to improve the heat transfer in areas where it is poor by using novel fin arrangements. The major problem in identifying local heat transfer coefficients has been the measurement of the local surface temperature. Liquid crystals are commercially available which exhibit changes of colour over discrete and reproducible temperature bandwidths. By calibration of the colours displayed, the liquid crystals can be used to measure the surface temperature, Yianneskis (1986).

A number of experimental techniques exist to measure the local heat transfer coefficient using liquid crystals, such as the transient and steady state techniques. Liquid crystals are used for these types of study as they cause no impairment to the flow or heat flux at the surface and a complete map of the heat transfer model can be obtained. Previously, thermocouples were used but they disturb the local heat flux, and the surface temperature can only be measured adjacent to the thermocouple, Fisher (1996). The heat transfer coefficient in the transient technique is determined from the response of the surface temperature to a step change in local fluid temperature. The steady state technique relies on a constant heat flux input to the surface being examined. Isotherms on the surface then correspond to lines of constant heat

transfer coefficient. The uniform heat flux surface is usually generated electrically using a surface heater of vacuum deposited gold on the surface. A major problem with this method is the lack of heat flux uniformity which can vary by as much as ±30%, Jambunathan et al. (1994). A novel idea to produce a uniform heat flux was discussed by Critoph and Holland (1996). This used a radiative light source to heat a black liquid layer directly by absorption. Uniform heat flux densities within ±2% were achieved with this technique. Comparisons of the transient and steady state techniques which were reported by Baughn et al. (1989) have shown that there can be large differences in the results due to the different boundary conditions used in each test. However, the two sets of results can usually be reconciled with an understanding of the various boundary condition effects. It is therefore important to compare the results for the two different techniques under identical flow conditions so that the results from the different methods can be validated.

1.1.3 Numerical methods

With the rapid increase in computer power over recent years numerical techniques are now becoming more popular. Computational Fluid Dynamics (CFD), even though not a mature technology, is increasingly used in the design process. CFD solves the discretised fluid equations over a domain, Shaw (1992), and thus can be used to evaluate the fluid, pressure and energy fields. This is advantageous in situations such as heat exchanger sections since a detailed picture of the flow field can be built up, enabling analysis of why the heat transfer is good or bad at particular

locations. CFD is not yet a mature technology so detailed experimental studies are still needed to compliment and validate the CFD results. Once validation is complete CFD can be used in its own right as a design tool for heat exchangers.

By combining experimental and numerical techniques both the local velocity and heat transfer coefficients can be obtained, thus regions of poor heat transfer and their causes can be identified. Many different heat transfer enhancement techniques have been used, i.e offset strip fins, wavy fins and turbulence generators, Brockmeier et al. (1993). Most of these use the principle of laminar boundary layer growth and separation to increase the heat transfer, but the penalty for this can be a large increase in the pressure drop through the heat exchanger. A new development noted by Bergles (1997) as particularly significant for the enhancement of heat transfer is the use of vortex generators. Vortex generators are shapes punched out of a fin, usually in the shape of a delta, and can have four different forms, Figure 1.1. When they are attached by the base they are known as rectangular and delta wings and when they are attached by their chord they are known as rectangular and delta winglets. The sharp leading edges of the vortex generator cause the flow to separate and form a longitudinal vortex in the downstream direction. These vortices can either be formed having a common flow down towards the plate, Figure 1.2a, or a common flow away from the plate, Figure 1.2b. If single winglets are used then the vortices formed can either be co- or counter-rotating. The vortices cause mixing of the hot air near the plate with the colder bulk air. Vortex generators also have the advantage that if placed correctly they can disrupt the normally stagnant

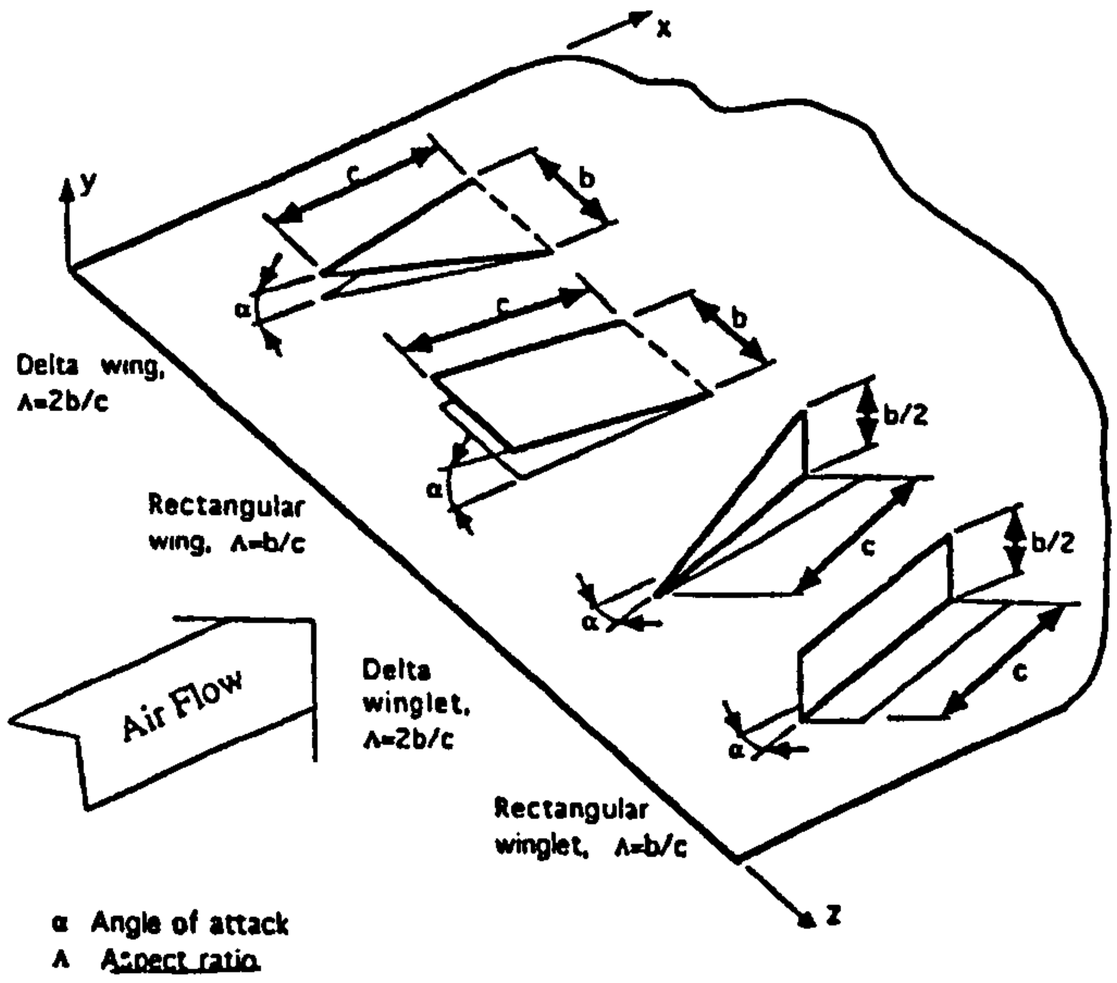

Figure 1.1: The four different types of vortex generator, a: delta wing, b: rectangular wing, c: delta winglet pair, d: rectangular winglet pair, from Fiebig (1993)

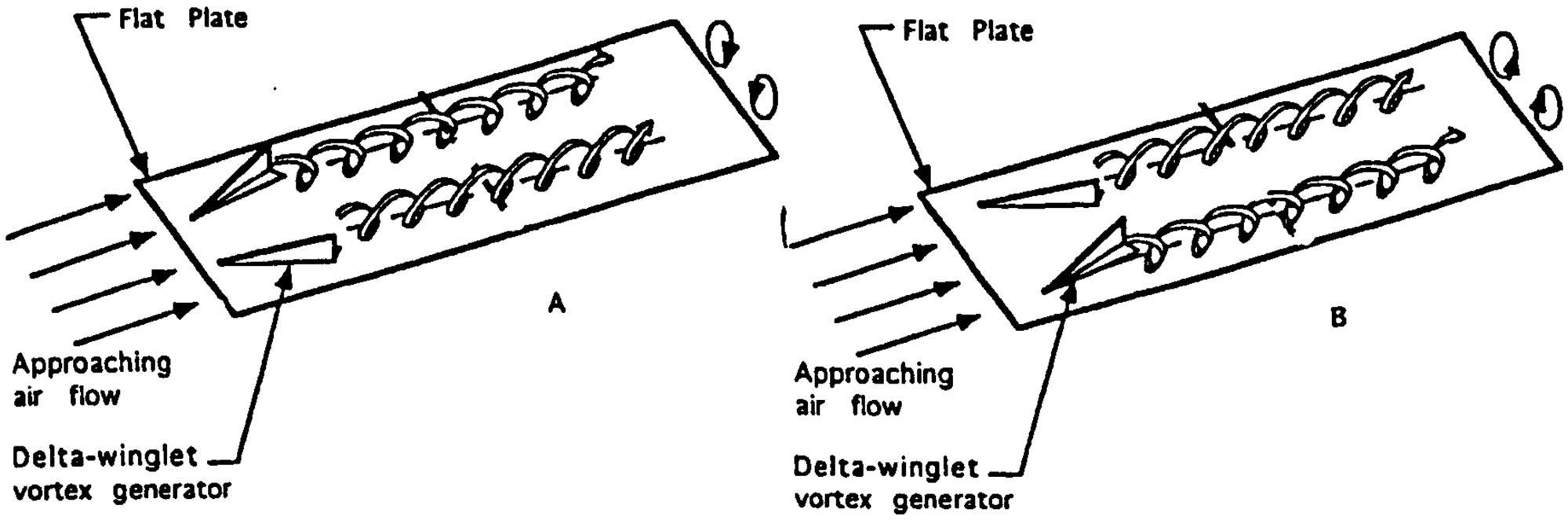

Figure 1.2: A schematic representation showing two vortex pairs. (a) Common flow down; (b) Common flow up, from Jacobi and Shah (1995)

wake region and thus improve the heat transfer there too. Previous studies such as Fiebig (1993) have shown that whilst the enhancement in heat transfer has been high, the penalty in pressure drop through the heat exchanger section has been low. Brockmeier et al. (1993) showed that vortex generators have also been very competitive with other types of heat transfer enhancing surfaces.

To validate a CFD model with an experimental model, the same boundary conditions, geometry, and Reynolds number have to be used. It was observed that this had rarely been achieved although many numerical and experimental studies on heat exchangers have been performed, both with and without vortex generators. Of the published numerical studies about vortex generators and vortex generators in heat exchanger sections, it was noted that results were computed using specially developed computer codes written by universities. These types of codes were usually tailored to suit the specific problem. These university written codes are not generally available to the designer of heat exchangers, who has to rely on commercially available CFD codes. These commercial codes are developed for general purpose fluid mechanics and their ability to predict heat transfer coefficients and pressure drops for the vortex generator situation needs to be analysed before it can be assumed correct. Further, it was observed that many of the studies carried out were with Reynolds numbers greater than 2000, i.e. fully developed turbulent flow. Kakaç (1982) stated that in many common applications a very important range of Reynolds numbers lie below 500. In the review paper of Jacobi and Shah (1995) careful low Reynolds numbers experiments were noted as a future research need.

The low Reynolds number is due to the high number of fins per unit length used in many common applications of compact heat exchangers resulting in a laminar flow regime.

1.2 Aims and Objectives

1.2.1 Aims

The aim of this investigation is:

To investigate in detail the local heat transfer characteristics of a fin-tube heat exchanger with and without vortex generators at low Reynolds numbers (Re < 700) with a view to identifying areas of poor heat transfer and the effect of vortex generators on the heat transfer and pressure drop.

1.2.2 Objectives

This investigation thus had three main objectives:

- To investigate the use of liquid crystals in determining heat transfer characteristics for both steady state and transient techniques.

- To model the surface temperature of a fin in a heat exchanger, using a commercial CFD package.

- To compare the results from the physical experiments with those from CFD.

1.3 Layout of thesis

In Chapter 1 the background to the problem is presented and areas where there are gaps in the existing knowledge identified. Chapter 2 then presents a literature review covering previous work on vortex generators. Chapter 2 is split into two main sections: the first reviews experimental and numerical techniques that enable the heat transfer and pressure drop to be measured, the second section reviews results obtained from the various experimental and numerical techniques with respect to the effect of vortex generators on the heat transfer and pressure drop.

The selection of the experimental technique to measure the heat transfer coefficient is discussed in Chapter 3 which also includes a comparison of the steady state and transient techniques where the boundary condition of constant heat flux has been used. The uncertainty in both these techniques has been analysed and where differences have been noted between the two sets of solutions, efforts have been made to reconcile the results. The test set-up of the chosen experimental technique is described along with the data reduction equations that enable the heat transfer coefficient to be analysed.

The use of a commercial CFD code to calculate the heat transfer coefficient and pressure drop in heat exchanger sections, with and without vortex generators, is described in Chapter 4. The meshing strategy used to model the various test sections is been described along with the boundary conditions that are needed to simulate the experimental problem. Validation of the numerical technique to ensure that the

resulting CFD solutions are near to grid-independent solutions is also discussed.

The results obtained from the experimental technique in Chapter 3 and the numerical technique in Chapter 4 are presented and discussed in Chapter 5. The experimental and numerical results are compared to assess the prediction of heat transfer and pressure drop by the CFD code. The effect of placing vortex generators in the flow field is discussed and with the aid of the CFD predictions the flow field is analysed. The effect of different vortex generator angles of attack and Reynolds numbers is discussed. Finally, in Chapter 6, some conclusions are offered.

Chapter 2

Literature Review

This chapter is a literature review which looks at previous work investigating fin-tube heat exchangers, and the use of vortex generators to enhance heat transfer in fin-tube heat exchangers. This chapter is split into two main parts. The first describes the experimental and numerical techniques that enable the heat transfer coefficient to be evaluated, including: a review of the governing equations of heat and fluid flow, the experimental techniques used to measure heat transfer, and the numerical methods used to predict heat transfer. Turbulence and its numerical modelling are very briefly reviewed as these are mentioned in later sections. In the second part of this chapter the results obtained using the various experimental and numerical techniques described in the first part are reviewed. This review starts by looking at previous work on vortex generators to enhance heat transfer and the effects of different vortex generator configurations in laminar and turbulent boundary layers. Plain channels and heat exchanger sections without vortex generators are then covered to assess the flow patterns before vortex generators are added. Finally, plain channels and heat exchanger sections with vortex generators are reviewed to determine their effects on heat transfer and pressure drop.

2.1 The Governing Equations of Fluid and Heat Flow

In this literature review it is perhaps prudent to begin with the governing equations of fluid flow and heat transfer. These governing equations describe the flow phenomena seen in the experimental tests such as recirculation zones behind tubes and high heat transfer rates in developing boundary layer regions. The following equations are also used in numerical techniques to predict the flow and heat transfer. The governing equations of fluid dynamics are formulations, appropriate to a fluid motion, of the usual laws of mechanics, i.e. conservation of mass and Newton's laws of motion, Versteeg and Malalasekera (1995). The governing equations of heat transfer are formulations of the laws of thermodynamics, namely conservation of energy.

2.1.1 Continuity equation

The continuity equation, Schlichting (1979), represents the concept that the mass of fluid is conserved into and out of a control volume:

$$\frac{\partial \rho}{\partial t} + \frac{\partial (\rho u)}{\partial x} + \frac{\partial (\rho v)}{\partial y} + \frac{\partial (\rho w)}{\partial z} = 0 \tag{2.1}$$

where ρ, is the density, u, v, w are the velocity components, t is time, and x, y, z, are the respective spatial co-ordinates.

2.1.2 The Navier-Stokes equations

The Navier-Stokes equations are a representation of Newton's second law of motion, that is, the rate of change of momentum equals the sum of the forces on a volume of fluid. Using the format of Versteeg and Malalasekera (1995) the substantive derivative of the rate of increase of momentum per unit volume in the x-direction can be defined as:

$$\rho\frac{Du}{Dt} = \rho\left(\frac{\partial u}{\partial t} + \mathbf{u}\,.\,grad\,u\right) \tag{2.2}$$

The Navier-Stokes equations can be written in the x, y, z directions respectively as:

$$\rho\frac{Du}{Dt} = -\frac{\partial p}{\partial x} + \frac{\partial}{\partial x}\left[2\mu\frac{\partial u}{\partial x} + \lambda\,div\,\mathbf{u}\right] + \frac{\partial}{\partial y}\left[\mu\left(\frac{\partial u}{\partial y} + \frac{\partial v}{\partial x}\right)\right] + \frac{\partial}{\partial z}\left[\mu\left(\frac{\partial u}{\partial z} + \frac{\partial w}{\partial x}\right)\right] + S_{MX} \tag{2.3}$$

$$\rho\frac{Dv}{Dt} = -\frac{\partial p}{\partial y} + \frac{\partial}{\partial x}\left[\mu\left(\frac{\partial u}{\partial y} + \frac{\partial v}{\partial x}\right)\right] + \frac{\partial}{\partial y}\left[2\mu\frac{\partial v}{\partial y} + \lambda\,div\,\mathbf{u}\right] + \frac{\partial}{\partial z}\left[\mu\left(\frac{\partial v}{\partial z} + \frac{\partial w}{\partial y}\right)\right] + S_{MY} \tag{2.4}$$

$$\rho\frac{Dw}{Dt} = -\frac{\partial p}{\partial z} + \frac{\partial}{\partial x}\left[\mu\left(\frac{\partial u}{\partial z} + \frac{\partial w}{\partial x}\right)\right] + \frac{\partial}{\partial y}\left[\mu\left(\frac{\partial v}{\partial z} + \frac{\partial w}{\partial y}\right)\right] + \frac{\partial}{\partial z}\left[2\mu\frac{\partial w}{\partial z} + \lambda\,div\,\mathbf{u}\right] + S_{MZ} \tag{2.5}$$

where p is the pressure, μ is the dynamic viscosity, λ is the second viscosity, $\mathbf{u}$ is the vector notation for velocity and S_M are the source terms.

The second viscosity, λ, arises in the Navier-Stokes equations due to volumetric deformation of fluid particles. However, its effect is generally small and a good

working approximation of $\lambda = -2/3\mu$ was proposed by Schlichting (1979). It is often useful to rearrange the viscous stress terms in the above equations to determine the effect of each term. The smallest contributer to the viscous stress is the term with the second viscosity included. Part of this term is included in the source term so that the Navier-Stokes equations reduce to (in the x-direction):

$$\rho\frac{Du}{Dt} = -\frac{\partial p}{\partial x} + div(\mu\, grad\, u) + S_{MX} \tag{2.6}$$

2.1.3 The energy equation

The energy equation is a representation of the first law of thermodynamics, that is, the rate of change of energy is equal to the sum of the heat addition to and the rate of work done on a fluid particle, Versteeg and Malalasekera (1995). Defining the substantive derivative for the rate of increase of internal energy:

$$\rho\frac{De}{Dt} = \rho\left(\frac{\partial e}{\partial t} + \mathbf{u}\,.\,grad\, e\right) \tag{2.7}$$

where e is the internal energy.

The energy equation can be written:

$$\rho\frac{De}{Dt} = -p\, div\, \mathbf{u} + div(k\, grad\, T) + \Phi + S_i \tag{2.8}$$

where k is the thermal conductivity and T is the temperature.

Note that Φ is the dissipation function, which is written:

$$\Phi = \mu\left\{2\left[\left(\frac{\partial u}{\partial x}\right)^2+\left(\frac{\partial v}{\partial y}\right)^2+\left(\frac{\partial w}{\partial z}\right)^2\right]+\left(\frac{\partial u}{\partial y}+\frac{\partial v}{\partial x}\right)^2 + \left(\frac{\partial u}{\partial z}+\frac{\partial w}{\partial x}\right)^2+\left(\frac{\partial v}{\partial z}+\frac{\partial w}{\partial y}\right)^2\right\}+\lambda(div\,\mathbf{u})^2 \tag{2.9}$$

and S_i is the source term:

$$S_i = S_E - \mathbf{u}.S_m \tag{2.10}$$

where S_E is the energy source and $\mathbf{S}_m$ is the momentum source.

The temperature can then be solved using the equation of state for a perfect gas:

$$e = c_v T \tag{2.11}$$

where c_v is the specific heat at constant volume.

2.2 Heat exchanger technologies

A heat exchanger is a device for transferring internal thermal energy between two or more fluids at different temperatures. Many different types of heat exchanger exist and they can be classified in many ways. Fraas and Özişik (1965), Shah (1981), Walker (1982) and Shah (1982a) broadly classify heat exchangers according to the transfer process, degree of surface compactness, construction features, flow arrangement and heat transfer mechanism. Under the classification of transfer process, the

fluids in the heat exchanger can either be in direct contact or indirect contact. In direct contact the heat transfer occurs between two imiscible fluids; an example of such transfer is the flow through a cooling tower. In the indirect case the fluids are separated, as in a car radiator. Tubular, plate, plate-fin, tube-fin and regenerative heat exchangers are all examples where the heat exchanger has been classified according to its constructional features. The principle flow arrangements for heat exchangers are parallel-flow, counterflow, cross-flow and multipass flow. This classification of flow arrangements also allows the fluids to be both unmixed or specifically for the crossflow heat exchanger design have mixed fluids. For the classification of heat transfer mechanism, the heat transfer can occur in a combination of any two of the following, (a) single phase forced or free convection, (b) phase change (boiling or condensation), or (c) radiation with or without combined convection. Typical examples of each situation are (a) the gas side of an automotive car radiator, (b) surface condensers for large steam power plants and (c) waste heat rejection from space vehicles. A compact heat exchanger is quite arbitrarily defined as a heat exchanger where the surface area density (usually the gas side) is greater than 700 m^2/m^3. Once a heat exchanger has been classified as compact it can be further classified by its construction features. For applications that involve heat transfer between a liquid and a gas and between two gases, Anon. (1994) has quoted many benefits of using compact heat exchangers.

The extended surface on the gas side of a compact heat exchanger is commonly made from plain sheets to minimise the cost of materials and labour in manufacturing,

Shah (1982a). However, as explained in the introduction, there is a limit on the maximum possible gas side heat transfer area for efficient heat transfer. To overcome this limit a number of heat transfer enhancement techniques have been used in the past. These include banks of louvres, offset strip fins and tabs and ripples, Baldwin (1989); which are made by punching the fin into the required shape. The advent of high power computing facilities has enabled time dependent solutions of enhancement techniques such as louvres to be studied in detail, Atkinson et al. (1998). Louvres which are commonly used in heat exchangers are now, as a result, more understood. However, they are beyond the scope of this work and for reviews of these heat transfer enhancement techniques the reader is referred to Shah and Webb (1983), Baldwin (1989) and Fisher (1996).

2.3 Technologies to measure and predict heat transfer

In this section the technologies that are currently being used to measure and predict heat transfer are reviewed. These can be put into two groups, namely experimental techniques and numerical methods. The former have been more widely used but as computing power increases so numerical techniques are becoming more popular.

2.3.1 Experimental techniques to measure heat transfer

The major problem in determining the heat transfer coefficient in internal or external flows is the determination of the relevant surface temperature. Once this is known

the heat transfer coefficient ($h = \dot{q}/\Delta T$) can be easily calculated. Two techniques have commonly been used to measure the local surface temperature: thermocouples and liquid crystal thermography.

Thermocouples have been used in a number of vortex generator studies in plain channels such as Eibeck and Eaton (1987), Igarashi and Iida (1988), Torii and Yanagihara (1989), Myrum et al. (1993) and Pauley and Eaton (1994). Due to the large number of thermocouples needed, over 160 in the Eibeck and Eaton (1987) study, the use of thermocouples has usually been limited. Another development in the measurement of surface temperature was the use of temperature sensitive paint. This method was described by Throckmorton and Stone (1974) and was used in heat transfer studies on finned tubes, Jones and Russell (1981), and a plain channel with vortex generators, Russell et al. (1982). The disadvantage of using temperature sensitive paint is that its use is restricted to one experiment before new paint has to be applied. The basis of this technique was however developed into the currently used liquid crystal technology. This is now the most commonly used method to measure surface temperature in heat transfer experiments.

Liquid crystals change colour over discrete and reproducible temperature bandwidths. By calibration of the colours displayed, the liquid crystals can be used to measure the surface temperature. The application of liquid crystal thermography for the measurement of surface temperature and heat transfer was reviewed by Yianneskis (1986). Baughn and Yan (1991a) reviewed the actual methods whereby

liquid crystals were used for the measurement of local heat transfer coefficients. The ease with which the surface temperature can be determined when liquid crystals are used was also discussed by Cooper et al. (1975), Hirsch et al. (1980) and Moffat (1990). Liquid crystals have been used in numerous heat exchanger/vortex generator studies which include Tiggelbeck et al. (1993), (1994), Critoph and Holland (1996), Fisher (1996), Schulz et al. (1996), Critoph and Fisher (1998) and Critoph et al. (1999).

Once the surface temperature can be measured, the most common ways to determine the heat transfer coefficient are the steady state and transient techniques. These techniques have been reviewed by Jones and Hippensteele (1987), Baughn et al. (1989), Baughn and Yan (1991b) and Leiner et al. (1996).

The heat transfer coefficient in the transient method is determined from the response of the surface temperature to a step-change in the local temperature, Jones (1991). The surface can either be considered as being part of a semi-infinite body (the thick wall approach), or as being described by the lumped capacitance model (the thin wall approach) where the temperature gradient through the thickness of the test section is assumed to be zero. Although Valencia et al. (1995) showed that the thick wall technique has some advantages over other techniques, particularly the steady state technique (to be discussed later in this section), in practice the thick wall technique is rarely used in channel flow type situations. This is due to the depth of the test section required to ensure that the heat transfer process can be

considered to be one-dimensional into a semi-infinite medium. Schultz and Jones (1973) have provided a guideline for the minimum thickness:

$$x > 4\alpha\sqrt{t} \tag{2.12}$$

where x is the minimum thickness and α the thermal diffusivity.

The thin wall transient technique has been used in numerous channel flow investigations with tubes and/or vortex generators. These include, Tiggelbeck et al. (1993), (1994), Critoph and Fisher (1998) and Critoph et al. (1999).

In the steady state technique ($\partial T/\partial t = 0$) the heat transfer coefficient is determined by an energy balance approach. This technique requires a constant heat flux boundary condition on the surface and has been described by Hippensteele et al. (1983, 1985, 1986), and Baughn et al. (1985, 1986). The constant heat flux boundary condition can be difficult to achieve, but is usually achieved by heating a very thin conductive coating. An early example of this was a copper coating used in a flat duct by Hatton and Wooley (1972). The difficulty in achieving uniformity of heat flux was highlighted by Jambunathan et al. (1994) who found that there could be as much as a $\pm 30\%$ variation in the measured heat flux when a stainless steel heater was used. A carbon sheet gave a variation of $\pm 4.5\%$ rising to $\pm 12\%$ for the commonly used gold sheet. A novel idea to reduce the variation in heat flux on the surface was discussed by Critoph and Holland (1996), Fisher (1996), Critoph and Fisher (1998) and Critoph et al. (1999). This technique used a powerful uniform

light source to heat the surface covered by liquid crystals directly by absorption. This method produces a steady and uniform heat flux of within ±2 % over the area of interest. The technique also has the advantage that the method of heating is non-obtrusive since it is by radiation. Therefore modifications to the fins can be easily achieved and the surface of interest can have curvature in two directions, unlike when a surface heater is used which limits curvature to one direction.

Comparisons of the steady state and transient techniques have been carried out by Baughn et al. (1986), Jones and Hippensteele (1987), Baughn et al. (1989), Valencia et al. (1995), Fisher (1996), Critoph and Fisher (1998) and Critoph et al. (1999). Valencia et al. (1995) investigated the effect of tangential conduction on the fin temperature when using liquid crystal thermography. They compared results for the steady state, thick and thin wall transient techniques with a numerical model that included three-dimensional conduction in the fin. The effect of tangential conduction smoothes the temperature distribution and differences of 100% or more are found between the numerical and the steady state experimental results. This discrepancy reduces to less than 20% for the thick wall transient case and less than 4% for the thin wall transient case. Critoph and Fisher (1998) and Critoph et al. (1999) investigated the tangential conduction in a heat exchanger section using the steady state technique. They reported that the calculated tangential conduction was a function of the area on which the calculation was based, and that the value of heat transfer had to be adjusted on average by only 2% to allow for tangential conduction. These much lower values are presumably due to the lower Reynolds number used

which requires a lower heat flux. In an impinging jet example, Baughn and Yan (1991a) reported that the results from the steady state and transient techniques were in excellent agreement. However, Jones and Hippensteele (1987) and Baughn et al. (1989) found that the distribution of the heat transfer coefficient varied considerably when different boundary conditions were used. Jones and Hippensteele (1987) found that the results could be made consistent in the case of a flat plate by using the flat plate integral techniques proposed by Kays and Crawford (1980). To try to reduce the differences in the boundary conditions, Fisher (1996) adapted the steady state test set-up, where a constant heat flux boundary condition was used, to a thin wall transient test, also with a constant heat flux boundary condition. The results for the transient test did not agree with the steady state results, the maximum difference being 50% at the trailing edge where the transient technique showed an increasing local heat transfer coefficient. It was shown that the difference in the results were due to differences in local bulk air temperature at the transition point of the liquid crystals. In the transient technique the bulk air temperature at the transition point will be lower than in the steady state case; this gives a higher heat transfer coefficient based on inlet temperature. The two sets of results can be reconciled by basing each set of results on the local bulk air temperature.

Uncertainty in the measurement of the heat transfer coefficient was analysed by Baughn et al. (1989) who found that the steady state technique had lower uncertainty compared to the transient technique. As noted by Ashforth-Frost (1994), the main source of uncertainty in the transient technique is the evaluation of the thermal

properties of the material used to model the fin. In the transient technique the uncertainty decreases with decreasing heat transfer coefficient, but in the steady state technique the uncertainty decreases with increasing heat transfer coefficient due to the corresponding rise in heat flux. The heat transfer by radiation from the surface being measured can have a significant effect on the value of heat transfer coefficient as noted by Baughn et al. (1989). In the steady state technique a correction can be applied to the value of heat transfer coefficient, such as that proposed by Fisher (1996), if the emissivity of the liquid crystal surface is known. This correction cannot be applied in the transient technique as the radiation flux is time dependent, Leiner et al. (1996).

Various other techniques can be used to measure the local heat transfer coefficient. A mass transfer coefficient can be defined analogously to the heat transfer coefficient. This is usually done by the Ammonia Absorption Method (AMM) described by Kottke et al. (1977) and Schulz et al. (1996). The ammonia is absorbed from a gas flow at a porous surface coating impregnated by a reactant solution. A fast colour changing reaction yields a surface colour distribution showing local surface concentration of absorbed ammonia. This is analogous to the local heat transfer coefficient. Infra-red thermography was used by Lorenz (1995) to measure the surface temperature directly, and other workers such as Kurosaki et al. (1988) have used laser holographic interferometry to determine the temperature profile of the flow around fins.

The analysis of liquid crystal isotherms has usually been achieved by manual methods where the isotherm is identified by eye. Kasagi et al. (1989) and Akino et al. (1989) described a process where a number of narrow band sharp cut-off monochromatic filters were used to produce clearly isotherms over a range of temperatures thus reducing the impact of human interpretation in the analysis. Automatic analysis of liquid crystal isotherms was described by Schulz et al. (1996) and Ashforth-Frost et al. (1992). The former work uses the reflected intensity of a mono-chromatic picture to identify the isotherm while the latter uses grey scale information. Full colour interpretation of liquid crystal isotherms was used by Behle et al. (1996) who related the hue values of the reflected light to the temperatures. Full automatic colour interpretation was achieved with this technique.

2.3.2 Numerical methods to calculate heat transfer

Computational methods to determine compact heat exchanger performance and design parameters have been used since the earliest days of the digital computer. These studies were limited in size and complexity, due to lack of available computing power, to the calculation of overall heat transfer and pressure drop. As Shah (1982b) reported the non-dimensional heat transfer ($j = StPr^{2/3}$) and local friction factor ($f = \Delta P D_h / 1/2 \rho u^2 L$) data had to be known for the compact heat exchanger surface considered in the analysis and the results were based on the effectiveness-Number of Transfer Units (ϵ-NTU) relationships of Kays and London (1955).

To exactly predict local velocity, pressure and temperature fields using the governing

partial differential equations the variables have to be calculated at an infinite number of points. This is obviously impractical so a technique of transforming the analogue partial differential equations into a form that can be readily handled by numerical methods has had to be used, Shaw (1992). This is known as numerical discretisation. It was not until the early 1980s that it was possible to solve the complex and often highly non-linear fluid flow equations for the local heat transfer, velocity and pressure fields. Some of the early work in this area was reported by Patankar (1982a, 1982b) and Spalding (1982a, 1982b).

The early work in the area of computational prediction of fluid flows and heat transfer has resulted in three commonly-used techniques, all of which discretise the governing equations in different ways. These methods are usually known as the finite difference, finite element and finite volume methods.

The finite difference technique uses a Taylor series expansion to determine the value of the dependent variable at two or more positions a small distance each side of a reference point, in terms of derivatives. By adding and subtracting the equations for these two positions the first and second order derivatives at the reference point can be found. Smith (1985) is a standard reference on the finite difference technique and Abbot and Basco (1989) provide a comprehensive review of the use of finite differences in fluid flow, as do Croft and Stone (1977) who described the technique for heat transfer calculations. The method assumes that terms of higher than a certain order can be neglected if the grid spacing is small. This leads to a truncation

error in the difference equations leaving the derivatives generally first-, second- or third-order accurate.

The finite element method for fluid flow and heat transfer evolved from the use of finite elements in the calculation of stress and strain. In this technique for fluid flow and heat transfer analysis, which is explained in detail by Zienkiewicz and Taylor (1989) and Lewis et al. (1996), the domain of interest is split into a finite number of sub-domains usually known as elements. The variation of the parameter of interest is prescribed as being linear between the nodes, but higher order variations can be calculated. As the governing equations usually contain second order derivatives, and the second derivative of a linear profile cannot be defined, a variational formulation of the governing equations needs to be used. In this form, the higher order derivatives are reduced to first order by integrating by parts. The Galerkin approach is used to transform the analogue equations into a numerical form. In using this approach an explicit form of the governing equations is produced. This explicit form can be expressed as a matrix equation, and after the application of boundary conditions, the equations can be solved.

The finite volume discretisation method was originally developed as a general purpose method for the prediction of heat and mass transfer, fluid flow and related processes by Patankar and Spalding (1972). The governing equation for the variable of interest is integrated over the control volume to yield a discretised equation for a point at the centre of the control volume. To calculate the gradients and hence

the fluxes at the control volume faces an approximate distribution of the properties between nodal points is used. As Patankar (1980) reported, this method has the advantage that the resulting solution would imply that integral conservation is exactly satisfied over the whole domain of interest.

The spatial flux discretisation can be achieved in a low- or high-order manner. Higher order schemes such as central differencing, linear upwind differencing (LUD) of Wilkes and Thompson (1983), monotone advection and reconstruction scheme (MARS) Anon. (1998) are second order accurate, and the quadratic interpolation of convective kinetics (QUICK) of Leonard (1979) is third-order accurate. These schemes preserve steep gradients in the flow variables but in some cases may provoke numerical instabilities. This can lead to spatial oscillations which are often termed numerical dispersion, Hirsch (1960). The most common first-order accurate scheme is upwind differencing, described by Courant et al. (1952), Gentry et al. (1966), Barakat and Clark (1966) and Runchal and Wolfshtein (1969). This method produces solutions which obey the physical bounds but give rise to smearing of gradients, unless the the flow field is convection dominated. This effect is known as numerical diffusion, Lai (1983) and Leschinziner (1980). In an effort to keep the superior accuracy of a higher-order method with the robustness of the upwind method, Spalding (1972) proposed a differencing scheme that uses a combination of central and upwinding differencing schemes. Variants of this procedure are now commonly used in numerical methods.

One of the fundamental problems of using CFD is the calculation of the pressure gradient term in the Navier-Stokes equations. For a given problem, if the pressure gradient is known the calculation of the velocity vectors is similar to that of any scalar variable. However, for many engineering applications of CFD the pressure field is not known and therefore has to be calculated as part of the solution. To overcome the problems associated with the non-linearities in the equation set and the pressure-velocity linkage, an iterative solution strategy is used. This iterative strategy uses an initial guess for the velocity and pressure fields. This guessed pressure field is used to solve the momentum equations, and then a pressure correction equation deduced from the continuity equation is solved to obtain a pressure correction field. This in turn used to update the velocity and pressure fields. The iterative process is continued until a converged velocity and pressure field is obtained. This is the basis of the SIMPLE (Semi-Implicit Method for Pressure-Linked Equations) algorithm developed by Patankar and Spalding (1972) and described by Patankar (1980). Other methods to calculate the pressure field from the velocity field include the PISO (Pressure Implicit with Splitting Operators) algorithm of Issa (1986) and reported by Issa et al. (1986) and Issa et al. (1991) which uses two corrector stages. The SIMPISO algorithm performs just one momentum corrector but uses a more elaborate treatment of the pressure gradient terms arising from grid nonorthogonality. A comprehensive comparison of different pressure-velocity solution algorithms by Jang et al. (1986) showed that for problems in which the momentum equations are not coupled to a scalar variable, the PISO algorithm showed robust convergence behaviour and required less computational effort than SIMPLE variants. However

when the scalar variables are linked to velocities, PISO had no significant advantage over the other methods.

At low Reynolds numbers the flow is smooth and adjacent layers of fluid slide past each other in an orderly fashion. However, above a certain Reynolds number a radical change in the fluid occurs, the fluid particles move in a random and chaotic motion. Accurate turbulence modelling, Versteeg and Malalasekera (1995), has always proved difficult because of the wide range of eddy scales and frequencies. Fortunately, for the majority of engineering applications of CFD it is only the time-averaged properties of the mean flow that are required. To model a time average of a fluctuating flow, the instantaneous property of the flow, such as velocity, is modelled as the sum of the average velocity and a time varying fluctuation component. This definition of the instantaneous property is substituted into the Navier-Stokes equations to form what are known as the Reynolds equations. However, in deriving the Reynolds equations at least six unknowns are added to the equation set in the form of the Reynolds stresses. There are now more variables than equations and this is known as the closure problem. Many suggestions have been made as how to account for the transport of turbulence and thus, Abbott and Basco (1989), it has become customary to classify turbulence models by the number of transport equations used for the turbulence quantities. Usually turbulence models use 0, 2 or 6 turbulent transport equations.

Prandtl's mixing length model is the most widely used zero equation turbulence

model. These models which have been developed by Baldwin and Lomax (1978) and Cebeci and Smith (1974) usually predict boundary layers, shear layers and mixing layers well, but are completely incapable of describing flows with separation and recirculation. Perhaps the most popular turbulence model as used in many CFD programs, is the two-equation k-ϵ developed by Launder and Spalding (1974). This model uses two equations, one for the kinetic energy, k and one for the rate of dissipation, ϵ to define the velocity and length scales respectively. The k-ϵ model has been reported as having excellent agreement for many industrially relevant flows, but produces poor results with large extra strains, such as curved boundary layer flow and swirling flows. The most complex turbulence model is the Reynolds Stress Equation model (RSM) which uses seven partial differential equations, one for the transport of each of the six independent Reynolds stresses and one for the scalar dissipation rate. This model has the advantage that it can calculate very accurately all the Reynolds stresses and the mean flow properties for more complex flows such as curved flows and non-circular duct flows. However, as seven extra partial differential equations are being modelled, the increase in computer time required is large.

What has been described here is only a very brief introduction to turbulence and its modelling, the reader is referred to Schlichting (1979), Bradshaw (1971), Abbott and Basco (1989) and Hinze (1975) for more detailed descriptions.

As the use of CFD becomes more widespread in engineering applications, determining the accuracy of numerical techniques has become more important. Previously,

results would have been calculated from a single mesh, but this practice has become unacceptable, Roache et al. (1986), Ferziger (1988) and Roache (1990). Many of the difficulties in numerical techniques were highlighted by Fisher and Rhodes (1996) who included the determination of accuracy as one of the main concerns in using CFD for engineering applications.

Errors arise from the various components of a numerical method, these include: iteration procedure, grid generation and the discretisation process. The discretisation errors are the difference between the converged solution and the exact solution of the partial differential equations. The latter may be obtained using very fine grids such as benchmark solutions which exist in the literature for selected problems. Freitas (1995) compared several commercially available CFD codes against such benchmarks.

As the cost of running very fine grids is usually prohibitively large except for the simplest of problems, two methods are now usually used to evaluate the accuracy of the solution. These are straightforward repeat calculations with successively finer grids, and the Richardson extrapolation technique. By choosing a variable at a consistent point in the domain and observing the changes in that variable as the grid is successively refined it should be noted that the variable tends toward a fixed value. At this point a mesh independent result is achieved. Roache (1993) reported that successive grid refinement is perhaps the most straight-forward and arguably the most reliable method for reporting on the qualification of numerical uncertainty.

However, this technique can be expensive in the time that it takes to build and run a number of different meshes. The Richardson extrapolation technique, first reported by Richardson (1910) and (1927) allows a large amount of information about mesh independence to be gained from a maximum of three successively refined grids. In this method the error is expressed as a Taylor series in the parameter of grid spacing, Ferziger (1993). Two solutions are needed on at least two successively refined grids and the error is determined from the differences. As noted by Demuren and Wilson (1993), the result is only valid when the grid spacing is small enough for the leading term in the Taylor series to be dominant. However, when this is not the case the error estimate is also large showing unacceptable error in the solution. If a third grid is used then the order of the numerical scheme can also be estimated. This is a useful check on the final mesh refinement used, as the order of grid convergence calculated using Richardson extrapolation should always be the same or higher than the order of the discretisation used in the numerical model. The main problem with the Richardson extrapolation technique, reported by Celik and Zhang (1993) is that there has to be monotonic convergence of the variable of interest over the successively refined grids. Richardson extrapolation was used by Nguyen and Maclaine-cross (1988) to obtain the incremental pressure drop in parallel-plate heat exchangers down to infinitesimal mesh size.

2.4 Experimental and Numerical Results

2.4.1 Previous reviews of vortices to enhance heat transfer

Previous reviews of the current state of knowledge of using vortices to enhance heat transfer were published by Fiebig (1993) and (1998). The first review covered all the work to date using vortex generators and included 87 references. The formation of longitudinal vortices is discussed in detail along with the the different types of vortex generators and their effect on heat transfer and pressure drop. In the later review the work covered was more specific to vortex generators in boundary layer type flow and in channel flow. There was no discussion of vortex generators in fin-tube heat exchanger applications.

A later review by Jacobi and Shah (1995) critically reviewed recent progress on vortex-induced heat transfer enhancement. The review covers all areas, from the application of vortex generators in boundary layer flow through to the use of vortex generators in multiple row fin-tube heat exchangers. Most interestingly they tried to summarise some of the vortex generator results from different research groups. These results show a large variation in values claimed for heat transfer enhancement and pressure drop. Future research needs were also identified in this review paper.

In a review by Fiebig (1995a) the enhancement mechanisms of vortex generators in channel were discussed in detail. It was noted that the enhancement mechanisms consisted of three types: developing boundary layers, swirl, and flow destabilization. The transition to unsteady flow and turbulence was discussed, which was found to

occur at a much lower Reynolds number (Re $\approx$ 350), than the corresponding number for plane channel flow. For transitional flow regimes at Reynolds numbers of around 350 the effect of different types of boundary conditions on numerical models was presented. For rectangular winglet pairs at an angle of attack, β, between 25° and 55° it was found that symmetry boundary conditions would result in steady flow whereas periodic boundary conditions would result in time dependent flow. Transitional flow regimes with vortex generators were also discussed by Fiebig (1995b), who included discussions on transverse vortices and the effects of ribs with vortex generators.

2.4.2 Early investigations of vortex generators

The use of vortex generators for flow control is not a new idea and it has been investigated widely. The aim of much of this research has been in preventing boundary layer separation on aircraft wings and was reviewed by Schubauer and Spangenberg (1960), who also tested a number of vortex generator shapes for their effect on boundary layer development. The use of vortex generators for heat transfer enhancement only started in the late 1960s and there is relatively little work published in the area.

The first published report of the use of vortex generators for heat transfer enhancement appears to be Johnson and Joubert (1969). In this study they taped delta winglets on a cylinder in cross-flow. The winglets were located at fixed angular positions. It was found that the local Nusselt number increase could be as much as 200% with a reduction in drag due to the delayed separation around the cylinder.

However, overall heat transfer results were less encouraging with only minor improvements achieved. The effects of small protruding shapes, such as cubes, hemispheres and cones, mounted on flat plates was shown by Sedney (1973) to cause streamwise vortices in the flow direction. These protrusions caused horseshoe vortices such as would occur with a tube mounted perpendicular on a flat plate. The effect of the longitudinal vortices could persist downstream for a distance up to 100 times the height of the disturbance if the height of the disturbance was comparable to the boundary layer thickness at that point.

Co-rotating and counter-rotating longitudinal vortices generated by delta-winglets at $\beta = 12.5°$ and 25° were investigated by Edwards and Alker (1974). For a Reynolds number of 61500 it was found that the best performance was achieved when the angle of attack of the vortex generator was increased, in this case up to 25°. For counter-rotating vortices the maximum increase in local heat transfer was 40% and for co-rotating vortices 15%. The elevated levels of heat transfer were found to persist many winglet heights downstream, with only a 10% decrease from the maximum value of heat transfer for a downstream distance of 17 winglet heights in the case of counter-rotating vortices. No pressure drop information was reported in this study.

2.4.3 Vortex generators in laminar boundary layer flow

For laminar boundary layer type flow Tori and Yanagihara (1989) and (1991) investigated a single delta winglet. As expected, they found that the heat transfer coefficient increased with the angle of attack of the vortex generator. The heat

transfer coefficient was also increased when the height of the vortex generator was increased. Velocity measurements indicated that the heat transfer increase downstream of the vortex generator was due to the onset of turbulence in the flow. Closer to the winglet the increase was due to high vortical motion in the fluid. In further papers, Yanagihara and Tori (1990), (1991), (1992) and (1993) investigated different types of vortex generator shapes including: winglet pairs, rows of up to eight co-rotating winglets and winglet pairs in a counter-rotating configuration. Comparisons between the co-rotating and counter-rotating vortices showed that directly behind the vortex generator, counter-rotating vortices had a bigger effect on heat transfer than co-rotating vortices. However, further downstream the difference was negligible. This did not agree with the finding of Edwards and Alker (1974). As shown in Figure 2.1, apart from the main longitudinal vortex a horseshoe type

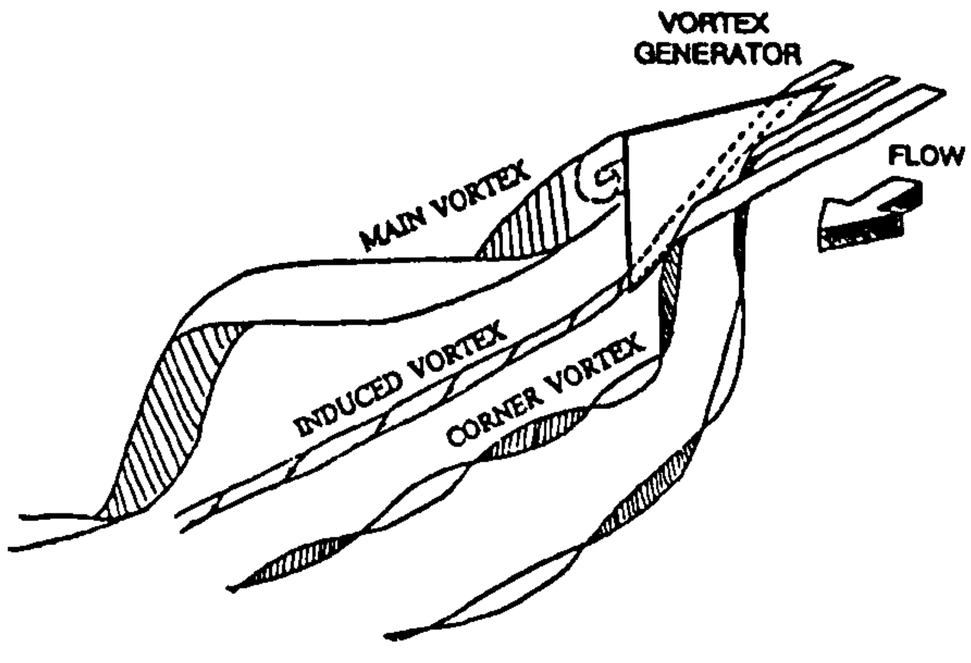

Figure 2.1: Vortex system generated by half-delta winglet, showing the main vortex along with the corner vortex and induced vortex, from Yanagihara and Torii (1993)

vortex was identified, which formed at the base of the vortex generator where it was fixed to the plate. An induced vortex was formed on the low pressure side of the vortex generator. Comparisons of vortex generator shape showed that rectan-

gular winglets offered the highest heat transfer enhancement. This was attributed to strong formation of main and corner vortices. Frontal area was shown to have a dominant effect on heat transfer. As is the case with other workers no pressure drop information was reported.

2.4.4 Vortex generators in turbulent boundary layer flow

A large number of papers have been published on vortex generators in turbulent boundary layers though only a few cover the effects of the vortices on heat transfer. The amount of work on vortex generators in turbulent boundary layers is presumably due to their application in boundary layer separation control and their similarity to Taylor-Görtler vortices occurring on concavely curved surfaces. Taylor-Görtler vortices can have serious implications for the life span of gas turbine blades. Detailed velocity measurements and heat transfer information behind a single delta winglet were published by Eibeck and Eaton (1985), (1986) and (1987), turbulent heat flux vectors and stress tensors were also measured by Wroblewski and Eibeck (1991). The longitudinal vortices were also found to persist a long distance downstream of the vortex generator as in the laminar case. Local increases in the Stanton number could be as large as 24% but local decreases of 14% were also noted in strong upwash areas. Overall heat transfer increases of around 10% were typically found. Mean velocity values showed localised boundary thinning in downwash flow and localised boundary layer thickening in upwash areas. This lead to an increase and decrease respectively in local heat transfer. They concluded from the velocity

measurements that the increase in heat transfer is due to distortion in the main flow rather than an increase in turbulent intensity. Delta winglet pairs and rows of winglets were studied by Pauley and Eaton (1988a), (1998b) and (1994). When the vortices have common flow down towards the wall it was found that the vortex cores were convected towards the wall and produced large boundary layer modifications leading to high heat transfer enhancement. However, when the common flow was away from the wall the vortex cores were lifted away from the wall reducing boundary layer modification. This was also noted by Mehta and Bradshaw (1988). As with the other studies no pressure drop information was given.

Computational models using the time-averaged Navier-Stokes equations with the standard k-ϵ model for turbulence were calculated for a single longitudinal vortex generated by a circular jet that issued through the wall into a turbulent boundary layer by Zhang and Collins (1993). They compared the calculated circulation to the circulation measured in a wind tunnel. This differed by only 11%. However, they did not compare measured vorticity or velocity distributions so no conclusions could be drawn as to whether the turbulence modelling was satisfactory. Mehta and Bradshaw (1988) doubted the applicability of the assumption of isotropic turbulent viscosity that is inherent in the k-ϵ turbulent model. This was confirmed by Lee et al. (1999) who compared a Reynolds Stress Model (RSM) with the standard k-ϵ and the experimental data of Pauley and Eaton (1988a). The RSM model was found to give better predictions for turbulent normal stresses and temperature distributions in the vicinity of the wall.

2.4.5 Experimental and numerical results for plain channels

The problem of fully developed laminar flow with heat transfer has a long history as it is one of the few problems where the governing equations can be solved directly. In early studies of the problem it was common to apply either a constant temperature or a constant heat flux boundary condition at the solid-fluid interface. With the assumption of a fully developed velocity profile, the theoretical Nusselt number distributions can be solved. Graetz (1883) was the first to solve this type of problem for tube flow. Numerous studies have been published on the Graetz problem each trying to reduce the underlying assumptions used to solve the governing equations. These have been extensively reviewed by Shah and Bhatti (1987) and Shah and London (1978) who also highlighted about 20 different channel shapes that could be applicable to heat exchanger design along with the many different boundary conditions needed to solve the governing equations.

Another problem applicable to heat exchanger design is that of simultaneously developing hydrodynamic and thermal boundary layers between parallel plates. This was first investigated by Sparrow (1955) for equal wall temperatures and Prandtl numbers between 0.01 and 50. With the same boundary conditions Hwang and Fan (1964) used a finite difference technique to calculate the theoretical Nusselt number distribution ($Nu = hd/k$). The results of Hwang and Fan (1964) were compared with an approximate analytical prediction by Rostami and Mortazavi (1990) who found good agreement except at low Prandtl numbers, due to the approximation used in the energy equation of a linear velocity profile. As with the Graetz prob-

lem many extensions of the original problem have been published, these have been reviewed by Kakaç and Yener (1982) and Kays and Crawford (1980).

In the results for boundary layers between parallel plates discussed above, it had been assumed that the fins had either a very high thermal conductance or an infinite one. This is clearly incorrect for many materials used in heat exchangers. Sparrow et al. (1978), Patankar et al. (1979) and Soliman et al. (1980) all concluded that the conductance of the fin has a marked effect on the surface heat flux variation. Fins with high thermal conductance had large variations of surface heat flux; when low conductance fins were used the surface heat flux was almost uniform.

Owing to the complexity of conjugate heat transfer problems the majority of the published work has been for the case of laminar flow. The mathematical difficulties in calculating Nusselt number distributions with conjugate heat transfer were highlighted by Luikov et al. (1971) and Mori et al. (1976). Both used an approximate analytical solution. A semi-numerical method was used by Barrozi and Pagliarini (1985) and a purely numerical approach was used by Campo and Schuler (1988).

Developing regions of velocity and thermal boundary layers, are of considerable practical as well as theoretical interest due to enhanced heat transfer levels in this region. Discretisation of the Navier-Stokes and energy equations by the finite difference method was carried out by Nguyen and Maclaine-Cross (1991) and Nguyen (1992). Both studies showed that the values of Nusselt number obtained were significantly greater than for classical Graetz-type solutions. Relationships for Nusselt

number against Reynolds number were given using the boundary condition types of constant wall temperature and constant heat flux. By means of extrapolation down to zero mesh size the maximum error reported for the prediction of Nusselt number was less than 1.6% for the Nguyen (1992) report.

Many predictions for Nusselt number distribution in plain channels assume a very small or zero fin thickness. However, with a finite fin thickness, intricate flow patterns are caused by a recirculation region that forms at the leading edge of the fin. Rahnema et al. (1997) modelled the two-dimensional continuity, Navier-Stokes and energy equations for an array of parallel flat plates with finite thickness. They noted that the heat transfer reduces in the recirculation region and then reaches a maximum at the re-attachment point. After re-attachment the Nusselt number distribution is similar to the entrance region of thin plates. In the separation region the value of friction coefficient ($c_f = 2w/\rho u^2 A_F$) is increased. Similar findings were reported by Hwang et al. (1996) who used the Naphthalene Sublimation technique (similar to AMM).

2.4.6 Experimental and numerical results for channels with vortex generators

Vortex generators in channel flow are more applicable to heat exchanger design than to boundary layer type flow. The use of vortex generators in channel flow was extensively reviewed by Fiebig (1998) who, along with his research group at Bochum, has contributed most of the work in this field. Only the key points will be

reviewed here.

The first work on longitudinal vortex generators in channel flow was published by Russell et al. (1982). In this study heat transfer and pressure loss information was reported. In preliminary investigations they first used triangular configurations of vortex generators at low angles of attack, and reported disappointing performance but did not give any details. This somewhat contradicts the work of Torii and Yanagihara (1989, 1991). When Russell et al. (1982) used punched vortex generators they found that greater increases in heat transfer were achieved when the punched hole was on the downstream side. Even better performance was obtained by using an embossed rectangular winglet pair where the height of the embossement was about half the channel height. On tests of a small matrix of plain fins and fins with vortex generators a 50% increase in heat transfer with a 40% increase in pressure drop was noted when vortex generators were used, the Reynolds number being approximately 240.

The local and average heat transfer for two rows of delta-winglet pairs which were punched from the fin material were experimentally measured by Tiggelbeck et al. (1993). Flow visualisation showed that, for the first row of delta winglets, the longitudinal vortex would break down and form a recirculation region at $\beta_{crit} = 70°$, whereas for the second row this reduced to $\beta_{crit} = 55°$. For a Reynolds number of 4600 (based on hydraulic diameter) and $\beta = 45°$ it was found that the second row of vortex generators acted as boosters for the first row and increased the local

heat transfer by 250%. For global values, the heat transfer was found to increase nearly linearly with Reynolds number, however the drag coefficient was found to tend towards a constant value with higher Reynolds number. The drag coefficient for a plain channel reduces linearly with increasing Reynolds number. With a Reynolds number of 6000 a heat transfer increase of 80% was found with a drag increase of 165% using two rows of vortex generators. The punched hole was on the upstream side (high pressure) of the vortex generator. No comparison was made with the hole on the downstream side.

The four basic types of vortex generator (a) rectangular wings (b) delta wings (c) rectangular winglet pairs and (d) delta winglet pairs were investigated by Tiggelbeck et al. (1994). Their effects on heat transfer and pressure drop for the Reynolds number range 2000 - 8000 were reported. To allow for comparisons between the different types, the angle of attack, vortex generator area, test fin area, blockage of the channel and channel geometry were all kept constant between tests. Results showed that delta winglets gave the highest average heat transfer enhancement followed by rectangular winglets. Delta wings gave the highest wing performance but gave considerably less enhancement than winglets. They concluded that winglets gave better performance than wings due to the upstream hole entraining less fluid through the hole. This concurs with the work of Yanagihara and Torii (1993) who showed that the corner and induced vortices were stronger on sharp edges. Tiggelbeck et al. (1994) also concluded that if the vortex generators were attached to the fin (i.e. without punched hole) then wings would give higher heat transfer en-

hancement than winglets. Due to the better performance of the winglets, only these were investigated further. Average Nusselt numbers were found to increase monotonically with Reynolds number at a greater rate than plain channels. The pressure drop increased monotonically with the angle of attack.

Early numerical studies of vortex generators in channel flow were reported by Biswas et al. (1988) and (1989), Fiebig et al. (1989) and Zhu et al. (1993). These studies dealt with mounted types of vortex generators with turbulent flow. A computational domain that included a delta wing with a punched hole was investigated by Biswas and Chattopadhyay (1992). Results from velocity vector plots showed that the main longitudinal vortex was reduced by a downward stream of fluid flow through the hole. Although there was some localised heat transfer enhancement around the hole they found a reduction in the overall heat transfer enhancement. For a channel with delta wings without holes at $\beta = 26°$, and a Reynolds number of 500 was compared to a plain channel, the average Nusselt number improvement was 34% and the friction factor increase of 79%. With the same geometry and a punched vortex generator the Nusselt number increase was 10% with a friction factor increase of 48%. This work was extended by Biswas et al. (1994) to include comparison with the experimental work of Fiebig et al. (1986). Only results averaged over a span were compared so no conclusion could be given for the applicability of the computational model to local effects.

For the case of a single delta winglet, Biswas et al. (1996) compared the predicted

local flow structure with those measured by a hot wire anemometer. Although this study did not include the effects of the hole left by punching, at a Reynolds number of 1580 and $\beta = 45°$ very good similarities were achieved between numerical model and experiments for local velocity. Values of j/f where presented which showed that even for $\beta = 15°$ the j/f value was 0.88 at the end of the channel.

A numerical model with the k-ϵ turbulence model was reported for a vortex pair by Zhu et al. (1993). These results were compared to the experimental results of Pauley and Eaton (1988b) and it was found that the velocity magnitude was correctly predicted within 13%. However, both the experimental results and the computational domain did not begin until 8.8 chord lengths downstream of the delta winglet. As a result the flow structure near the vortex pair was not calculated, so it could not be determined how well the k-ϵ model predicted local features.

For low Reynolds numbers the highest heat transfer enhancement was found to occur at $\beta = 45°$ for Re = 350 by Grosse-Gorgemann (1996). At low Reynolds numbers it was also found that self-excited fluctuations (i.e. the onset of turbulence) started at a Reynolds number of about 260. This is much lower than the corresponding value for a plain channel. This critical Reynolds number was found to decrease with decreasing winglet height and decreasing angle of attack.

2.4.7 Experimental results for heat exchanger sections

Local heat transfer coefficients

Details of local heat transfer are very important in the design of high performance heat transfer surfaces. This enables the effects on the local heat transfer and flow regime to be quantified when fin modifications are employed rather than averaged effects. The ammonia mass transfer technique was used by Krücklels and Kottke (1970) for an in-line geometry at Reynolds numbers of 3700 and 19000. The Naphthalene mass transfer technique was used by Saboya and Sparrow (1974), (1976a) and (1976b) for a staggered geometry with one, two and three rows respectively at Reynolds numbers ranging from 200 to 1000. They both reported high mass transfer at the leading edge of the fin where the boundary layer was developing and low mass transfer in the wake regions behind the tubes. They also reported high mass transfer in the horseshoe vortex regions in front of the tubes. For the in-line arrangement the mass transfer was lower for the vortex region in front of the second row tubes than the front row tubes. In the staggered arrangement the mass transfer in the horseshoe vortex regions was found to be dependent on the Reynolds number. At low Reynolds numbers, the highest mass transfer occurred in front of the first row tube; this reduced as the number of tube rows was increased. At higher Reynolds numbers all mass transfer levels were increased but the second row horseshoe vortex region had a larger maximum value than the first row. The third row horseshoe vortex region showed lower levels of mass transfer when compared to the first and second tube-rows. No pressure drop information was given in this study.

The effect of the horseshoe vortex on mass transfer was identified by Sparrow et al. (1984) who measured local mass transfer rates around a single cylinder attached to a wall, with the Reynolds numbers in the range 3500 to 23000. In the vortex region, a higher mass transfer was seen compared to the surrounding plate; this showed the presence of the horseshoe vortex was beneficial to increasing heat transfer. A similar study of a cylinder in channel flow by Ireland and Jones (1986) showed that the maximum heat transfer coefficient occurred at the stagnation point upstream of the cylinder. A single cylinder on a flat plate was also studied by Fisher and Eibeck (1990) using liquid crystal thermography. They reported that heat transfer levels were also increased downstream of the cylinder with peaks in the heat transfer occurring symmetrically about the centreline of the tube. They also noted that the peak augmentation level was reduced by 9% when the Reynolds number was increased from 7.7×10^4 to 1.3×10^5. This was attributed to a decrease in the boundary layer thickness resulting in a smaller horseshoe vortex.

Fin efficiency and local temperature distribution were reported by Rosman et al. (1984) for one- and two-row heat exchangers in the Reynolds number range 200 — 1200. They found the fin efficiency was higher for a two-tube row configuration than a single row, and the fin efficiency increased with increasing thermal conductivity of the fin. For a one-tube row configuration the fin efficiency was seen to decrease when the tube was moved toward the rear of the fin although the isothermal Nusselt numbers were higher.

All the heat transfer effects reported by Saboya and Sparrow (1974), (1976a) and (1976b) were also reported by Baldwin (1989) who used a temperature sensitive paint to measure local heat transfer coefficients for staggered row heat exchangers. Results were reported for heat exchangers with 1, 2 and 4 rows for a Reynolds number range of 100 — 3200. A four-times full scale model was also used to study the flow field by means of dye-streak flow visualisation. This showed that a horseshoe vortex was present at both the upper and lower tube-fin intersections of every tube. The horseshoe vortex was found to be very complex and could contain a number of smaller vortices, see Baker (1979). At the lowest Reynolds numbers it was seen that the horseshoe vortex in front of the first row was the largest and the horseshoe vortex structure in front of the second row comprised of three smaller vortices. The horseshoe vortex in front of the third row was seen to be the smallest as it was in the wake region of the first row. When the Reynolds number was increased all flow regions were seen to become more active. The horseshoe vortex in front of the second row tube was seen to be more active than that for the front row, leading to higher levels of heat transfer. The wake region behind the first tube row was particularly inactive leading to low heat transfer, but the fluid flow activity in the wake regions of subsequent tube rows was greater, leading to higher heat transfer.

Local heat transfer coefficients and pressure drop information were reported at a Reynolds number of 263 by Fisher (1996) using liquid crystal thermography on a staggered tube arrangement with two tube rows. All the trends in heat transfer coefficient reported by Saboya and Sparrow (1976a) were seen. The results were

presented as section cuts through the geometry, as opposed to span averaged results, and the increased heat transfer in the wake region of the second row tube could be seen. The results were presented for only one Reynolds number so the effect of increasing Reynolds number on heat transfer and pressure could not be seen.

Effect of fin pitch on overall heat transfer

For many years the standard text for heat exchanger design was Kays and London (1955) updated in 1964 and 1984 (refs). This work presented $j - f$ data over a range of Reynolds numbers for a large number of different surfaces and geometries. All the trends show decreasing values of j and f with increasing Reynolds numbers, indicating higher levels of heat transfer and pressure drop with increasing Reynolds number.

To increase understanding of the effect on heat transfer of changing the fin pitch, Rich (1973) carried out a systematic study of eight, four-row staggered heat exchanger geometries, where the ratio of channel height to tube diameter (H/d) was varied between 0.084 and 0.64. He concluded that the overall heat transfer coefficient was independent of the fin spacing. For a one-row configuration, Shepherd and Ithaca (1956) determined that over the range $H/d = 0.212$ to 0.834, for a small fin spacing at low velocities, the heat transfer coefficients were higher. At higher velocities there was no difference. These trends were supported by Elmahdy and Briggs (1979) who found that the overall heat transfer coefficient increased as the fin spacing decreased. However, McQuiston and Tree (1971) reported decreasing

overall heat transfer coefficient with decreasing fin spacing.

For a direct expansion (DX) plate finned-tube heat exchanger with 10 coils, Turaga et al. (1988) reported that the j and f factors decreased when the fin density was increased, due to the corresponding rise in air mass velocity. Correlations were given for both j and f in the Reynolds number range 300 to 1500 but as the results were based on fixed air flow velocity entering the coil, no conclusions could be made regarding the effects of channel height on the heat transfer. For a two tube-row staggered heat exchanger it was found by Chen and Ren (1988) that H/d had little effect on the Nusselt number when H/d = 0.336 - 0.516 in the Reynolds number range $4.5 \times 10^3 - 2.7 \times 10^4$. When the fin spacing was decreased in the high Reynolds region ($Re > 1.2 \times 10^4$) a slight decrease was observed whilst in the low Reynolds number region ($Re < 7 \times 10^3$) hardly any change occurred. The friction factor was found to increase dramatically when H/d was less than 0.193. Flow visualisation was also used to asses the extent of the vortex structures. This indicated that at small fin spacings the vortex structure was reduced. As the fin spacing was increased the vortices became stronger until a maximum was reached. Correlations were given for both j and f. These trends were also reported by Baldwin (1989) in both correlation form and flow visualisation. However, in the same study Baldwin (1989) reported a noticeable increase in the j-factor for the largest channel height on the two tube-row configuration.

The effect of fin spacing on heat transfer was also reported by Kayansayan (1994).

Measurements were made for H/d between 0.131 and 0.425 and the results were presented in the form of a correlation that included a finning factor ($\epsilon = A_0/A_{t0}$). This factor included the effects of transverse and longitudinal tube pitch. The j factor was found to increase when ϵ increased but as the finning factor included the effects of tube pitch the effect of fin spacing could not be isolated. For Reynolds numbers less than 7000, Wang et al. (1996) found that the j and f factors were nearly independent of fin pitch confirming the trends of Chen and Ren (1988). However, for a Reynolds number less than 1000 a reduction in the friction factor at the largest channel height was apparent.

Effect of tube-row number on overall heat transfer

On increasing the number of tube rows from 1 to 6, Rich (1975) found the overall heat transfer coefficient decreased. At low Reynolds numbers (typically below 2000) with a multi-row heat exchanger geometry, the j-factors showed a marked decrease. This trend was also observed by McQuiston (1978), but in a review paper by Shah and Webb (1983) the trend was discounted and attributed to experimental error. However, the trend of decreasing j-factors with multi-row tubes at low Reynolds numbers was also reported by Baldwin (1989), Seshimo and Fuji (1991) and Wang et al. (1996). In the study by Wang et al. (1996) care was taken in the experiments to achieve an energy imbalance of less than 3%, and the authors stated that the effect was not due to experimental error. The results showed that the friction factor was independent of the tube row number and decreased with increasing Reynolds number. Below a Reynolds number of 2000 the tube row number had a marked effect

with the j-factor decreasing for increasing tube rows. The authors also noted that this effect occurred at the smallest fin spacing. The reducing j-factor was attributed to standing vortices behind the cylinders and from the work of Chen and Ren (1988) reduced overall vortex activity. As the Reynolds number increased above 2000 there was no variation of heat transfer coefficient with tube row number. Norberg (1994) showed that a reduction in the channel height around a cylinder a higher Reynolds number could be achieved before time dependent flow started. In a similar study at Reynolds numbers below 1200, Turaga et al. (1988) reported no variation in j and f when the number of tube rows was increased from 3 to 8.

Effect of tube shape on overall heat transfer

The effect of using elliptical tubes in place of circular tubes was investigated by Brauer (1964) and Schulemberg (1966). A reduced pressure drop through the heat exchanger was observed with minimal reduction in heat transfer. Local mass transfer coefficients were reported by Ximenes (1981) for a one- and two-row elliptical plate-fin heat exchanger. These showed a smaller reduction in mass transfer in the wake region compared to the circular configuration. For tube and shell heat exchangers Merker and Hanke (1986) showed that oval tube heat exchangers are advantageous when a very compact design with a very low pressure drop on the shell was needed. This was also shown by Bordalo and Saboya (1995) who found pressure drop reductions of up to 25% compared to circular tubes. Another advantage of oval tubes is an increase in fin efficiency of up to 18%, which was reported by Rocha et al. (1997). They also concluded that a two-row configuration was always more efficient that a

one-row configuration.

2.4.8 Numerical Results for Heat Exchanger sections

With the advent of modern digital computers it became feasible to use numerical codes to predict heat transfer, flow field and pressure drop information for a wide variety of heat exchanger configurations. An early barrier to using numerical techniques was the complexity of the geometry. A number of early workers tried to overcome the problem of fitting a mesh around square fins and circular tubes. In their pioneering work, Thom and Apelt (1961) used conformal mapping to generate a grid where uniform but different potentials were maintained on two quarter-cylinders arranged in a staggered alignment. Le Feuvre (1973) adopted a Cartesian grid similar to that used by Thomas and Szewcyzk (1969) with the tubes in the in-line arrangement. The spacing between nodes was adjusted so that all the rear wall nodes fell on the cylinder surfaces of the tubes. This type of mesh had the advantage that it retained a simple form for the convective flow equations. However, these types of mesh suffered a number of numerical problems. For the type of mesh used by Thom and Apelt (1961) the governing connective flow equations had to be re-arranged into a more complex form to allow for conformal mapping. The conformal mapping also led to a reduction in the number of nodes around the front and rear stagnation points, precisely where they are most needed for accurate solutions. The mesh of Le Feuvre (1973) keeps the simple form of the governing equations as the mesh is purely in Cartesian co-ordinates but it was found that this

mesh was particularly susceptible to numerical diffusion due to the streamlines near the cylinder cutting diagonally across the grid.

Launder and Massey (1978) built the grid around the tubes in polar co-ordinates. This reduces the numerical diffusion around the cylinder as the steepest gradients of the flow properties are in the radial direction. The region between the polar co-ordinate meshed tube area, in a staggered arrangement of tubes, was filled with a mesh aligned with the Cartesian co-ordinate areas. This Cartesian mesh was independent of the polar region and the two were joined by introducing a false row of nodes in the region of overlap. A two-dimensional model was built using the finite-difference discretisation method, with symmetry boundary conditions and the assumption of fully developed flow at the inlet. Numerical data were presented for stream function, vorticity contours, surface pressure and Nusselt number around the tube. Good agreement was found with the experimental work of Bergelin et al. (1949, 1952). Vorticity contours were also compared with Thom and Apelt's (1961) solutions. This showed that large amounts of diffusion had occurred in the earlier work due to insufficient node density.

Two-dimensional numerical models of heat exchanger cores were presented for five tubes in an in-line arrangement by Fujii et al. (1984), and by Wung and Chen (1989a), (1989b) for tubes in an in-line and staggered array. Wung and Chen concentrated on Reynolds numbers below 800. For in-line arrays, increasing the Reynolds number has the effect of increasing the wake region size until the wake attaches

itself onto the front of the next tube. The size of the wake region also increases with increasing Reynolds number for a staggered array. It was suggested by Wung and Chen that the wake region could be reduced in size by reducing the longitudinal pitch of the tubes.

The effect of fin spacing and longitudinal tube pitch for a heat exchanger configuration consisting of a series of cylinders arranged in-line and placed equidistant between two parallel plates was investigated by Kundu et al. (1991a) and (1991b). They presented numerically predicted streamlines for various fin heights to tube diameters, and various tube pitches to tube diameters for Reynolds numbers up to 200. With a small fin pitch the flow is steady for all Reynolds numbers, but as the fin pitch is increased the flow becomes unsteady and vortex shedding is seen behind the cylinders. Increasing the tube pitch reduces the periodicity of the flow in time dependent mode. The pressure drop across each tube was found to be nearly constant with the exception of the first and last tube, which could indicate that fully developed flow conditions had occurred after the first tube. Global heat transfer data were presented for various Reynolds numbers, fin spacings and tube pitches.

A comparison between an un-finned and a finned heat exchanger was performed numerically by Faghri and Rao (1987). For a Reynolds number range 1 - 1000 they found a surprising result that the finned tube configuration decreased the heat transfer rate. This was attributed to the fins being placed in the stagnation regions at the front and rear tubes. This study was performed using a two-dimensional finite

volume-code and, as will be discussed later, three-dimensional effects can radically alter the flow and temperature distributions in fin-tube heat exchangers.

The first three-dimensional numerical modelling of a plate-fin tube heat exchanger was performed by Yamashita et al. (1986a) and (1986b). This was a fundamental model consisting of a pair of parallel plates and a square cylinder passing perpendicularly through the plates, which simulated the plate-fins and the tube respectively. Flow and temperature fields were calculated using an unsteady finite difference technique at a Reynolds number of 200. A horseshoe vortex was noted in front of the cylinder which was seen to contain three-dimensional flow. The effects of the plates were seen to influence the wake region by increasing the Reynolds number where a time-dependent Von Karman vortex street started to form. From the temperature field it was seen that high levels of heat transfer occurred in the horseshoe vortex region and low levels in the wake region.

A three-dimensional simulation of flow around one and two tube-row staggered array heat exchangers was reported by Baldwin (1986) and (1989). A commercial CFD code, PHOENICS, (Parabolic, Hyperbolic or Elliptic Numerical Integration Code Series), was used. These are two examples of the use of a commercial CFD code in heat exchanger research which is very rarely published in open literature. Due to problems caused by lack of memory only the flow field was calculated. Very coarse grids had to be used, but horseshoe vortices and separation regions were identified around the tubes.

For all numerical investigations reviewed in this section, apart from Baldwin (1986) and (1989), the inlet boundary condition was specified using periodically fully developed flow. This boundary condition maps the fluid vectors at outlet to the inlet. Although this reduces the size of the computational domain, inlet features of hydrodynamically and thermally developing boundary layers cannot be modelled. Using an inlet type of boundary condition increases the global heat transfer and pressure drop when compared to a periodic-type boundary. Mitra et al. (1991) and Bastani et al. (1991) compared flow and heat transfer at Reynolds numbers 400 and 1200 in a one-row heat exchanger element using spacewise periodic boundary conditions, with an in-line two-row heat exchanger element. For the second row tube at a Reynolds number of 400 there was less than 9% difference in the heat transfer and less than 5% in the pressure drop when comparing the two types of inlet boundary condition. This increased to a difference of 20% in the heat transfer for a Reynolds number of 1200, although the difference in pressure drop remained less than 5%.

To calculate realistic inlet and outlet conditions Jang et al. (1996) modelled all four rows of a staggered and in-line heat exchanger with a three-dimensional numerical code. The inlet boundary condition was one of uniform flow and at the outlet the streamwise gradients were set to zero (Neumann-type boundary condition). For Reynolds numbers in the range 60 to 900 the average heat transfer coefficient was 15 to 27% and the pressure drop 20 to 25% higher than the corresponding in-line configuration. The effect of the number of tube rows and the fin spacing on the average heat transfer and pressure drop were investigated for tube row numbers from

1 to 6 and fin spacings of 8 to 12 fins per inch. This is a interesting extension of the experimental work of Wang et al. (1996). The average Nusselt number reduced as the number of tubes was increased from 1 to 6 but was nearly independent of the tube row number after 4 rows. The average pressure drop increased with the number of rows, but after a Reynolds number of 400 there was a very sharp turning point in the pressure drop *vs* Reynolds number plot. At this point the pressure drop values for all the rows started converging to a constant value. For the pressure drop to be nearly independent of the tube row number by Reynolds numbers of 1000 is consistent with the work of Wang et al. (1996). For the fin spacing the heat transfer and pressure drop were seen to increase as the fin pitch increases from 8 to 12 fins per inch. Although this is not in agreement with Wang et al. (1996), there were small deviations from independence on the fin pitch in the experimental results at Reynolds numbers less than 1000 which were consistent with the numerical results of Jang et al. (1996).

The results of using two- and three-dimensional models of two-row staggered heat exchanger geometries were reported by Xi and Torikoshi (1996). In the two-dimensional model the streamwise tube pitch could be used to enhance the instability of the flow. In the three-dimensional model, instability in the flow did not occur when the streamwise pitch was increased. The authors argued that full three-dimensional models were important for analysing the interference effects of the plates on the flow field.

The numerical investigations reviewed until now all used the assumption of isothermal fins. This assumption is only true when the fin thermal conductivity is very large or infinite. For a real heat exchanger the fin has a finite value of thermal conductivity that does not meet this assumption. The implication for numerical studies is that the three-dimensional flow and temperature field has to be calculated taking into account the conduction of the fin. This type of problem was first solved by Fiebig et al. (1995a) whose paper is reviewed in detail in a later section (2.4.9). Conjugate heat transfer in staggered circular finned-tube heat exchangers was investigated by Jang et al. (1998). It was shown that the one-dimensional approximation overestimates the fin efficiency and the error increased with the fluid velocity. They also found that the isothermal fin approximation can lead to an over-prediction in heat transfer by 5 - 35%.

2.4.9 Heat exchangers with vortex generators

Experimental investigations

The first report of vortex generators in fin-tube heat exchangers was published by Russell et al. (1982), in the paper that principally presented plain channel results with vortex generators. The vortex generators used were the embossed type (see section 2.4.6) and at a Reynolds number of 1000 they reported an increase in j of 50% with a corresponding increase of f of 20%. Although these results appeared to be very promising they were obtained by comparison with standard correlations that could themselves have been in error by as much as 10% to 30%.

Experimental results on a single tube with vortex generators were reported by Fiebig et al. (1990). A single set of delta winglet pairs were mounted one tube diameter, downstream of the tube at $\beta = 45°$. This position was suggested as optimal. At a Reynolds number of 5000 the overall heat transfer was increased by 20% and the pressure drop decreased by 10%. A numerical model of the same geometry was constructed by Fiebig and Sanchez (1992) to include a finite value of fin thermal conductivity as is inherent in all real heat exchangers. This reduces fin efficiency when compared to the ideal case. For a Reynolds number of 2000 they reported that a heat exchanger with vortex generators had a 25% increase in heat duty, or the pumping power could be reduced by 80% for the same heat duty, when compared to a heat exchanger without vortex generators. Changes of more than 10% were noted in the fin efficiency when compared to the case without vortex generators.

Numerical Investigations

Numerical investigations with a conjugate heat transfer model of a single tube with and without vortex generators was reported by Fiebig et al. (1995a) and (1995b). Numerical results showed that for fin-tube heat exchangers with thin fins and high Reynolds numbers in laminar flow, but without vortex generators, heat transfer reversal (HTR) could occur in the wake region. The fin around the tube is cooled intensely by the horseshoe vortex leading to relatively low temperatures around the the tube, so the fluid temperature in the recirculation region could locally have a higher temperature than the fin. HTR occurs when the slow recirculating fluid in the wake region comes into longer contact with the tube and eventually heats up to

near the tube temperature. In the second paper quoted above vortex generators are shown to significantly alter and reduce the size of the recirculation region behind the tube; this leads to avoidance of HTR.

A numerical study of a single tube with a delta winglet pair was reported by Biswas et al. (1994). Their results were compared with the experimental results of Valencia et al. (1992). For a Reynolds number of 646 the general trend in spanwise-averaged Nusselt number was correctly predicted, but at some locations there was a relatively high discrepancy. This was attributed to the numerical model over-predicting the strength of the longitudinal vortices. In the computational model the fin was isothermal and the consequences of this assumption were ignored when comparing the numerical results to the experimental results. Due to the very thin fin of finite conductivity used in the experiments it was not possible to maintain isothermal conditions.

For finned oval tubes (FOT), flow structure, heat transfer and pressure loss information were reported by Chen et al. (1998a, 1998b) with the inclusion of vortex generators. An oval tube gives less heat transfer and less pressure drop than a corresponding circular tube. The addition of vortex generators can increase the heat transfer level to that of a round tube whilst retaining the lower pressure drop. For a Reynolds number of 300, the cases of one, two and three vortex generators on the fin were investigated numerically. A thermohydraulic performance factor $R_p = (j/j_0)/(f/f_0)$ was introduced, which showed that the configuration with two

delta winglets gave the best performance by this measure, at $R_p = 1.01$.

Heat exchangers with vortex generators and multiple tubes

Heat exchanger cores with vortex generators were reported by Valencia et al. (1992) and Fiebig et al. (1993) for both in-line and staggered round tube arrangements. For a Reynolds number range in the range 600 to 2700 heat transfer coefficients and pressure loss information were obtained experimentally. For the in-line case the addition of delta winglet vortex generators at $\beta = 45°$ caused a 55 - 65% increase in heat transfer coefficient and a 20 - 45% increase in friction factor. The staggered arrangement without vortex generators gave a 25 - 30% higher friction factor than the in-line case. With the addition of vortex generators the friction factor was increased by only 3%, and the average heat transfer increase was only 5% at the highest Reynolds number. This work was extended by Fiebig et al. (1994) and Valencia et al. (1996) to include flat fins. With the tube mounted very close to the leading edge of the fin, a 100% increased in heat transfer was reported with a 100% increase in the pressure drop. With the tube moved 12 non-dimensionalised channel heights from the leading edge a 50% increase in heat transfer and a 30% increase in pressure drop were reported for a vortex generator positioned in front of the tube. Similar results were obtained with delta winglets positioned half way down the tube on either side.

The influence of periodically fully developed flow and inlet flow as inlet boundary conditions was numerically studied by Bastani et al. (1999). For a two tube in-line

arrangement it was found that entry flow conditions had a more pronounced effect on heat transfer and pressure drop increase than fully developed periodic flow. A goodness factor, $G = (Nu/Nu_0)/(f_{app}/f_{app\,0})$ was introduced as the ratio of the increase in Nusselt number to the increase in friction factor. For entry flow $G =$ 0.852 and 0.960 for Reynolds numbers of 400 and 1200 respectively. For a periodic element $G = 0.78$ and 0.71 for the same two Reynolds numbers.

2.5 Summary

Techniques that enable the local heat transfer coefficient and pressure drop values to be measured and predicted for heat exchanger cores with and without vortex generators have been broadly classified into two groups namely, experimental and numerical. In experimental analyses of the local heat transfer coefficient, the steady state and transient techniques are commonly used. Liquid crystals are the most widely used method for measuring surface temperature. In the transient technique, where the boundary condition of constant temperature has been applied, less conduction in the fin has been noted than with the steady state technique. However, more realistic heat transfer coefficients were recorded when using the steady state technique than when using the transient technique with a constant heat flux boundary condition. If this boundary condition is applied for both cases the two sets of results could be made compatible by basing both sets results on the local bulk air temperature.

With the advent of powerful computing facilities the use of numerical codes to predict the local heat transfer coefficient and pressure drop has increased significantly. The three most commonly used methods to discretise the governing equations and thus, with the appropriate boundary conditions, solve the problem of interest are (a) finite difference, (b) finite element and (c) finite volume method. The discretisation of the governing equations are generally achieved with either a first or second order accuracy, although higher order schemes are possible. Although more complex second order discretisation is recommended for the greater accuracy of the results. The error in the solution due to insufficient mesh points can be determined either either by using successively refined grids or by using Richardson extrapolation. With the latter method, three successively refined grids is needed to be able to calculate the relative error from a mesh independent solution, and the order of grid convergence.

Local heat transfer coefficients for plain channels showed high heat transfer in the leading edge region which reduced monotonically towards a constant value. High heat transfer coefficients were also seen in the leading edge of heat exchanger sections, but low values were seen in the wake regions behind the tube. The horseshoe vortex which forms in front of tubes showed enhanced levels of heat transfer. The effect of fin-pitch and tube-row number on heat transfer was found to be essentially independent of Reynolds number when the Reynolds number was greater than 2000. However, with a small fin-pitch and a large tube-row number, standing vortices behind the cylinder could lead to a reduction in heat transfer.

Two-dimensional models of heat exchanger sections were found to under-predict the value of Reynolds number where a time-dependent vortex street would form. Three-dimensional models were needed to accurately predict the horseshoe vortex region which formed around the front of the tubes. A periodic type boundary condition calculated less heat transfer and pressure drop when compared to an inlet type boundary condition, although for Reynolds numbers less than 400 the second tube-row was well predicted.

Vortex generators, which are a fairly new development in heat transfer techniques have been found to enhance heat transfer under steady conditions, by producing a corkscrew motion. This motion is persistent in both laminar and turbulent flows. Winglet type vortex generators such as delta winglets and rectangular winglets can enhance heat transfer, on average, by more than 30% over an area several hundred times the size of the vortex generator. The dominant parameters which effect the heat transfer enhancement and pressure drop increase are the ratio of vortex generator to fin area, and the angle of attack of the vortex generator. Increasing either of these two parameters increases the heat transfer enhancement and pressure drop. Increasing the Reynolds number in the range of Reynolds numbers from 2000 to 8000 has the same effect. The pressure drop increase is mainly due to the form drag of the vortex generators. The Reynolds number at which self-excited amplitude oscillations occur, and thus the onset of turbulence in the flow, is reduced when vortex generators are introduced into the flow. Where the vortex generator has been punched from the fin it has been observed that winglet type vortex generators

gave higher heat transfer and pressure loss increase than wings. Where the vortex generator was mounted onto the fin the opposite trend has been noticed.

Vortex generators placed in in-line and staggered heat exchanger sections have been seen to increase the heat transfer and pressure drop. The heat transfer enhancement arises due to disruption of the normally stagnant wake region. With the application of vortex generators the occurrence of HTR can be avoided. One of the most appealing features of vortex generators is that they can be easily incorporated into compact heat exchangers. Manufacture can be by the same methods as have been developed for louvered fins and offset strip fins.

From the literature review it is apparent that there has been very little work published on vortex generators below a Reynolds number of approximately 800. This applies to both experimental and numerical investigations. To build a numerical model that can be validated against experimental results a detailed knowledge of the appropriate experimental boundary conditions must be available. The numerical model can then be made to have consistent boundary conditions. Although previous numerical models have tried to replicate experimental data they have mostly used privately written CFD codes, although it is the general purpose CFD code that is generally available to the heat exchanger designer. Without a joint experimental/numerical study, this leaves open to doubt the consistency of the boundary conditions that have been used.

Chapter 3

Experimental Investigation

This chapter describes the design, development and validation of an experimental method to calculate the heat transfer coefficient in a model of a compact heat exchanger with and without vortex generators. The analysis of the local heat transfer coefficient by the steady state and transient techniques is investigated and the data reduction equations derived for both cases. The results from both techniques are compared and where differences are found between the two sets of results these differences are explored to make the two sets of results compatible.

An uncertainty analysis on the measured variables is carried out for both the transient and the steady state techniques. From this the steady state technique is chosen for the analysis of local heat transfer coefficients. Other factors that contribute towards the overall uncertainty, such as radiation losses and tangential conduction are quantified and their effects on the overall uncertainty determined.

The experimental test set-up and test conditions are described together with the analysis of the liquid crystal isotherm images. Finally, the manner in which the local and overall heat transfer coefficient is calculated, using the data reduction

equations and the liquid crystal isotherm images is described.

3.1 Thermochromic Liquid Crystals

The most significant optical characteristic of thermochromic liquid crystals is that their colour changes with temperature. This change is reversible and is the basis for their application in fluid flow experimental work and also thermal mapping, from which heat transfer measurements can be made. The molecules of cholesteric liquid crystals are arranged in layers with the axis of the molecules parallel to each other and also parallel to the plane of the layers. Unlike the other types of liquid crystal (smectic, nematic) the molecules can be rotated in one layer with respect to the next, in the direction of the longitudinal axis. This effect arises from the very weak interactions between the molecules which can be altered by a number of external factors. Cholesteric liquid crystals which are commercially available exhibit changes of colour over discrete and reproducible temperature bandwidths. If calibrated, the colour wave length of the reflected light can be used as a measure of temperature. The mechanism which creates the temperature influenced colour change is described in detail by Fergason (1968) and Jones et al. (1986). Further, Akino et al. (1989) discussed an image processing technique that excludes subjective judgement of colour.

A self-adhesive sheet containing microencapsulated thermochromic liquid crystals (type R35C1W, manufactured by Hallcrest Ltd, Poole) was used in this study. This

liquid crystal type changes colour from black to first red, then through the other colours of the visible spectrum to blue with increasing temperature, and finally returns to black. The claimed red start temperature is 35°C and the temperature bandwidth over all colours is 1°C. The temperature bandwidth of the red colour is claimed to be 0.1 – 0.15°C. Calibration for the liquid crystals was provided by fast response thermocouples. These thermocouples were also used to check if any degradation, e.g. change in colour play, of the liquid crystals had occurred due to long exposure to strong light sources.

3.2 Experimental Techniques

3.2.1 Transient Technique

The transient method uses the surface temperature transient when the surface is exposed to a step change in fluid temperature as a measure of the surface heat flux and the corresponding heat transfer coefficient. Many methods have been used to achieve the step change in fluid temperature relative to the surface. Clifford et al. (1983), Ireland and Jones (1985, 1986), Metzger and Larson (1986), Metzger et al.(1991), Ashforth-Frost et al. (1992), Tiggelbeck et al.(1993, 1994), Gillespie et al. (1994), Van Treuren et al.(1994), Valencia et al. (1995) and McMahon and Murray (1996) used the instantaneous introduction of preheated warm air to raise the temperature of an ambient temperature surface. O'Brien et al. (1986), Jones and Hippensteele (1987), Baughn and Yan (1991a) and Yan et al. (1992) used a pre-heated surface which was exposed to an ambient temperature fluid. A differ-

ent approach was taken by Fisher (1996) and Critoph et al. (1999) who suddenly exposed an ambient temperature surface to a strong radiant light source.

3.2.2 Analysis of Transient Technique

The transient technique uses the time taken to heat up the test specimen from an initial known temperature to a set final temperature to determine the local convective heat transfer coefficient. The heat input is monitored by observing the liquid crystal isotherm patterns with respect to time. If the test specimen is (i) made from a material with a sufficiently high thermal conductivity and (ii) chosen to be thin, such that the temperature gradients inside the body are much smaller than those that occur in the surrounding fluid, then the temperature variation through the specimen (in the z direction) can be ignored. Chapman (1984) provides a guideline for the maximum thickness according to:

$$Bi = \frac{h(V/A)}{k} < 0.1 \tag{3.1}$$

where Bi, h, V, A, k are the Biot number, heat transfer coefficient, volume, area and thermal conductivity of the solid respectively.

Using these criteria to set the maximum thickness, the interior temperature was independent of position to within 5% according to Chapman (1984) and Kreith and Black (1980). Therefore, the lumped capacitance system which uses the assumption of an isothermal body could be used.

Since the Biot number was 0.02 for $h \approx 100\,\mathrm{W/m^2K}$ the temperature variation in the z direction could be neglected. The temperature equation for transient heating of a fin, by a heat flux input, contained between two flow channels is given by:

$$\dot{q} = 2h(T_w - T_\infty) + kz\left(\frac{\partial^2 T}{\partial x^2} + \frac{\partial^2 T}{\partial y^2}\right) + \rho c_p z \frac{\partial T}{\partial t} + \dot{q}_{rad} \tag{3.2}$$

where $\dot{q}$, T_w, T_∞, c_p, $\dot{q}_{rad}$ are the heat flux input, wall temperature, ambient temperature, specific heat at constant pressure and the radiation losses respectively.

In the experiment the surface is subjected to an airflow of temperature T_∞, a constant radiative heat flux input $\dot{q}$, and the surface heat transfer coefficient h. The following boundary conditions are therefore used for the analytical solution of equation 3.2:

Initial condition	$T = T_0 \quad \text{at} \quad t = 0$	(3.3)
Radiative heat flux input	$\dot{q} = \text{constant}$	(3.4)
Convective heat transfer rate	$\dot{q} = h[T(t) - T_\infty]$	(3.5)

The solution to equation (3.2) neglecting the conduction and radiation terms (see Section 3.4) and subject to the initial and boundary conditions described in Appendix A, is:

$$h = \frac{-\rho c_p z}{2t} ln\left[1 - \frac{2h}{\dot{q}}(T_w - T_\infty)\right] \tag{3.6}$$

This equation can be solved iteratively and a Matlab programme has been developed (see Appendix B) to solve it for the locally averaged heat transfer coefficient over the top and bottom surfaces at any time t.

3.2.3 The Steady State Technique

The steady state technique is based on a constant heat flux boundary condition to produce isotherms on the surface which correspond to lines of constant heat transfer coefficient. The constant heat flux boundary condition can be achieved in a number of ways. The most popular method is a thin conductive coating (usually vacuum-deposited gold) placed on the surface of interest, Baughn et al. (1985, 1986). Other ways to achieve the heat flux boundary condition have included electric heating of a copper coating, Hatton and Wooley (1972) and a radiative light source that heats the surface directly by absorption, Critoph and Holland (1996), Fisher (1996) and Critoph et al. (1999). The surface temperature can be measured in a number of ways: Baughn et al. (1985), Eibeck and Eaton (1987), Yanagihara and Torii (1992) and Pauley and Eaton(1994) used thermocouples while Oker and Merte (1981) used the resistance of the coating itself. More recently liquid crystals have been used as a measure of the surface temperature by Simonich and Moffat(1982), Baughn et al. (1986), Hippensteele et al. (1983, 1985, 1986) and Tiggelbeck et al. (1993, 1994). Moffat (1990) has reviewed and referenced a number of different steady state techniques.

3.2.4 Analysis of the Steady State Technique

The steady state technique relies on a constant heat flux input onto the surface where the heat transfer is to be measured. Since the heat flux can be changed by adjusting the electrical current, when a conductive coating is used, or by increasing the light

intensity when a radiative heat flux input is used, the surface temperature can be increased or decreased. When considering an energy balance on an element with the system in steady state, i.e. the heat flux input is balanced by the heat output through forced convection, conduction and radiation, an isotherm on the surface corresponds to a line of constant heat transfer coefficient. The energy balance for a fin contained between two flow channels and heated by a constant heat flux input is given by the equation:

$$\dot{q} = 2h(T_w - T_\infty) + kz\left(\frac{\partial^2 T}{\partial x^2} + \frac{\partial^2 T}{\partial y^2}\right) + \dot{q}_{rad} \tag{3.7}$$

As with the transient technique (section 3.2.2), it is assumed that there is no temperature variation through the fin, therefore the surface temperature is the same as the internal temperature. This assumption limits the values of heat transfer coefficient that can be measured accurately, the maximum value being that for which the internal temperature gradient is still negligible compared to the temperature difference used in defining the heat transfer coefficient. Note that the conduction terms are neglected and a correction applied for the radiation loss term (see Section 3.4). When steady state conditions are met ($\partial T/\partial t = 0$) equation 3.7 can be rearranged for the heat transfer coefficient, which at a position of particular colour (temperature) is given by:

$$h = \frac{q}{2(T_w - T_\infty)} \tag{3.8}$$

This h is the locally averaged value of heat transfer coefficient between the top and bottom surfaces.

For the test section used, Figure 3.1, the energy flows are all calculable. The radiant

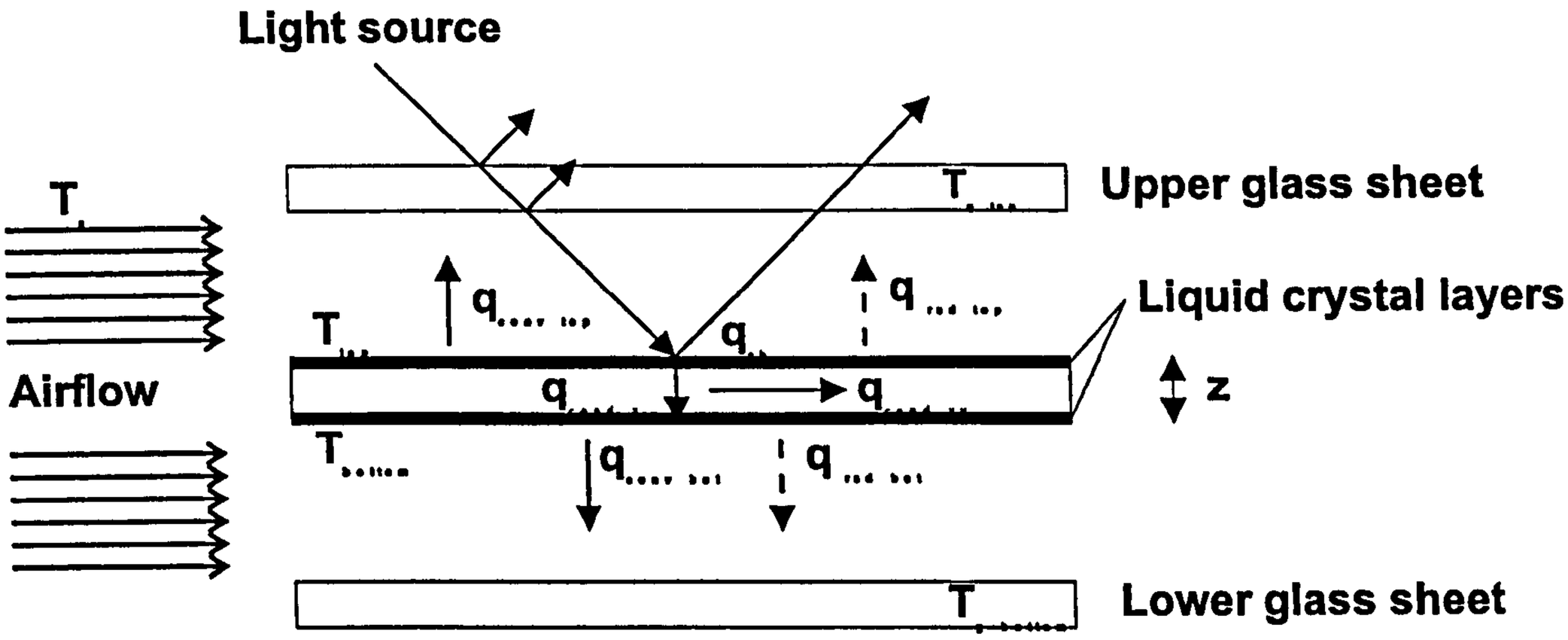

Figure 3.1: Energy flows in test section

energy absorbed by the upper liquid crystal layer is q_{ab} (W/m^2). An energy balance equation for the upper surface is:

$$q_{ab} = q_{conv\,top} + q_{rad\,top} + q_{cond\,z} + q_{cond\,xy} \tag{3.9}$$

$$q_{ab} = q_{conv\,top} + q_{rad\,top} + \frac{k(T_{top} - T_{bot})}{z} + kz\left(\frac{\partial^2 T}{\partial x^2} + \frac{\partial^2 T}{\partial y^2}\right) \tag{3.10}$$

The energy balance for the lower surface is:

$$q_{cond\,z} = q_{conv\,bot} + q_{rad\,bot} \tag{3.11}$$

The top and bottom surface convective heat fluxes are given by a heat transfer coefficient based on the difference between the air inlet and the surface temperatures:

$$q_{conv} \equiv h(T - T_a) \tag{3.12}$$

The net low temperature radiation exchange between the middle and the top or middle and bottom sheets is given by:

$$q_{rad} = \frac{\sigma(T^4 - T_g^4)}{\frac{1}{\epsilon_{lc}} + \frac{1}{\epsilon_g} - 1} \tag{3.13}$$

In order to calculate h_{top} or h_{bot} at a location, the radiative fluxes and conduction flux in the plane of the sheet need to be known. They are both typically an order of magnitude or more below the convective fluxes and so do not need to be known with great precision. The calculation of these quantities is discussed in section 3.3.1.

The radiation loss term is deducted from q_{ab} to give the convection flux from both the top and bottom surfaces $q_{convtot}$. The calculation of the coefficients varies depending upon whether or not the fin is symmetrical, and thus has the same coefficient expected on both top and bottom surfaces. The calculation also depends upon whether the thermal resistance through the fin is significant. If the resistance is significant and the top and bottom surfaces have a different h, two sets of contours are obtained, one from the top layer of liquid crystals and the other from the bottom layer. Two nominal heat transfer coefficients based on the air inlet temperatures can be calculated, being defined by:

$$H = \frac{q_{conv\,tot}}{T_a - T_{lc}} \tag{3.14}$$

$$H' = \frac{q'_{conv\,tot}}{T'_a - T'_{lc}} \tag{3.15}$$

The use of a prime ($'$) indicates contours on the bottom surface. In obtaining the sets of contours radiant heating is applied to the top surface only.

Analysis of the thermal resistance networks applied to both surfaces at the same location gives the heat transfer at the top and bottom surfaces, based on inlet temperature, as a function of the properties of the middle glass sheet, H and H':

$$h_{top} = H + \frac{k}{z}\left(\frac{H}{H'} - 1\right) \tag{3.16}$$

$$h_{bot} = \frac{k}{z}\left(\frac{H'}{H} - 1\right) \tag{3.17}$$

In the experiments reported here the two flow channels are identical so h_{top} and h_{bot} are equal. This enables the solution of h either (i) as a function of H and H', in which case the thermal resistance of the glass is not needed, or (ii) as a function of H and k/z, in which case only the top set of contours need to be measured:

$$\frac{1}{h} = \frac{1}{H} + \frac{1}{H'} \tag{3.18}$$

$$h = \frac{H}{2} - \frac{k}{z} + \sqrt{\left(\frac{k}{z}\right)^2 + \left(\frac{H}{2}\right)^2} \tag{3.19}$$

The latter method was chosen both for convenience and because the results are not a strong function of k/z. Equation 3.19 may be expressed implicitly as:

$$h = \frac{H}{1 + \left(\frac{1}{1+\frac{hz}{k}}\right)} \tag{3.20}$$

In the case of the 0.7 mm thick glass fin used an error of 10% in k/z with a typical h of 40 W/m^2K results in a change in h of only 0.2%.

3.2.5 Comparison of the Two Techniques

Comparisons between the transient and steady state techniques, using radiative light as the heat flux input, have been carried out by Fisher (1996) and Critoph et al. (1999). Significant differences in the heat transfer coefficient are seen between the two techniques with differences of up to 50% in the trailing edge region where the transient technique predicts an increasing heat transfer coefficient. This is physically unlikely as the developing boundary layer is growing from the leading edge towards the trailing edge. These differences could be due to the different boundary conditions of the two techniques as reported by Baughn et al. (1989). The transient technique approximates a uniform temperature boundary condition and the steady state technique provides a uniform heat flux boundary condition. However, Baughn et al. (1989) showed that for heat transfer around a pin fin the differences between the two techniques was not large and were consistent with the effect of different thermal boundary conditions.

The big difference between the two techniques at the trailing edge is probably due to the increase in the bulk air temperature as it passes through the test section. For both the transient and steady state technique the heat transfer coefficient is defined using the air inlet temperature as this is easily measured. Jones (1991) reported that although all local heat transfer coefficients can be referred to the inlet temperature, these local heat transfer coefficients will be quite different to those based on the local bulk temperature. This was also reported by Wang et al. (1994) who measured the local heat transfer coefficient over the full surface of a

pedestal bank, using the fin boundary condition of constant temperature with the model initially at uniform temperature, where it was heated by a hot air stream. They found that the heat transfer coefficient calculated from an upstream value of temperature dropped through the array as the flow loses temperature potential and the heat flux dropped. By defining the heat transfer coefficient using a local driving temperature, higher values of local heat transfer coefficient were obtained.

In these tests the convective heat flux at a location is a function of the flow temperature gradient normal to the wall at that location. In the two different tests, which have the same flow fields, the local air temperatures are very different when the wall temperature reaches the predetermined temperature.

When using the steady state technique the heat transfer coefficient is defined using the air inlet temperature. The total energy input per unit width to the fin, up to some location x along a streamline is, Fisher (1996) and Critoph et al. (1999):

$$q(x) = \int_0^x h(T_w - T_\infty)dx \tag{3.21}$$

The total energy input and therefore heat transfer coefficient can also be defined using the locally varying value of bulk air temperature:

$$q(x) = \int_0^x h_{local}(T_w - T_{a(x)})dx \tag{3.22}$$

where $T_{a(x)}$ is the bulk air temperature value. When considering the same location and the same heat flux input, the values in the integrals must by definition have the

same values, but $T_{a(x)}$ will be higher than T_∞. Because of this, h_{local} will be higher than h since the temperature difference between the wall and free stream is less. When using the steady state technique to measure low heat transfer coefficients near the trailing edge, low heat flux inputs are used so the rise in bulk air temperature is not great. As progressively higher heat flux inputs are used to measure higher heat transfer coefficients, the position of interest moves towards the leading edge where the bulk air temperature approaches the inlet temperature. As a result the differences between h and h_{local} are not large when using the steady state technique.

In the transient test the bulk air temperature will be lower than in the steady state technique as the model never reaches equilibrium conditions. This results in higher values of heat transfer coefficients, calculated from the inlet temperature. From knowledge of the bulk air temperature for each technique, which can be calculated from an energy balance between the fin and the air, the heat transfer coefficients based on bulk air temperature can be found. These results for both the transient and steady state techniques should be consistent. To carry out this analysis in a full three-dimensional test section with tubes present, a knowledge of the streamlines is needed. As this information was not available the problem is reduced to two dimensional channel flow and the values of bulk air temperature calculated.

In the steady state technique the bulk air temperature at a particular position can be calculated from a knowledge of the power input and the mass flow rate. Figure 3.2 shows the increase in local heat transfer coefficient when it is based on local

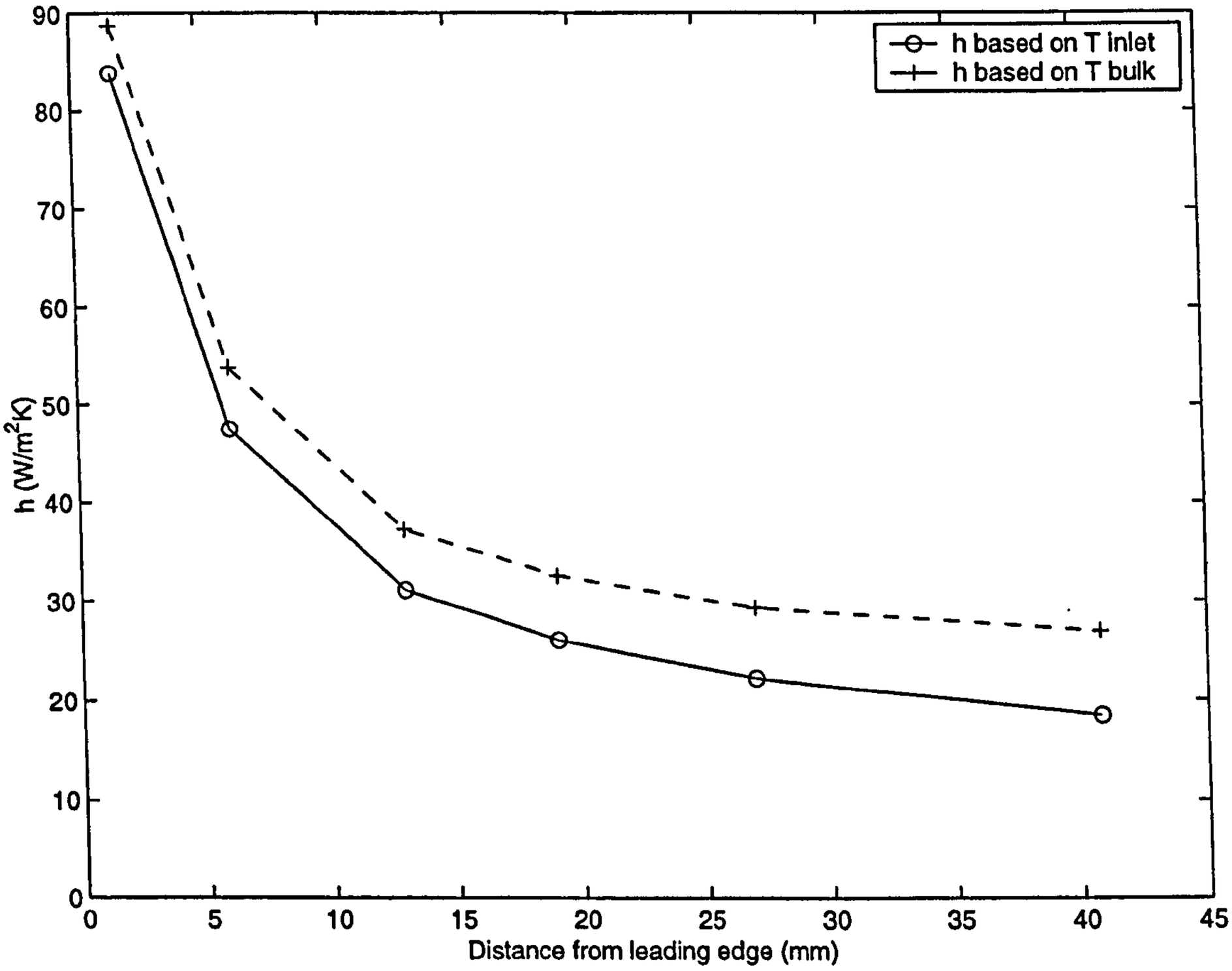

Figure 3.2: Comparison of the steady state result for h when based on T_{inlet} and T_{bulk}

bulk air temperature as opposed to inlet temperature. This agrees with the findings of Wang et al. (1994).

A finite difference scheme was used to find the local bulk air temperature in the transient case. The grid used, shown in Figure 3.3, describes a unit length of fin being heated by a heat flux. For this unit length, the fin is surrounded on both sides by fluid (notation for space being n) and having a heat transfer coefficient from the fin. To indicate a new time step a prime ($'$) has been used.

Three equations were used to find the solid temperature and the gas temperature

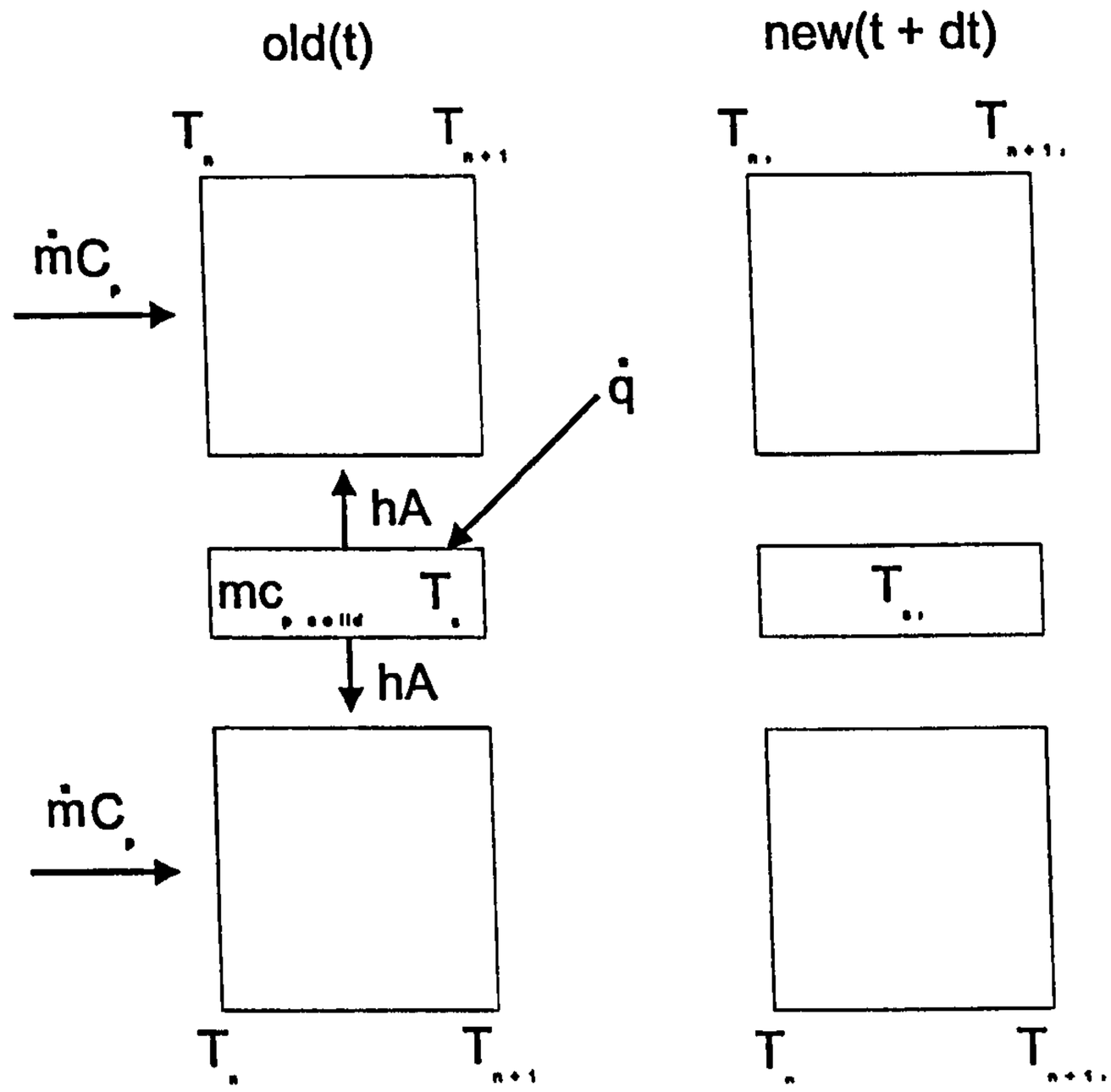

Figure 3.3: Space and time grid for the finite difference scheme to calculate bulk air temperature in the transient case

at a new time step. The heat transfer into the fluid control volume is given by:

$$Q = 2hA\left(\frac{T_s + T_{s'}}{2} - \frac{T_n + T_{n+1} + T_{n'} + T_{n+1'}}{4}\right) \tag{3.23}$$

where: Q, T and A are the heat transfered, temperature and surface area respectively

The steady flow energy equation is:

$$Q = 2\dot{m}c_p\left(\frac{T_{n+1} - T_n + T_{n+1'} - T_{n'}}{2}\right) \tag{3.24}$$

where $\dot{m}$ and c_p are the mass flow rate and heat capacity for the fluid respectively.

The heat input from the solid glass element of interest is given by:

$$Q = q_{in}A + \frac{Mc_{p\,solid}}{dt}(T_s - T_{s'}) \tag{3.25}$$

where q_{in} and M are the heat flux input and the mass of the unit length respectively

By combing equations 3.24 and 3.25 an expression for the solid temperature at each location at the next time step is given:

$$T_{s'} = T_s - \frac{dt}{Mc_{p\,solid}}[\dot{m}c_p(T_{n+1} - T_n + T_{n+1'} - Tn') - q_{in}A] \tag{3.26}$$

By substituting equation 3.26 back into equations 3.23 and 3.24 an expression for the gas temperature at any location at the next time step is given by:

$$T_{n+1'} = \frac{2T_s - T_{n+1}\left[A + \frac{1}{2} + B\right] + T_n\left[A - \frac{1}{2} + B\right] + T_{n'}\left[A - \frac{1}{2} + B\right] + \frac{dt}{Mc_{p\,solid}}q_{in}A}{\left[A + \frac{1}{2} + B\right]} \tag{3.27}$$

$$A = \frac{dt}{Mc_{p\,solid}}\dot{m}c_p$$

$$B = \frac{\dot{m}c_p}{hA}$$

An initial condition and an inlet boundary condition are required for the solution of the equations that contain $T_{s'}$ and $T_{n+1'}$. The initial condition is that at $t = 0$ the gas and solid temperatures are equal to the ambient temperature:

$$T_s = T_\infty \qquad \text{at} \qquad t = 0 \tag{3.28}$$

$$T_n = T_\infty \qquad \text{at} \qquad t = 0 \tag{3.29}$$

The inlet boundary condition is a Dirichlet-type boundary condition where the inlet temperature always stays constant at every time step:

$$T_1 = T_\infty \qquad \text{for all } t \tag{3.30}$$

The heat flux input and the time step were both selected by the user; and to verify that the time step was small enough, and therefore whether stability was maintained, a check that $T_{n+1'} < T_{s'}$ was carried out at each location as the programme proceeded. The heat transfer at each location was found by fitting a third order polynomial to the experimental steady state heat transfer coefficient using the "polyfit" command in Matlab. A Matlab programme (listed in Appendix C) was written to solve for $T_{s'}$ and $T_{n+1'}$. Results for the gas and solid temperatures are shown in Figure 3.4.

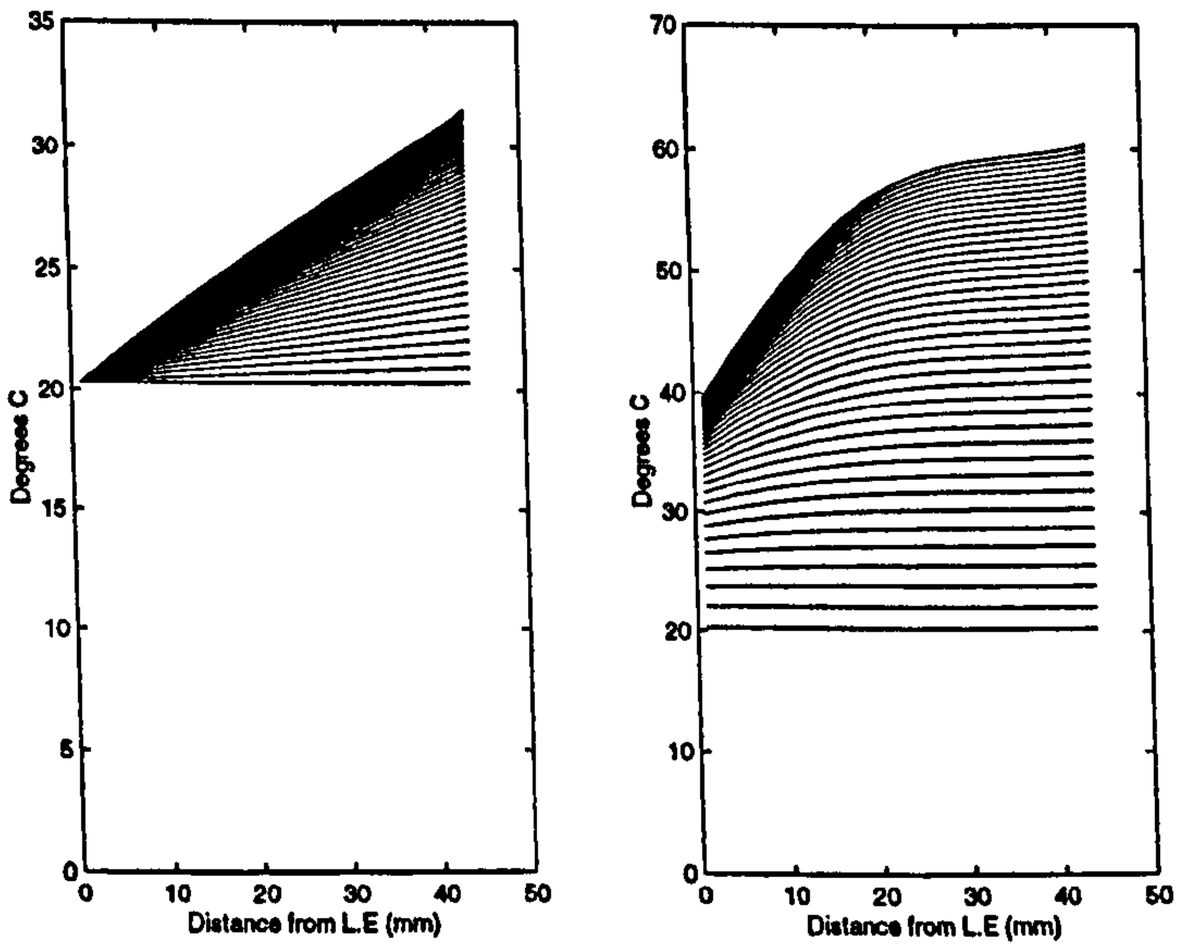

Figure 3.4: Gas and solid temperatures for transient heating

The local heat transfer coefficient calculated from inlet temperature and local bulk air temperature using the steady state technique is shown together with a theoretical curve taken from Shah and Bhatti (1987) in Figure 3.5. This derivation used

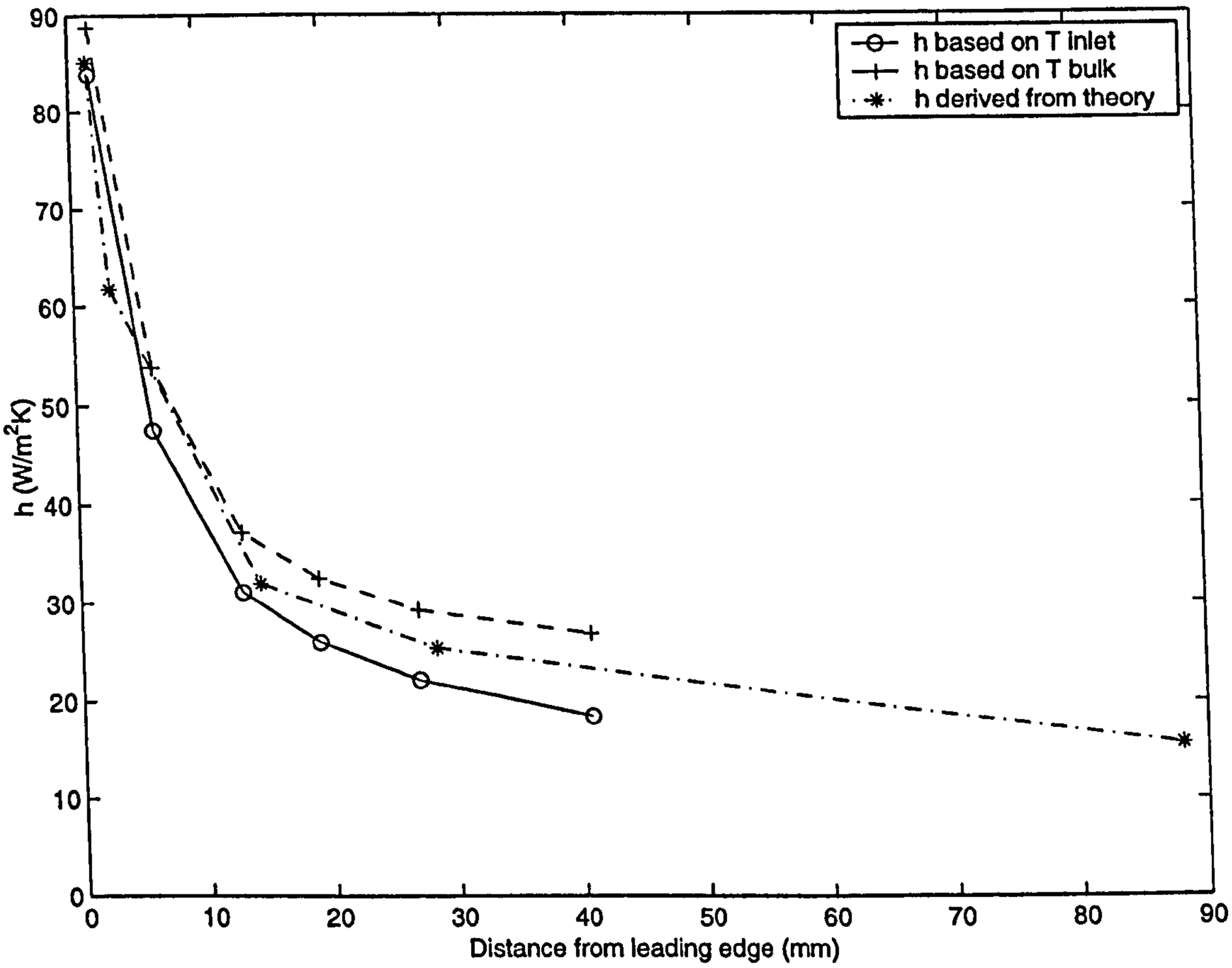

Figure 3.5: Comparison between the theoretical heat transfer coefficient and experimental values based on T_{inlet} and T_{bulk}

boundary conditions of the second kind, i.e. prescribed heat flux on one wall and an insulated boundary on the other. Although these types of boundary conditions are not strictly the same as the experimental arrangement, the only other type of boundary condition that can be used for theoretical development of Nusselt number with a constant heat flux boundary condition are the fourth kind. With this type of boundary condition a uniform heat flux is applied on one wall and the other wall is

maintained at the entering fluid inlet temperature. Over the length of interest in the test piece there was negligible difference between the two different types. It is clear that the heat transfer coefficient based on local temperature is close to the theoretical curve and also comparatively far away from the curve that describes the heat transfer coefficient based on inlet temperature. This is because the theoretical curve has been derived using the bulk fluid temperature as the reference temperature. The heat transfer coefficient based on the inlet temperature lies below both the theoretical curve and the curve based on local air temperature confirming that a more realistic value of heat transfer coefficient can be obtained when the heat transfer coefficient is referred to the local bulk air temperature.

The local bulk air temperature, calculated using equation 3.27 and shown in figure 3.3a, was used to calculate the local heat transfer coefficient. Comparison between the local heat transfer coefficients calculated by different methods showed that the heat transfer coefficients calculated from equation 3.6 increased towards the trailing edge. This occurred because the equation has been derived with the air inlet temperature as reference. Any reduction in the difference between the air inlet temperature and the liquid crystal colour transition temperature causes an increase in the heat transfer coefficient as reported by Fisher (1996) who found that a reduction of 5°C between the two temperatures caused approximately 3% increase in the heat transfer coefficient. The trend of an increasing heat transfer coefficient can therefore be expected with this derivation of the equation as the bulk air temperature rises towards the trailing edge.

As a further test of the transient technique, the predicted and actual event transition times were compared. The local heat transfer coefficient obtained from the steady state test was used to predict the times to transition in a transient test. The simulated and actual times are shown in Figure 3.6.

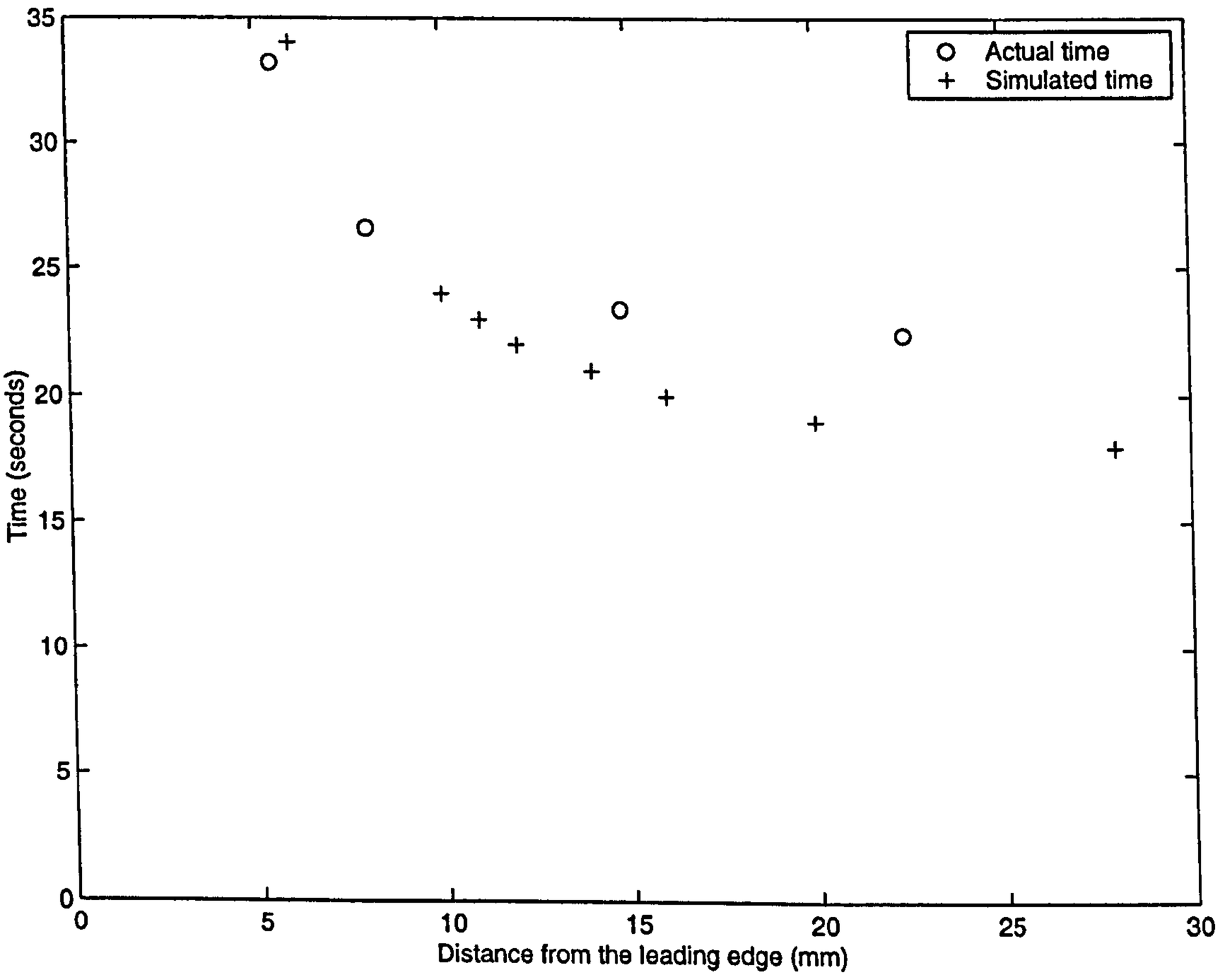

Figure 3.6: Comparison of actual and simulated times to event temperature transition

3.3 Selection of Experimental Technique

In the selection of the experimental technique the transient technique using a constant heat flux input has been discounted due to the unrealistic results obtained un-

der conditions explained in Section 3.2.5. However, comparisons of the uncertainties involved in the transient technique based on heated air and an ambient temperature surface have been carried out in order to establish the uncertainty in each technique. Extensive analysis and discussion of this procedure has been presented by Moffat (1985) and Coleman and Steele (1989).

The uncertainty analysis undertaken used the approach of Kline and McClintock (1953) and Moffat (1988) based on the relationship:

$$\delta h = \left[\sum_{i=1}^{N} \left(\frac{\partial h}{\partial X_i} \delta X_i \right)^2 \right]^{\frac{1}{2}} \tag{3.31}$$

where δh is the overall uncertainty and δX_i is the uncertainty in each variable.

The partial differentiation of the terms in equation 3.8 and the addition of the uncertainty in each measured variable gives an expression for δh:

$$\frac{\delta h}{h} = \left[\left(\frac{\delta q}{q} \right)^2 + \left(\frac{\delta T_{lc}}{T_{lc} - T_\infty} \right)^2 + \left(\frac{\delta T_\infty}{T_{lc} - T_\infty} \right)^2 \right]^{\frac{1}{2}} \tag{3.32}$$

Inspection of the above expression shows that δh, the uncertainty in h, increases as the heat transfer coefficient decreases because of the reducing heat flux input. For Reynolds numbers of around 300 the heat transfer coefficient varies between 20 and 100 W/m^{2}K, Fisher (1996). The experimental uncertainty with the experimental variables, shown in Table 3.1, ranged from 7.5% when $h = 20$W/m^{2}K to 4.3% when $h = 100$W/m^{2}K.

Variable	Uncertainty
Heat flux input $\dot{q}$	0.28 mv (25 W/m^2)
Indication temperature of TLC coating	0.2 K
Air temperature T_∞	0.4 K

Table 3.1: Uncertainties in the measured variables for the steady state technique

In the transient technique, δh decreases as the heat transfer coefficient decreases due to the increase in the total test time. The uncertainty in the test time and in the event temperatures is, however, small in comparison to the uncertainty in the thickness of the glass sheet. This uncertainty is not a function of the experimental test conditions but does make a large contribution to the overall uncertainty. Due to the lower uncertainty it offers, the steady state technique was selected for this investigation.

3.3.1 Estimation of the uncertainties in the non-measured variables in the experimental technique

In the previous section the uncertainties in the measured variables were considered. A number of other factors have also to be considered in the determination of the heat transfer coefficient. These are radiation losses, transverse conduction losses and the thermal absorptivity of the liquid crystals.

The emissivity of the liquid crystals changes with colour and according to Baughn et al. (1989) with the thickness of the liquid crystal layer. They reported an emissivity constant of 0.5 for a silk-screened liquid crystal coating rising to 0.9 for a thicker

brushed-on coating. Jones (1991) also reported an emissivity constant of 0.5. As there appeared to be no data for the self-adhesive type liquid crystal used in the experiments in section 3.4 a remote infra-red sensing camera was used to determine the emissivity. By holding the surface temperature constant at a predetermined temperature (indicated by colour) the emissivity was adjusted until the temperature displayed by the camera was the same as indicated by the liquid crystals. This indicated an emissivity of 0.95 when apparently red and 0.97 when apparently black. Using an emissivity of 0.93 for the top glass sheet, as suggested by Kreith and Black (1980), the liquid crystal transition temperature and the temperature of the top glass sheet measured by an infra-camera, the heat loss could be calculated from equation 3.13. This heat loss was approximately 2% of the heat flux input at higher heat transfer coefficients.

The effect of tangential conduction is to smooth out local variations in the value of the heat transfer coefficient. High values of tangential conduction occur when the distribution of heat transfer coefficients has local extremes with large second derivatives, Tiggelbeck et al. (1993). Tangential conduction was investigated by Valencia et al. (1995) by comparing experimental results of a vortex generator on a flat plate against numerical simulations using the three-dimensional Navier-Stokes equations and the energy equations. They found that large differences could be found between the two. Tiggelbeck et al. (1993) have also investigated tangential conduction for the transient case.

Tangential conduction was calculated using a two-dimensional conduction model (equation 3.7) of the glass fin, assuming the measured local heat transfer coefficients to be correct. The temperature at every node (i,j) on the surface was calculated from the relationship:

$$T_{i,j} = \frac{L^2(\dot{q} + hT_{inlet} - \dot{q}_{rad}) + kd(T_{i,j+1} + T_{i+1,j} + T_{i,j-1} + T_{i-1,j})}{hL^2 + 4kd} \tag{3.33}$$

where L and d are unit length and thickness of the glass sheet respectively

A Neumann type boundary condition $(\partial T/\partial x)_{i,j} = 0$ was applied at the edges of the domain and Guass-Seidel iteration was used to calculate the temperature at every node to an accuracy residual such that there is 0.0005°C between the temperatures of every node for successive iterations. The proportional difference made to the local heat transfer coefficient depends on the local value of the second derivative of the glass temperature with respect to distance. This becomes greater towards the leading edge as the gradient in the heat transfer coefficient increases. The net energy into or out of a control volume gives the tangential conduction and is calculated from:

$$Q_{net} = kt(T_{i,j+1} + T_{i+1,j} + T_{i,j-1} + T_{i-1,j} - 4T_{i,j}) \tag{3.34}$$

This is expressed as a ratio to the power input over the same area. The effect of tangential conduction is a function of the size of the chosen area of interest. The bigger the area of interest the smaller the effect. Table 3.2 shows the effect of tangential conduction for three different locations in two different areas of interest, with the heat transfer coefficient based on the new calculated temperature. For

Distance from leading edge (mm)	% correction factor for 0.2 mm x 0.2 mm resolution	% correction factor 0.4 mm x 0.4 mm resolution	Heat transfer coefficient (W/m^2K)
1.0	18.3	4.0	73.3
2.9	2.5	-	59.8
15.4	5.5	1.4	37.0
24.3	1.0	0.4	37.0

Table 3.2: Variation in conduction correction factor with position and resolution

locations more than approximately two millimetres from the leading edge, and using a resolution of 0.4 mm the error is less than 2%. This shows that areas of high tangential conduction are small in comparison to the overall size.

The absorptivity of the liquid crystal layer was also considered at this stage. No data was available from the manufacturers. An absorptivity factor of 0.95 was estimated to permit calculation of the absorbed heat flux density. The remaining reflected energy was ignored, as it is very small.

3.4 Arrangement of the Test Model

The model of the compact heat exchanger consists of three fins manufactured from glass, 0.7mm thick, and two air flow channels. Two air flow channels were chosen so that all the heat flux is dissipated in the air streams rather than the surrounding air.

The middle fin is covered on both sides with liquid crystals which are in the form of self adhesive 175 micron thick polyester sheets which have a pressure-sensitive adhesive backing. The difference in thermal resistance of the glass and liquid crystals due to different thermal conductivity and diffusitivity is ignored. The three glass fins are held at the correct fin spacing (4mm) by spacers. The buoyancy parameter has been checked for the fin spacing and velocity used. For the experimental conditions used $Gr/Re^2 \approx 0.001$. This is satisfies the condition that $Gr/Re^2 \ll 1$ which was given by Chapman (1984) as a guideline as to where buoyancy forces could be neglected.

A fast response K type foil butt-bonded thermocouple (2μm thick) was mounted directly onto the glass plate with glue beneath the liquid crystal layer. The thermocouple has a response time of 5 ms quoted by the manufacturers. Using ambient temperature water the thermocouple has been calibrated to within 0.1°C against a standard mercury-in-glass thermometer. The thermocouple is mounted next to the region of interest and used for continuous calibration of the liquid crystals. A second thermocouple is placed in the same position on the underside for liquid crystal calibration and to check the temperature on the bottom surface. Thus, the temperature difference across the glass sheet can be confirmed to be negligible and hence the Biot number is small.

3.4.1 Experimental test pieces

Various experimental test pieces were built for this study. First, a plane channel model was built for comparison against plain channel models with vortex generators. Rectangular and delta winglet pairs were tested for an angle of attack $\beta = 15$, 45 and 60° at Reynolds numbers = 65, 326 and 653. The test combinations for the different Reynolds numbers and angles of attack are shown in Table 3.3. The rectangular winglet pairs, Figure 3.7, were mounted 2.66 mm from the leading edge and were 2 mm high. The delta winglet pairs, Figure 3.8, were also mounted 2.66 mm from the leading edge and were 3.5 mm high at the training edge. They were not the full channel height (4 mm) to simplify the construction of the test sections. The base lengths for both types of vortex generator pairs was 8 mm.

velocity (m/s)	$\beta = 15°$	$\beta = 45°$	$\beta = 60°$
1	-	√	-
5	√	√	√
10	-	√	-

Table 3.3: Test conditions for experiments

Two staggered tube arrangements were investigated. The first had 20 mm diameter tubes on a 50.8 mm (2 inch) equilateral triangular pitch. This was tested at Re = 261. The second staggered tube arrangement, Figure 3.9, had 32 mm diameter tubes which were placed on a 55.4 mm stream-wise pitch and a 64 mm transverse pitch. This model was also tested with delta winglet pairs with the same test

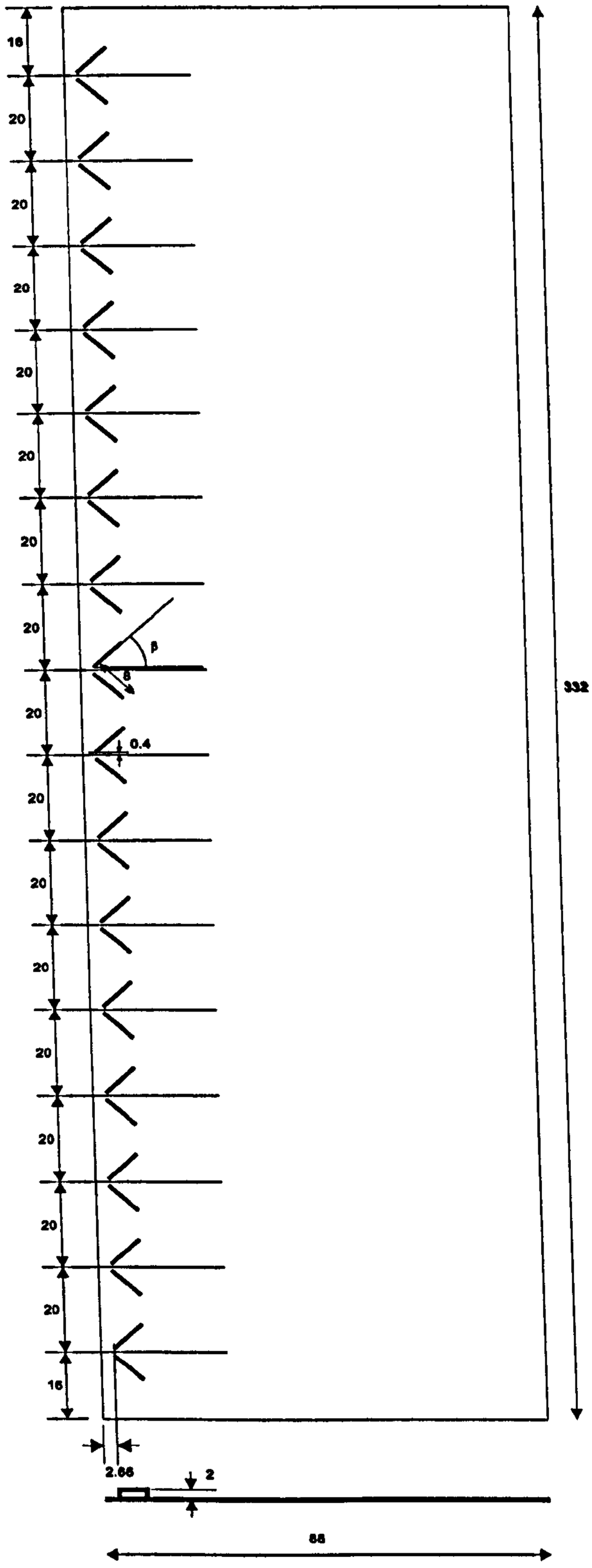

Figure 3.7: Dimensions for rectangular winglet pairs in a plain channel

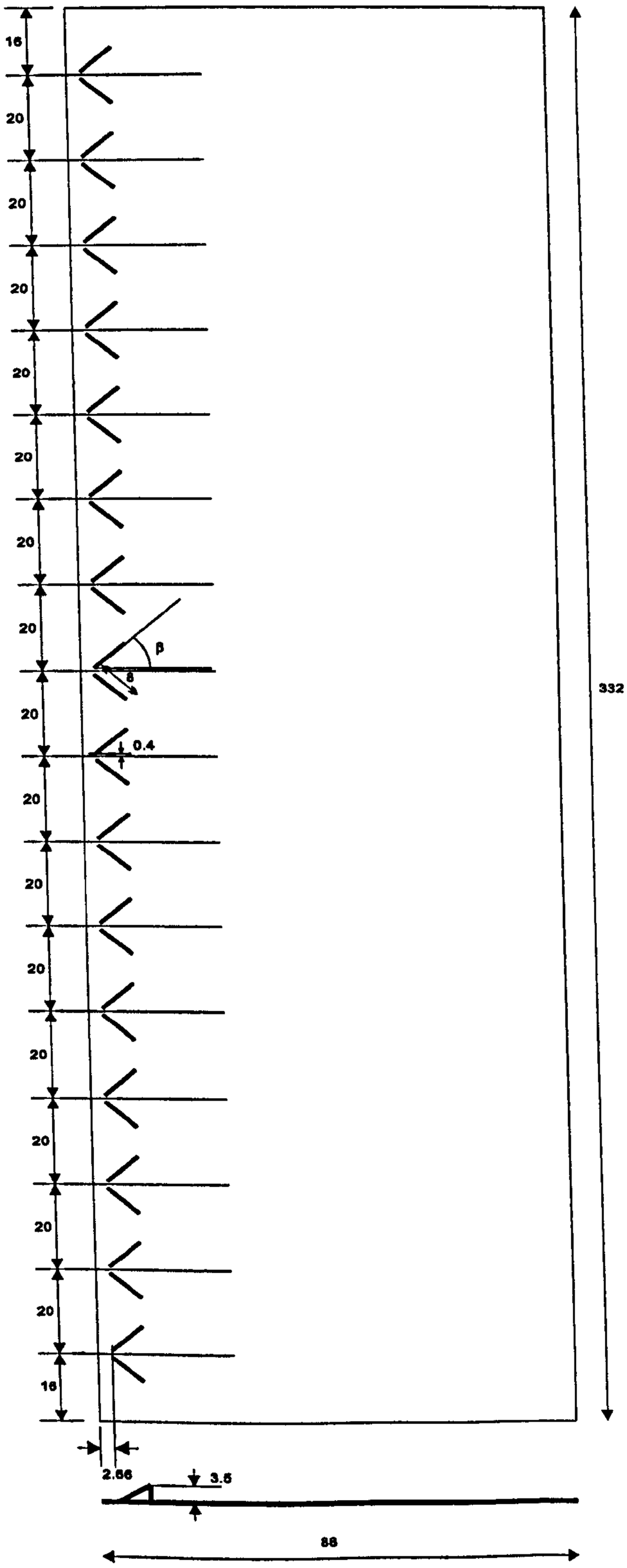

Figure 3.8: Dimensions for delta winglet pairs in a plain channel

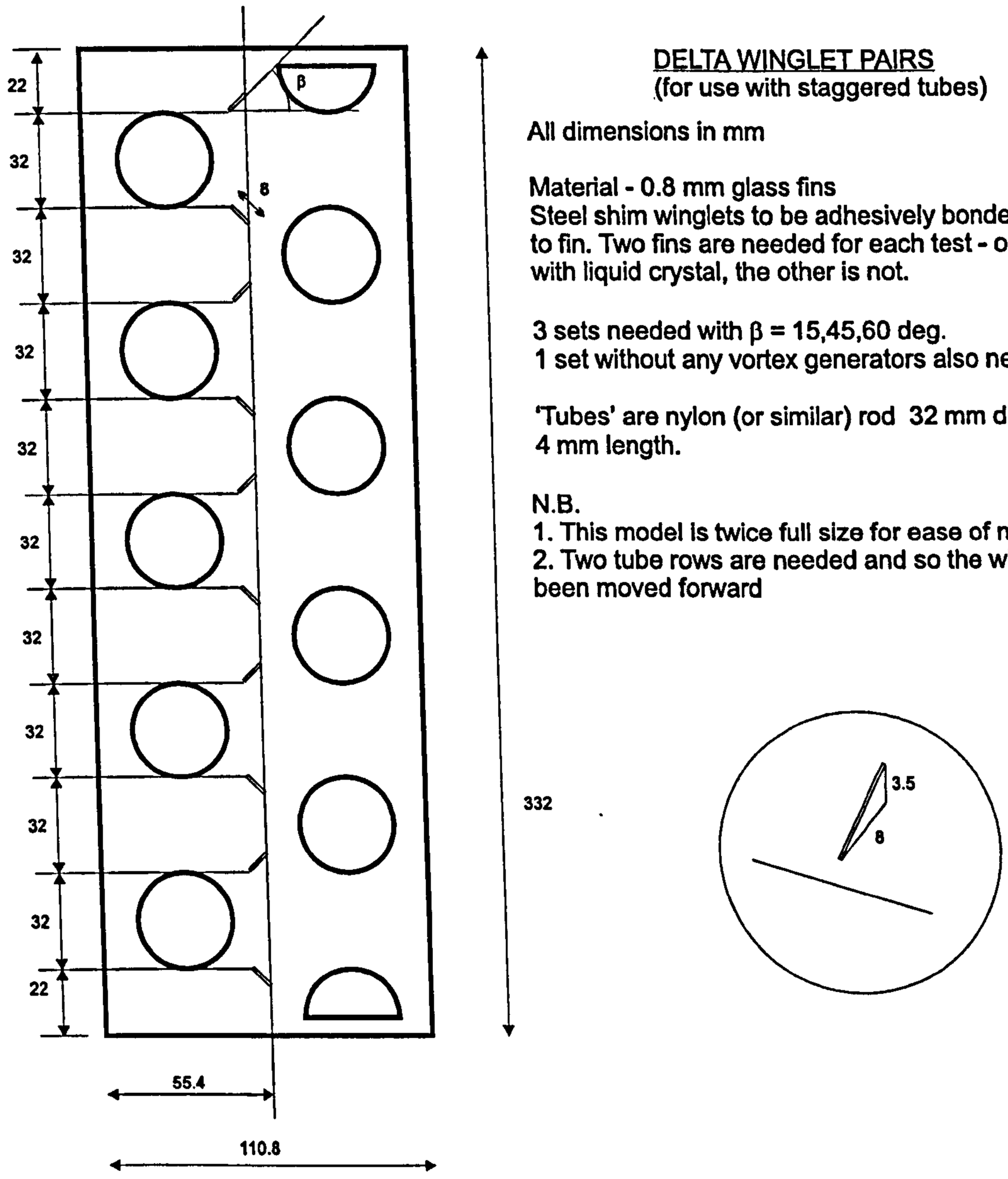

Figure 3.9: Dimensions for a staggered tube array with and without vortex generators

combinations as shown in Table 3.3. An in-line heat exchanger section, Figure 3.10, was also tested with and without vortex generators. The tubes were 32 mm in diameter and were mounted on a 64 mm stream-wise and transverse pitch. These models were again tested at the Reynolds numbers and angles of attack shown in Table 3.3.

An embossed type plate-fin heat exchanger, Figure 3.11, was also investigated. The embossed surface was created by moulding expoy resin pieces and were 1.5 mm high, 3 mm wide and 11 mm long. These were arranged in-line and were adhesively bonded to the liquid crystal layer. Only one angle of vortex generator was investigated, $\beta = 45°$, at the Reynolds numbers shown in Table 3.3.

The final models experimentally investigated were to compare the relative effects of a round and elliptical tube as shown in Figure 3.12, and Figure 3.13. These two geometries were compared at Re = 1224 and Re = 1567.

3.4.2 Experimental Arrangement

Figure 3.14, shows the experimental arrangement for the investigation of the heat transfer coefficient of the compact heat exchanger. The model of the heat exchanger was succeeded by an inlet plenum. This was manufactured from aluminium and supported extensions of the spacers between the flow channel, so that the assembly was held in front of the aperture in the aluminium manifold. The outer surfaces of the glass were held as closely as possible to the manifold and the gap sealed with

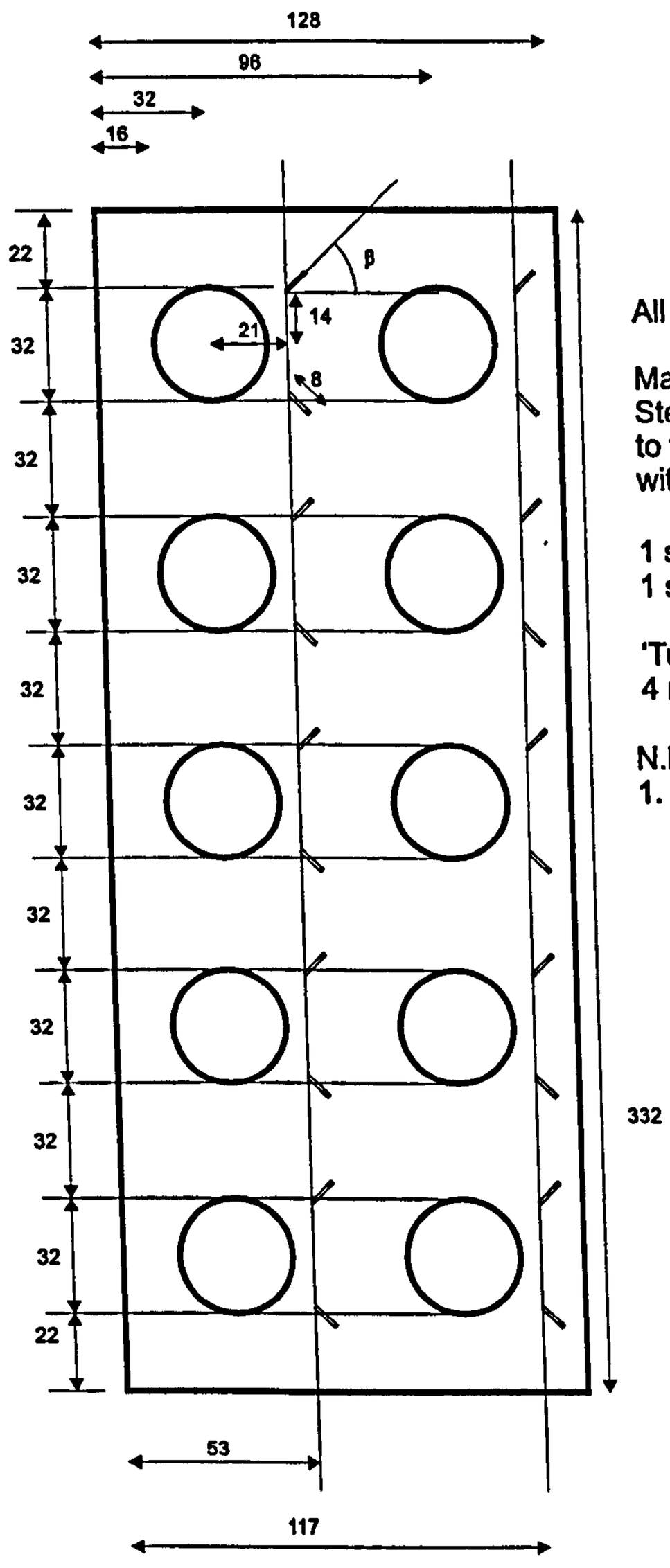

DELTA WINGLET PAIRS
(for use with in-line tubes)

All dimensions in mm

Material - 0.8 mm glass fins
Steel shim winglets to be adhesively bonded to fin. Two fins are needed for each test - one is coated with liquid crystal, the other is not.

1 set needed with $\beta = 45$ deg.
1 set without any vortex generators also needed.

'Tubes' are nylon (or similar) rod 32 mm diameter, 4 mm length.

N.B.
1. This model is twice full size for ease of manufacture

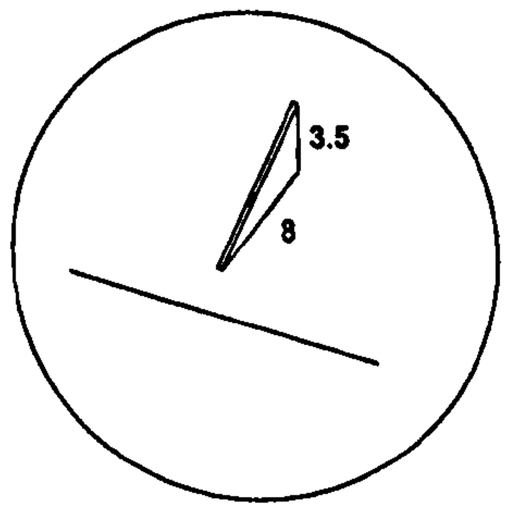

Figure 3.10: Dimensions for an in-line tube array with and without vortex generators

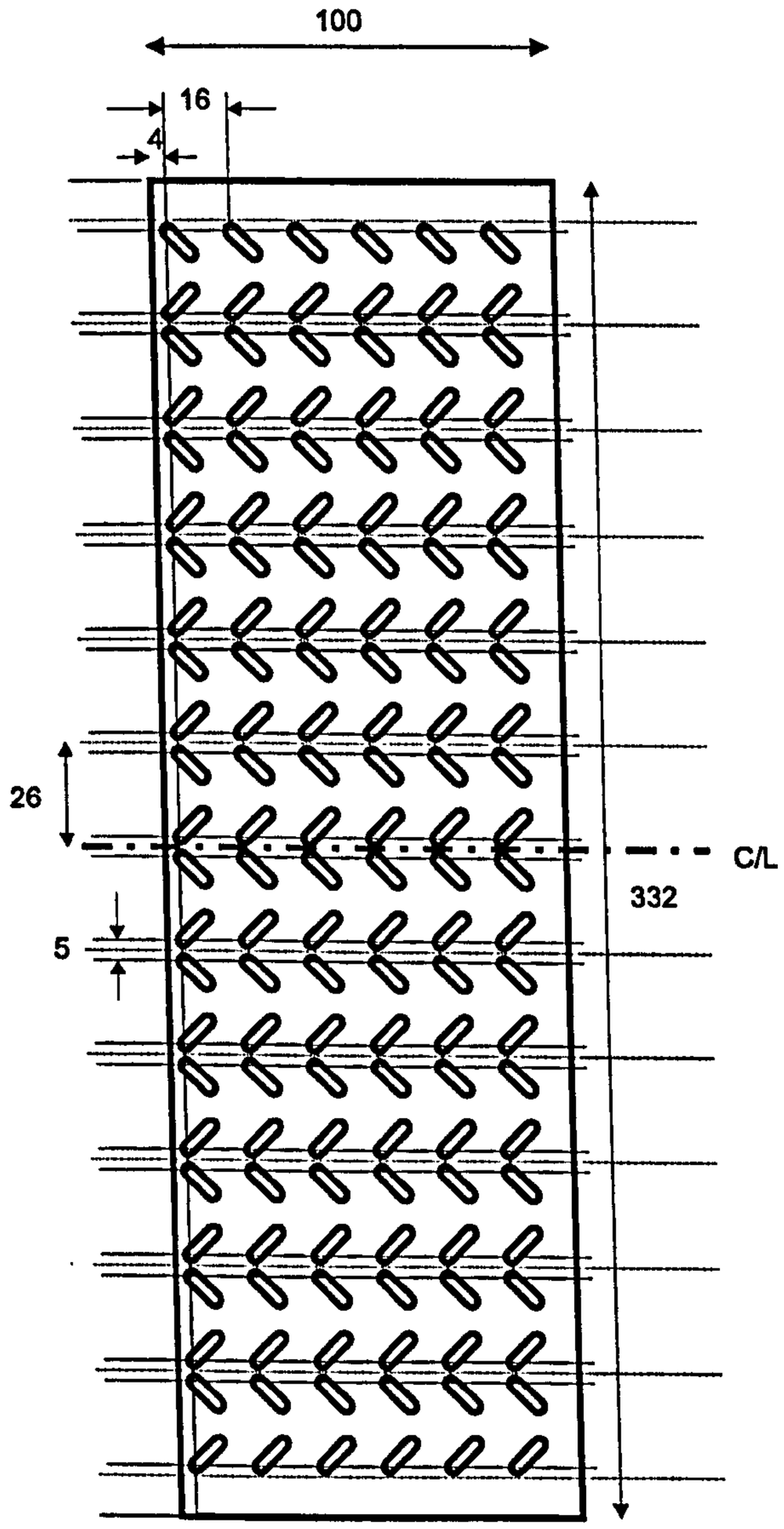

Embossed winglet has approximate semicircular cross-section:

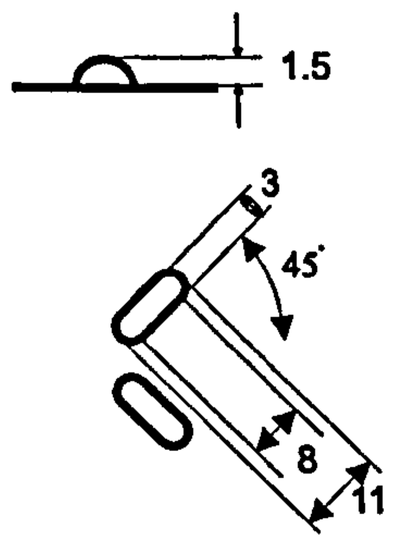

Embossed rectangular winglet pairs (RWP)

All dimensions in mm

Material : 0.8 mm glass with RWP adhesively bonded if necessary

Figure 3.11: Dimensions for an embossed fin vortex generator

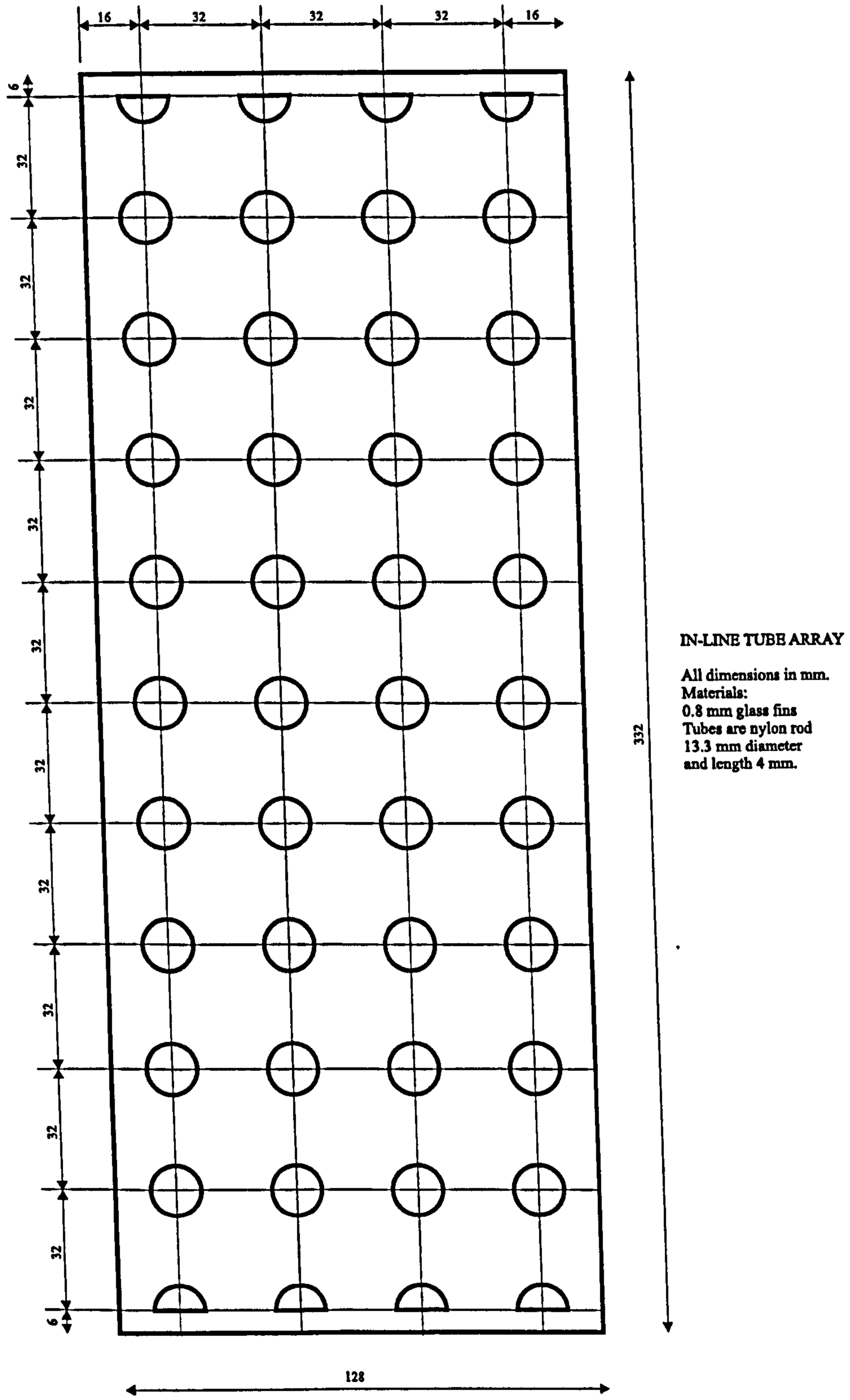

Figure 3.12: Dimensions for round tube heat exchanger section

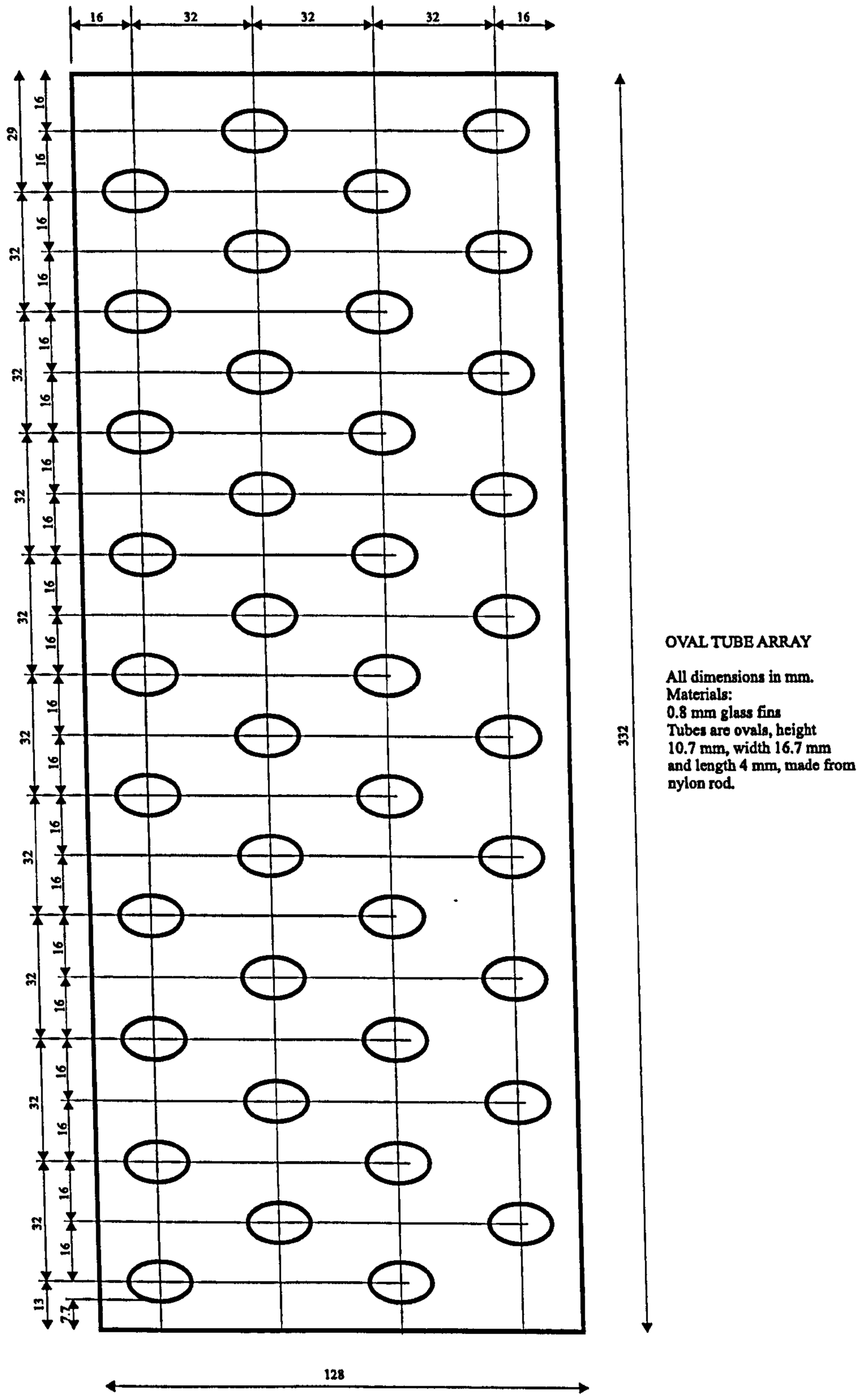
16
32
32
32
16
29
16
16
32
16
16
32
16
16
32

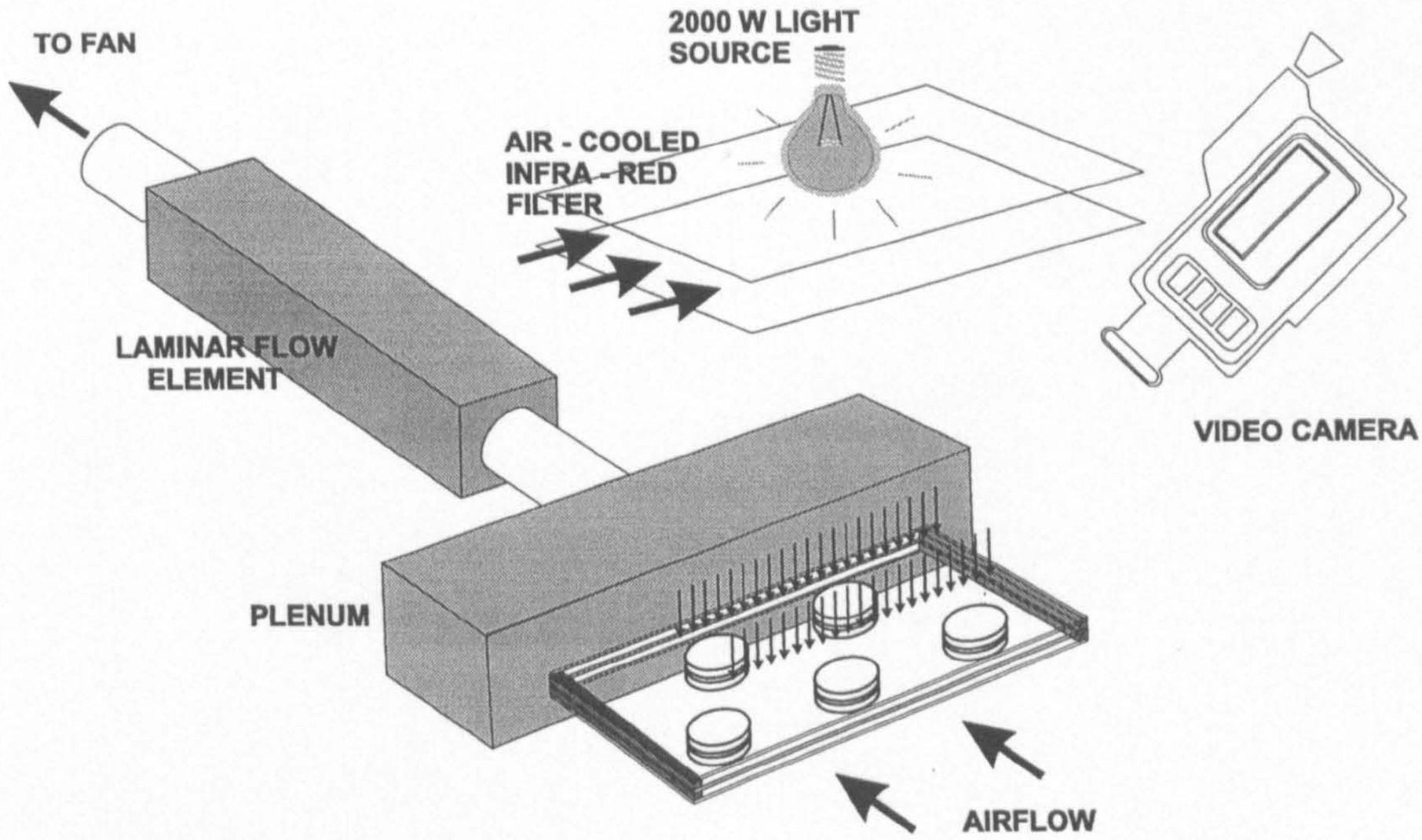

Figure 3.14: Experimental test set-up

adhesive tape. The inlet plenum was connected via a length of pipe to a laminar flow element (manufactured by AirFlow Developments). This allowed measurement of the cooling air flow rate as it provided a linear pressure drop increasing with volumetric flow rate. The pressure drop across the laminar flow element was measured to within 0.1 Pa by a digital manometer. Air was drawn through the experimental rig by a fan which was mounted in a fan plenum. The pressure drop across the heat exchanger element was measured by a differential pressure transducer which produced a linear output voltage ($0 - 5$ V) in the range $0 - 50$ Pa. A digital multimeter was used to measure the output voltage.

The top liquid crystal layer, situated on the central glass sheet was heated by absorbing the light which passed through the upper glass sheet. A 2000 watt tungsten photographic flood lamp was used for this purpose because of its high output and

even distribution. Energy intensities of greater than 2000 W/m^2 could be achieved by using an integrated electronic unit to control its brightness. The area of interest was calibrated to better than $\pm 2.5\%$ constant light intensity using a Kipp & Zonen CM5 solarimeter. The heat flux uniformity compares favourably with surface heaters which were investigated by Jambunathan et al. (1994) for their heat uniformity. They reported at best $\pm 4.5\%$ variation in heat flux for a carbon sheet heater, rising to $\pm 12\%$ for a gold surface heater and $\pm 30\%$ for a stainless steel surface heater. The Kipp and Zonen CM5 solarimeter measured light intensity only in the visible light and ultra violet light range. To avoid the effects of infra-red radiation on the light intensity readings and to reduce heating of the top glass sheet by infra-red radiation, an infra-red filter was placed immediately below the light source. This consisted of two glass sheets mounted in a box with a high rate of cooling air being drawn between the plates. Approximately 4.4% of all radiation is reflected from each glass-air interface. To account for the effect of the top glass sheet in the heat exchanger model, a covering glass sheet was placed over the solarimeter during calibration to reproduce the transmission loss.

The liquid crystal isotherms were recorded for different heat flux input levels by a Cannon Ex2 Hi8 camcorder equipped with a CL8 120 mm zoom lens. When a flat plate was being measured only one surface had to be recorded. The top surface was chosen as it was found that clearer, more sharply defined isotherms existed. This meant that the test image had to be manipulated before analysis could begin because the camera was not normal to the surface due to the light source being directly

overhead. The camera angle was fixed during calibration and experimentation.

On starting work with the steady state technique the isotherms were run over the tip of the thermocouple to calibrate the liquid crystal. This was also repeated at the end of the test to check if any drift in colour play had occurred. To measure low heat transfer coefficients, low heat flux inputs were used. About ten seconds of the image would be recorded when the isotherm reached steady state condition. For low heat transfer coefficients this equilibrium could take up to 30 minutes. About 10 increasing heat flux levels were used to measure the whole range of heat transfer coefficients. Steady state conditions were achieved in a matter of a few minutes for higher heat flux inputs and the whole test lasted in the region of three hours.

Frames of the liquid crystal isotherms from the Hi8 camcorder were selected and converted to high resolution 736 x 560 pixel 256 colour GIF images using Screen Machine 11, a "frame grabber" installed in a personal computer. Due to the camera being at an angle to the test section a distorted image was seen on the GIF image, reproduced in black and white in Figure 3.15. To correct this, the GIF image

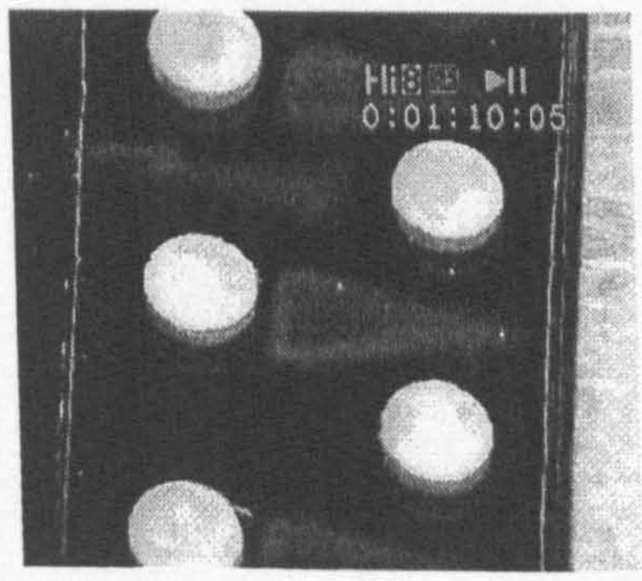

Figure 3.15: Original distorted GIF image recorded from the camcorder

was imported into a graphical manipulation package Corel Draw, where it could be stretched and rotated to return it to the shape that a camera normal to the surface would have recorded. Ellipses were drawn around the ends of the tubes, and the sizes and positions of these ellipses were measured and recorded. The equilateral triangular pitch was verified by calculating the geometric translation required to rotate and then stretch or shrink the image. Using the undistorted image a box was placed around the area of interest enclosing half of each tube on either side: it was assumed that the flow pattern was symmetrical about the mid-points of the tubes. This box and ellipses were returned to its original distorted shape so it could be placed on top of the original GIF image and hence the contour of constant temperature could be traced. This contour was traced by eye using the "draw" function in Corel Draw, Figure 3.16. The GIF image was then deleted leaving the

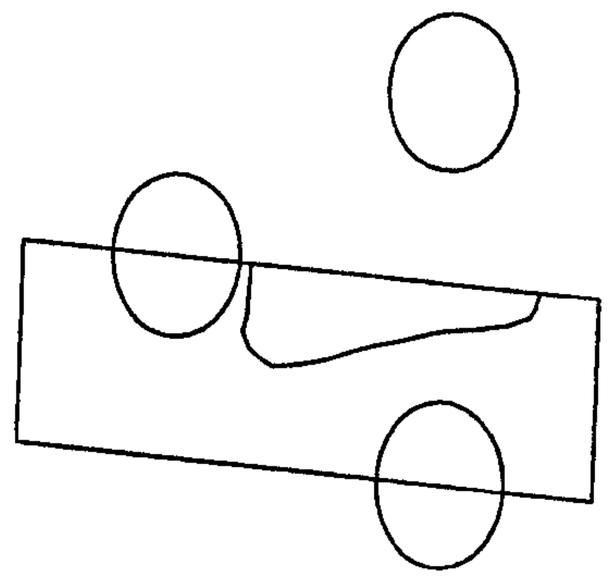

Figure 3.16: Distorted isotherm and region of interest

isotherm and ellipses. This image was then re-translated back to the true shape using the stretch and rotation calculated previously as shown in Figure 3.17. This translation was checked by verifying that the ellipses were now circular and the pitch geometry was correct. The circles were then deleted leaving the isotherm which was

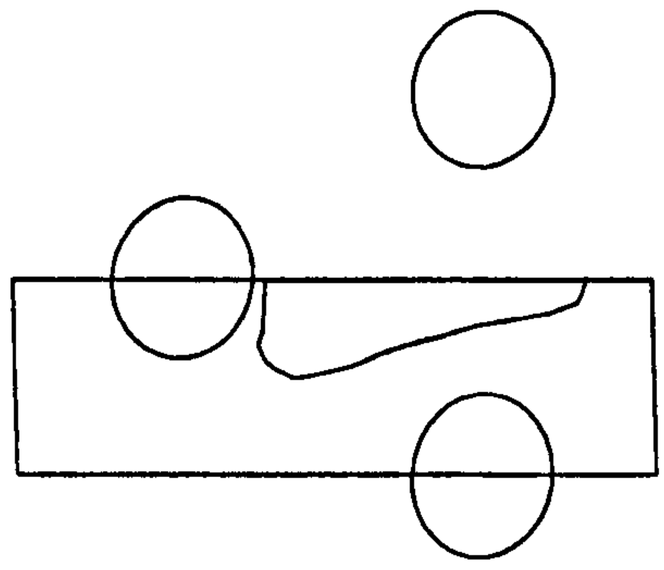

Figure 3.17: Corrected isotherm and outline

saved as a GIF file which corresponds to a certain heat transfer coefficient, Figure 3.18. The heat transfer coefficient was calculated using equation 3.8. The GIF

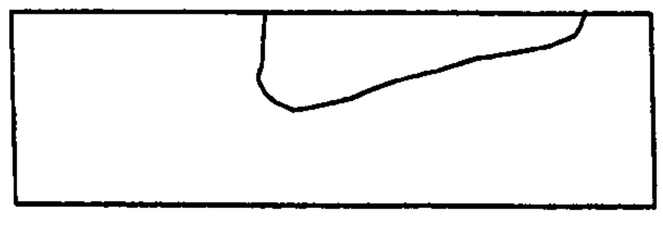

Figure 3.18: GIF file ready for importing into Matlab

files of the isotherms and the corresponding heat transfer coefficients were combined using the "griddata" function of Matlab. This command interpolates between the differently spaced isotherms with known values of heat transfer coefficient and uses an inverse distance method to calculate the value of heat transfer coefficient at points on a regularly spaced grid. The programme containing the griddata function (Appendix E) also calculates an average value of heat transfer coefficient over the whole area.

3.5 Summary

An experimental method using liquid crystal thermography to measure the surface temperature and thus heat transfer coefficient has been designed, developed and validated. Using an uncertainty analysis based on the derived data reduction equations the steady state technique was chosen in preference to the transient technique. The uncertainty in the heat transfer coefficient was estimated to be less than 4%. Uncertainties in non-measured variables were also quantified: the radiation losses were less than 2% and the tangential conduction was also on average less than 2%, when more than 2 mm from the leading edge. The data collection and analysis system has been described. This uses a camcorder, frame grabber, Corel Draw and Matlab, the output is a contour map of the heat transfer coefficient.

Comparisons between the steady state and transient techniques using a constant heat flux input have also been made. Reasons for the large differences in the heat transfer coefficient given by each technique have been given and ways to make the two techniques more compatible have been explored.

Chapter 4

Computational Investigation

This chapter describes the use of a commercial CFD code for the prediction of velocity, pressure and temperature fields in heat exchanger sections with and without vortex generators. The various techniques which were mentioned in the literature review, and which are applicable to this chapter have been expanded so that they are explained in detail. The manner in which the appropriate governing equations of heat and fluid flow are discretised, along with the solution procedure to calculate the variables of interest has been explained. The domain over which the discretised equations have been applied and the boundary conditions needed to solve the problem have been specified. Particular attention has been paid to the boundary conditions and problem specification so that the experimental work covered in this thesis can act as a validation case for the numerical technique. Owing to the importance of achieving mesh independent solutions, the results achieved have been tested by two different methods to ensure mesh independence. To validate the numerical results, a number of predicted parameters have been compared against the experimental results. These have included the velocity profile, isotherm positions, average heat transfer coefficients and pressure drop values.

4.1 Solution Procedure

The numerical code used in this study uses the finite volume method to discretise the governing equations of fluid motion and energy transfer. The code used was a commercial CFD code from Computational Dynamics Limited, STAR (Simulation of Turbulent flow in Arbitrary Regions), which has a pre- and post-processor PROSTAR. Two different versions of STAR were used in this investigation. A single processor version of STAR was used for models with a low number of cells, and STAR-HPC, a parallel code enabled up to 16 processors to be used simultaneously by decomposing the mesh and sending each sub-meshed part to an individual processor. Generally during this study only eight processors were used, this could potentially reduce the numerical computation time by eight times when compared to a single processor.

4.1.1 The finite volume method

The key step in the finite volume method is the integration of the governing equations over a three-dimensional control volume. Considering the conservative form of the steady state momentum equation, the integration over the control volume yields, Versteeg and Malalasekera (1995):

$$\int_{(CV)} div(\rho\phi\,\mathbf{u})dV = \int_{(CV)} div(\Gamma\, grad\,\phi)dV + \int_{(CV)} S_\phi dV \qquad (4.1)$$

where ϕ is some general variable and Γ is the diffusion coefficient.

The convection and diffusion terms (the left hand term and the first term on the right hand side) are re-written as integrals over the entire bounded surface of the control volume using Gauss' divergence theorem. Equation 4.1 can be written as:

$$\int_A \mathbf{n}.(\rho\phi\mathbf{u})dA = \int_A \mathbf{n}.(\Gamma\, grad\, \phi)dA + \int_{CV} S_\phi dV \tag{4.2}$$

STAR expresses the convection and diffusion terms as average values over the cell faces. The last term in equation 4.2 represents any sources or sinks of the transported property as well as any additional flux terms. These are in general expressed in a quasi-linear form.

4.1.2 Governing equations applied to problem

For the various models built, the governing equations were not used in their full form as a number of simplifications could be made. The first simplification, already made in Section 4.1.1, is the assumption that the final converged solution is not time dependent and thus the time terms can be removed from all equations. This can be justified for the work carried out in two ways.

For plain channels with vortex generators, the formation of longitudinal vortices is caused by the pressure difference across the vortex generator and flow separation at the leading edge. The formation of longitudinal vortices is due to a shear layer instability and because of this the longitudinal vortex becomes unsteady and self-sustained oscillations set in at a critical Reynolds number. A finite volume code

which carried out a direct numerical simulation of the three-dimensional unsteady conservation equations was used by Fiebig (1997) to evaluate the critical Reynolds number where flow instability and thus time dependent flow occurred. He found that, for a rectangular winglet at an angle of attack of $\beta = 45°$ and a height ratio (height of vortex to channel height) of 0.5, self-sustained oscillations started for a three-dimensional geometry at a Reynolds number based on channel height of around 300. All numerical simulations carried out in this study were in the laminar flow regime and most had a Reynolds number based on channel height of less than 300.

When a cylinder is placed in a channel it is well known that a recirculation region occurs behind the cylinder due to flow separation around the tube. Up to a Reynolds number of 47 based on cylinder diameter a closed recirculation region is formed by two transverse vortices, Noack and Eckelmann (1994). At higher Reynolds numbers the interaction of the two separated shear layers leads to oscillations and the formation of a Von Karman vortex street. This type of flow is highly time dependent. However, by placing the cylinder between parallel plates, such as would occur in a compact heat exchanger, the flow instability is considerably damped allowing higher Reynolds to be achieved before time dependent flow occurs. Chen (1993) carried out a numerical simulation of this case with the unsteady fluid flow conservation equations. He reported that when the ratio of the channel height to tube diameter was 0.2, no time dependent flow was found up to a Reynolds number based on channel height of 1000. As reported earlier, the Reynolds number of the numerical

simulations carried out in this study was much lower.

It should be noted that the effect of boundary conditions can also have an effect on the stability of the numerical solution. By applying a symmetry boundary condition on the sides of the domain, Fiebig et al. (1995a) found that steady flows were obtained at higher Reynolds numbers in comparison to using a periodic boundary condition. This was because of the damping added to the system by the symmetry boundary condition. However the symmetry boundary condition is often used because of its simplicity resulting in less CPU time.

Due to the low flow velocity used in the CFD modelling (around 1 m/s) compressibility effects could be ignored, and as a result the density ρ is constant and the continuity equation becomes $div\,\mathbf{u} = 0$. This also results in the second viscosity in the Navier-Stokes equations λ being ignored, Section 2.1.2. This leaves the viscous stresses twice the local rate of linear deformation times the dynamic viscosity. Changes in the density due to natural convection and temperature losses due to radiation were also considered at this stage. Simulations showed negligible difference between a constant density solution and a variable density solution. This was because the rise in temperature of the air over the test section was small (approximately 10^0C) and the buoyancy parameter (Gr/Re^2) was found to be approximately 0.001, much less than the value of 1 when natural convection becomes dominant. A model with and without radiation was run and showed negligible difference between the two.

4.1.3 Solution algorithms

With the exception of the two-dimensional plane channel model the differencing scheme used was MARS, Anon. (1998). This is a second-order differencing technique that avoids the undesirable under- and over-shoots when there is a discontinuity in the flux gradient. The MARS routine calculates a set of monotone gradients for the advected flow property to second-order using a multidimensional Total Variation Diminishing (TVD) scheme, Harten (1983), (1984) and Jameson and Lax (1984). The advected flow property is then extrapolated to the cell faces using the monotone gradients. An advection scheme takes over and uses the two values to produce a single cell face value according to the direction of the mass flux through the face. When TVD conditions exist no new local extrema can be created and the value of a local minimum or maximum is non-decreasing and non-increasing respectively. Hirsch (1990) has comprehensively reviewed TVD schemes and monotone conditions. The MARS routine also has the advantage that it is extremely robust, models can be started from zero initial conditions with the second order accurate scheme, and convergent behaviour will be found. Previously, when Linear Upwinding Differencing (LUD) was used, the model had to start from a converged first-order accurate initial field before convergent behaviour was found.

For the two-dimensional plain channel model, first order upwind differencing was used. This is a first-order accurate differencing that selects the nearest upwind value of ϕ when differencing. As the flow field in the plain channel model was convection dominated, with no steep gradients in the temperature or flow fields,

upwind differencing gave results in excellent agreement with higher order differencing schemes.

As the flow field was assumed to be steady-state, STAR allows two algorithms to calculate the pressure gradient term in the Navier-Stokes equations and thus the velocity field. Comparisons between the algorithms showed that the SIMPLE algorithm was faster than SIMPISO, therefore the SIMPLE algorithm was used. The SIMPLE algorithm makes an initial guess of the pressure (p^*) and velocity (u^*, v^*, w^*) fields. From this guessed pressure field the discretised momentum equations are solved yielding a guessed velocity field. The correct velocities u,v,w and pressures p can be related to the guessed components by the addition of correction factors u', v', w', p'. This enables a correction formulae for the velocities to be written in terms of the corrections to the pressure field. As the flow field also has to satisfy the constraint of continuity, the velocity correction can be substituted into the continuity equation to solve the pressure correction equations. The correct pressure and velocity fields can then be solved in an iterative manner. The non-linearities in the equation set are solved in an inner loop whilst the corrected velocities are being calculated.

To model the heat flux input mechanism in a similar manner to the experimental model, a user-coded subroutine (Appendix E) was used. This was first reported by Holland et al. (1997) and uses a thin layer of cells placed between the fluid and the top of the middle fin. In these cells the required heat flux was specified, which is converted to a source term per unit volume by the subroutine where it

is used by the energy equation. An energy balance is then used to determine how much of the heat flux is conducted into the fin and how much is convected into the air-stream. The energy equation is also solved in an iterative manner after the corrected pressure and velocities have been calculated in the SIMPLE algorithm. The energy equation is therefore decoupled from the flow and pressure fields. Heat transfer in finned-tube heat exchangers is a conjugate problem, Fiebig et al. (1995b), therefore the temperature has to be determined simultaneously within the fluid and the neighbouring solid. STAR allows this option in the steady-state case by simply applying a degenerate form of the energy equation (2.8) which only considers the energy flux due to heat conduction.

Convergence of the solution is taken when the normalised residual sum of each variable is typically 4 orders of magnitude smaller than the initial residual. Using a SUN SPARC Ultra workstation running STAR with 256 Mb memory with 2 Gb disk space on a model of around 400,000 cells solving for the velocity, pressure and temperature fields, convergence takes around 15 hours.

4.2 Mesh specification

4.2.1 Prostar

All the models for the various different geometries were built using the pre-processor, PROSTAR. PROSTAR uses body-fitted meshing, and allows a number of different cell types to be used such as: hexahedra, prisms, tetrahedra, pyramids and poly-

hedra to be used. These different cell types along with the capability for creating unstructured non-orthogonal grids, local mesh refinement and arbitrary coupling between mesh blocks allows complex geometries to be built.

The basic entities available for building a mesh in PROSTAR are vertices, cells, shells, patches and blocks. The following definitions are given from the STAR-CD manual:

- A vertex is a point in three-dimensional space defined by a coordinate triplet and possessing an index number for identification.

- A cell is a three-dimensional volume whose shape is defined by vertices created at its corners.

- A shell is a two-dimensional surface whose shape is defined by vertices created at its corners.

- A spline is a smooth curve defined by vertices along its length.

- A patch is a smooth or curved surface whose outer parameter is defined by four splines and/or straight lines which is internally filled with shells.

- A block is a three-dimensional volume bounded by smooth, curved or flat surfaces, whose edges consist of eight splines and/or straight lines.

There are four basic methods within PROSTAR for setting up a mesh. Firstly a three-dimensional mesh can be extruded by a given number of layers from an existing surface. The second technique is the multi-block method where the solution

domain is divided into a series of conveniently shaped blocks that define the geometry of the model. Sub-division of each block into individual cells is then possible. PROSTAR carries out the procedure of sub-division automatically. Thirdly, the opposite approach can be used whereby the solution domain is built up from individual cells. Finally PROSTAR allows for data import of either entire meshes built by CAD/CAE systems such as SAMM, ICEM CFD Tetra, PATRAN and ANSYS, or geometric definitions of models in the form of surfaces, splines or points generated by external CAD/CAE systems in IGES or VDA format.

4.2.2 Plain channel model

The two-dimensional plain channel flow model has been built using the multi-block approach. As the model was only two-dimensional, the mesh was only one cell thick in z and due to the simplicity of the model the mesh was of structured type. The model built corresponded to the experimental model and therefore had two flow channels and three fins. Along its length (88mm), 88 cells were used, Figure 4.1 and through the depth of the channel (4mm) 26 cells were used. Near the wall, mesh refinement was used to capture the steep velocity gradients in the boundary layer. It was originally hoped to model the fluid inlet as a box around the test section inlet to model the possibility that the fluid could approach the inlet in any direction. This however caused difficulties with convergence as the fine scale fluid structure forming around the leading edge of the fins could not be modelled due to very fine meshing being required. The inlet chosen consisted of extensions to the fluid flow

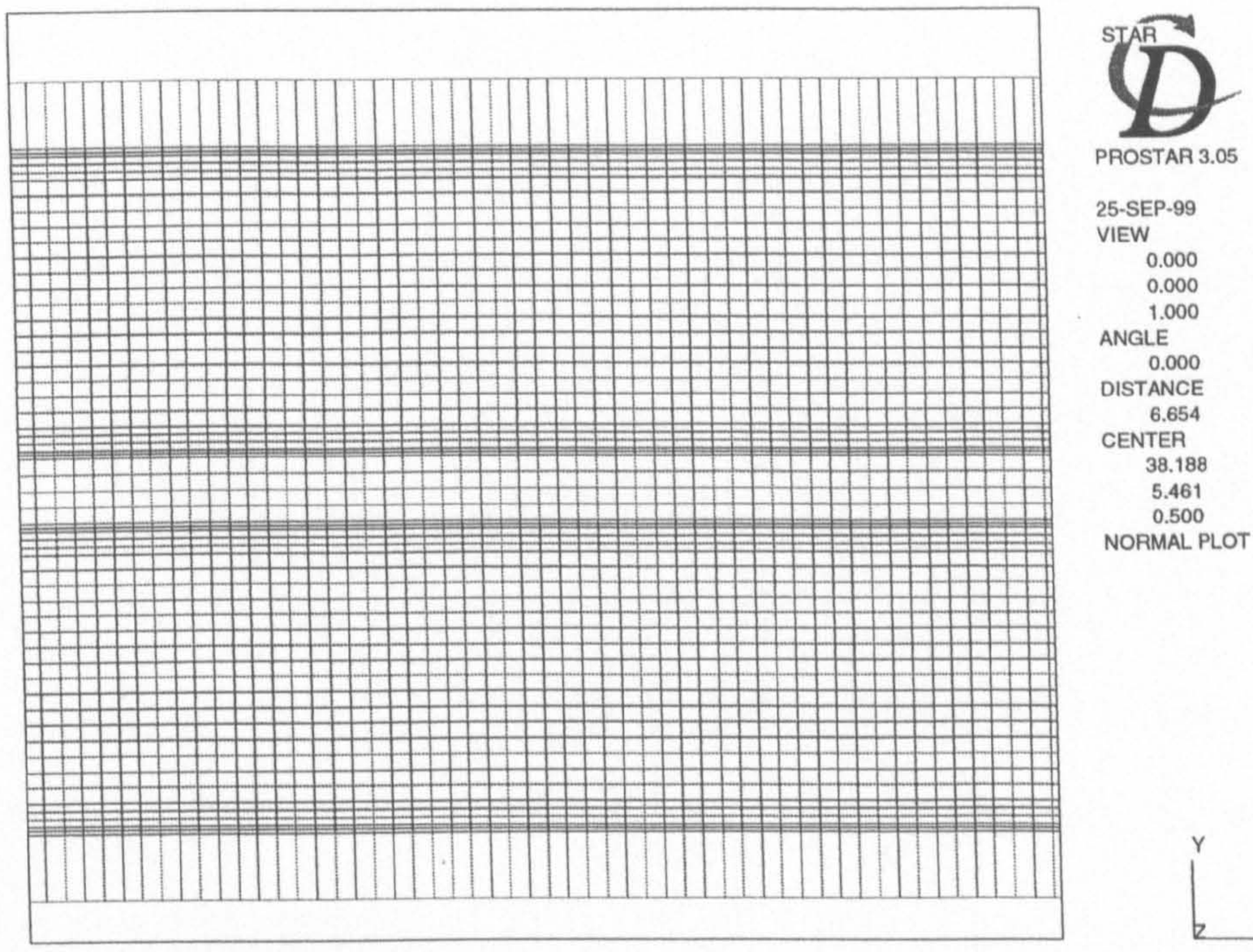

Figure 4.1: Mesh distribution for plain channel model

channels in the upstream direction to a position where the pressure was constant over the whole of the inlet.

4.2.3 Staggered and in-line heat exchanger sections

The meshing strategy for staggered and in-line heat exchanger sections both used the same methodology of creating patched areas with shell cells and then extruding these cells to make up a three-dimensional mesh. As the Reynolds number was low, symmetry of the flow could be assumed round the tubes. This meant that the computational domain could be reduced in size by applying symmetry boundary conditions through the centres of the tubes at an interval of one tube pitch. Two different sizes of staggered tube and one size of in-line tube heat exchanger section

was investigated.

The mesh generated for the heat exchanger section cases consisted of a mixture of H-O forms of mesh. The first step was to create the half O-ring meshes around the tubes. These were created by placing vertices in polar coordinates in a semi-circle with the same radius as the tubes. Another set of vertices is placed in another semi-circle at a bigger radius creating a four-sided area. Splines were then put through the vertices to create a curve. This four-sided area could then be patched using hexahedra shell cells, these are shown in Figure 4.2. These O-ring meshes were created separately to the rest of the mesh as it was believed there would be complex flow structures in this region and therefore a higher mesh density is needed. The H-form meshes are created by taking the 45° points on each of the outer splines and creating four sided patch areas with the outer dimensions of the domain. This surface mesh created with shell cells was then extruded to make two flow channels and three fins in common with experimental test section. The in-line heat exchanger was created in a similar fashion, the shell cell surface from which the mesh was extruded is shown in Figure 4.3. As with the plain channel geometry the inlet was extended far enough up stream so that the pressure would be constant on the inlet boundary. The outlet was also extended downstream of the test section exit to allow the flow to become fully developed and outward facing after the recirculation region behind the last tube.

Some comment should be made here about the quality of the mesh. When using

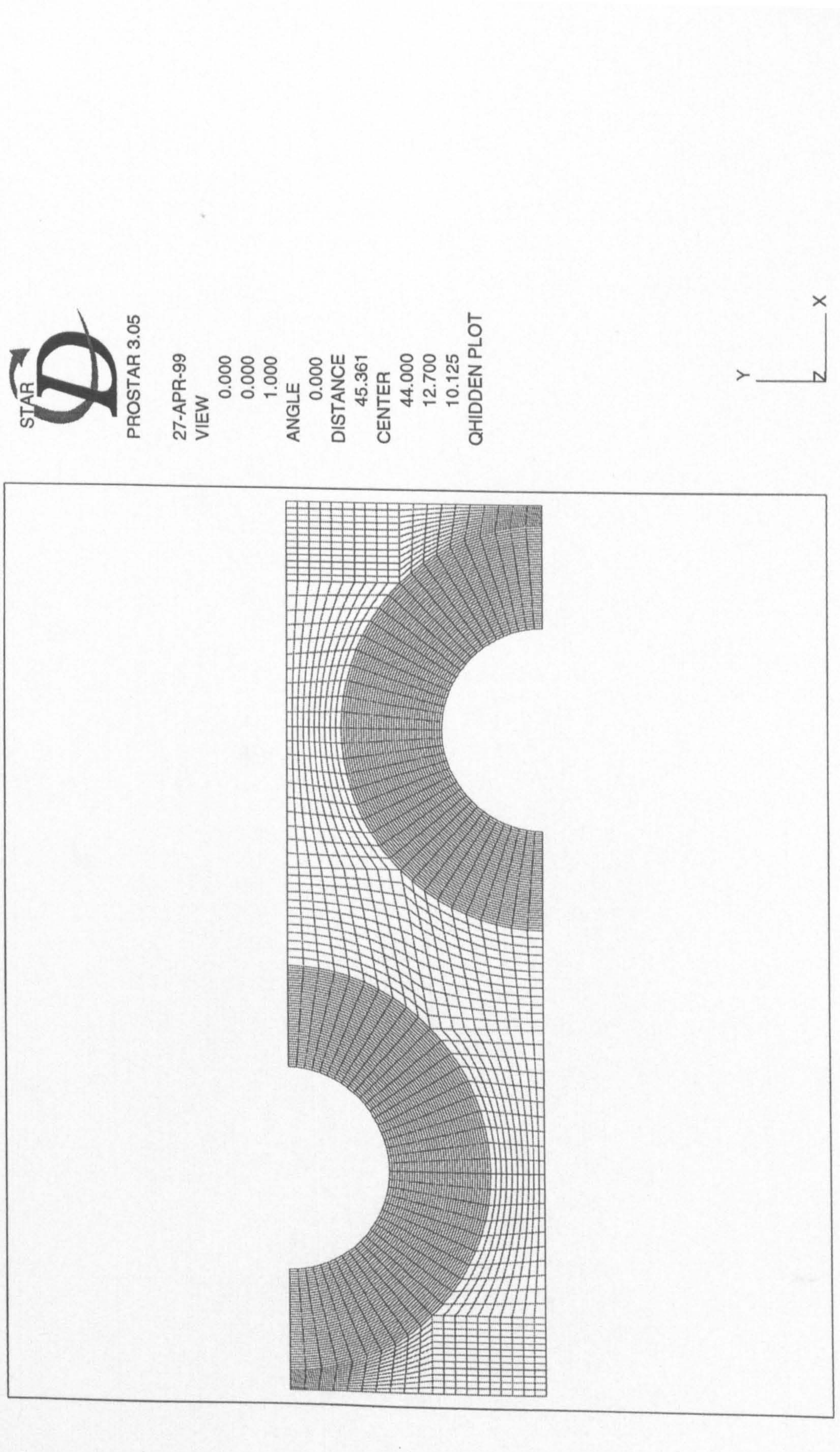

Figure 4.2: Mesh for staggered fin-tube heat exchanger

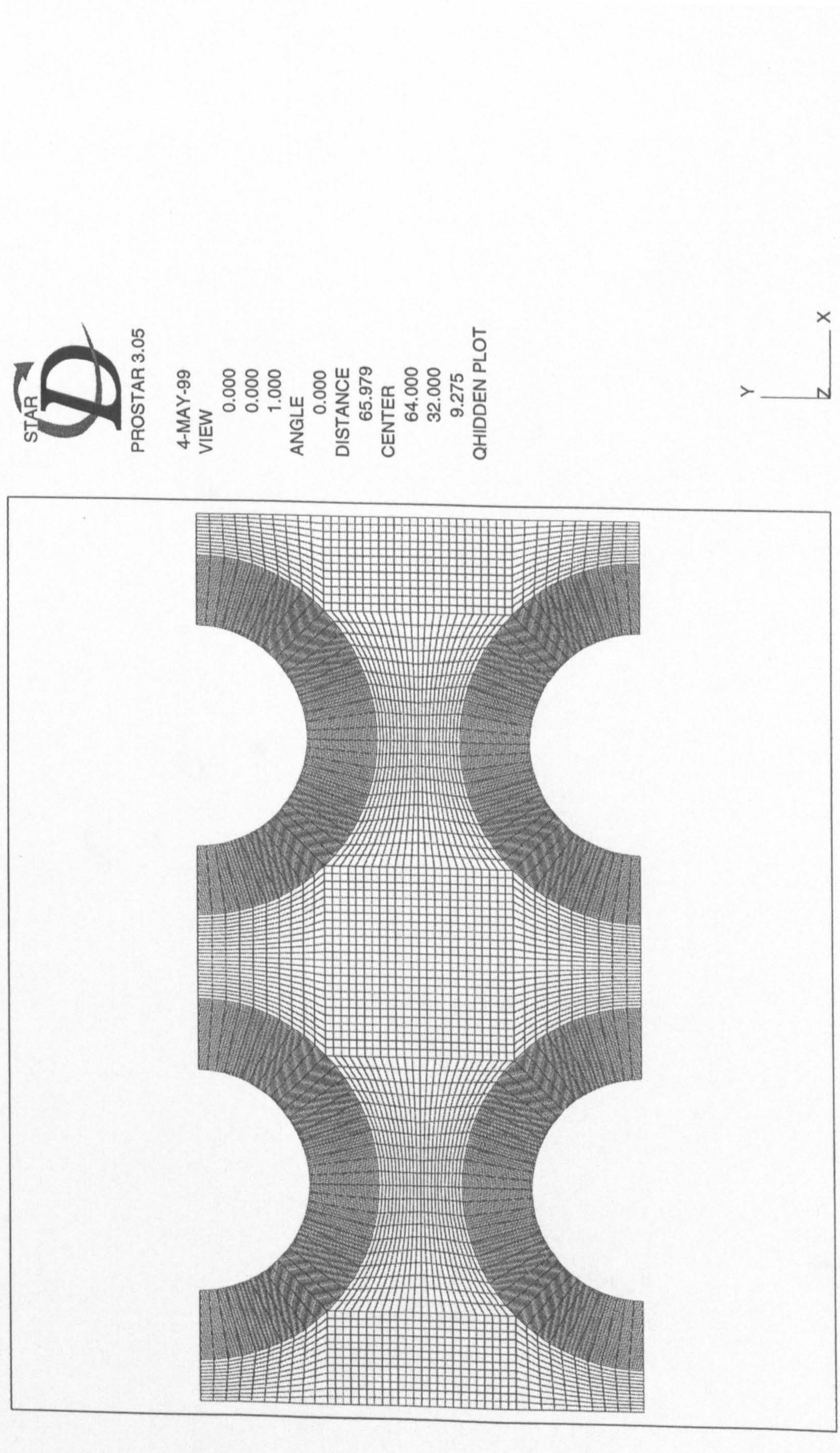

Figure 4.3: Mesh for in-line fin-tube heat exchanger

hexahedral cells the deviation from its ideal shape, in this case a 'brick', is measured in three ways, namely, aspect ratio, internal angle and warp angle. The aspect ratio is the ratio of the lengths of the sides of the cell where the longer side should be in the flow direction. The internal angle and warp angle are deviations from the ideal 'brick' shape where the angles on every face of every cell is 90° and every quadrilateral face is planar. The warp angle can be defined as the angle between two triangles created from the four points of a quadrilateral face. STAR gives guidelines on the upper limits for these factors, but these are normally exceeded particularly in the case of aspect ratio in the flow direction. These mesh distortions should be kept to a minimum to avoid numerical errors or stability problems. To help avoid these situations STAR supports a number of routines to help reduce the internal angles, warpage and aspect ratios below recommended levels. Generally with the meshes built the upper limits given by STAR were exceeded but these cells were limited to a tiny percentage of the overall number of cells used.

4.2.4 Vortex generator models

The vortex generators were all modelled on flat fins before the generator with the best performance was modelled in heat exchanger sections with tubes. Four different types of vortex generator were modelled, rectangular winglet pairs (DWP), delta winglet pairs (DWP), rectangular winglets (RW) and embossed vortex generators.

The rectangular winglet pair vortex generator model was modelled using patches and shell cells. The vortex generator positions were identified, shown in Figure 4.4

as the bold line AB. Patches, which require the definition of four corner points, were created around this vortex generator position, shown in Figure 4.4 as the four sided areas which join up with the boundaries of the domain. By specifying how

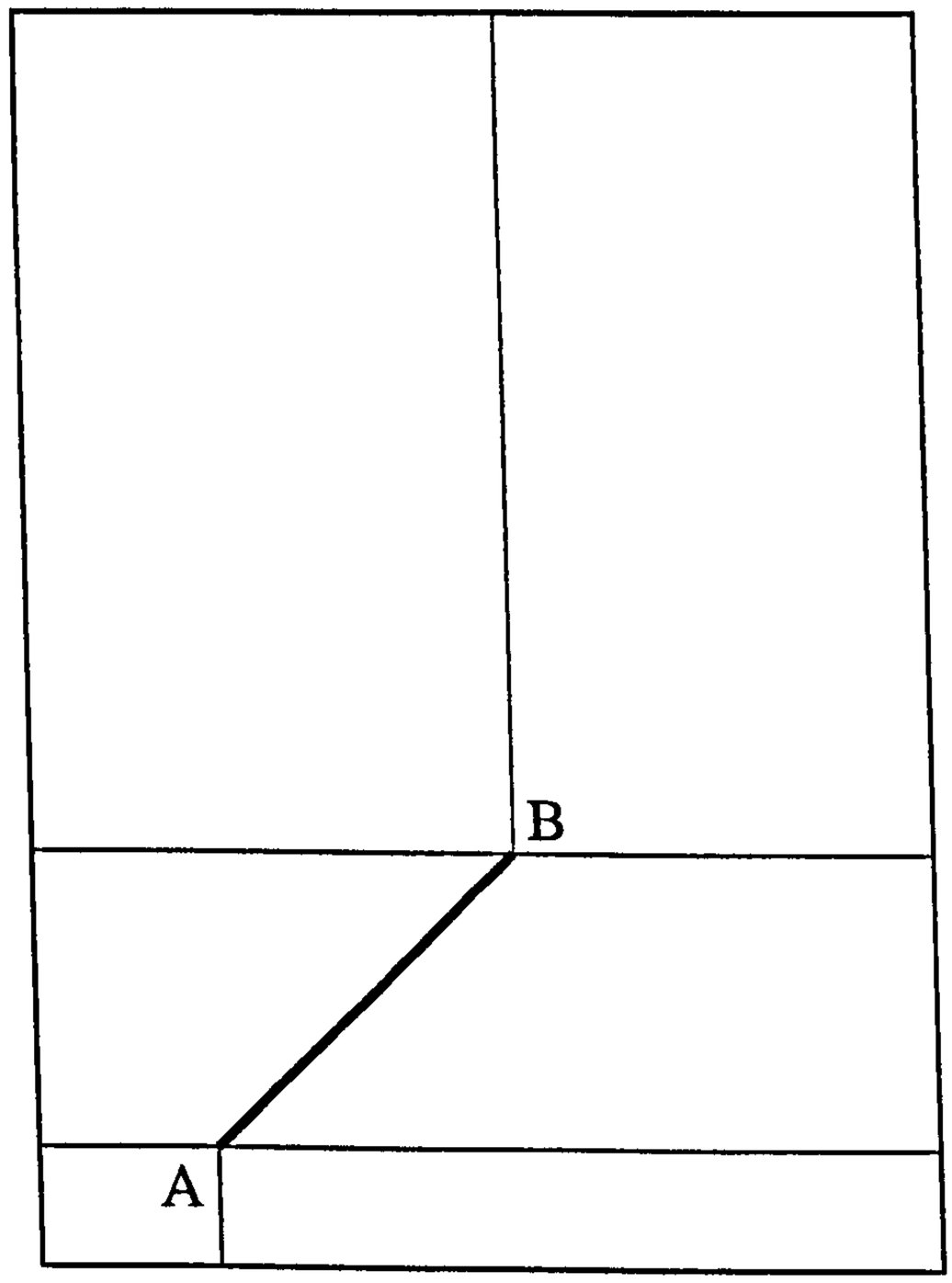

Figure 4.4: Meshing strategy of rectangular winglet pair vortex generator. The vortex generator position is defined by patches

many cells are needed in the x and y directions, PROSTAR automatically divides the area into the required amount of shells, Figure 4.5. The shell surface was then extruded to form three-dimensional volumes which formed the three fins and two flow channels. To create the vortex generators, baffles were placed on the sides of the cells to the correct height. Baffles are effectively zero-thickness, two-dimensional cells which have solid properties. Baffles were used instead of extruding solid cells as the thickness of the vortex generator was, in comparison, much thinner than the

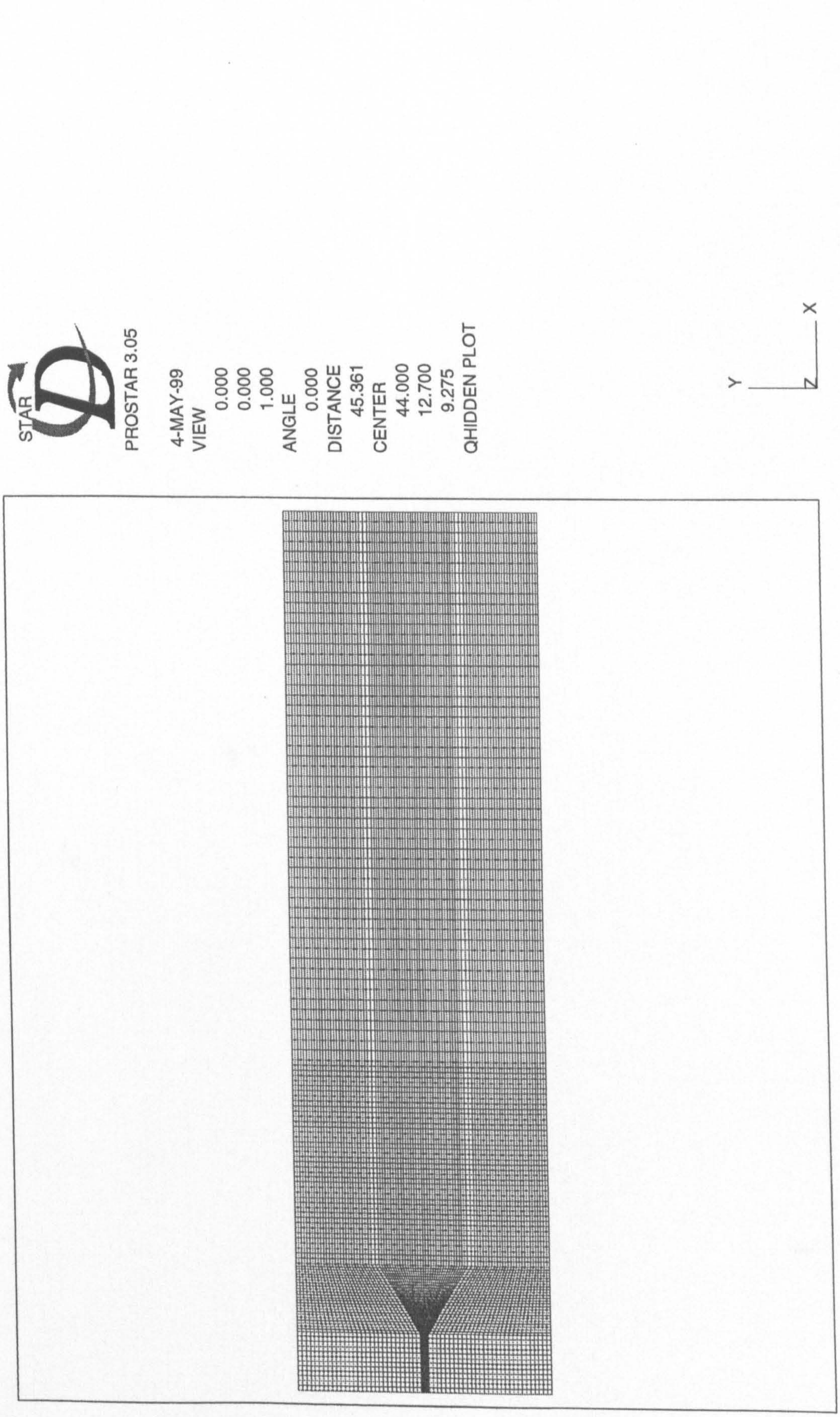

Figure 4.5: Mesh for rectangular winglet pairs

glass sheet which was used as the fin in the experimental setup.

The delta winglet pair model was built by the multi-block approach and the use of patches and shell cells. To create the triangular shape of the vortex generator an H-O mesh type was used. A side view of the triangular shaped mesh is shown in Figure 4.6. As can be seen, the shape is defined by three regions, a square and two

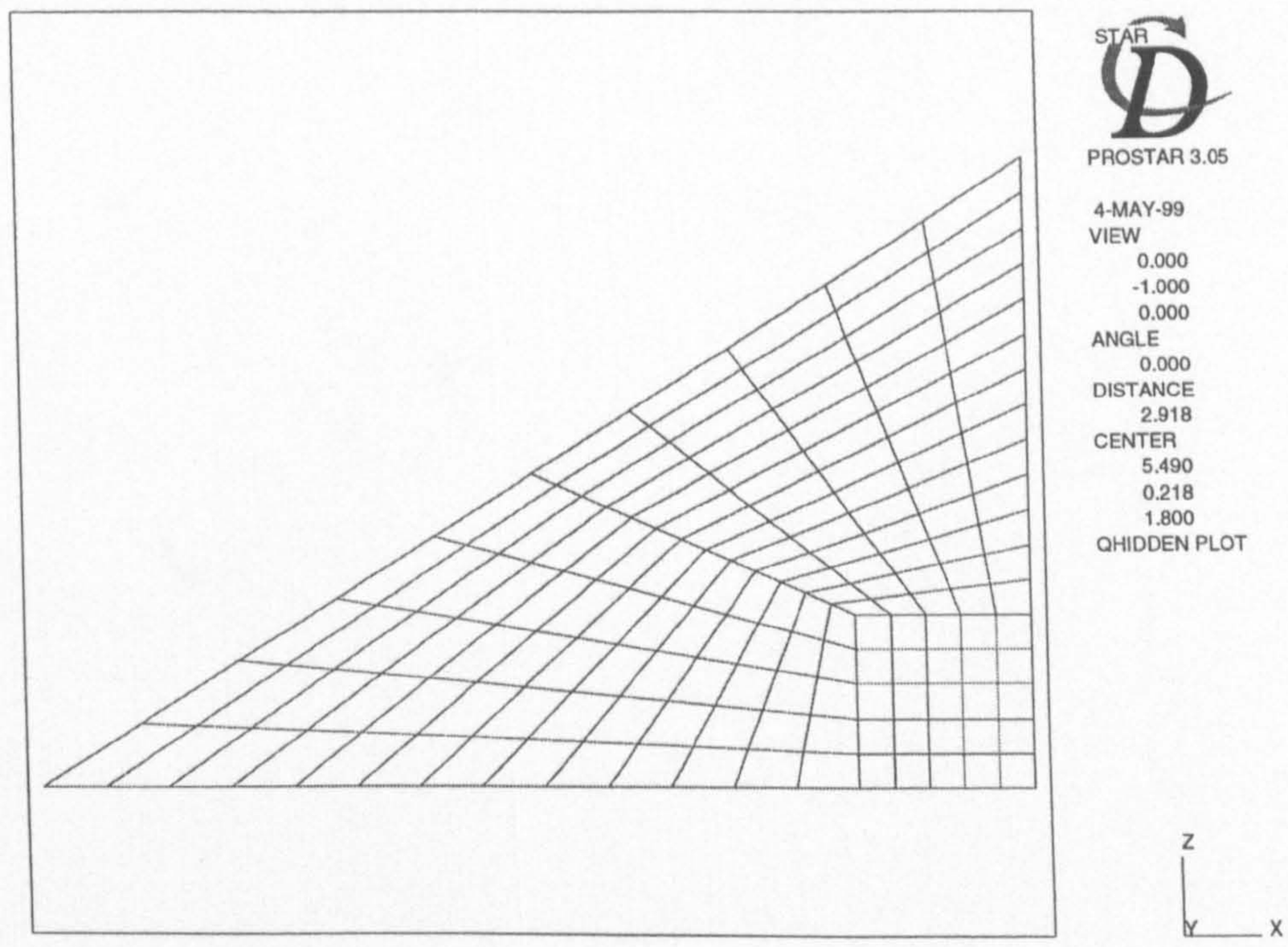

Figure 4.6: H-O mesh to define vortex generator shape

four sided shapes bounded by the out-sides of the triangle and the square. To create the vortex generator positions multi-blocking was used. In using multi-blocking, eight corner vertices have to be defined before each block can be sub-divided into the required number of cells. An exploded block plot, Figure 4.7, shows that three big blocks define the vortex generator position. Baffle cells are placed in the gaps between the big blocks to define the vortex generator. Note that each of the three

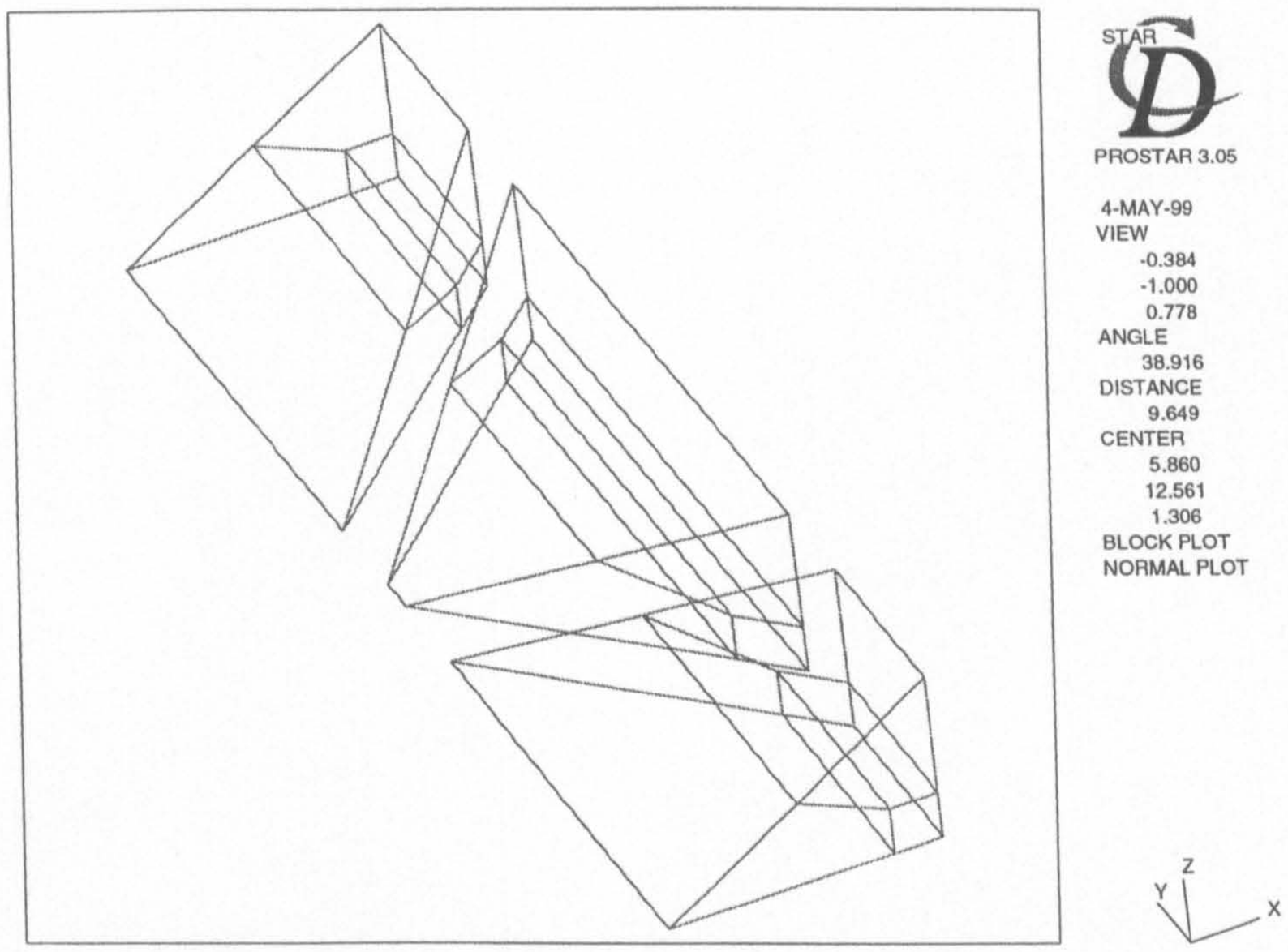

Figure 4.7: Blocks to define vortex generator position

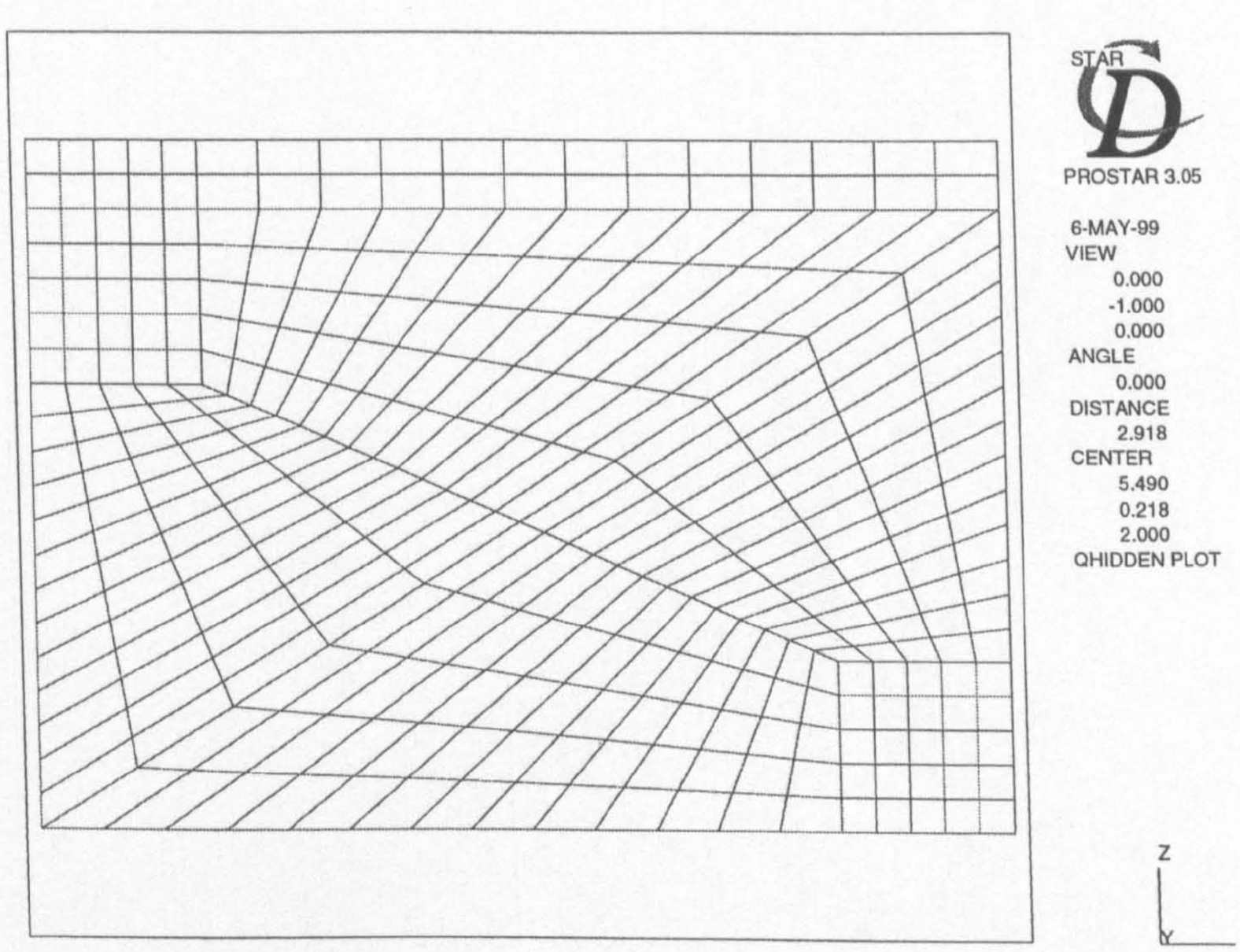

Figure 4.8: Two sets of H-O mesh to create a cube

big blocks are sub-divided into three smaller blocks that make up the H-O mesh. This block pattern was rotated through 180° to form a rectangle of cells, Figure 4.8. The rest of the domain of interest was built around this cube using patches and shell cells. These were extruded until the whole of the domain was filled with cells. The mesh for the rectangular winglet used a very similar multi-block approach. The only difference between the two meshes is that only one vortex generator was modelled and this vortex generator has parallel sides, thus the block ends were parallel.

The fourth type of vortex generator, an embossed rectangular winglet was created by the cell layer method and multi-blocking. The actual vortex generator was created by meshing the two curved ends of the vortex generator in spherical co-ordinates and the main body of the vortex generator model in a cylindrical co-ordinate system, Figure 4.9. The fluid cells were then built around the solid vortex generator by multi-blocking. Firstly, fluid cells were built up around the main body of the vortex generator until the solid cells were placed in a rectangular box. Blocks of fluid cells were then extended out on both sides to the 45° points of the semicircular end of the vortex generator, Figure 4.10, where another block covered the end. Extra blocks were added so that the top of the vortex generator was covered. This was continued until the vortex generator was completely enclosed in a rectangle of fluid cells. The rest of the mesh was built around these rectangles by multi-blocking until the whole of the domain was filled with cells.

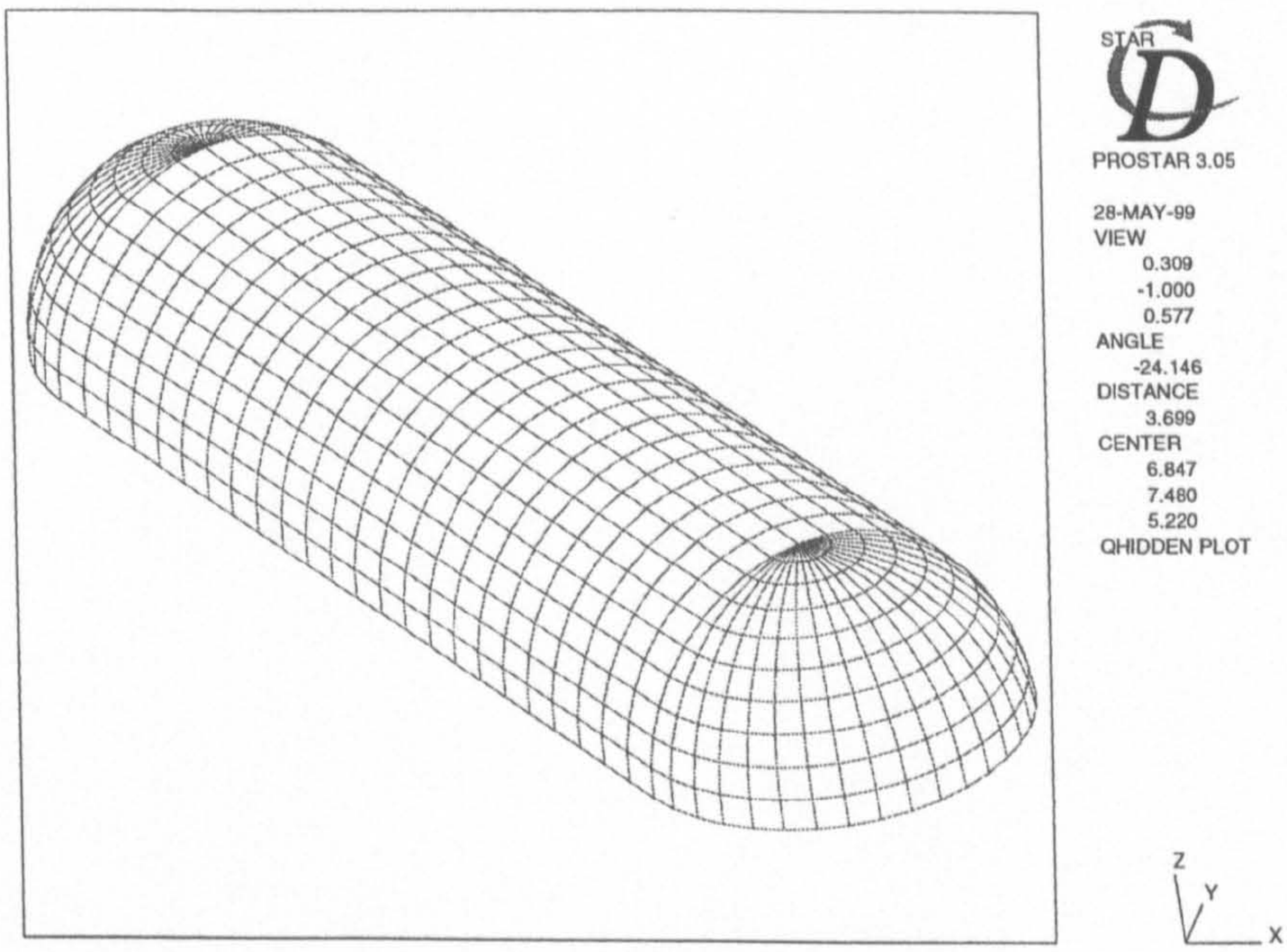

Figure 4.9: Embossed vortex generator modelled using spherical and cylindrical co-ordinate systems

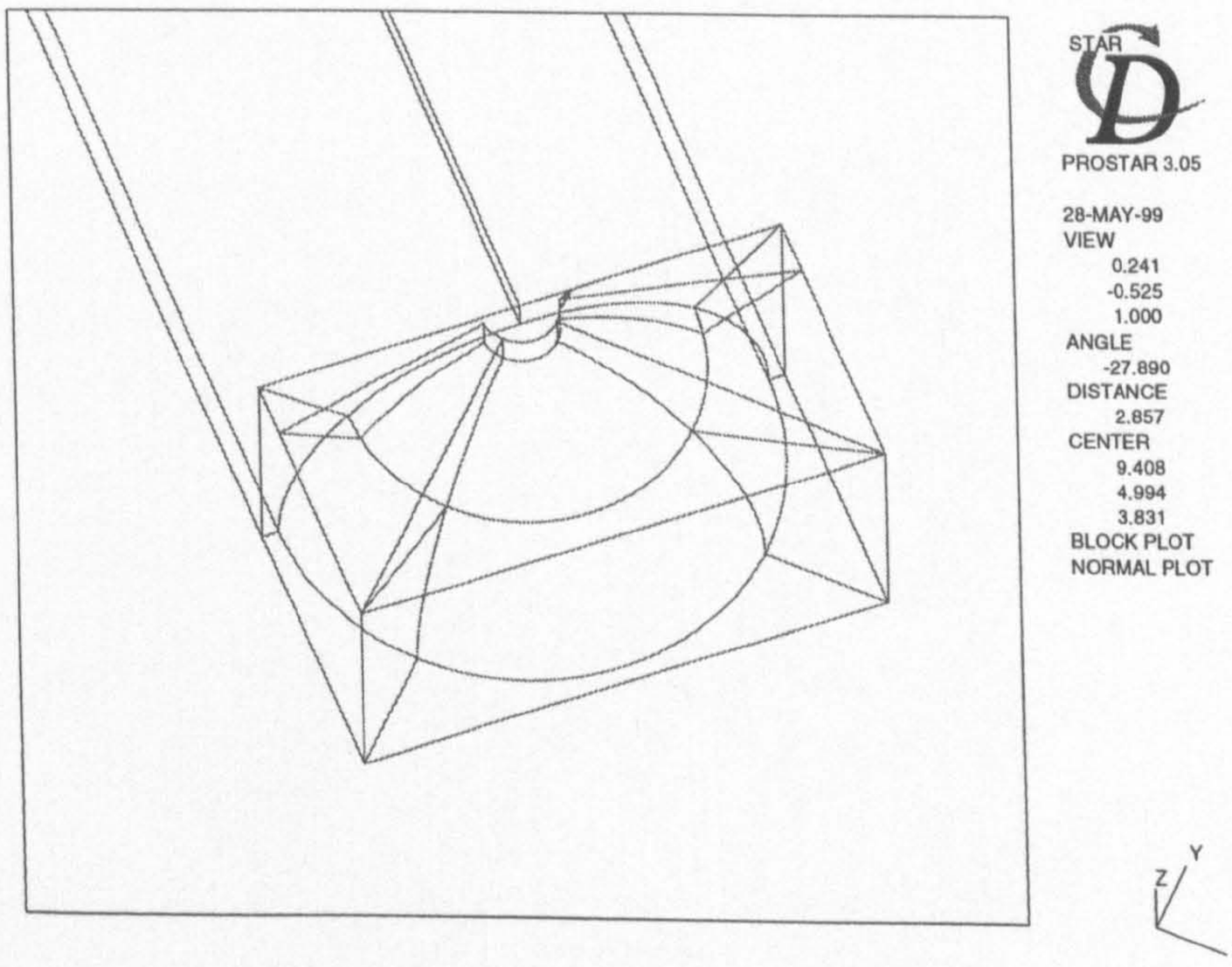

Figure 4.10: Block structure for modelling embossed vortex generator

4.2.5 Vortex generators in heat exchanger sections

The CFD models which included vortex generators in heat exchanger sections were created by adopting both the meshing strategies carried out in creating the vortex generators and heat exchanger sections by themselves. Firstly the blocks to create the vortex generators were built and then the patches and shell cells were created to model the tubes and domain of the heat exchanger section. This lead to a need for greater refinement in the angular direction of the polar co-ordinate region round the tube. This was needed so that the cell interfaces between the vortex generator blocks and the polar co-ordinate region would be consistent in the wake region of the first tube and the horseshoe vortex region of the second tube. This is shown in Figure 4.11 and Figure 4.12 for the staggered and in-line tube arrangement respectively.

4.3 Boundary and initial conditions

As one of the main aims of this study was to validate the numerical code the boundary conditions for the numerical model had to match the physical boundary conditions as closely as possible. This caused some difficulty especially with the inlet boundary condition. The blockage at the leading edge of the test section cannot be avoided in the experimental rig and therefore the velocity profile is not known along with the influence that the wall has on the velocity profile. Several different boundary conditions were tried so as to assess which combination yields a solution nearest to the results obtained from the experimental data. The boundary conditions can take two forms, namely, inlet type boundaries or mass outflow boundaries. With the

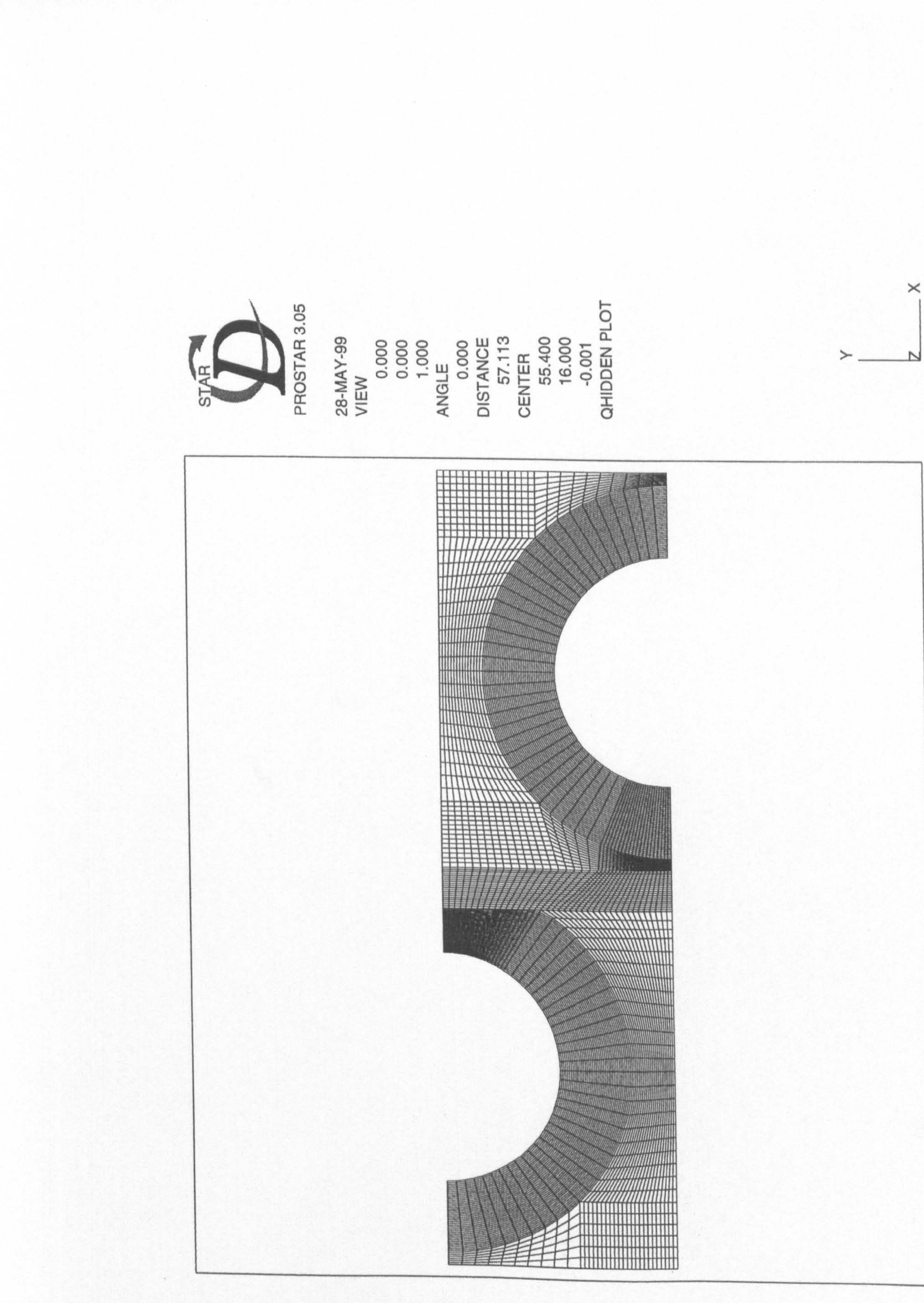

Figure 4.11: Mesh for staggered tubes with vortex generators

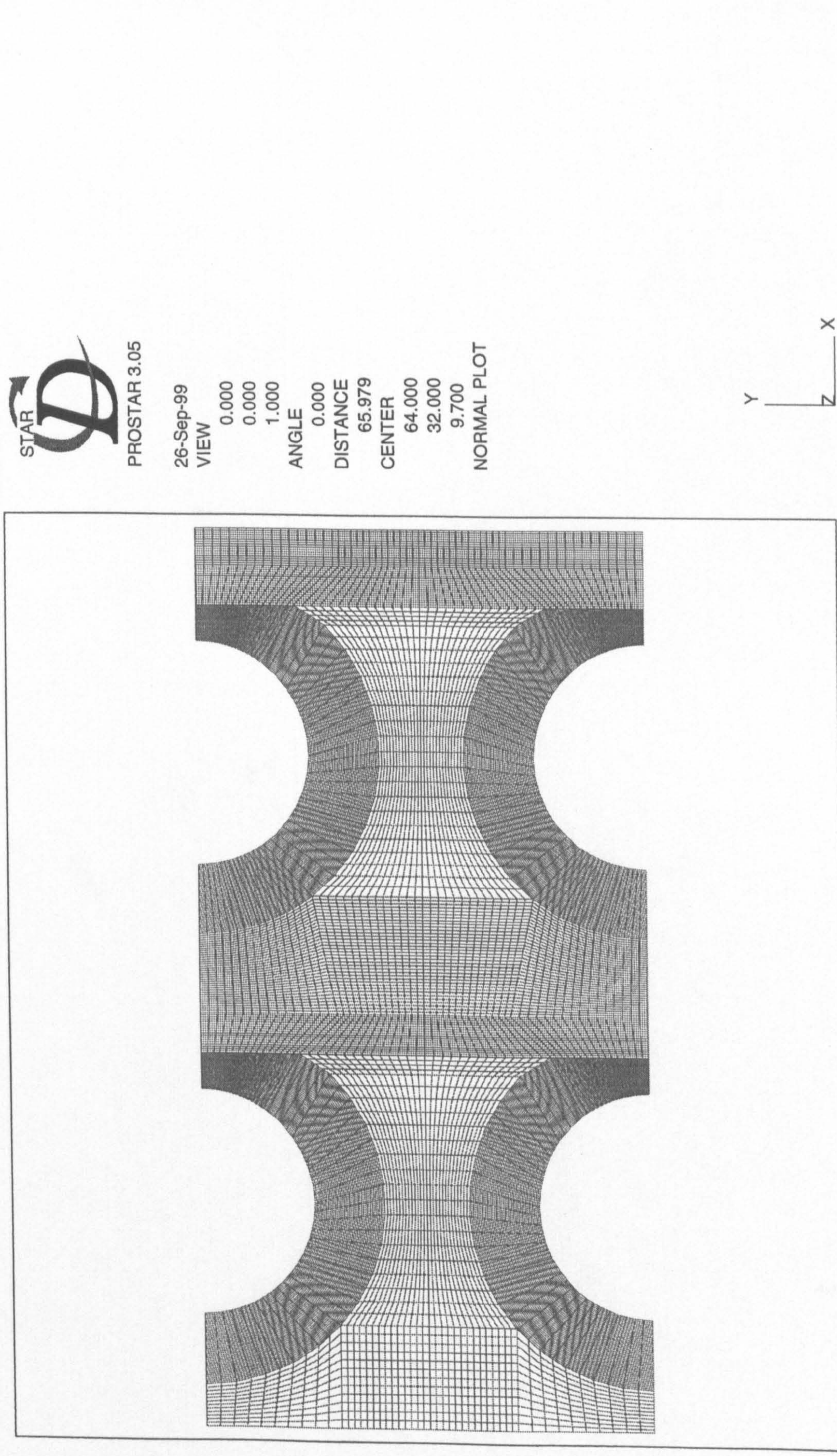

Figure 4.12: Mesh for in-line tubes with vortex generators

first type the distribution of all variables apart from pressure are prescribed directly at the centres of the faces on the boundary and the fluxes are calculated directly. With the second type, the distribution of the flow variables is extrapolated from upstream to arrive at the boundary values. Implicit to this is that all flow should be directed outwards. The velocities are then scaled to give the required mass flow rate. When the mass outflow type of boundary is being used the pressure has to be prescribed at the inlet boundary. The velocities at the inlet are linked to the local pressure gradients by the momentum equations, which together with satisfying continuity over the inlet boundary cells allows the magnitude and direction of the local flow to be calculated.

Mass outflow type of boundary conditions were chosen as they were found to represent the physical data more fully. The pressure and ambient temperature were specified upstream of the test section inlet. This was because the pressure could be expected to be uniform and therefore the velocity constant across the whole inlet. The mass flow rate outlet type boundary was specified downstream of the test section outlet to allow the flow to become fully developed after the recirculation region. The flow should always be outward facing and fully developed as STAR uses the assumption of zero gradients of the flow variable at outlet, i.e

$$\frac{\partial u}{\partial \underline{n}} = \frac{\partial v}{\partial \underline{n}} = \frac{\partial w}{\partial \underline{n}} = \frac{\partial T}{\partial \underline{n}} = 0 \tag{4.3}$$

At solid surfaces the no-slip condition ($u = v = w = 0$) is assumed. In the region between the test section inlet and where the pressure is specified the slip boundary

condition is used. This is to allow a plug-type velocity profile to form at the test section inlet.

On the sides of the domain symmetry conditions were specified. This assumes that there is no flow or scalar flux across the boundary. This can be written:

$$\frac{\partial u}{\partial \underline{n}} = 0 \quad \frac{\partial w}{\partial \underline{n}} = 0 \quad \frac{\partial T}{\partial \underline{n}} = 0 \tag{4.4}$$

In using this type of boundary condition the assumption of axisymmetry of the fluid flow has to be used. As discussed earlier in this chapter the Reynolds number of the flow is low enough so that two steady recirculation regions were formed axisymmetrically behind the tube.

In cases where the energy equation has been used to model heat transfer, the heat flux was specified in the interference cells between the fluid and solid. To model the heat flux absorbed by the top glass sheet a heat flux was also prescribed on the top of the top glass fin.

All initial conditions were taken as zero for the pressure and velocity fields. The only exception to this was when a restart file was used after some change to a boundary condition value such as inlet temperature.

4.4 Accuracy of the numerical technique

Two techniques were used in this study to assess the discretisation error (errors due to insufficient grid refinement), of the various CFD models built. Firstly, Richardson extrapolation was used as this allows a relatively simple method for obtaining quantitative measures of the truncation errors. However, one of the well known problems with applying Richardson extrapolation is the need to use monotonically converging variables. Where monotonically converging values have not been found, the discretisation error has been calculated from systematic grid refinement.

For a second order method, Celik and Zhang (1993) expressed the error, ϵ, in the numerical method as:

$$\epsilon_h = \phi - \phi_h = a_2 h^2 + a_4 h^4 + \cdots \tag{4.5}$$

where ϕ is the exact numerical solution to the discretised equations, ϕ_h is the approximate numerical solution, h is a characteristic discretisation parameter and a_2 a_4 are coefficients.

When the grid being used is refined by a factor α, equation 4.5 can be rewritten for a new grid size αh as:

$$\phi = \phi_h - \frac{(\phi_h - \alpha_{\alpha h})}{(1-\alpha^2)} - a_4\alpha^2 h^4 - a_6\alpha^2(1+\alpha_2)h^6 + \cdots \tag{4.6}$$

As equation 4.6 is in the form of a polynomial, when h is small the leading terms

dominate. Therefore equation 4.6 can be written:

$$\phi - \phi_{\alpha h} = C(\alpha h)^2 \tag{4.7}$$

where n is the order of the method and C is a coefficient

When solutions are obtained at two sets of coarser grids with $\alpha = 2$ and $\alpha = 4$, from the solution of the finest grid size h, three equations can be derived to solve for the three unknowns, n, ϕ_{ext} and C

$$n = \frac{\ln\left[\frac{(\phi_{2h} - \phi_{4h}}{\phi_h - \phi_{2h}}\right]}{\ln 2} \tag{4.8}$$

$$\phi_{ext} = \frac{(2^n \phi_h - \phi_{2h})}{(2^n - 1)} \tag{4.9}$$

$$C = \frac{(\phi_{ext} - \phi_h)}{h^n} \tag{4.10}$$

where ϕ_{ext} denotes an extrapolated value and replaces ϕ

A relative grid refinement error can be defined using the extrapolated value:

$$e_t = \frac{|\,(\phi_{ext} - \phi_h)\,|}{\phi_{ext}} \tag{4.11}$$

A more useful indicator of the percentage difference between the solution obtained and a mesh independent solution for second order discretisation, providing a sufficiently small value of h is used can be written as:

$$\epsilon_h = \frac{(\phi_h - \phi_{2h})}{(\alpha^2 - 1)} \tag{4.12}$$

Where non-monotonically converging variables were found, the discretisation error has simply been calculated by the percentage difference of the variables concerned between two successively refined grids.

The main purpose of the single channel model was validation of the velocity profile and testing of the heat flux input sub-routine. For this model, the mesh was refined until there was a good comparison between the predicted velocity profile and a fully developed laminar velocity profile (see Section 4.5). As a result, there is no direct analysis of mesh independence for this model.

Up to ten positions in the computational domain could be chosen for analysing the grid convergence of the solution. These were generally placed in areas of high flow gradients such as separating flows, horseshoe vortex regions and wake regions. By specifying a position in the domain, STAR will linearly interpolate from the vertex values to obtain the value of the required variable at that point.

For the numerical models of delta and rectangular winglet pairs and rectangular wings, three meshes were built of each different type. These meshes were refined by a factor of two, starting with the coarsest mesh, in both the x, y and z directions so that Richardson extrapolation could be used determine how far the solution was from a mesh independent solution and the system order. For the delta winglet pair model with a total of 463664 cells, the maximum error from a grid independent solution was $\epsilon_h = 8.5\%$ and a system order of 3.3. Only two sets of monotonically converging variables were found, so the difference between the two most successively

refined grids were also calculated. This showed a maximum difference of 5.7%. For the rectangular winglet pair model, which had a total of 394664 cells, $\epsilon_h = 5.7\%$ at a maximum and the maximum difference between the two finest meshes was 10.4%. As would be expected the order of grid convergence was usually above 2, as a second order accurate differencing scheme was being used. However, in a few locations the order of grid convergence drops below 2. This can be attributed to a number of factors. The Richardson extrapolation technique makes the assumption that the only factor attributing to the discretisation error is the mesh density. However, other factors contribute such as mesh skewness and cell-to-cell volume changes. These tend not to be a function of mesh density and may get worse as the mesh is refined. Another contributing factor is that the interpolation to get the value at the required point is only first-order accurate. All these factors will have the effect of reducing the of accuracy of grid convergence.

For the plain channel model with rectangular wings $\epsilon_h = 2.7\%$ and the maximum system order was 4.8. The difference between the two most successively refined grids, the finest which had 452096 cells, was 4.8%. For the final vortex generator model in a plain channel, embossed rectangular wings, no formal mesh refinement studies were carried for reasons that will be explained in Chapter 5. However, the total number of cells used, 165546, was consistent with the mesh density used in the other vortex generator models considering that the overall dimensions of the model were smaller.

For the first of the staggered heat exchanger sections the maximum error between the two most successively refined grids was 5.5%. This compares to a a maximum value of $\epsilon_h = 0.06\%$ and an order of grid convergence of 8. For the second of the staggered heat exchanger sections the maximum error from a grid independent solution using Richardson extrapolation was 5.9% and 8.6% using successive grid refinement. The maximum values for the in-line heat exchanger are $\epsilon_h = 8.2\%$ and a system order of 3.5. Again as with the other meshes a few of the system order values fell below 2.

The final two meshes built, staggered and in-line heat exchanger sections with vortex generators, generally had a higher cell count to capture the more complex flow patterns. For the staggered mesh with vortex generators, only two meshes were built, the finest mesh having 407816 cells. Using Richardson extrapolation, $\epsilon_h =$ 5.2% and the maximum difference between the two meshes was 11.5%. No system order was calculated for this mesh. For the in-line mesh with vortex generators, ϵ_h = 4.1% and the maximum difference between the finest mesh, which had 792256 cells, and the mesh which had half as many cells in the x, y and z directions was 16.7%. The maximum system order achieved was 5.9 although as in some of the other cases, some of the system orders fell below 2.

4.5 Validation of the Numerical Technique

Due to the difficulties of modelling the fluid flow equations and other difficulties involved in using CFD, Fisher and Rhodes (1996) reported that validation should

be used to test the numerical techniques predicative capabilities against detailed test data. From the experimental data two field variables were obtained, overall pressure drop and surface temperature of the middle fin. From the CFD model both variables where calculated, the local surface temperature allowed the heat transfer coefficient to be calculated and the pressure drop showed the relative effects of the different vortex generator types.

Before any validation was carried out on a three-dimensional model with tubes and/or vortex generators a number of useful validation tests could be carried out on simple two-dimensional channel flow. The first was validation of the fully developed laminar flow velocity profile. It is well known that after approximately 10 channel heights downstream of an inlet, Plint and Böswirth (1978), the velocity profile follows a parabolic relationship with the maximum velocity 1.5 times the mean velocity. This is shown in Figure 4.13 where the solid line represents the velocity profile calculated from STAR and the circles are the values calculated from a parabolic velocity profile. For a mean flow of 1 m/s the maximum error was 0.4%.

The simple two-dimensional channel flow model also enabled the heat flux input sub-routine to be tested. By specifying a heat flux in the sub-routine that was the same as the experimental heat flux input, the predicted and experimental isotherm positions could be compared providing the inlet temperature to the test section was consistent in both cases. For the case where the heat flux input $\dot{q} = 436.5\,\mathrm{W/m^2}$ the CFD predicted an isotherm position of 29.8 mm from the leading edge. The

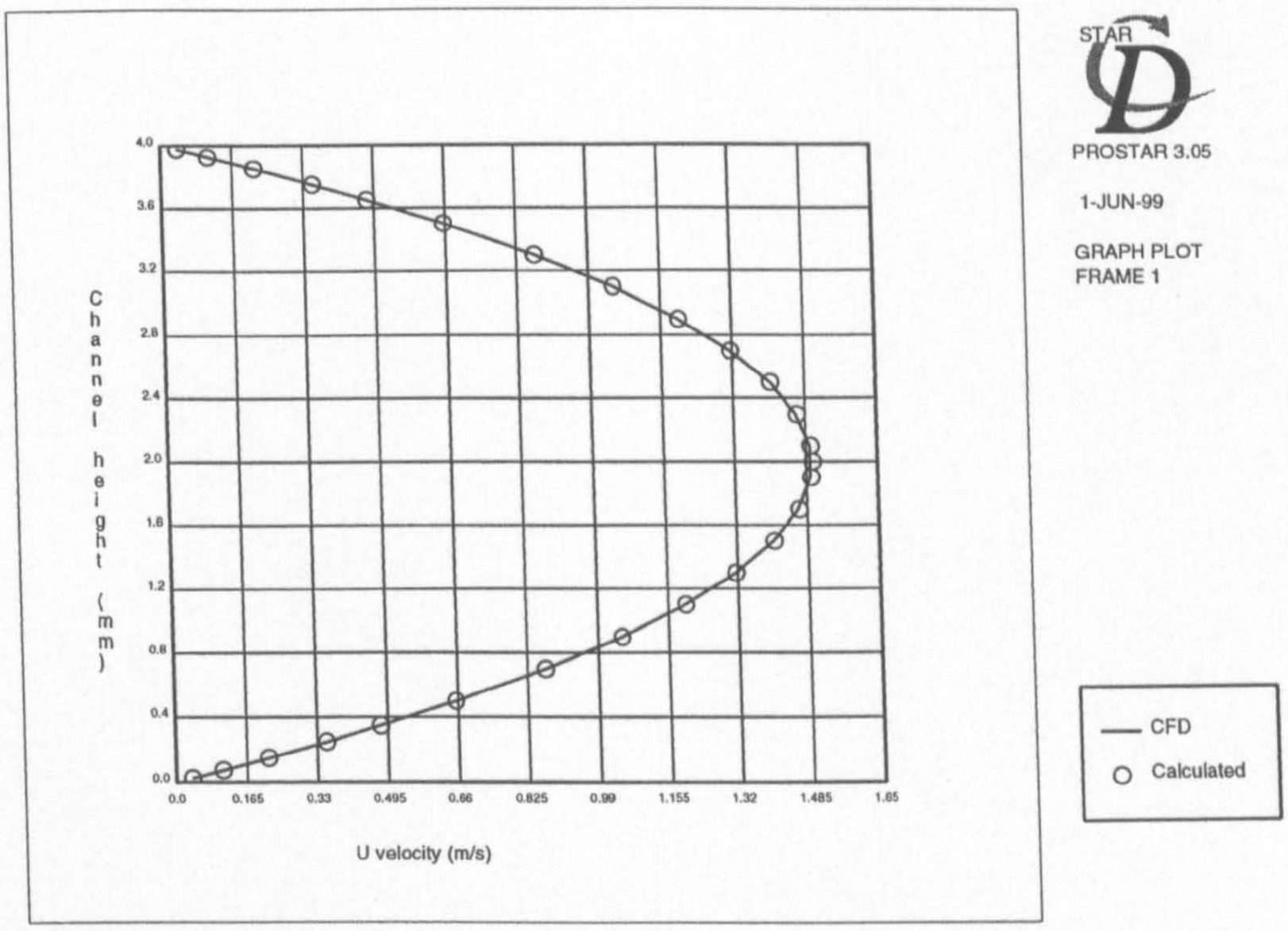

Figure 4.13: Comparison of calculated and numerical predicated velocity profiles for $u = 1$ m/s

experimental value was 27.0 mm. The difference between the two isotherm positions was within the temperature bandwidth of the red transition colour of the liquid crystals. The difference between the predicted and measured pressure drops through the test section was 4.3% with the CFD model over-predicting the pressure drop. It should be noted here that the measurement of the pressure drop is slightly different for the experimental and numerical tests. In the experimental case a differential pressure transducer was used, as explained in Chapter 3. This measures the pressure drop from the back of the test section by assuming zero velocity at the expanded plenum top was, relative to ambient pressure. In the case of the CFD model the pressure difference was read directly from an area averaged inlet and outlet pressure.

Further validation could take place on a three-dimensional mesh. Half an O-ring mesh was built to find the necessary mesh refinement to model the horseshoe vortex adequately and thus find the position of the stagnation point in front of the tube. Figure 4.14, shows the position of the experimental stagnation point against the

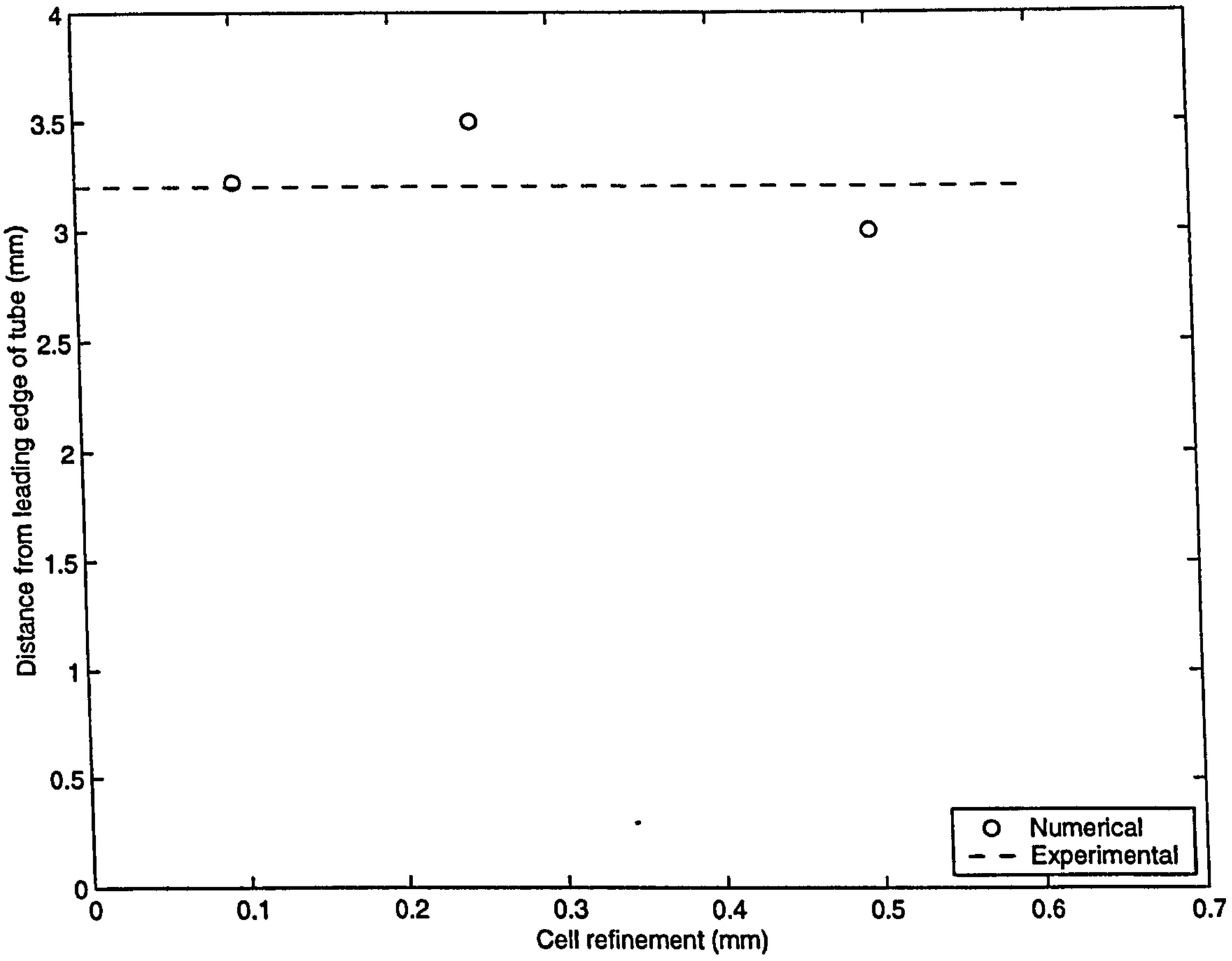

Figure 4.14: Vortex extent ahead of the tube against mesh refinement

numerical position for different mesh refinements. It is interesting to note that both a course and fine mesh could be used, the latter has been chosen to capture the fine detail in the flow structure. When using the fine mesh there is negligible difference between the two positions.

The comparison between the predicted and experimental isotherm position for the

delta winglet and rectangular winglet pairs is shown in figures 4.15 and 4.16 respectively. Clearly the agreement between the experimental and predicted isotherms is not as good as that achieved with the plane channel, reasons for this will be presented in Chapter 5. For the delta winglet pair case the numerical model under predicted both the average heat transfer and pressure drop by 19.7% and 14.6% respectively. The same under-prediction occurred in the rectangular winglet pair model where the values were 32.4% and 16.1% for the average heat transfer and pressure drop.

No validation of the rectangular winglets and embossed vortex generators were carried out. This will be explained in chapter 5

The predicted and measured isotherm positions for the staggered tube arrangement at $\dot{q} = 485.1\,\mathrm{W/m^2}$ is shown in Figure 4.17. Excellent agreement can be seen between the two with the worst discrepancies occurring near the separation points of the front and rear tubes. The error at the separation point of the front tube occurs because in the experimental model the tube is glued onto the liquid crystal layer allowing tangential conduction to move heat into the lower temperature area below the tube where no heat flux is applied. In the CFD model the fin is modelled as a real fin, i.e, there was no fin where the tube was. The error in the isotherm position near the separation point of the rear tube arises because in the experimental setup the camera is at an angle to the surface. This hides the isotherm position behind the rear tube. The difference in pressure drop between the experimental and numerical

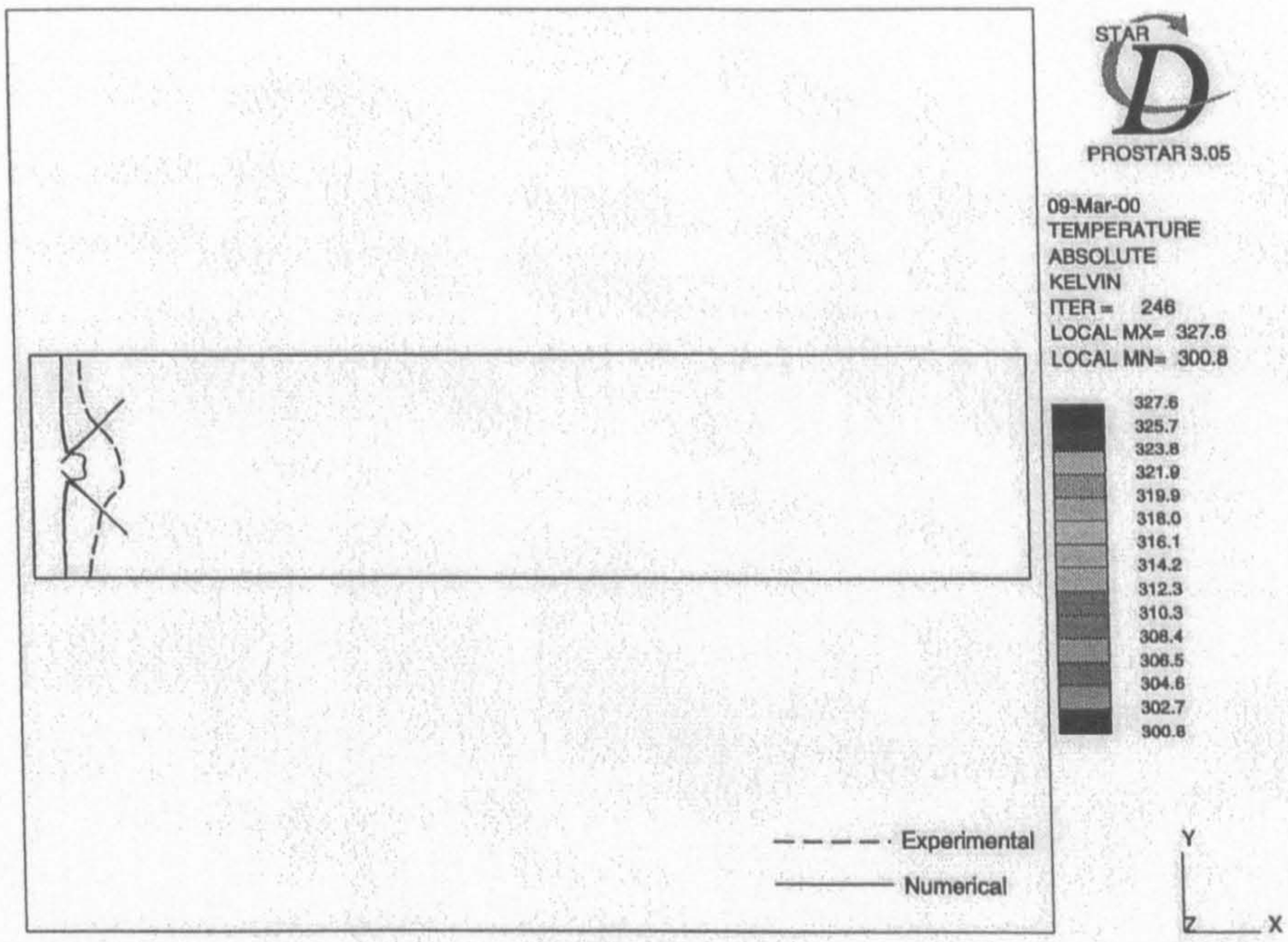

Figure 4.15: Comparison of predicted and experimental isotherm positions for delta winglet pairs. Transition temperature of 35°C

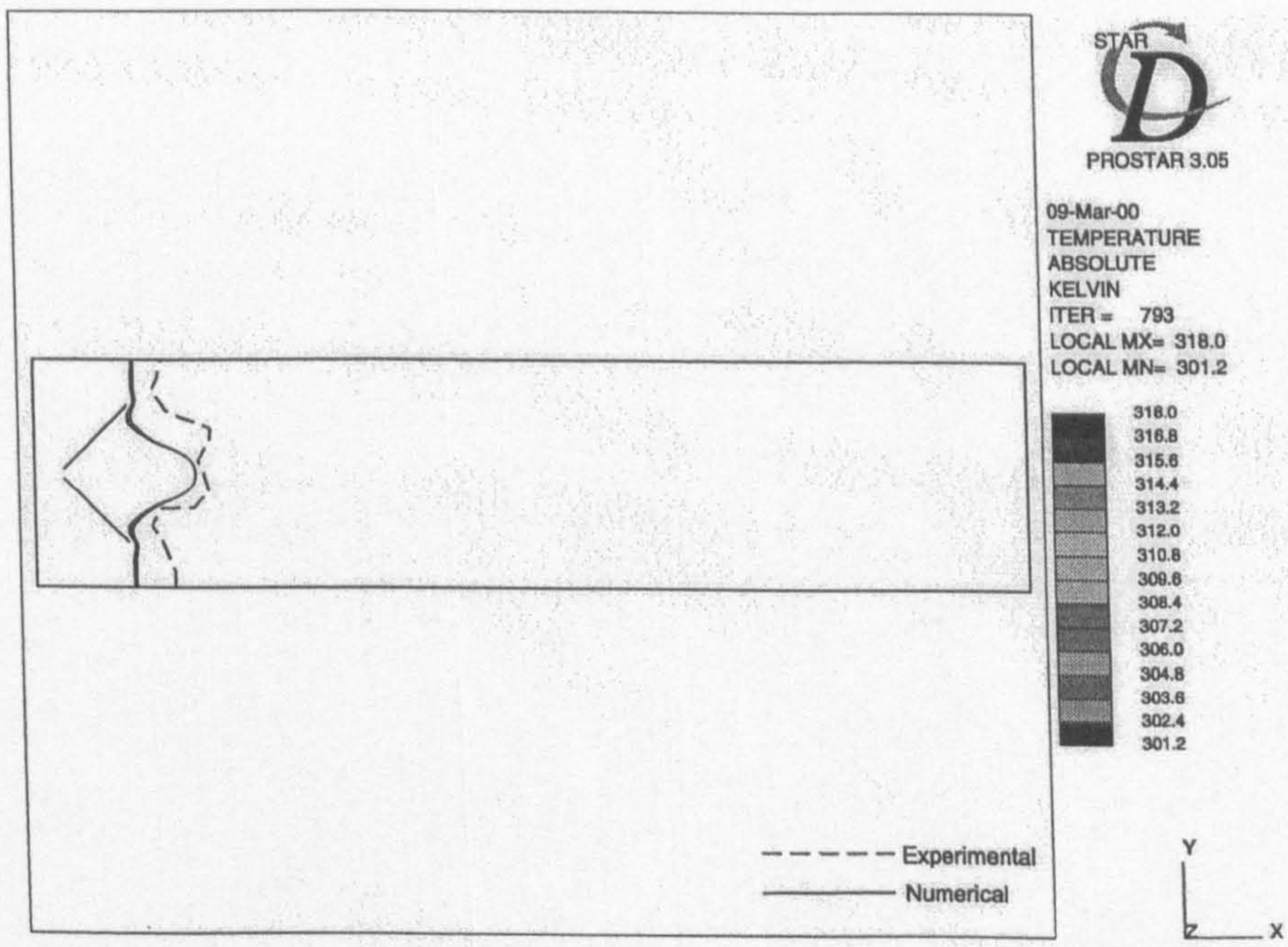

Figure 4.16: Comparison of predicted and experimental isotherm positions for rectangular winglet pairs. Transition temperature of 35°C

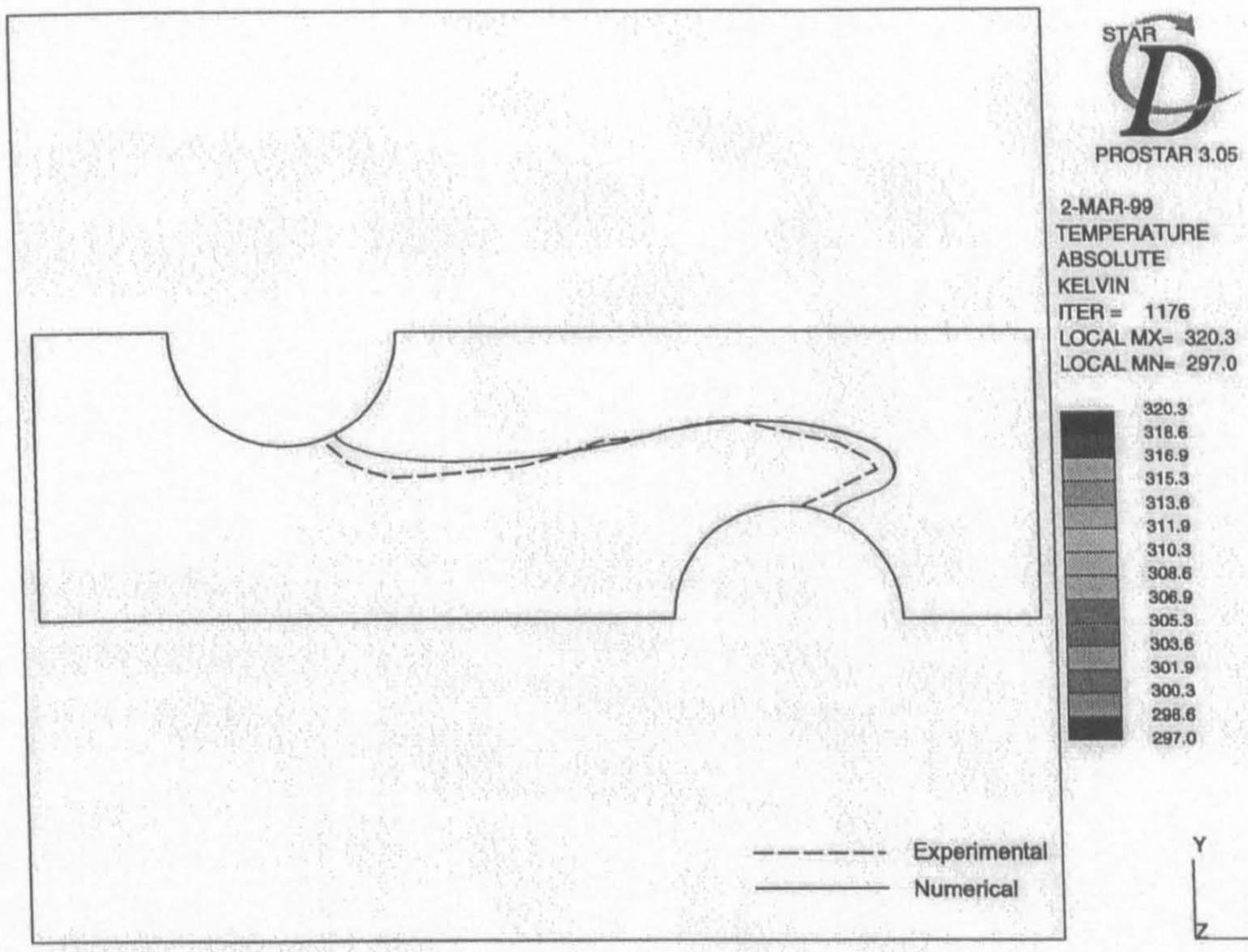

Figure 4.17: Comparison of predicted and experimental isotherm positions for a staggered tube heat exchanger. Transition temperature of 35°C

results was 4.5% with the CFD model over predicting the pressure drop. Good agreement can also be seen between the predicted and experimental isotherms for the second staggered tube heat exchanger investigated, figure 4.18. The difference between the experimental and predicted pressure drops was 24.8% with the CFD model over-predicting the pressure drop.

The isotherm positions for the in-line tube arrangement at a heat flux level of $\dot{q} = 650.7\,\mathrm{W/m^2}$ is shown in Figure 4.19. Clearly the agreement is not as good as the other cases. To move the predicted isotherm to the correct position a reduction in the inlet temperature of 0.8° or a reduction in the heat flux of $\dot{q} = 50\,\mathrm{W/m^2}$ was required. These values are approximately twice the value of the experimental uncertainty of

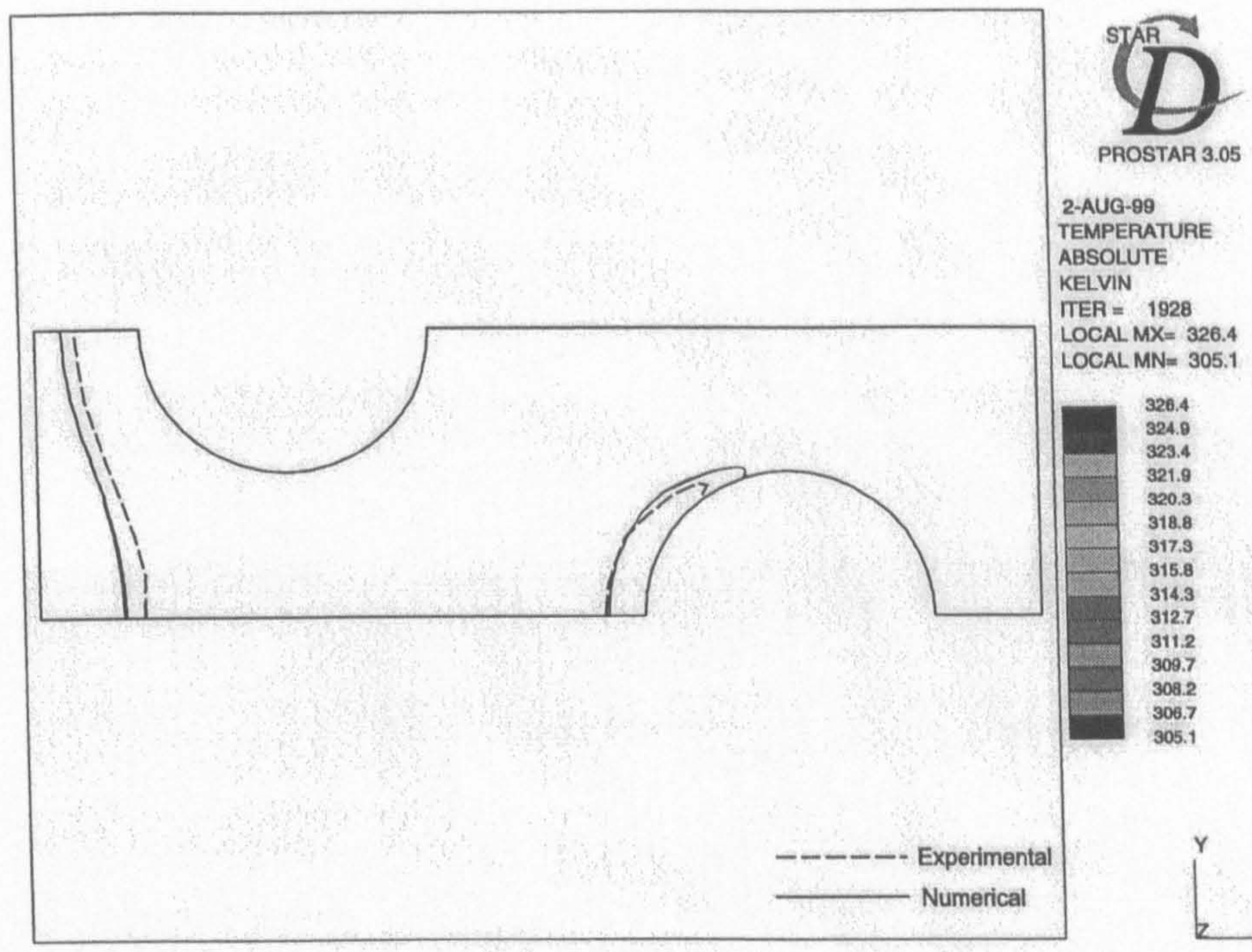

Figure 4.18: Comparison of predicted and experimental isotherm positions a staggered tube heat exchanger. Transition temperature of 35°C

the respective variables. However, by applying the maximum uncertainty on both variables, the isotherm can be moved to the correct position. The difference in the measured and predicted pressure drops was 15% with the CFD model over predicting the pressure drop.

The comparison between the predicted and experimental isotherms for the staggered and in-line heat exchangers with vortex generators is shown in Figures 4.20 and 4.21 respectively. The isotherm positions around the vortex generator are being predicted well, but the other isotherms nearer the leading edge being less well predicted. The differences between the predicted and experimental pressure drops for the two geometries are 12.7% and 16.8% respectively with the CFD model over predicting

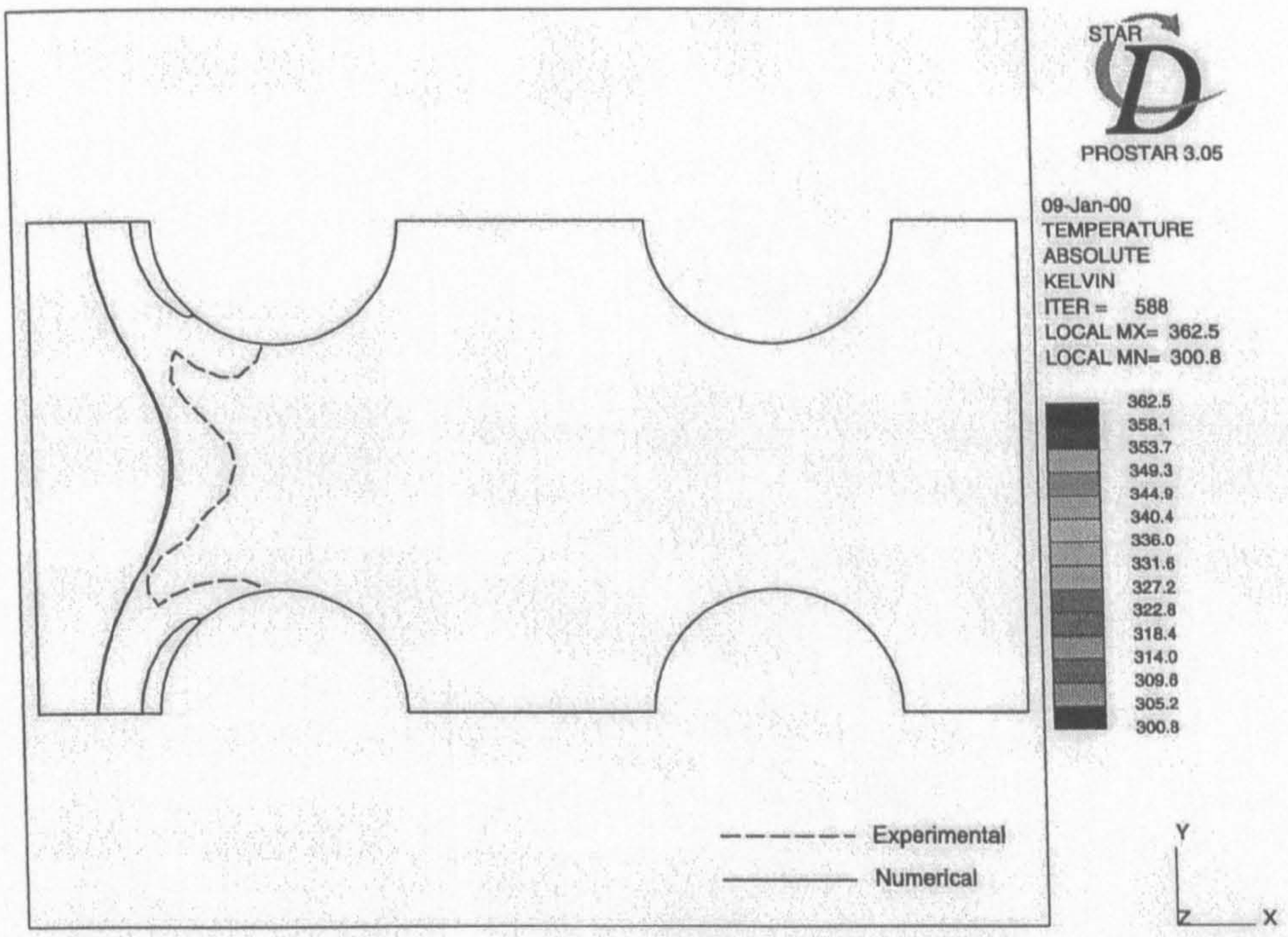

Figure 4.19: Comparison of predicted and experimental isotherm positions for an in-line heat exchanger. Transition temperature of 35°C

the pressure in both cases. As with all the models, differences between the predicted and measured isotherm positions and pressure drop values will be discussed further in Chapter 5.

4.6 Summary

In this chapter the numerical modelling and solution procedure of the various heat exchanger sections, using a commercial CFD code, has been discussed. The models investigated were: plain channels, delta and rectangular winglet pairs, rectangular winglets, embossed vortex generators, staggered tube geometries, an in-line geometry and staggered and in-line tubes with vortex generators.

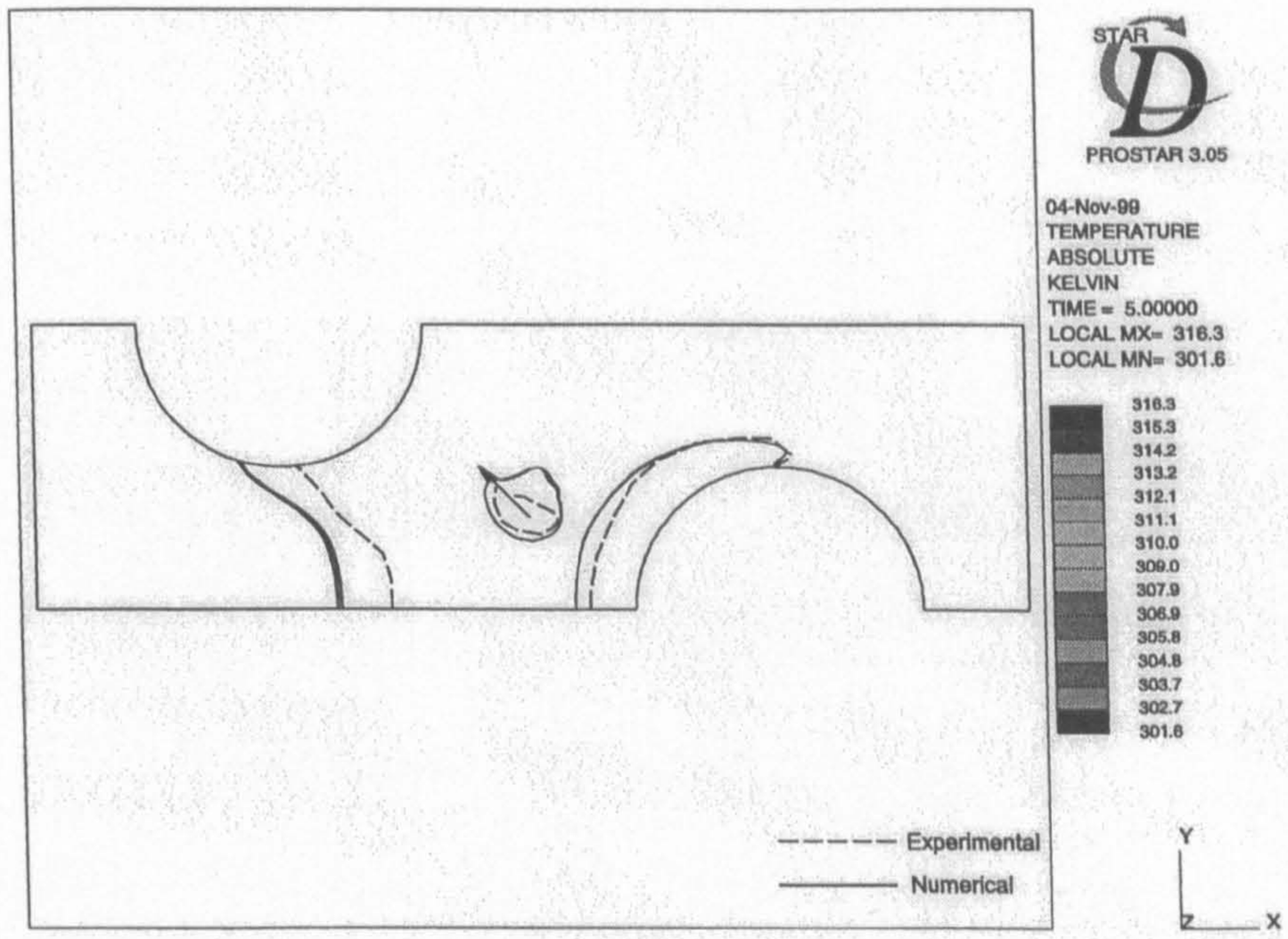

Figure 4.20: Comparison of predicted and experimental isotherm positions for a staggered tube heat exchanger with vortex generators. Transition temperature of 35°C

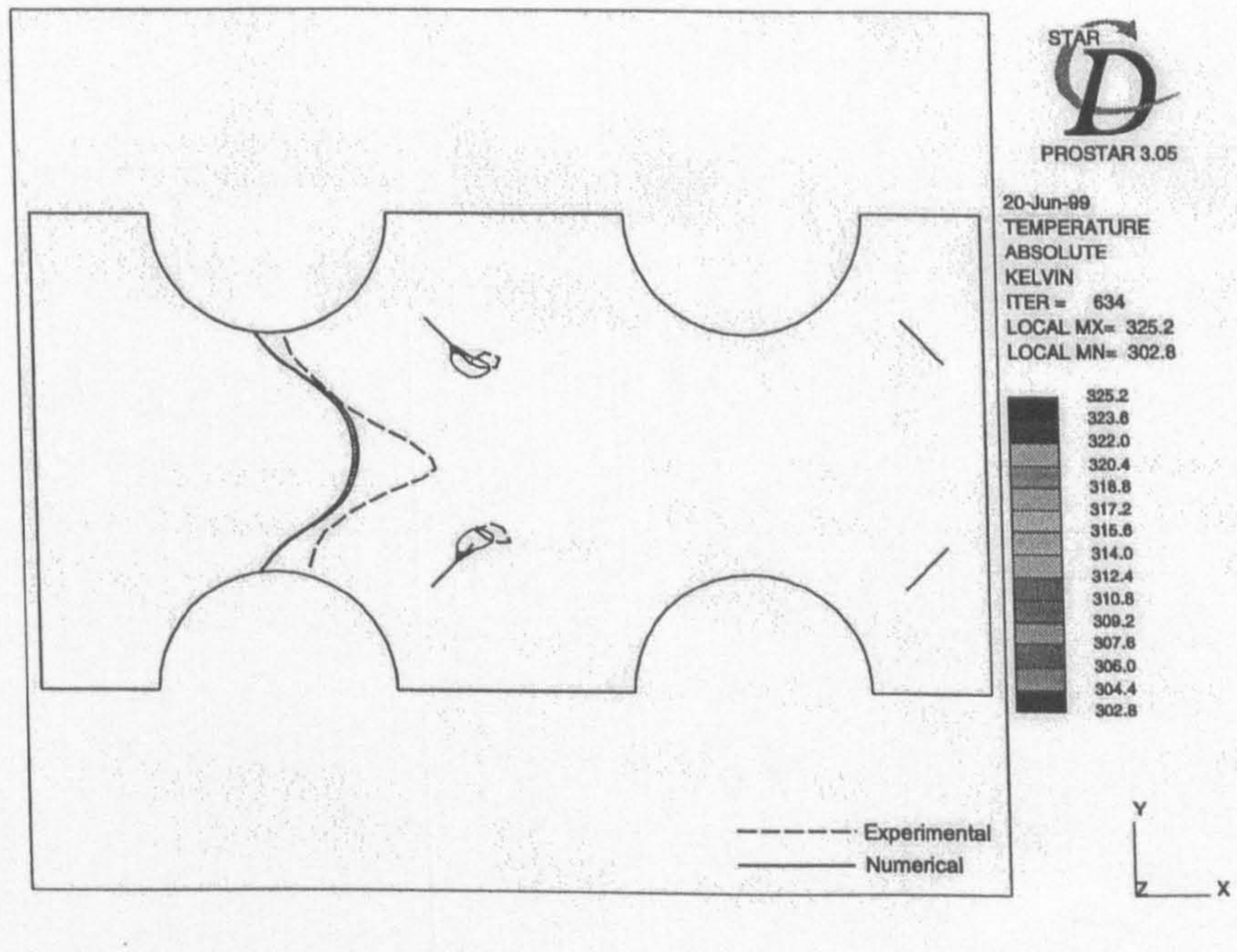

Figure 4.21: Comparison of predicted and experimental isotherm positions for an in-line heat exchanger section with vortex generators. Transition temperature of 35°C

A commercial CFD code was used that uses the finite volume method to discretise the governing equations. Due the the low Reynolds number being modelled it was found that the steady state condition could be used. This reduced solution times and memory requirements. The solution algorithm used was SIMPLE with the MARS differencing scheme as these were found to give accurate results. The boundary conditions of specifying the pressure at upstream infinity and the mass flow rate at outlet were chosen, as these were found to represent the experimental conditions. A user programmed sub-routine was used to specify the heat flux on the surface of the fin.

The mesh generation procedure, using PROSTAR, for the models listed above has been described. These used a number of different mesh building techniques, such as block meshing, which resulted in a hexahedral mesh being created. The accuracy of the numerical technique has been analysed using Richardson extrapolation and successive mesh refinement. Where three successively refined models were analysed the order of grid convergence was also found. For the delta and rectangular winglet pairs, rectangular winglets, the two different staggered geometries, the in-line geometry, the staggered and in-line heat exchanger geometries with vortex generators, the difference from the results obtained and a mesh independent solution were: 8.5%, 5.7%, 2.7%, 0.06%, 5.9%, 5.2% and 4.1%. The system orders were 3.3, 2.5, 4.8, 8.0, 3.5, - and 5.9 for the cases listed above. The system order was occasionally found to fall below two due to mesh skewness and cell to cell volume changes.

Validation of the numerical results against experimental results were carried out for all cases apart from rectangular winglets and embossed vortex generators. The numerical model of the plain channel was found to over-predict the average heat transfer and pressure drop by 5.9% and 4.0% respectively. The fully developed laminar velocity profile was found to have a maximum error of 0.4%. A half O-ring mesh was used to find the necessary mesh refinement to model the fine flow structure around the front of the tube. With the finest mesh modelled the error between the predicted and measured stagnation positions was negligible. The comparisons for the average heat transfer coefficient between the numerical model and experiments are: -19.7%, -32.4%, -7.1%, -21.9%, -16.2%, -23.3% and -11.4%. The pressure drop comparisons are: -14.6%, -16.4%, +8.7%, +25.3%, +16.8%, +12.7% and +25.4%. Where there has been poor prediction of isotherm position, average heat transfer coefficients and pressure drop values, reasons for these discrepancies will be presented in Chapter 5.

Chapter 5

Presentation and Discussion of Results For Plain Channels With Vortex Generators

In this chapter the results from the experimental and numerical models, using the techniques explained in Chapter 3 and Chapter 4, will be presented and discussed. The results presented and discussed are: plain channels, rectangular and delta winglet pairs, rectangular winglets and embossed vortex generators. Firstly for each case the experimental results will be presented, this is followed by the presentation of the numerical results. The results from the physical experiments are compared to the results obtained from the CFD package. Insights into the heat transfer coefficient distributions obtained from the experimental results are then discussed in light of the numerical results. In the final part of each section the results for different flow velocities and angles of attack of the vortex generator are presented where they are applicable.

5.1 Plain channel

5.1.1 Experimental results

The position at which the liquid crystals first change colour indicates the area of lowest heat transfer coefficient. An insight into the temperature gradient at this location can also be gained from the width of the isotherms, the thinner and more closely packed together the higher the temperature gradient. For the plain channel case the liquid crystals first changed colour with wide isotherms at the rear of the test section. This is expected due to the development of the boundary layer which results in reduced heat transfer coefficients. As the heat flux input was increased, and thus the heat transfer coefficient at the isotherm, the isotherms moved towards the leading edge with the isotherms getting thiner indicating higher temperature gradients. The trend of decreasing heat transfer coefficient with increasing length from the leading edge is shown in Figure 5.1 for Re = 263. The average heat transfer coefficient measured from the expériment was 22.5 W/m^2K with a pressure drop through the test section of 2.66 Pa.

5.1.2 Numerical results

The numerically predicted heat transfer coefficient distribution is shown in Figure 5.1 along with the experimental values. As can be seen the predicted trends of heat transfer compare well with the experimental data. The largest deviation of the predicted results from the experimental data arises in the region $x = 0$ - 10 mm from the leading edge. This is due to two factors. Firstly, this is the region that has the

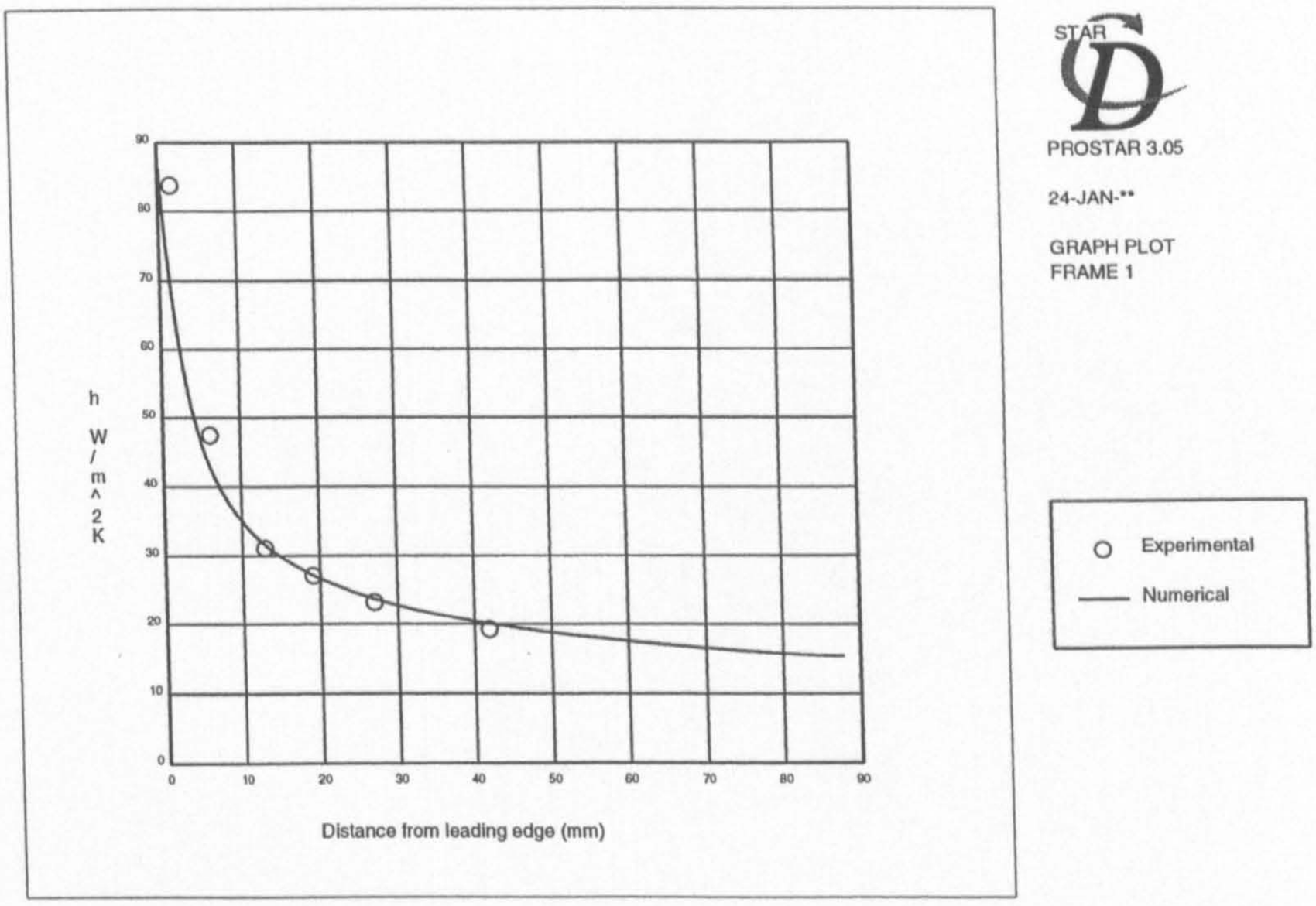

Figure 5.1: Comparison of experimental and numerical heat transfer coefficient distribution for a plain channel

highest tangential conduction because of the high temperature gradients. As shown in Section 3.3.1 the effect of tangential conduction gets larger towards the leading edge. In the experimental data analysis the tangential conduction is ignored, this leads to an over-prediction in the measured heat transfer coefficient, whenever tangential conduction becomes significant. The second reason for deviations from from the experimental results is that the exact velocity profile is not known at the inlet of the test section in the experimental set-up. The numerical model over-predicts the average heat transfer coefficient at 23.9 W/m^2K but the difference was within the uncertainty of the experimental method. The numerical model has predicted well the heat transfer coefficients in the region where the boundary layers forming on the top and bottom of the channel meet. From laminar boundary layer theory this

should occur at 12 mm from the leading edge. The numerical model has predicted 13.3 mm. In a numerical model of a plain channel by Chen et al. (1998a) the inflection point in the heat transfer coefficient distribution caused by the two boundary layers meeting was poorly predicted when compared to the theoretical result of Shah and Bhatti (1987). This lead to an under-prediction in the average heat transfer coefficient of 3.2%. It is also interesting to note that in the work by Chen et al. (1998a) that they have considered the conduction in the fin to be one-dimensional, this has lead to accurate predictions near the leading edge. In common with Chen et al. (1998a) the numerical model has slightly over-predicted the pressure drop through the test section at 2.78 Pa.

5.2 Plain channel with delta winglet pairs

5.2.1 Experimental results

Several isotherm positions for the plain channel section with delta winglet pairs are shown in Figure 5.2, for an increasing heat flux input. As is to be expected the isotherms first change colour near the trailing edge where the heat transfer coefficient is lowest. The isotherms have a distinct undulating pattern when compared to the case without vortex generators where the isotherms are straight. This undulating pattern is caused by the vortices issued from the vortex generator and causes improvements in the heat transfer coefficient in the downwash region of the vortices. As the heat flux is increased the pattern moves towards the leading edge, with the undulations getting shallower. As the isotherm position moves past the vortex gen-

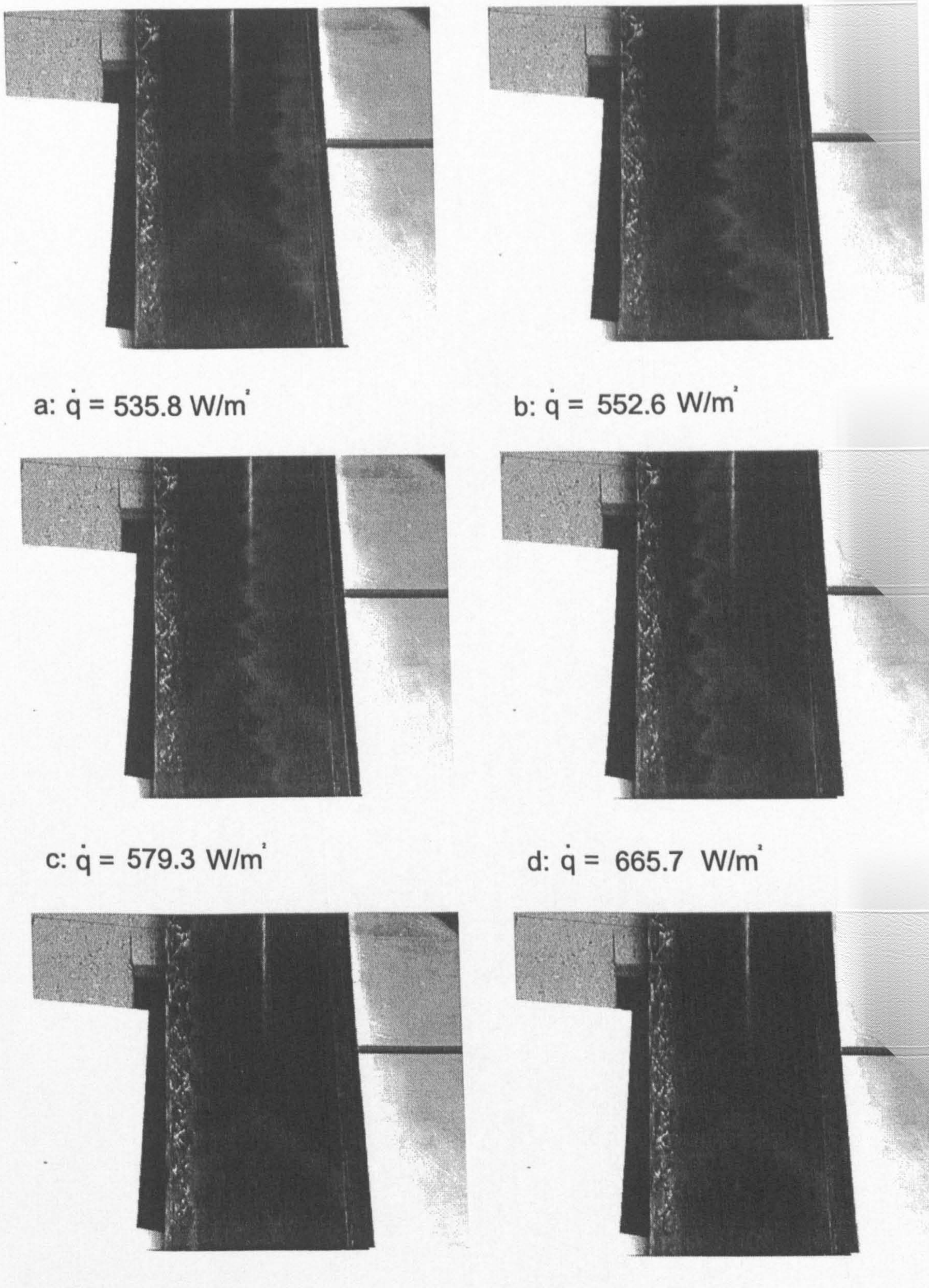

Figure 5.2: Isotherm positions with increasing heat flux input for a plain channel with delta winglet pairs

erator position the isotherm shapes return to straight lines, as is observed in the plain channel case.

5.2.2 Numerical results

Velocity vectors directly behind the delta winglet pair vortex generators are shown in Figure 5.3, where the main flow is going into the paper. As the flow reaches

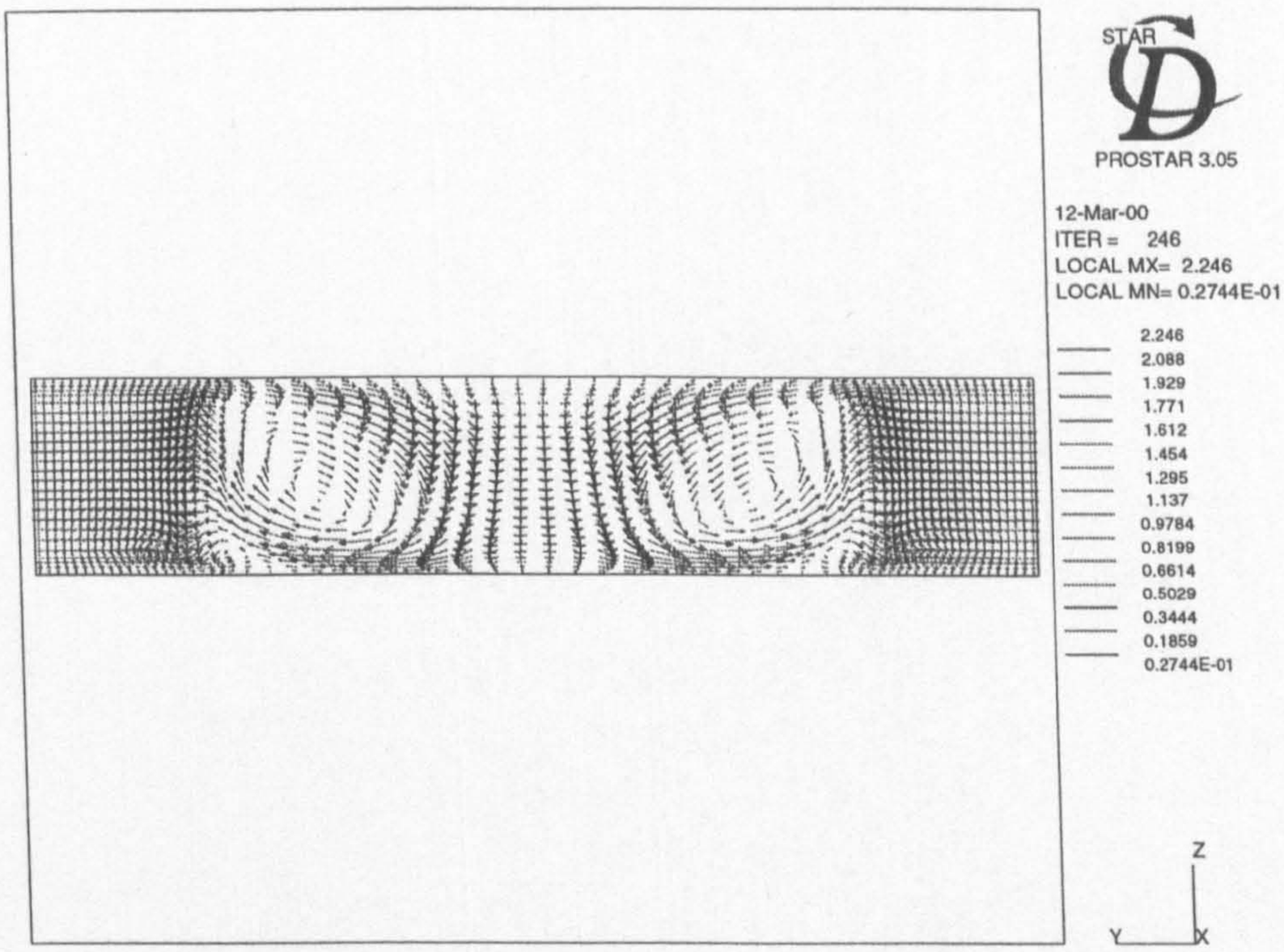

Figure 5.3: Velocity vectors directly downstream of the vortex generators

the vortex generators it is accelerated over the vortex generator, separates at the edge and is sucked into the low pressure region behind. This produces a circulating secondary flow in the direction perpendicular to the main flow, which is carried downstream in the form of a vortex. The vortex generators used are mounted in what is termed 'common flow down' situation, thus the fluid motion is directed

toward the plate. This type of configuration was reported by Pauley and Eaton (1988a) to have a greater effect on heat transfer than the opposite 'common flow up' situation. From Figure 5.3 it can be seen that two vortices have been formed, and that at a maximum the secondary flow has almost reached the main stream velocity.

The resulting heat transfer coefficient distribution is shown in Figure 5.4, also

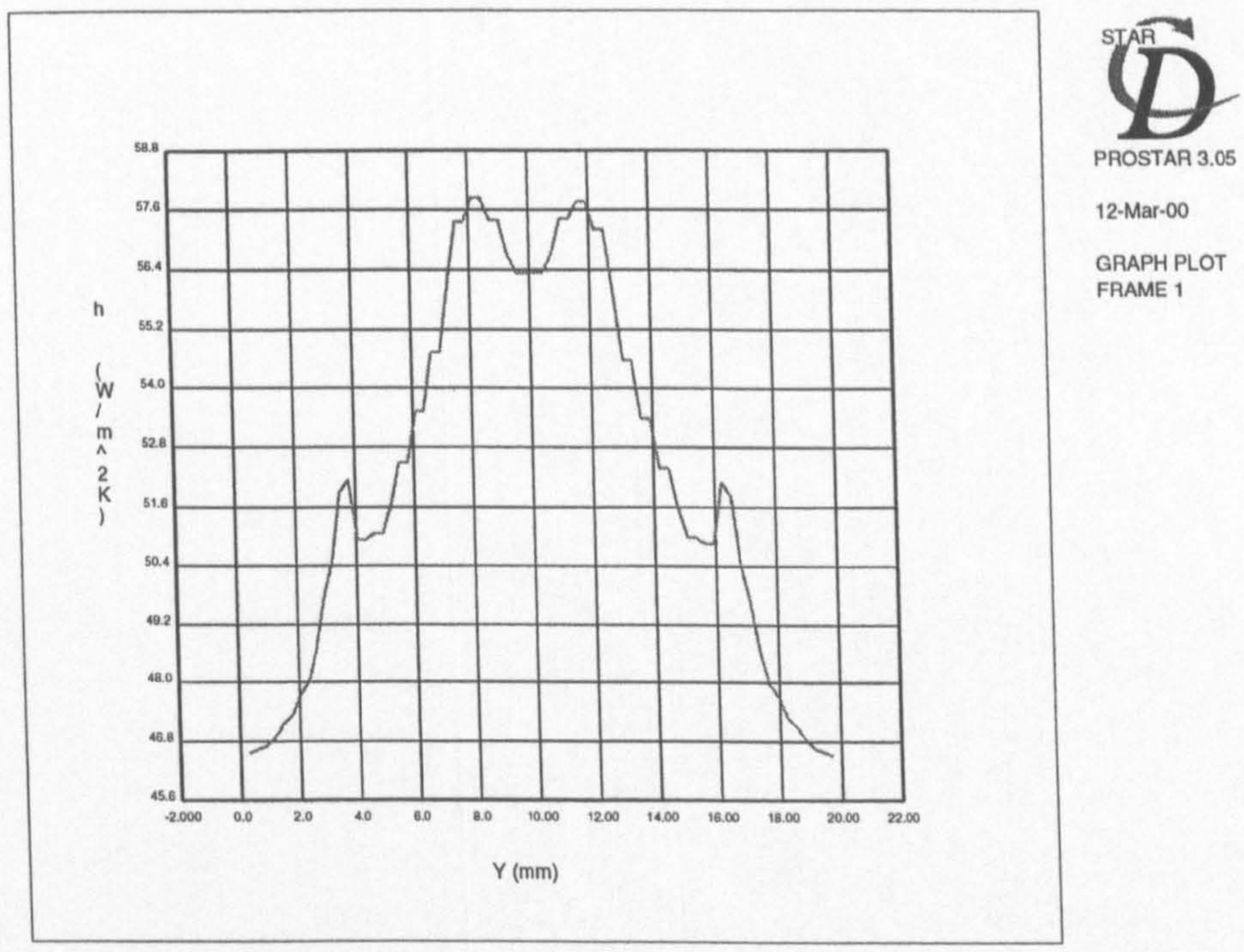

Figure 5.4: Heat transfer coefficient distribution directly downstream of the vortex generators

directly behind the vortex generators. The two distinct peaks in the heat transfer coefficient at y = 8 and 12 mm are caused by the strong downwash locally thinning the boundary layer and thus increasing the heat transfer. At the centre line of the test piece, the fluid direction is almost totally downward facing. As this fluid hits the fin it stagnates causing some localised thinning of the boundary layer, but

due to the lower velocities involved the increase in heat transfer is not as high as in the neighbouring downwash regions. Moving away from the primary peaks in the heat transfer coefficient the enhancement falls as the velocities reduce and thus boundary layer thinning also reduces. At y = 4.0 and 16.0 mm there is a small secondary peak in the heat transfer coefficient. This arises due to an induced vortex forming in the corner between the back side of the wing and the fin as a result of the redirectioning of the near-wall flow caused by the lower pressure behind the generator. This causes a small rise in the heat transfer coefficient before the heat transfer coefficient drops towards the plain channel value at the edges of the test section. At this position directly behind the vortex generator the maximum increase in heat transfer coefficient is 30%.

As the vortices persist downstream, the secondary velocities reduce and the core increases in radius. This has the effect of reducing the heat transfer enhancement but widening the distance between the peaks in the heat transfer coefficient. The increasing radius of the core also has the effect of reducing the trough in the heat transfer between the peaks. The numerically predicted heat transfer coefficient at $x'/H = 2$ (where x' is the distance from the rear of the vortex generator) is shown in Figure 5.5. This shows a maximum enhancement of 27.1% over the plain channel case which was modelled numerically. The numerical prediction in the spanwise heat transfer coefficient is qualitatively very similar to Tiggelbeck et al. (1994) for the same position. He predicted a maximum increase in the heat transfer of 50% although the delta winglet pairs used had an angle of attack of 30^0 and the Reynolds

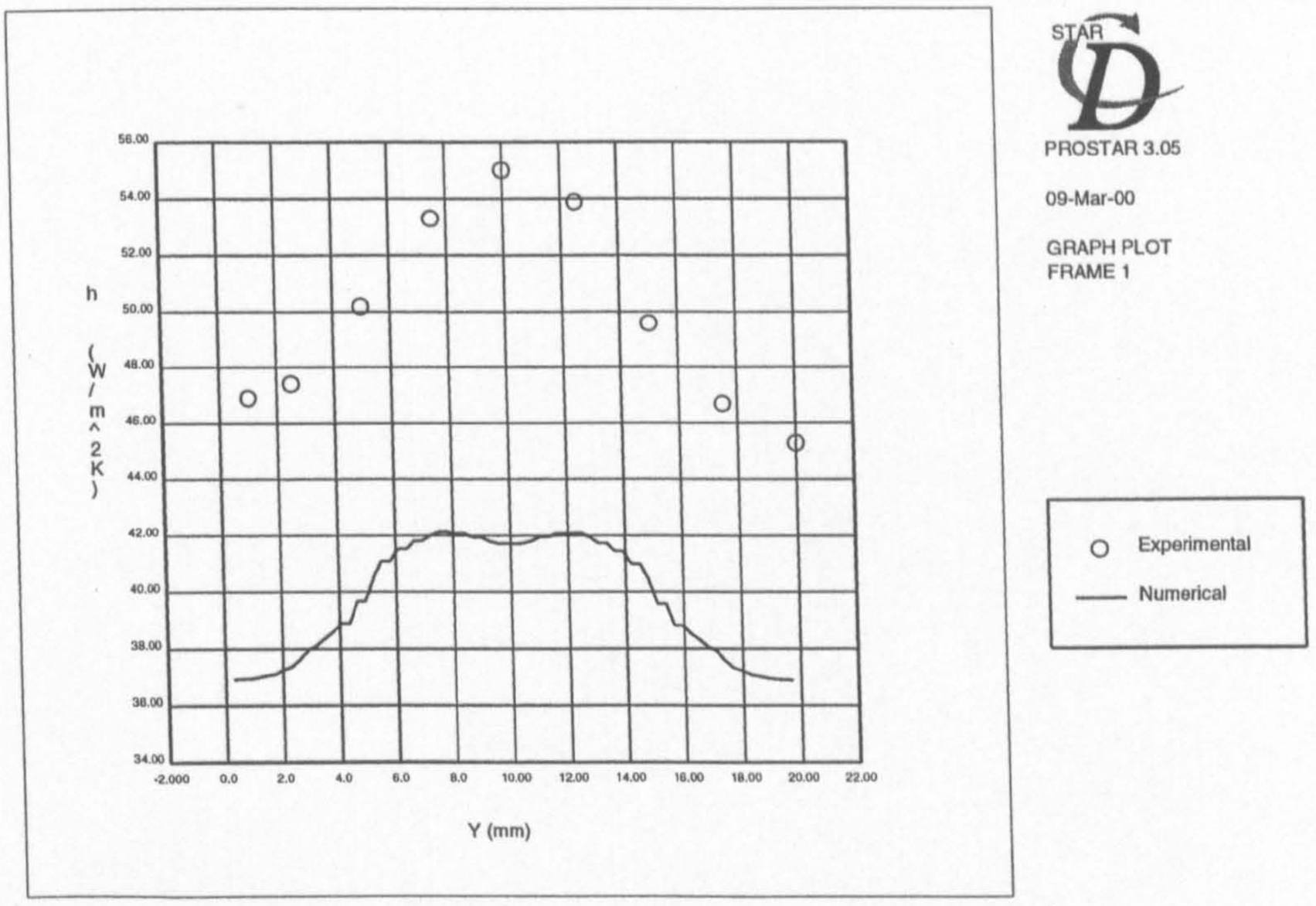

Figure 5.5: Heat transfer coefficient distribution at $x'/H = 2$ downstream of a channel with delta winglet pairs

number was 4600.

The experimental data from the delta winglet pair case is also plotted in Figure 5.5. Although qualitatively the distribution is similar the numerical model appears to under-predict the heat transfer coefficient. The maximum deviation is 23.6% between the two sets of results. The most noticeable deviation between the two distributions is that the experimental model fails to show a local minimum in the heat transfer coefficient at the centre line of the test section. This probably arises due to the positioning of the vortex generators in the experimental case resulting in vortex cores that are closer together than in the numerical model. The experimental results are artificially high in this region due to conduction occurring in the fin. This

has been explained in section 5.1.2.

As the vortices persist still further downstream, the secondary velocities reduce still further and the cores grow bigger. It is interesting that when the vortices are in 'common flow down' pairs they move apart as they develop in the streamwise direction producing an ever widening region of boundary layer thinning between the vortices. This can be seen from Figure 5.6 which shows the predicted heat

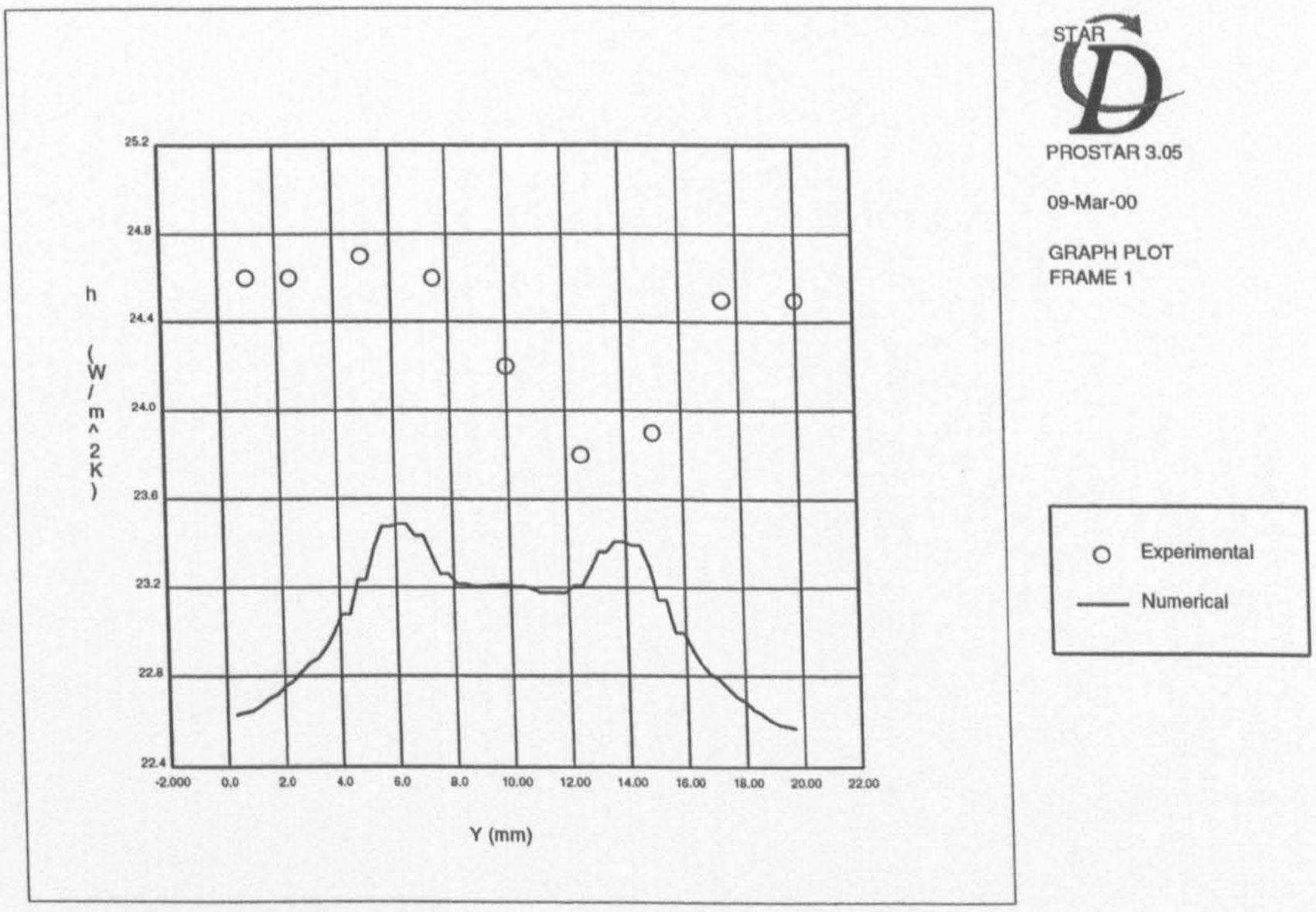

Figure 5.6: Heat transfer coefficient distribution at $x'/H = 12$ downstream of a channel with delta winglet pairs

transfer coefficient distribution at $x'/H = 12$. The peaks in the spanwise heat transfer coefficient, which appear artificially high due to the scale being used, are now at y = 6.0 and 14.0 mm. There is also a larger area of enhanced heat transfer coefficient between the peaks when compared to the position $x'/H = 2$. At $x'/H = 12$ the

maximum heat transfer coefficient is still 20.4% above the plain channel case.

The experimentally measured heat transfer coefficient at $x'/H = 12$ is also plotted in Figure 5.6. The maximum deviation between the results has fallen to 8.9% with the numerical model under-predicting the heat transfer coefficient. First inspection of the experimental data shows that the trends between the two sets of data are incompatible. However, in the experimental case it appears that the vortex cores have shifted almost half a test section (10 mm) to the left. This could be due one or more vortex cores having a higher value of circulation due to some of the vortex generators either being bigger or having a larger angle of attack. The vortex cores would then be convected in a certain direction. If it is considered that the lowest experimental value at $y = 12.5$ mm should in-fact be at $y = 20.0$ mm then the numerically predicted and measured trends compare well.

The numerical model predicted an average heat transfer coefficient of 30.1 W/m^2K which was 30.6% less than that measured from the experiments. This can be partially explained by tangential conduction effecting the experimental results towards the leading edge. The pressure drop predicted by the numerical model was 3.5 Pa which was 14.6% below the experimental value. In many ways it would be expected that a numerical model would under-predict pressure drop as the channels are perfectly aligned and there are no discontinuities in the surface. This tolerance in manufacturing the test pieces cannot be expected in reality.

Along with the ever widening cores of the vortices when the flow is 'common flow

down' convection of each vortex by the flow field holds the vortices close to the wall on which the vortex generators are mounted. When the vortices have 'common flow up' type flow the vortex cores are convected away from the fin into the centre of the channel. In the case of the experiments carried out here, the average heat transfer coefficient is only calculated from the surface on which the vortex generators are mounted. In the case where the average heat transfer coefficient is measured from both the top and bottom fin surfaces, 'common flow up' vortices could be advantageous. Where vortex generators could be used, one way to utilise the increased heat transfer coefficient is to increase the fin pitch in order to reduce the amount of raw materials used. When this occurs it could be beneficial to use 'common flow up' vortices as the increase in heat transfer would then occur on both the top and bottom fin surfaces.

5.2.3 Experimental results at different flow velocities and angles of attack

The average heat transfer coefficient and pressure drop through a plain channel with delta winglet pairs with $\beta = 45°$ is shown in Figure 5.7, along with the data for a plain channel without vortex generators. At the lowest Reynolds number, 65, there is a 7.3% increase in the average heat transfer coefficient with a corresponding rise in pressure drop of 6.9%. By Re = 329 these values have increased to 19.2% and 9.8% respectively. At the highest Reynolds number, 757, the increase in the average heat transfer coefficient has increased to 33.7% with a pressure drop increase of 7% over the plain channel.

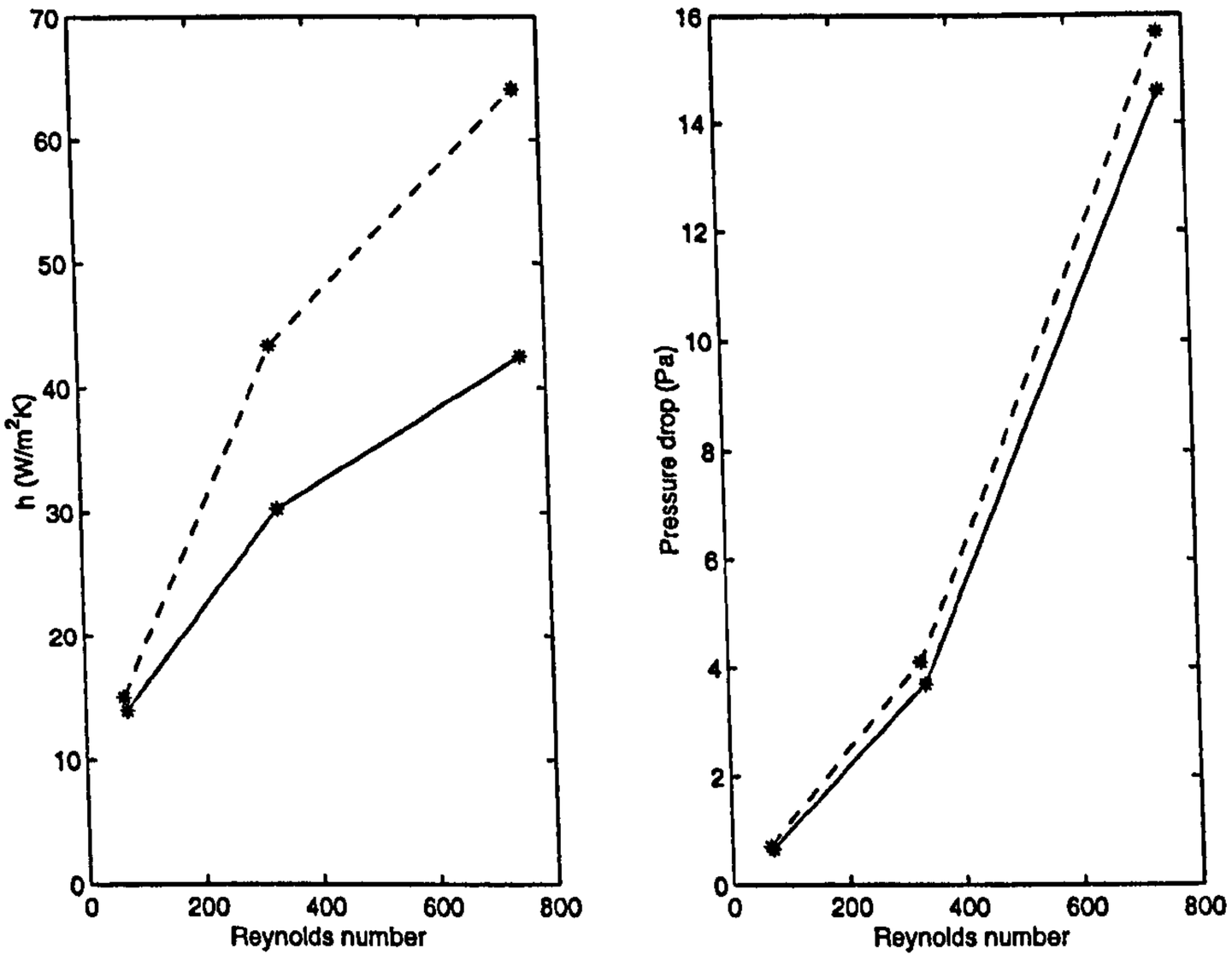

Figure 5.7: Average heat transfer coefficient and pressure drop increase with Reynolds number for a channel with delta winglet pairs at $\beta = 45°$ (dotted line with vortex generators, plain line without vortex generators)

The effect of the angle of attack of the vortex generators on the average heat transfer coefficient and pressure drop are shown in Figure 5.8. The results have been non-dimensionalised against the plain channel result without vortex generators. Three angles of attack were investigated, $\beta = 15°, 45°$ and $60°$ at a Reynolds number of 329. As can be expected both the average heat transfer coefficient and pressure drop values increase with angle of attack. At $\beta = 15°$ the increase in the average heat transfer coefficient is 29.2% with a negligible increase in pressure drop. Fiebig (1995) reported that the increase in pressure drop only becomes noticeable when angles of attack of greater than 15° are used. At $\beta = 45°$ the average heat transfer coefficient increases to 30.4% with a 9.8% increase in pressure drop. For $\beta = 60°$, these values are further increased to 31.9% and 19.6% respectively.

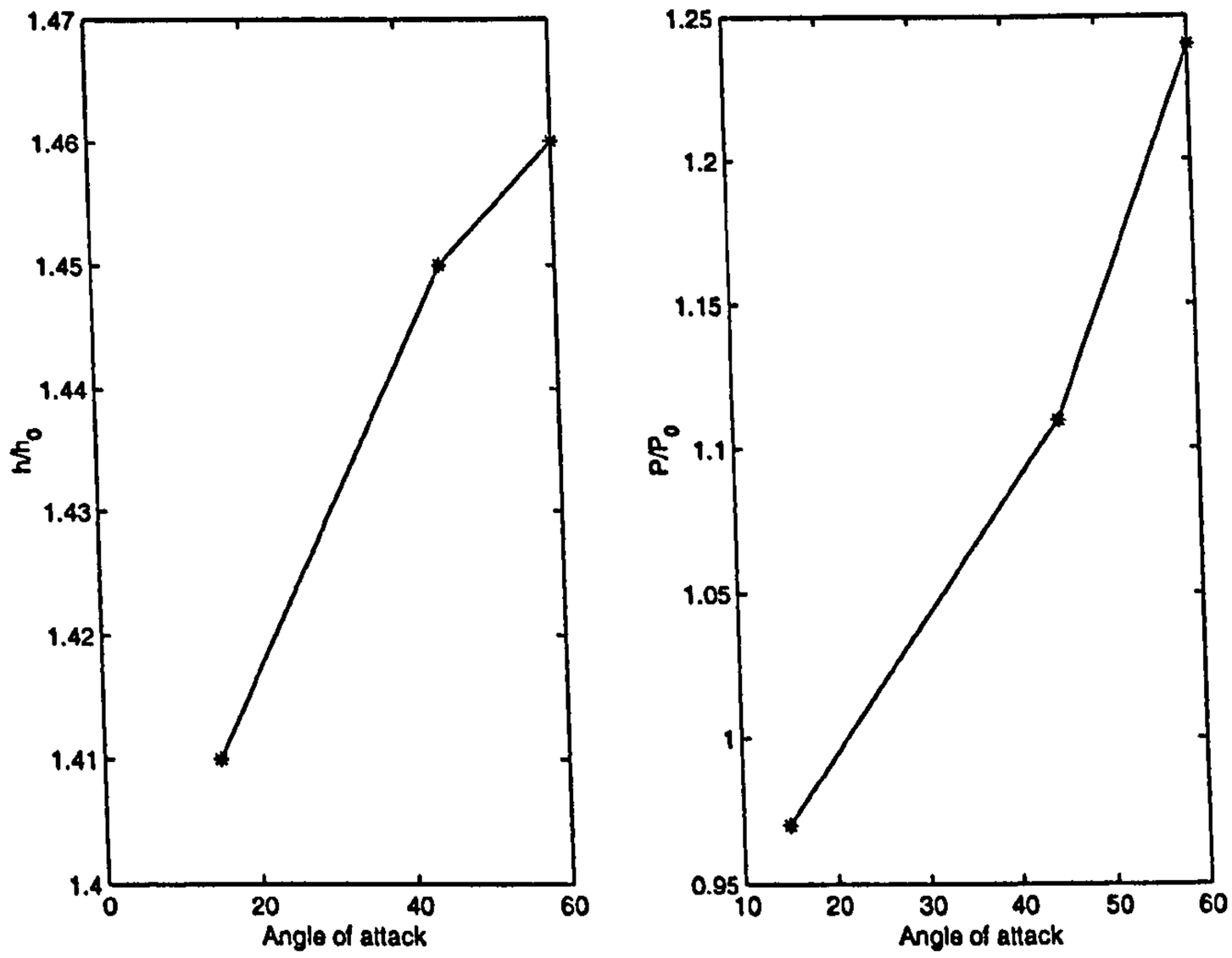

Figure 5.8: Average heat transfer coefficient and pressure drop increase with angle of attack, results non-dimensionalised against plain channel case

The increase in heat transfer and pressure drop can be expected with increasing angle of attack and has been widely reported, viz Fiebig (1998). The increase in heat transfer arises from stronger circulation values being produced at increasing angles of attack. The stronger the circulation the higher the secondary velocities produced by the vortex generator and thus more boundary layer thinning results. The increase in the pressure drop arises from two different effects. Firstly as the angle of attack increases the projected area of the vortex generator increases and thus the form drag. Secondly, with a higher angle of attack stronger vortices are produced which results in steeper velocity gradients near the wall. As a consequence the frictional losses are also increased.

5.3 Plain channel with rectangular winglet pairs

5.3.1 Experimental results

The experimentally recorded isotherms are qualitatively similar to those recorded in the plain channel case with delta winglet pairs. As a result no isotherm plots will be presented here. Where there are differences between the two cases, these will be discussed in the next section.

5.3.2 Numerical results

The formation of the longitudinal vortices occurs in exactly the same way as for the plain channel case with delta winglet pairs. However, due to the different shape of the vortex generators, there are differences in the flow structure and hence small differences in the isotherm shapes between the two cases. Shown in Figure 5.9 are the velocity vectors directly behind the rectangular winglet pair vortex generators. This can be compared to Figure 5.3 which is the velocity vectors in the same position for the delta winglet pairs. It is noticeable that in the case of the rectangular winglet pairs the vortex cores are much closer together, reducing the stagnation region size around the centre line. Also noticeable is the lack of any induced vortices beside the main vortex. In this region there is boundary layer thickening due to the upwash of the flow.

The resulting heat transfer coefficient distribution directly behind the vortex generators is shown in Figure 5.10. Due to the main vortices being closer together it can be seen that the width over which the the heat transfer is enhanced is smaller

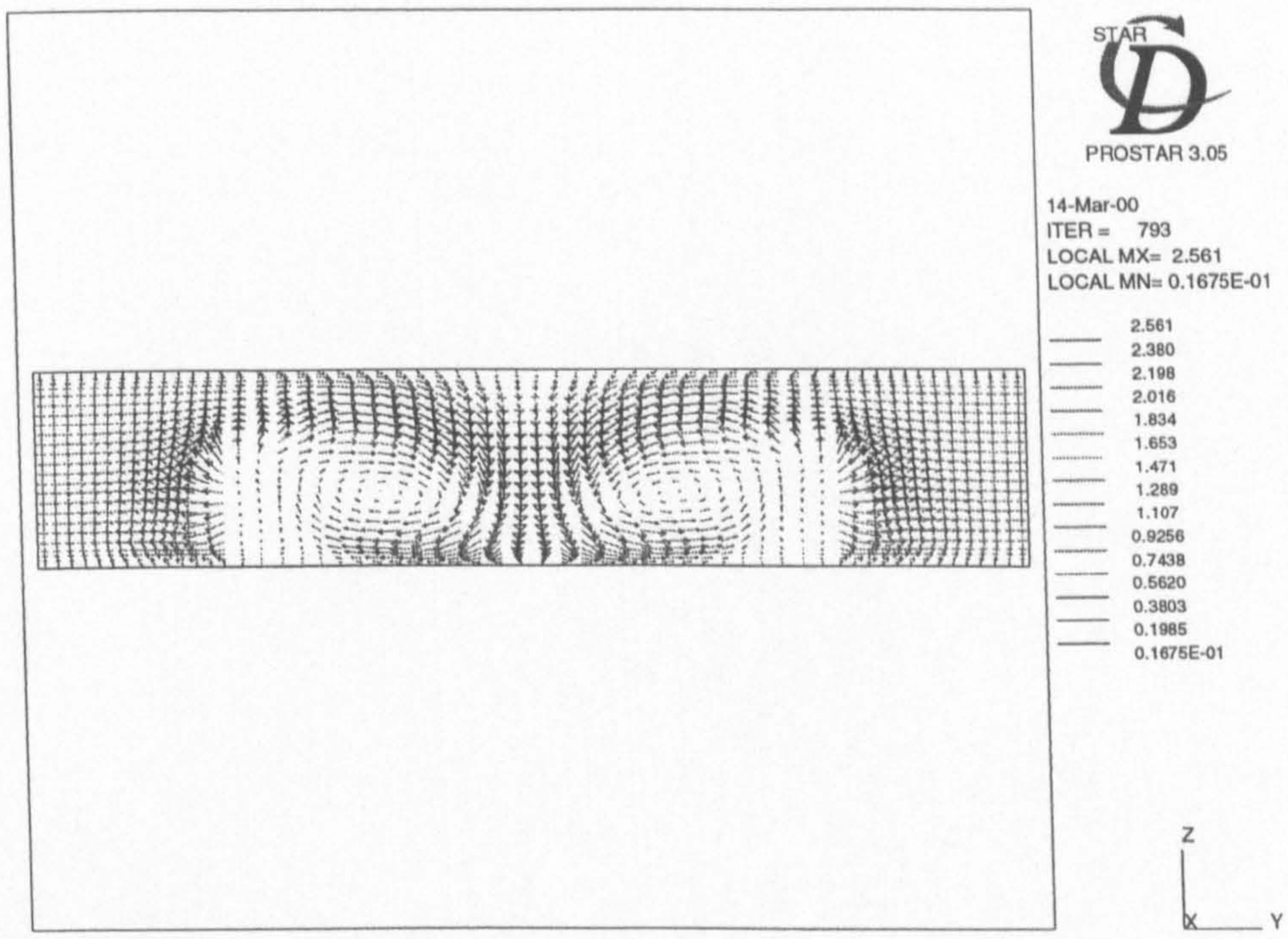

Figure 5.9: Velocity vectors directly downstream of the vortex generators

than in the case of the delta winglet pair. However, the drop at the centre line is also smaller. Due the thickening of the boundary layer in the upwash region of the vortices, the heat transfer coefficient is actually reduced to below the value of the plain channel at y = 5.0 and 15.0 mm. Either side of these troughs, going towards the outer edges of the domain, the values return to the plain channel value.

The experimental and numerically predicted values of heat transfer coefficient at $x'/H = 2$ is presented in Figure 5.11. As can be seen there is a discrepancy between the predicted trend and the one that was measured experimentally. Inspection of the velocity vector plots at this point showed that the highest velocity was in the downwash region between the two vortex cores. It was also noted that due to the vortex cores being so close together that there was not a region of stagnating flow

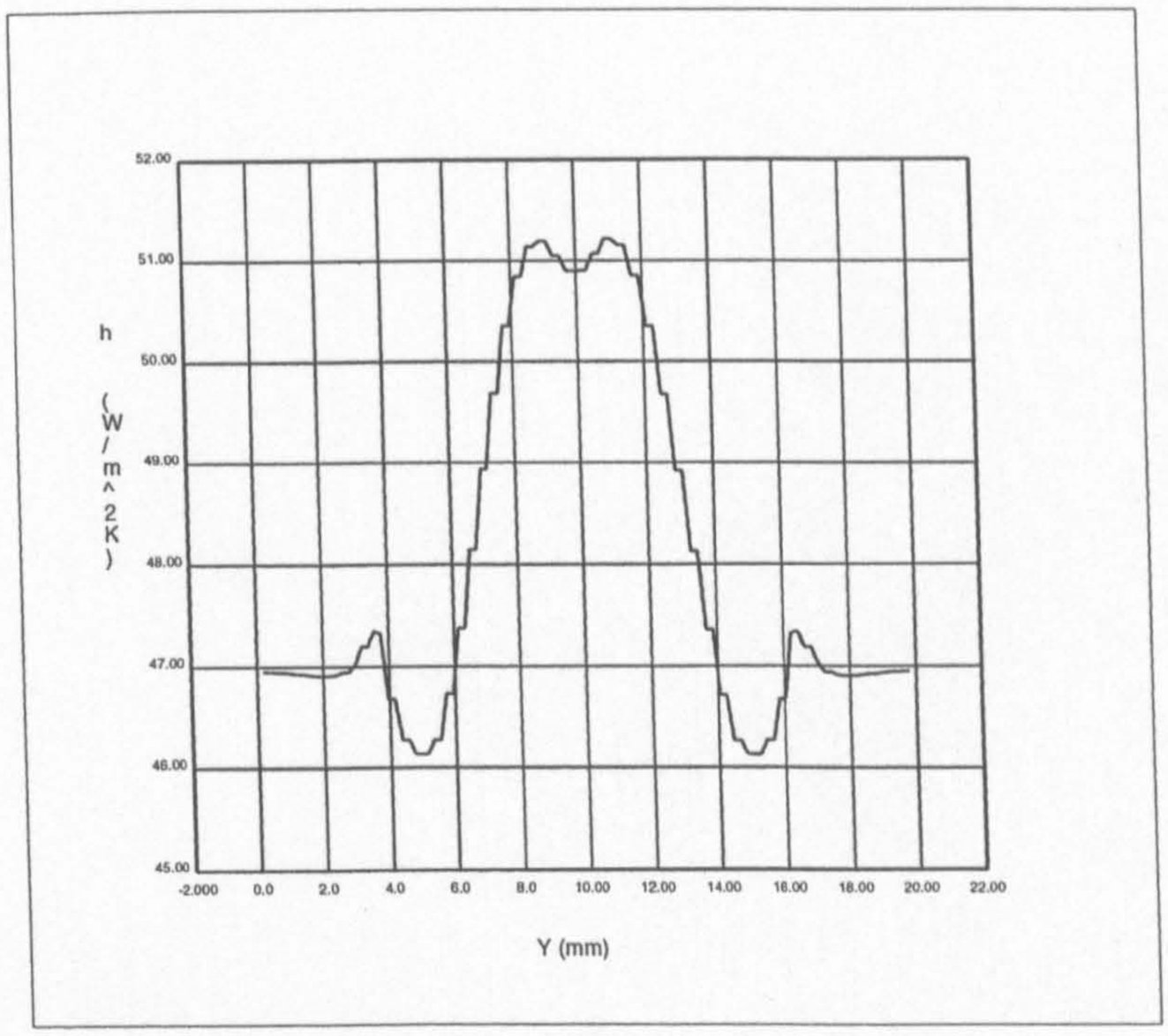

Figure 5.10: Heat transfer coefficient distribution directly downstream of the vortex generators

such as had occurred in the delta winglet pair case. The thermal boundary layer was seen to be thinnest in the centre of the channel gradually getting thicker until the upwash region, where there was a large increase in the thickness. This results in a heat transfer coefficient distribution which has a maximum on the centre line of the channel and reduces to the plain channel value on the edges of the domain.

The experimentally measured values of the heat transfer coefficient show a distinct local minimum on the centre line of the channel, followed by a local maximum, where upon the values drop down towards the plain channel result. This type of distribution was observed by Tiggelbeck et al. (1994) for rectangular winglet pairs at a Reynolds number of 4600 and $\beta = 30°$. They also observed a local rise in the heat

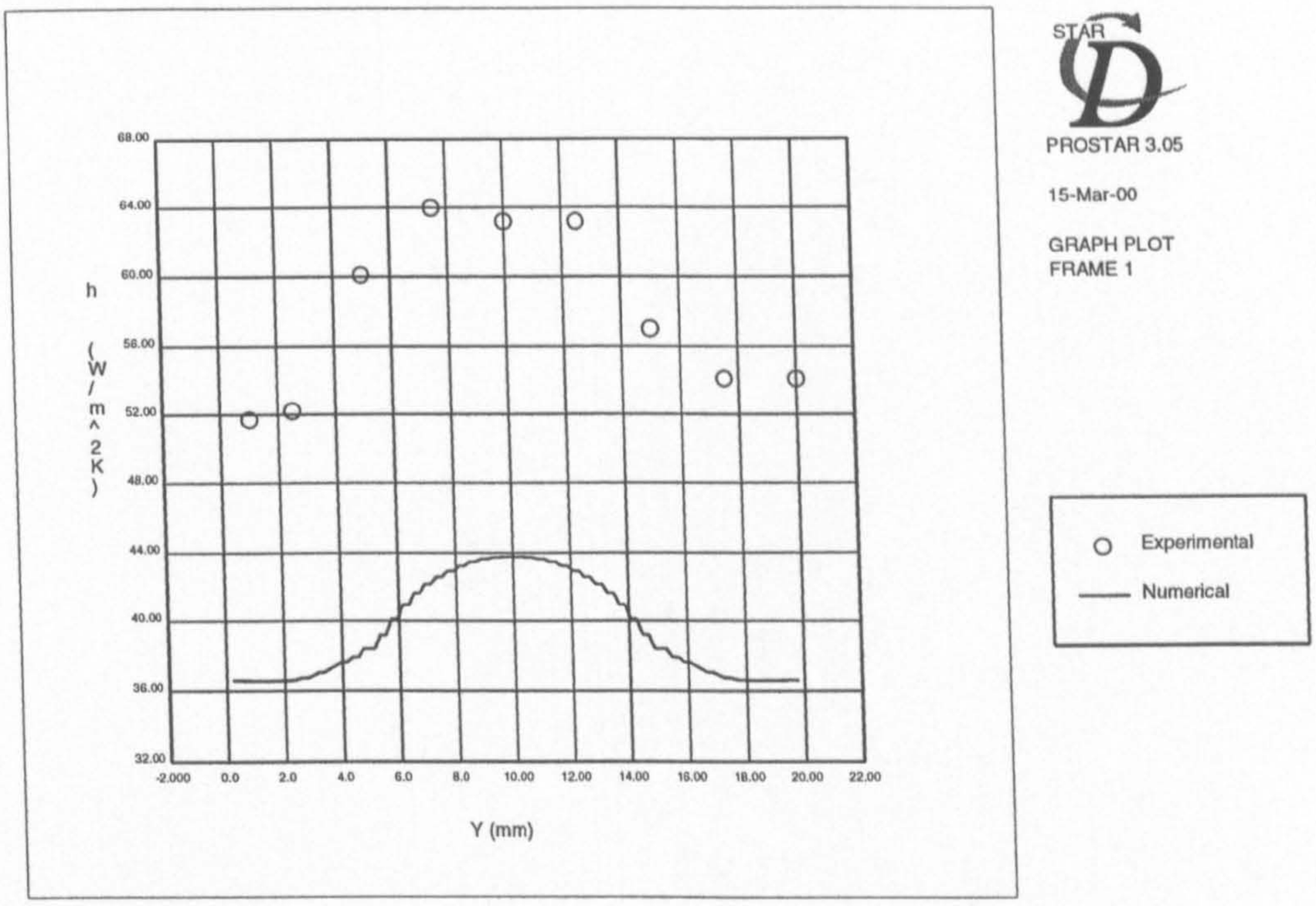

Figure 5.11: Heat transfer coefficient distribution at $x'/H = 2$ downstream of the rectangular winglet pair vortex generators

transfer coefficient at the positions of the downstream outer edges, presumably due to induced vortices. The induced vortices were not noted in the current experiments which were at a much lower Reynolds number than the Tiggelbeck et al. (1994) study. At $x'/H = 2$ there was a maximum local heat transfer coefficient of 30.4% over the plain channel result. This is a very similar result to the delta winglet pairs, but the area over which the enhancement acts is smaller for the rectangular winglets.

As the vortices persist further downstream, the cores get weaker and grow larger in a very similar fashion to the delta winglet pairs. This results in a predicted heat transfer coefficient distribution that is very similar to that of the delta winglet pairs. The heat transfer coefficient distribution for the rectangular winglet pairs is

shown in Figure 5.12, for the predicted and experimentally measured results. The

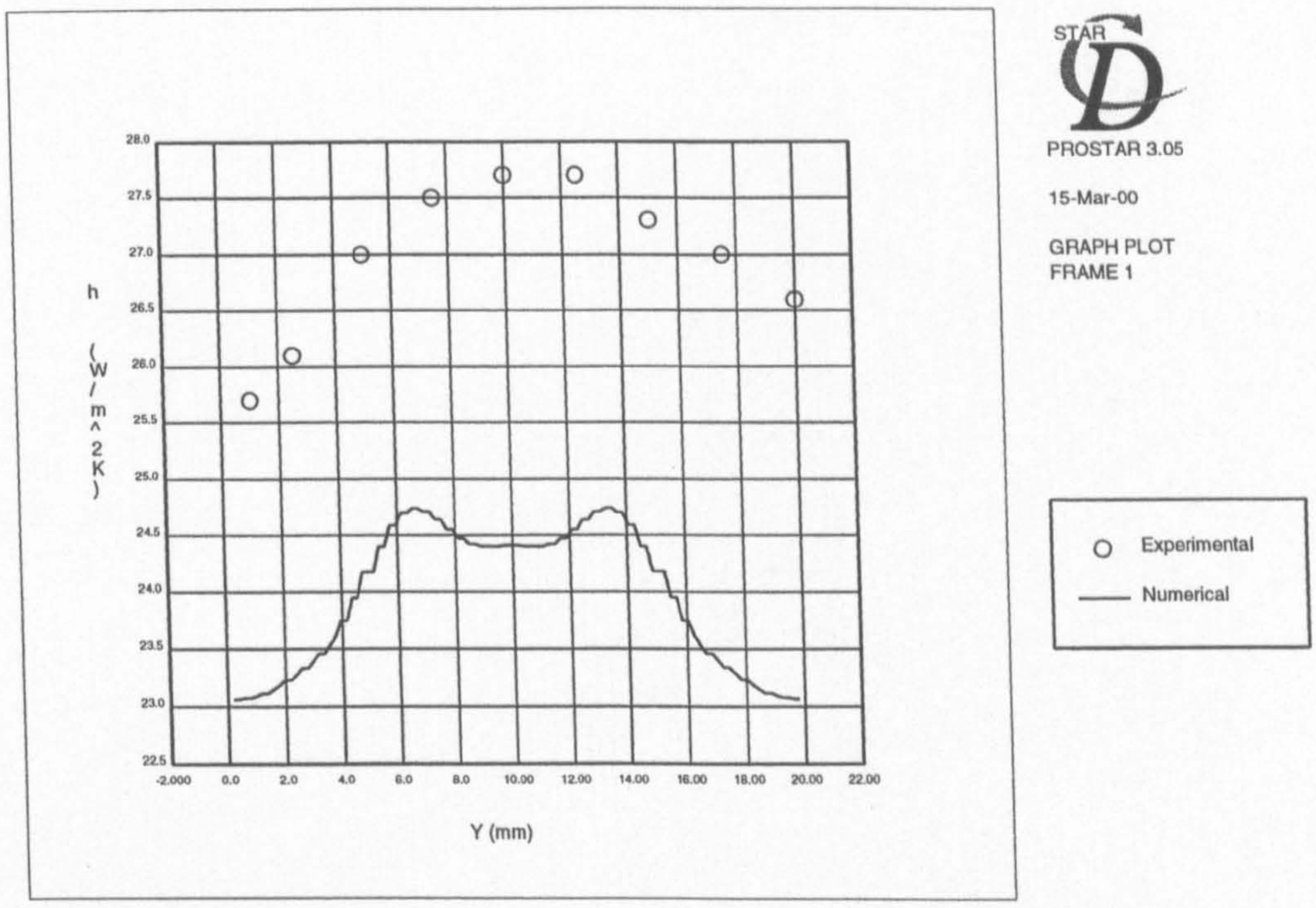

Figure 5.12: Heat transfer coefficient distribution at x′/H = 12 downstream of the vortex generators

predicted distribution shows enhanced levels of heat transfer coefficient around the centre line, peak values in the downwash region which reduce to the plain channel vales towards the outer edges of the domain. This type of distribution is again very similar to the delta winglet pairs. Once again there is disagreement between the numerically predicted heat transfer coefficient distribution and that measured experimentally. This is somewhat surprising considering the actual isotherms measured experimentally show a temperature distribution that is similar to what was predicted numerically. By looking at the contour map generated from the interpolation programme in Matlab, it was seen that for some reason the contours generated between the experimentally recorded results were poorly predicted. This has not

been observed in any other of the experimental cases. As with the delta winglet pair case, the local heat transfer coefficient predicted by the numerical model was less than that recorded experimentally. The maximum local increase in the heat transfer coefficient at $x'/H = 12$ was 24.3% which was slightly higher than the delta winglet pair case. For the overall average values the numerical model under predicted the average heat transfer coefficient by 32.4% and also under-predicted the pressure drop by 16.1%.

5.3.3 Experimental results at different flow velocities and angles of attack

The plain channel test section with rectangular winglet pairs was completed for three different Reynolds numbers, Re = 65, 336 and 757 with an angle of attack $\beta = 45°$ and also at a Reynolds number of 336 for three different angles of attack, $\beta = 15°, 45°$ and $60°$. Figure 5.13 compares the average heat transfer coefficient and pressure drop for $\beta = 45°$. At the lowest Reynolds number, 65, there is a 9% increase in the average heat transfer coefficient with a corresponding rise in pressure drop of 8.2%. For a Reynolds number of 336 the values have increased to 33.3% and 15.9% respectively. For the highest Reynolds number the enhancement values are 41.0% and 11.0% respectively.

For a Reynolds number of 336, the non-dimensionalised values of average heat transfer coefficient and pressure drop are shown in Figure 5.14, for the three different angles of attack considered. As would be expected all angles increase the average

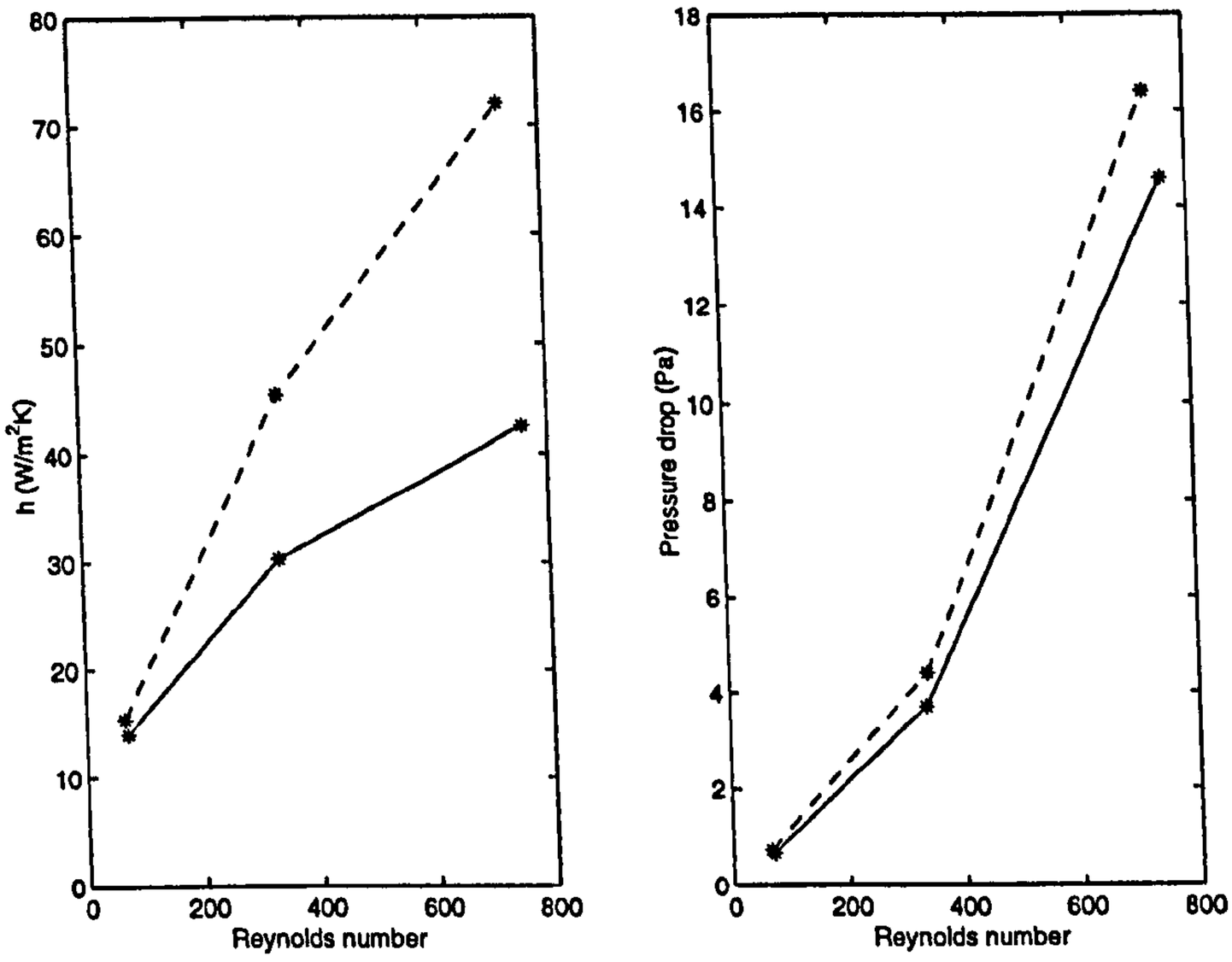

Figure 5.13: Average heat transfer coefficient and pressure drop increase with Reynolds number for a channel with rectangular winglet pairs at $\beta = 45°$ (dotted line with vortex generators, plain line with out vortex generators)

heat transfer coefficient and pressure drop. For an angle of attack of 15°, the average heat transfer coefficient is increased by 21.9% with an increase of pressure drop of 2.6%. These values increase to 33.3% and 15.9% for $\beta = 45°$. However, for $\beta = 60°$, the increase in the average heat transfer coefficient is slightly reduced to 30.8% whilst the enhancement in pressure drop increases to 32.7%.

The reduction in the average heat transfer coefficient for angles of attack greater than 45° is due to the effect of vortex breakdown. Vortex breakdown was investigated by Zhang et al. (1991) for a delta wing. When the angle of attack of the vortex generator was below a critical value, a stable vortex is formed where the fluid particles circulate around the vortex axis by maintaining the equilibrium of centrifugal forces and pressure forces. When the angle of attack is increased above

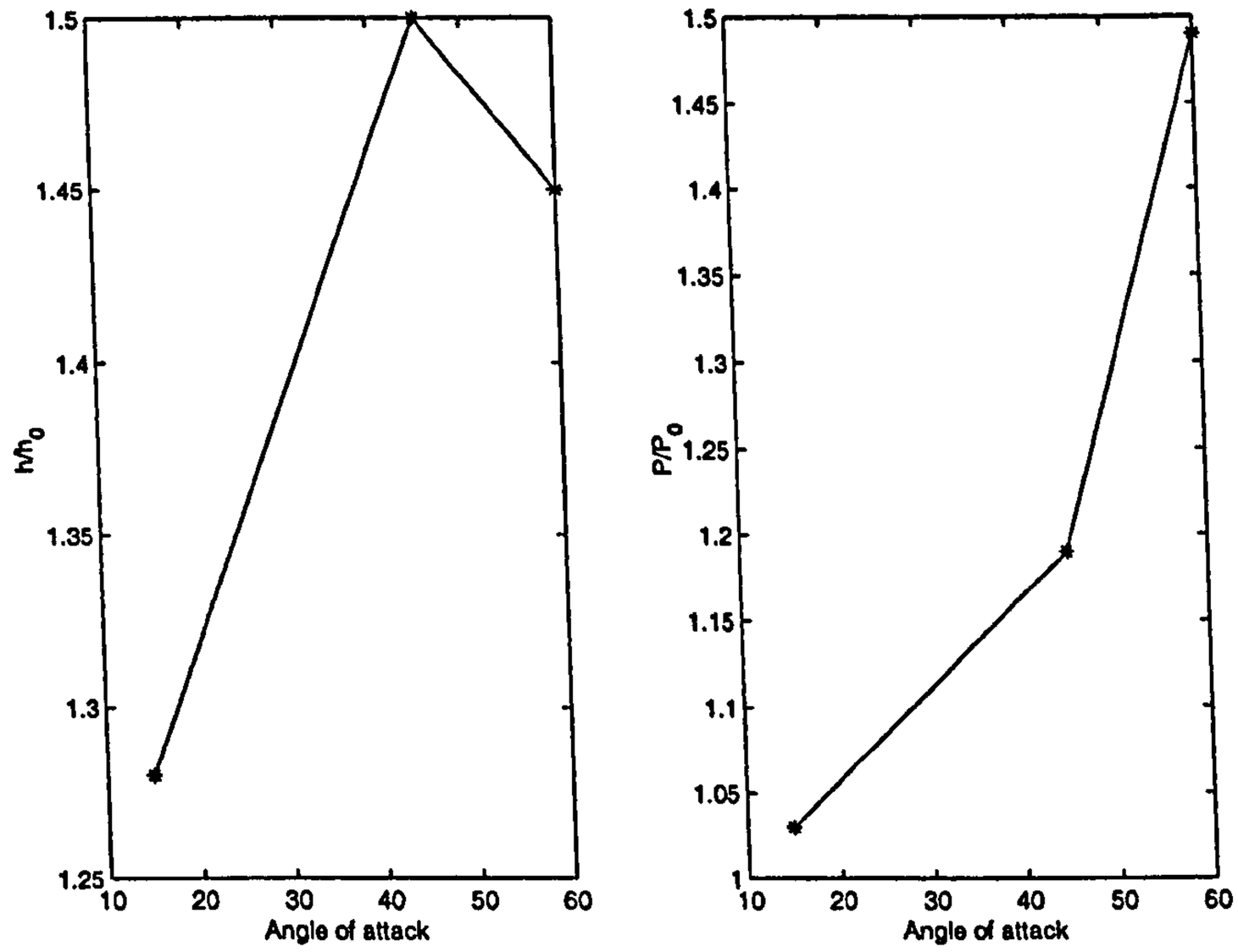

Figure 5.14: Average heat transfer coefficient and pressure drop increase with angle of attack, results non-dimensionalised against plain channel case

the critical level, there is a sudden expansion of the vortex core, which causes a large change in the velocity distribution and abrupt stagnation of the axial velocity. These effects combine to reduce the enhancement in heat transfer, but also increase the pressure drop. The effect of vortex breakdown for rectangular winglet pairs was also noted by Tiggelbeck et al. (1994) for a Reynolds number of 4600. This also occurred at $\beta = 45°$, for greater angles of attack, the heat transfer enhancement reduced and the pressure drop increased. Although vortex breakdown is a situation that should be avoided, it should be noted that there are still high levels of heat transfer enhancement. However, the pressure drop increase is still large.

Correlations for both heat transfer and friction factor were presented by Grosse-Gorgemann (1996) for the rectangular winglet pair, in the Reynolds number range

350 – 1000. Although the majority of the dimensions were similar a larger longitudinal pitch was used and a smaller fin length when compared to the current study. From numerical studies he proposed the correlation: $Nu/Nu_0 = 0.13Re^{0.436}$ and $f_{app}/f_0 = 0.065Re^{0.66394}$. These are non-dimensionalised values against a plain channel for Nusselt number and friction factor respectively. The correlation predicted an enhancement level of 1.64 for Re = 336 and 2.19 for Re = 653. The experimental values recored from this study are slightly lower at 1.5 and 1.69 respectively. These results agree well considering the slightly different geometries used.

5.4 Plain channel with rectangular wings

5.4.1 Numerical results

Owing to manufacturing considerations, rectangular wings were not tested experimentally for any Reynolds numbers or angles of attack. The rectangular wings were however, modelled numerically for $\beta = 45°$ and Re = 336. In Figure 5.15, the velocity vectors directly behind a rectangular wing at an angle of attack, $\beta = 45°$ and Re = 336 are shown. At this location it is evident that there is very little swirl in the flow. The only vortices that have formed are two small vortices near the top of the vortex generator. At this location directly behind the rectangular wing it would be expected that the vortex would be at least as high as the vortex generator because the fluid should separate along the whole length of the sharp edge of the vortex generator. In this case, this has not happened due to a recirculation region that forms behind the vortex generator. The recirculation region is caused

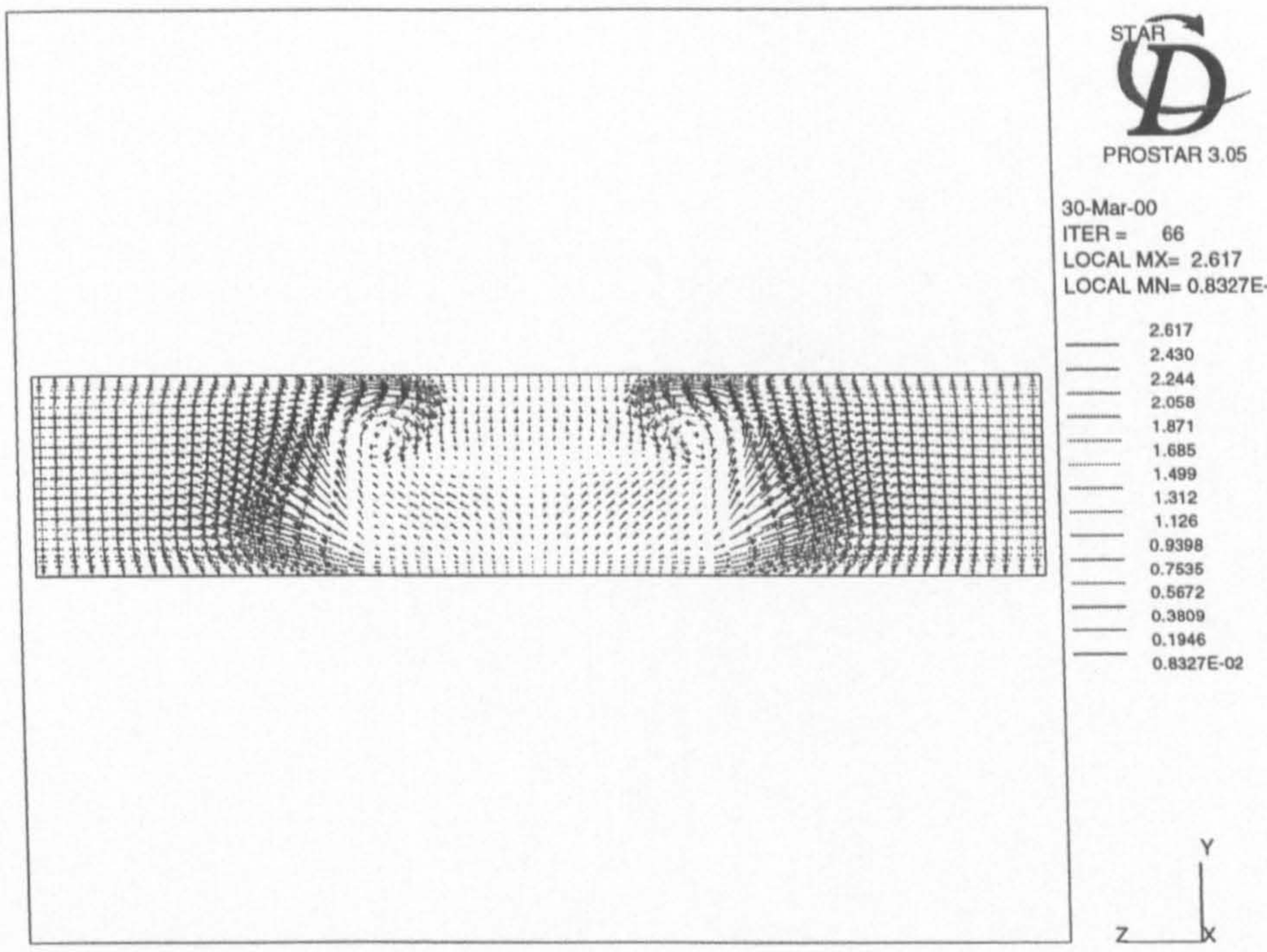

Figure 5.15: Velocity vectors directly downstream of a rectangular wing

by the high angle of attack. As the fluid moves downstream, the recirculation region reduces in size and thus the vortex cores grow to fill the whole channel.

By a distance of $x'/H = 2$ downstream of the vortex generator the vortex cores have grown in size to fill the channel. The heat transfer coefficient distribution at this point is shown in Figure 5.16. It is noticeable that along with having the smallest region of influence in the spanwise direction, the rectangular wings also have the biggest troughs in the heat transfer coefficient distribution. When the vortices fill the channel they are very close together, which results in the small region of influence, and also have large upwash regions which results in a heat transfer coefficient below that of a flat plate. As the vortices move downstream they reduce in size and strength in a similar fashion to the other vortex generator types.

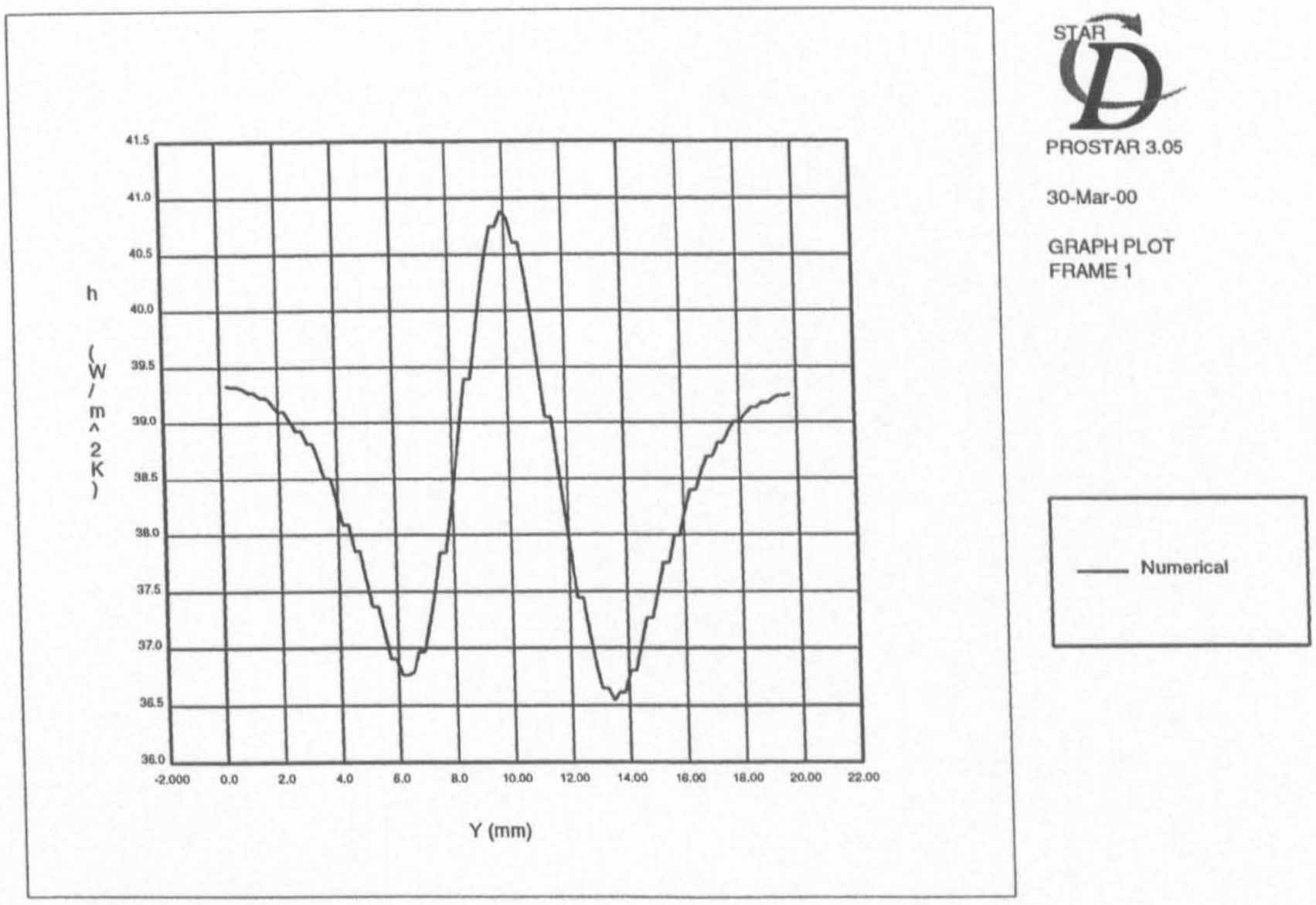

Figure 5.16: Heat transfer coefficient distribution at x′/H = 2 downstream of a rectangular wing in a plain channel

The average heat transfer coefficient numerically calculated for the rectangular wing was 29.5 W/m^{2}K with a pressure drop of 3.9 Pa. These are enhancements over the plain channel case of 14.6% and 44.6% respectively. These results are relatively poor in comparison to the other types investigated and this is in agreement with Tiggelbeck et al. (1994) who studied these cases at higher Reynolds numbers.

5.5 Embossed vortex generators

5.5.1 Experimental results

The isotherm patterns for the embossed vortex generators are shown in Figure 5.17 for increasing heat flux input. At low heat flux inputs, Figure 5.17a, the liquid

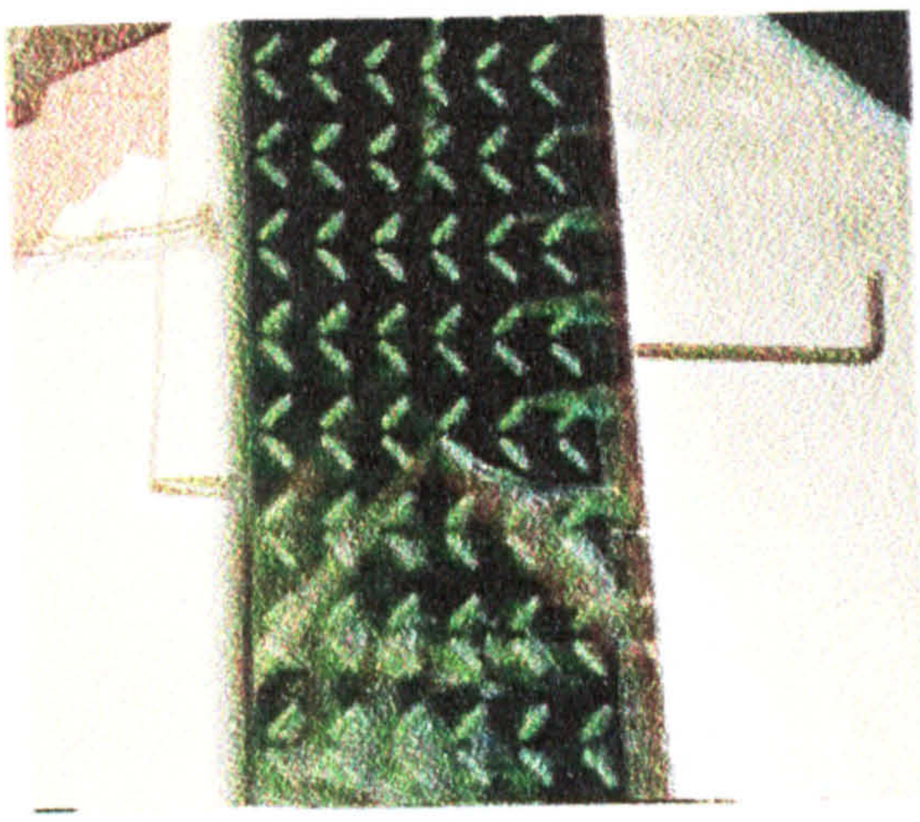

a: $\dot{q}$ = 388.3 W/m^2

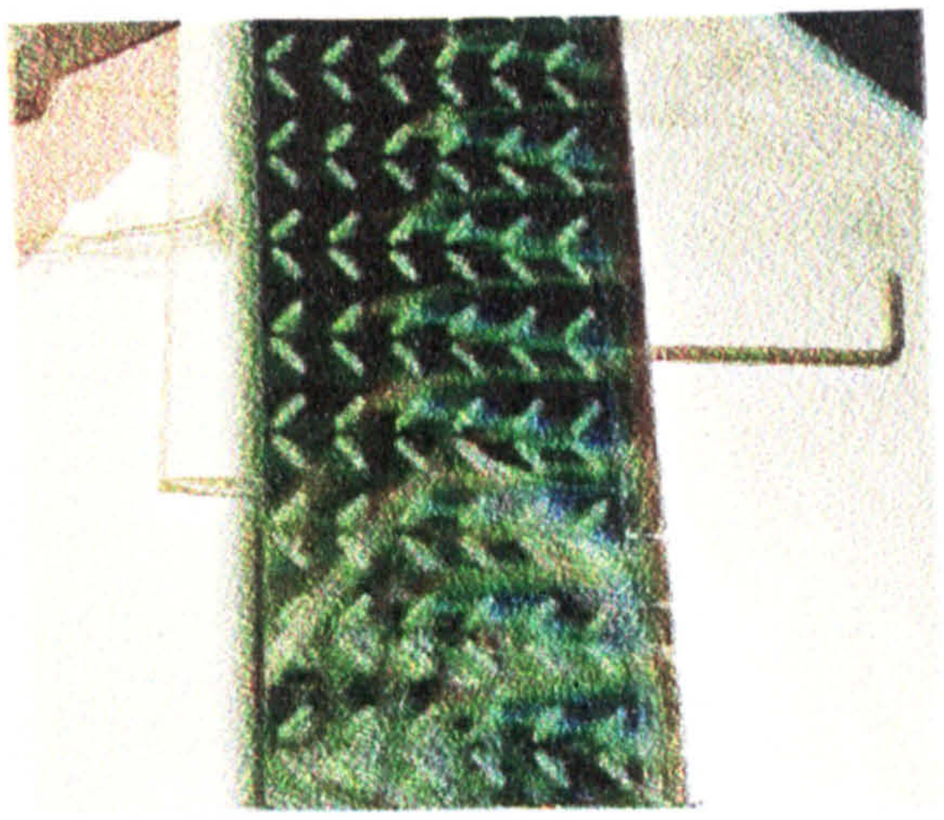

b: $\dot{q}$ = 398.9 W/m^2

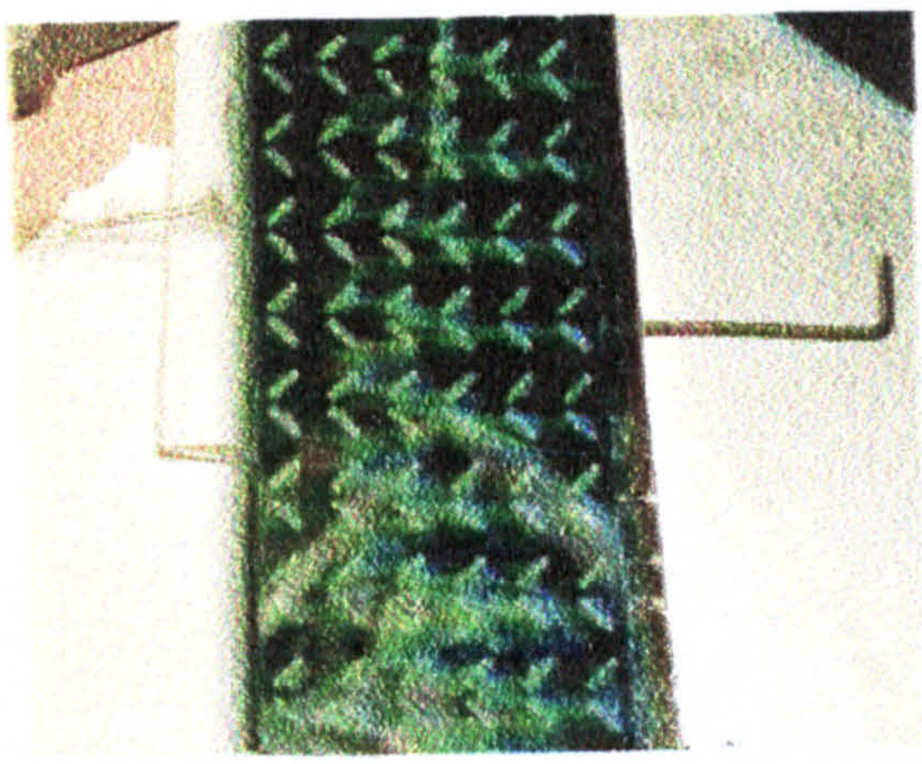

c: $\dot{q}$ = 434.2 W/m^2

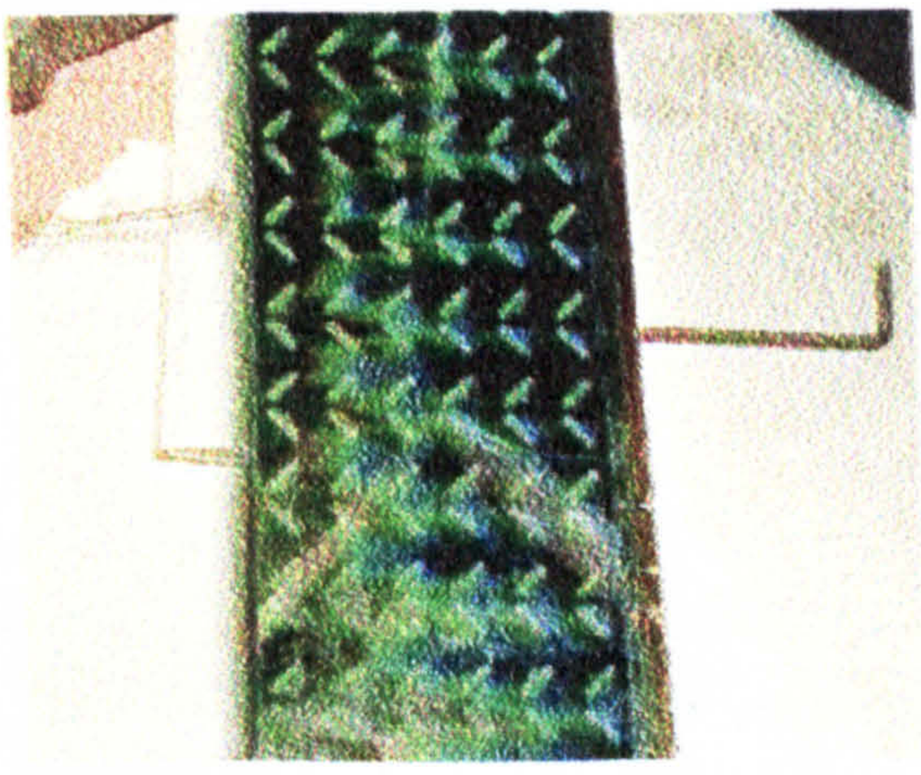

d: $\dot{q}$ = 466.2 W/m^2

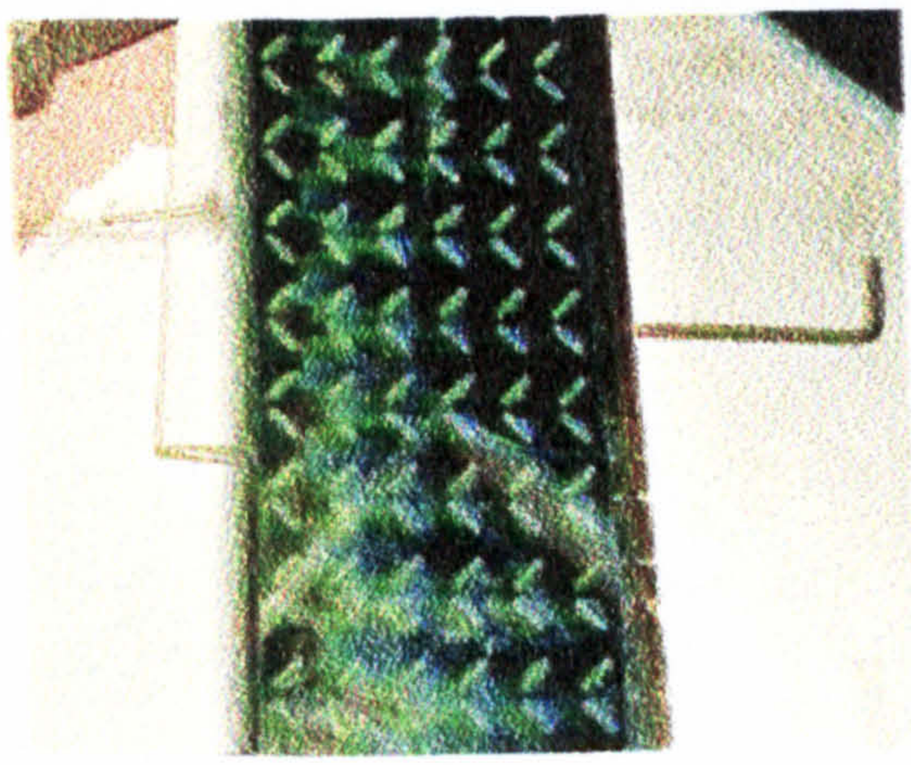

e: $\dot{q}$ = 521.3 W/m^2

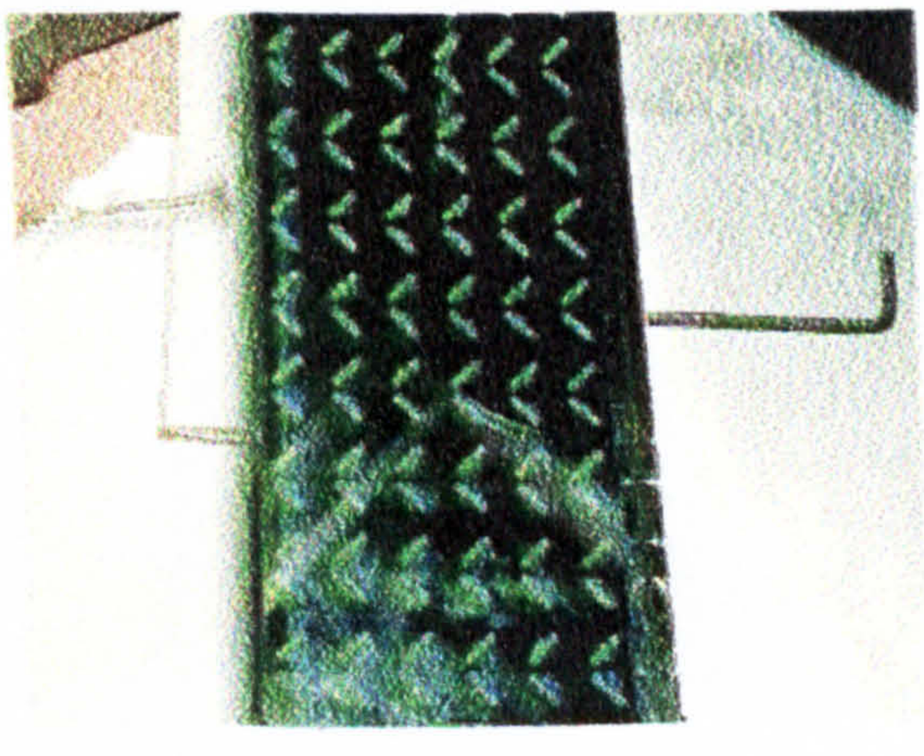

f: $\dot{q}$ = 703.6 W/m^2

Figure 5.17: Isotherm position for increasing heat flux input

crystals change colour in alternating wake regions of the vortex generators near the trailing edge of the fin. The liquid crystals would be expected to change colour first near the trailing edge. However, for the liquid crystals to change colour in alternating wake regions of the vortex generators was unexpected. As the heat flux input is increased, Figures 5.17b, 5.17c and 5.17d the liquid crystal isotherms move toward the leading edge. They still have a periodic nature, where they change colour first on one side of the vortex generator pair, before they change colour in the same place on the other side. It was expected that the isotherms would have been symmetrical about the centre line of each row of vortex generators. By the time the isotherms reached the rear of the first set of vortex generators, Figure 5.17e, the isotherms patterns have finally reached a symmetrical nature about the centre lines of each vortex generator row. Increasing the heat flux further, Figure 5.17f, the isotherms continue to move toward the leading edge and also get thinner indicating increasing heat transfer coefficient with increasing temperature gradient.

5.5.2 Numerical results

Due to the unexpected isotherm patterns in the experimental results, a numerical model was built to try and recreate the experimental fluid flow and thus heat transfer patterns. Owing to the excessive time it took to build the computational mesh, only one set of vortex generators were built. It was expected that by the fifth set of vortex generators in the flow direction that the flow would be periodic, resulting in the fact that periodic boundary conditions could be used in the numerical model.

The resulting flow field and thus temperature distribution from the numerical model which had periodic boundary conditions was symmetrical about the centre of the vortex generator pairs. This suggests that in the experimental case the flow field was unlikely to be periodic at this point and the effect of there being more than one set of vortex generators in the flow direction might be significant in the cause of the un-symmetrical flow patterns observed.

In manufacturing the test piece, where the individual embossements were glued onto the fin, it was very unlikely that all the individual embossements were mounted at exactly the correct angle and position. It was postulated that due to at least one, if not more embossements being at an incorrect angle that the flow field over one vortex generator might be tripped into going into a certain direction. The resulting pressure field, due to the governing equations being elliptic, would then move the fluid flow over all the vortex generators in the same direction.

Considering the mathematical solutions for flow around a cylinder in an infinite domain, three solutions are possible, Figure 5.18. The first two are stable solutions

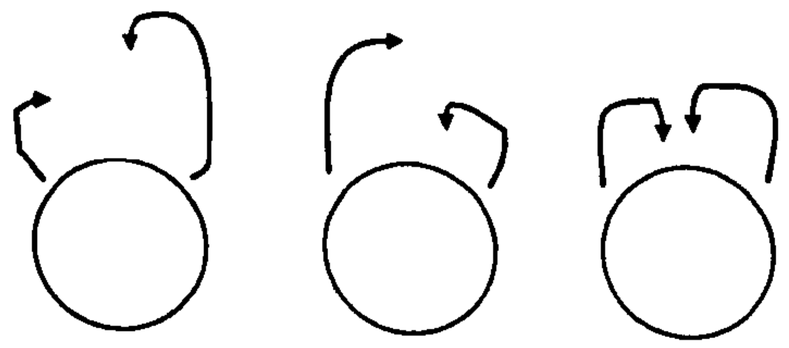

Figure 5.18: Flow patterns around a cylinder

and the third is quasi-stable. Any disturbance to the flow field in the third case might result in either of the first two flow patterns being achieved. As the fluid flows over

the front of the vortex generators, which is essentially a round surface, the fluid might be tripped into one of the steady state solutions for flows around a cylinder. Once this has occurred on one vortex generator, the pressure field will dictate that it happens on all.

To test this hypothesis, the periodic boundary conditions on the inlet and outlet of the domain were replaced with a prescribed velocity profile at the inlet and an outlet boundary condition. The velocity profile at inlet had a small amount of shear prescribed in the flow direction so that the fluid flow would reach the vortex generators in an un-symmetrical manner. The resulting flow pattern directly behind the vortex generators and the temperature distribution are shown in Figures 5.19 and 5.20 respectively. It can be seen from Figure 5.20 that the wake region is larger for the vortex generator near the bottom of the plot and there is more enhancement behind the vortex generator near the top. However, it was found that the size of the wake regions could be altered depending on how much shear was put on the velocity profile. It was hoped that the flow could be tripped into a certain flow pattern, and this flow pattern would be independent on the amount of shear used on the velocity profile. Whilst the above reasoning gives goes some way to describing the interesting flow phenomena, the only way to test numerically the flow field is to model more than one set of vortex generators in the flow direction. The interaction between the vortices from one set of vortex generators on the next vortex generator could then be identified and thus the cause of the interesting flow field identified.

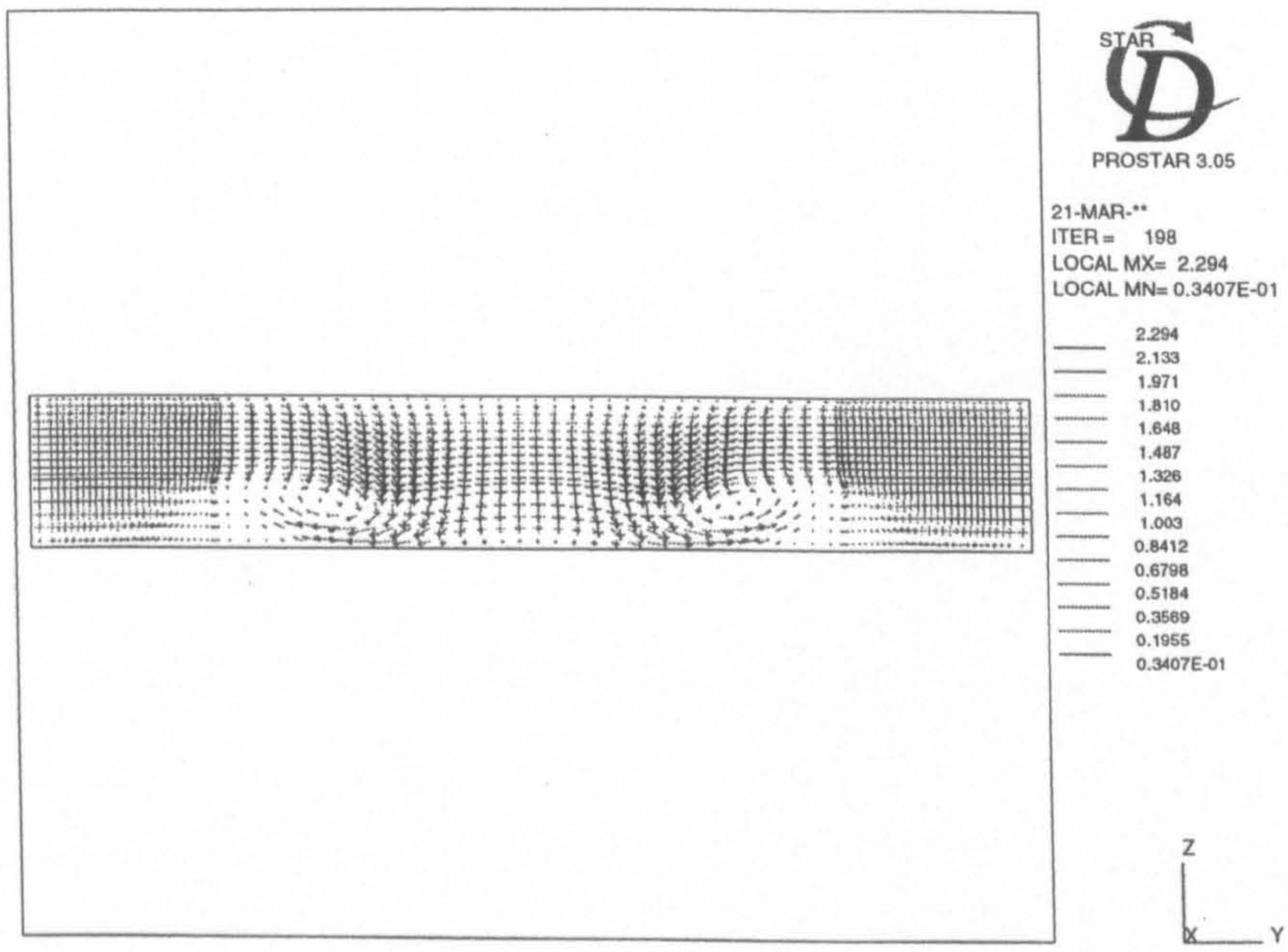

Figure 5.19: Velocity vectors directly downstream of a set of embossed vortex generators

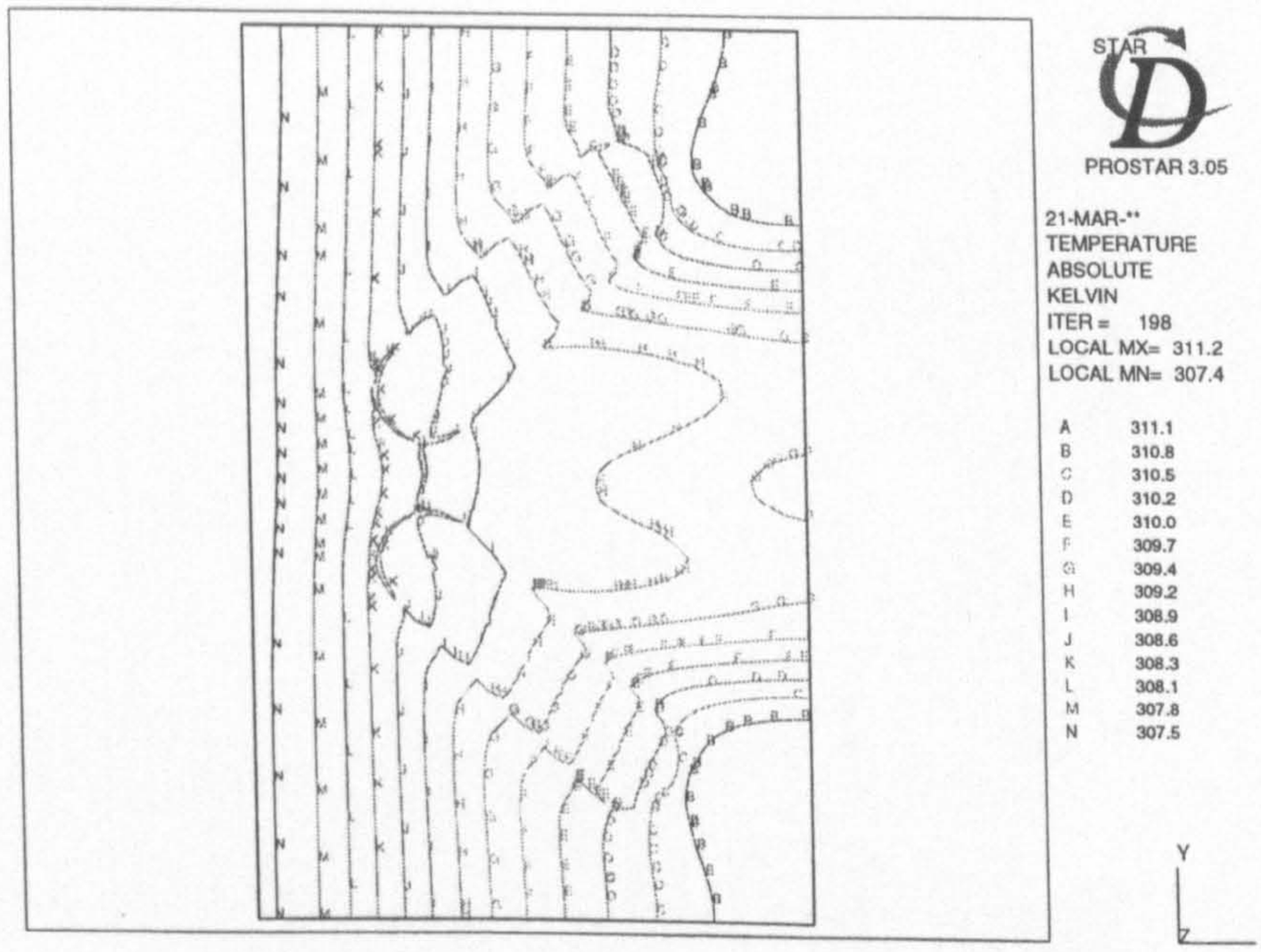

Figure 5.20: Temperature distribution on a fin with embossed vortex generators

It is interesting to note from Figure 5.19 that a different vortex shape is produced when compared to both the delta and rectangular winglet pairs. For the delta winglet pair case the vortex generated becomes elliptical in cross section and tilted from the wall plane. In the case of the embossed vortex generator, the vortex is very circular and remains very close to the wall on which the embossements are mounted. Using a Laser Doppler Anemometry (LDA) system, Mitra (1999) measured the velocity components and thus circulation values behind embossed vortex generators on a flat plate. The circulation values were found to be approximately 20% lower than the delta winglet pair case. He also reported that the vortex cores were very circular in shape and close to the wall. The lower levels of circulation are caused by their being no definite separation point on the curved surface of the embossements, resulting in a smaller separation zone and thus weaker vortices when compared to delta or rectangular winglet pairs. For winglet pair models, the line of separation is always fixed. However, for the embossed vortex generators the line of separation can change with with flow conditions such as the Reynolds number used and the angle of attack. These factors lead to lower circulation values and thus lower heat transfer enhancement.

5.5.3 Experimental results at different flow velocities

The embossed vortex generator models were tested at three different Reynolds numbers, Re = 65, 326 and 655, for an angle of attack $\beta = 45°$. The results from the embossed vortex generator model were compared to the results for a plain channel

which were generated numerically for the same Reynolds numbers.

Figure 5.21 compares the average heat transfer coefficient and pressure drop values

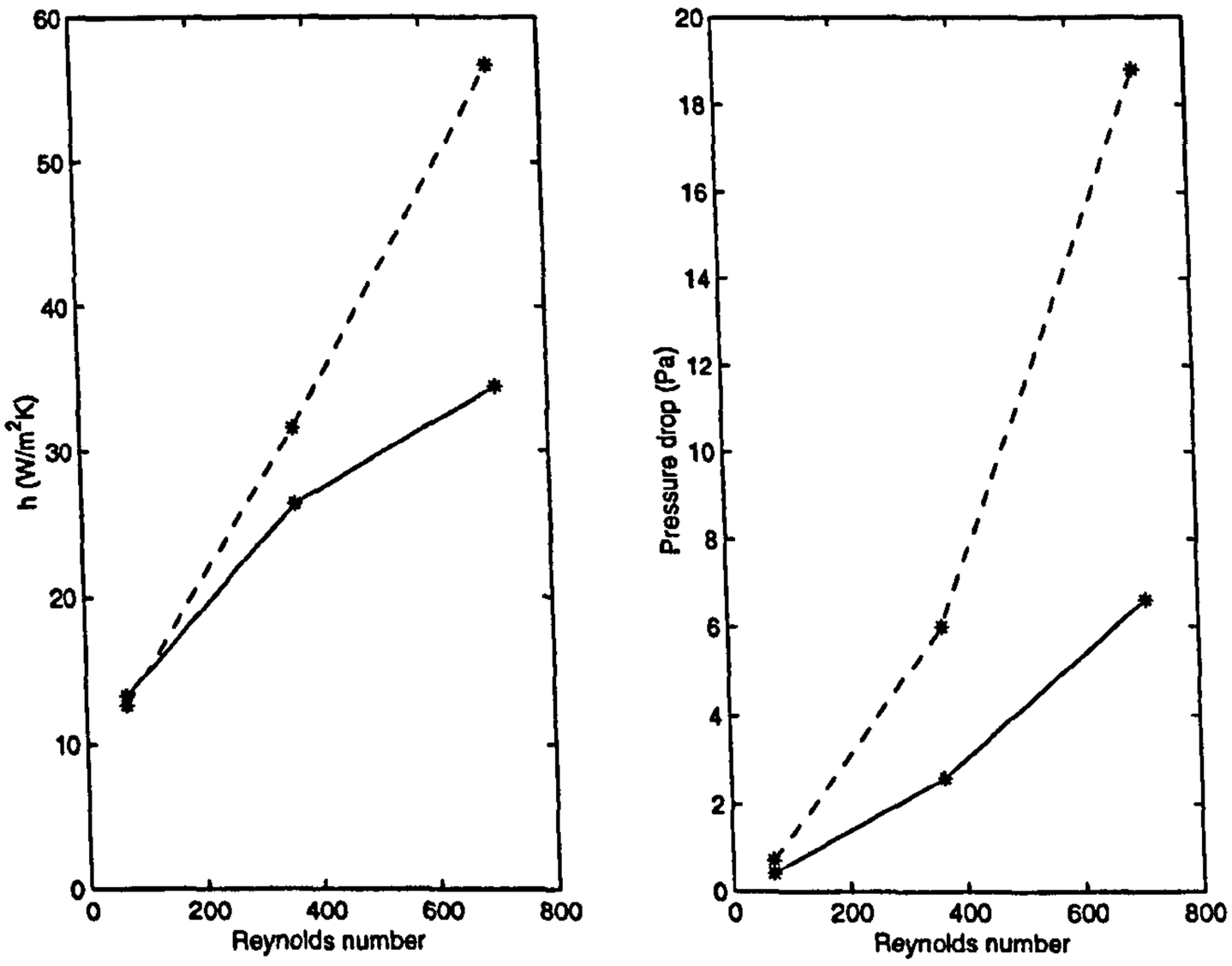

Figure 5.21: Average heat transfer coefficient and pressure drop increase with Reynolds number for a channel with embossed vortex generators at $\beta = 45°$ (dotted line with vortex generators, plain line with out vortex generators)

for a fin with embossed vortex generators against a plain fin. At Re = 65, the average heat transfer coefficient is slightly reduced by 4.7%. The area under the vortex generators are not used in calculating the average heat transfer coefficient and it was also not possible to calculate the heat transfer from the vortex generator itself. This will lead to some small discrepancy between the plain channel heat transfer coefficient and that recorded with the vortex generators in place. The pressure drop increase is however, increased by 40.8%. This would indicate that at this low Reynolds number, no or only very weak vortices are being formed and the fluid flow is essentially channel flow over obstructions. This would account for

the large pressure drop increase. As the Reynolds number is increased to 326, the average heat transfer coefficient enhancement is 16.8% with a 56.7% increase in pressure drop. At the highest Reynolds number, 655, these enhancement values have risen to 39.1% and 64.9% respectively.

It is interesting to note that the heat transfer coefficient increase over the range measured is almost linear. When embossed vortex generators are used at Reynolds numbers greater than approximately 300, the increase in heat transfer coefficient is always larger than that associated with a plain channel. It should also be noted however, that the increase in pressure drop is always bigger than the increase in heat transfer coefficient. This trend was observed by Mitra (1999) for a single set of embossed vortex generators.

5.6 Summary

In this chapter the experimental and numerical results for the cases investigated have been presented. The cases investigated were: plain channels, delta and rectangular winglet pairs, rectangular wings and embossed vortex generators.

In the plain channel case, which was modelled both experimentally and numerically at Re= 236 the heat transfer coefficient was found to decrease down the length of the channel due to boundary layer development. The numerical predication of the average heat transfer coefficient, pressure drop and heat transfer coefficient distribution agreed well with the experimental results. Deviations between the two sets of

heat transfer coefficient results were noted near the leading edge due to high values of tangential conduction occurring near the leading edge in the experimental model. Deviations near the leading edge were noted in all the comparisons between the numerically predicted and experimentally recorded results.

When vortex generators were placed in the plain channel both the values of average heat transfer coefficient and pressure drop were found to increase. Vortex generators cause the flow to separate over the sharp leading edge which produces longitudinal vortices to form in the downstream direction. This increases heat transfer by locally thinning the boundary layer in the downwash regions and increasing the mixing of the cooler bulk air temperature with the warmer fluid near the fin. With the increase in heat transfer, an increase in pressure drop results due to form drag and increased velocity gradients at the wall leading higher levels of shear stress.

Although the formation of the vortex is similar for all types of vortex generator, the actual shape and size of the vortex is different for all the cases investigated. In the case of the delta winglet pair the vortex is elliptical and tilted to the wall plain, for the rectangular winglet pairs the vortex is also elliptical but is not tilted. For the embossed vortex generators the vortices are circular. As the vortices travel downstream they grow in size and move apart, this has the effect of reducing the increase in heat transfer but increasing the area over which the enhancement acts.

The delta winglet pairs were found to give the greatest enhancement in average heat transfer coefficient and the least increase in pressure drop for a Reynolds number of

326 the the angle of attack was increased from 15° to 60°. The values for the increase in average heat transfer coefficient are +29.2%, +30.2% and +31.9%. The values for pressure drop were -2.8%, +9.8% and +19.6%. These can be compared against the rectangular winglet pairs for the same Reynolds numbers and angles of attack were the increase in average heat transfer coefficient was +21.9%, +33.3% and +30.8% with pressure drop enhancements of +2.6%, +15.9% and +32.7%. When the angle of attack was held constant at $\beta = 45^0$ and the Reynolds number was increased from 65 to 653 the rectangular winglets gave slightly better results with +9.0%, +33.3% and 41.0% for the average heat transfer coefficient and +8.2%, 15.9% and 11.0% for pressure drop. The values for the delta winglet pair were +7.3%, +30.3% and +33.7% for the average heat transfer coefficient and +6.9%, +9.8% and 7.0% for pressure drop. Although the rectangular pairs offer slightly greater increase in the heat transfer coefficient when the Reynolds number is increased, the pressure drop increase is always greater, as a result delta winglet pairs are preferred.

The rectangular wings offered the lowest increase in the heat transfer coefficient at the one angle of attack investigated numerically. For Re = 236 and $\beta = 45°$ a large recirculation region was seen behind the vortex generator which inhibited the formation of the longitudinal vortices. As a result the increase in the heat transfer coefficient was only 10.8% with an increase in the pressure drop of 35.0%. The flow pattern behind the vortex generator showed signs of what is termed 'vortex breakdown'. When this happens, the vortex core expands and the flow stagnates resulting in a decrease in heat transfer coefficient enhancement and an increase in

pressure drop. This was also observed for the rectangular winglet pairs at angles of attack greater than 45°. Where the wing type vortex generators were compared against numerical models the general trends in the heat transfer coefficient were well predicted. Differences between the two sets of results were generally around 20% near the leading edge due to tangential conduction occurring in the numerical model. Nearer the trailing edge these differences reduced to around 4%.

A special type of wing vortex generator was also investigated. The embossed winglet pairs were punched into the fin and thus do not have the gap in the fin that is inherent with the other types of wing vortex generator. This allows embossed vortex generators to be used in gas-gas type heat exchangers. As there is no sharp edge on the embossed vortex generators weaker vortices are produced which results in lower heat transfer enhancement. The vortex cores produced are very circular and remain very close to the wall on which the vortex generator is punched. In the experimental model the heat transfer coefficient was found to be un-symmetrical around the centre line of the vortex generator pairs. This is presumed to be due to inaccuracies in the building of the test piece that has effected the flow field and thus heat transfer coefficient distribution. A numerical model could be made to have an un-symmetrical heat transfer coefficient distribution by the application of shear on the inlet velocity profile.

The increases in the heat transfer coefficient over the Reynolds number range 65 – 655 for embossed vortex generators with $\beta = 45°$ were -4.7%, +16.8% and 39.1%.

The values for the pressure drop were +40.8%, +46.7% and +64.9%. It was found that the increase in pressure drop was always greater than the increase in heat transfer coefficient.

Over the range of Reynolds numbers and angles of attack investigated the increases in average heat transfer coefficient for the delta and rectangular winglet pairs was very similar. However, in all cases the pressure drop increase for the delta winglet pairs was less. Due to the lower pressure drop enhancement and the higher angles of attack that could be achieved before vortex breakdown, delta winglet pairs were chosen for inclusions in heat exchanger section tests.

Chapter 6

Presentation and Discussion of Results For Heat Exchanger Sections With and Without Vortex Generators

From the previous chapter it was found that delta winglet pairs offered the highest heat transfer enhancement with the lowest pressure drop increase. As a result, in this chapter delta winglet pairs are tested in heat exchanger sections. The heat exchanger sections investigated are staggered and in-line tube heat exchanger cores. In each case the heat exchanger sections are tested first without vortex generators as a base case so that the effect on average heat transfer coefficient and pressure drop can be quantified. As in the previous chapter, firstly the experimental results will be presented followed by the numerical results for each case. The results from the physical experiments will then be compared to the results obtained by the CFD package. Insights into the heat transfer coefficient distributions are then discussed in light of the numerical results. In the final part of each section the results for different flow velocities and angle of attack of the vortex generator are presented where applicable. Finally, the effects on average heat transfer and pressure drop

by the tube shape and position are presented. Round and oval tubes are compared experimentally in the staggered and in-line arrangements.

6.1 Staggered tube heat exchanger sections

6.1.1 Experimental results

The liquid crystals first changed colour in a cone shape behind the first tube row. This was a reasonably wide area indicating low heat transfer and a low temperature gradient, Figure 6.1a. As the heat flux was increased the isotherms moved both upstream and downstream; going upstream the isotherms attached itself to the tube and downstream the length increased with the isotherms getting thinner indicating higher heat transfer with increasing temperature gradient. As the isotherms were getting longer behind the first tube row, the liquid crystals changed colour behind the second tube row, eventually the two sets of isotherms behind the first and second tube rows joined, Figure 6.1b and 6.1c. The isotherms in-front of the second row tube and behind the first row tube moved towards each other, meeting in the centre and creating an area of comparable heat transfer, Figure 6.1d. This area got bigger as the upstream end isotherm moved towards the leading edge and the downstream end moved towards the rear tube, Figure 6.1e. This area changed through the colour spectrum leaving one reasonably wide isotherm between the front tube rows. As the heat flux input was increased further this isotherm moved towards the leading edge getting thinner indicating increasing heat transfer with increasing temperature gradient, Figure 6.1f.

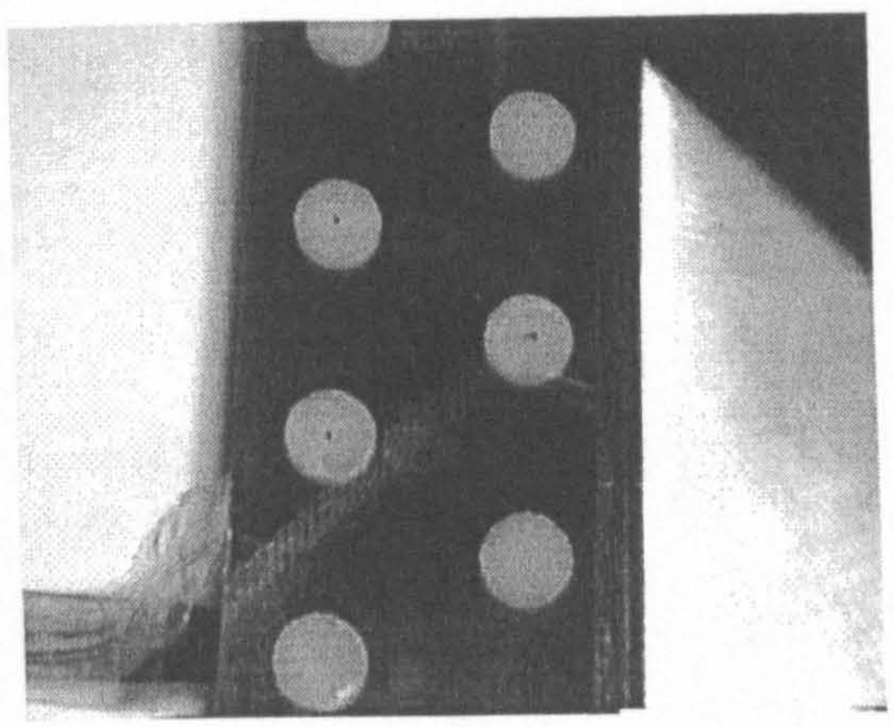

a: $\dot{q}$ = 455.3 W/m^2

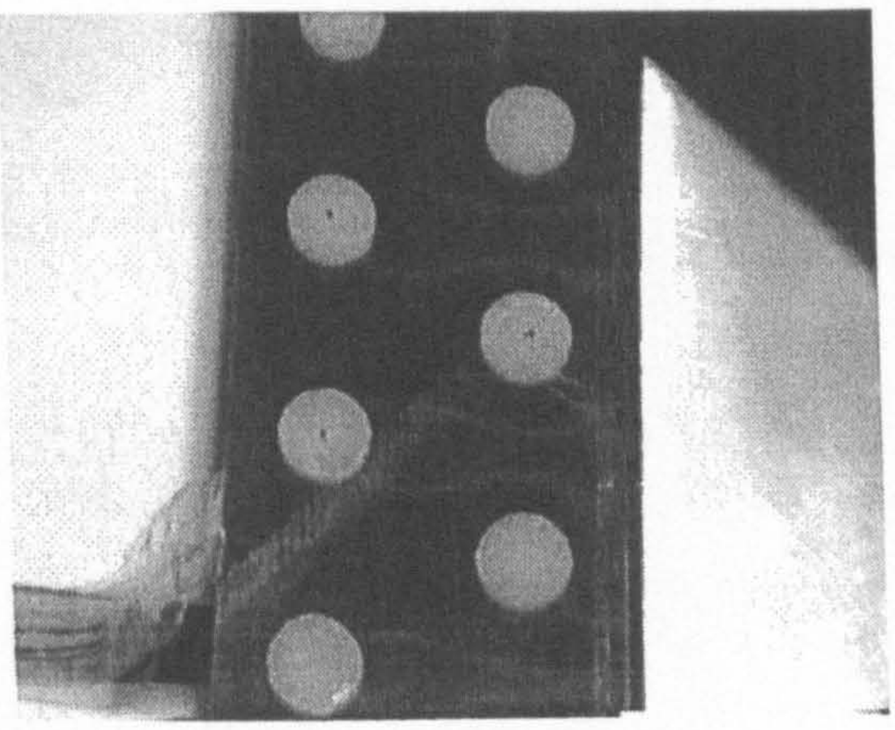

b: $\dot{q}$ = 508.0 W/m^2

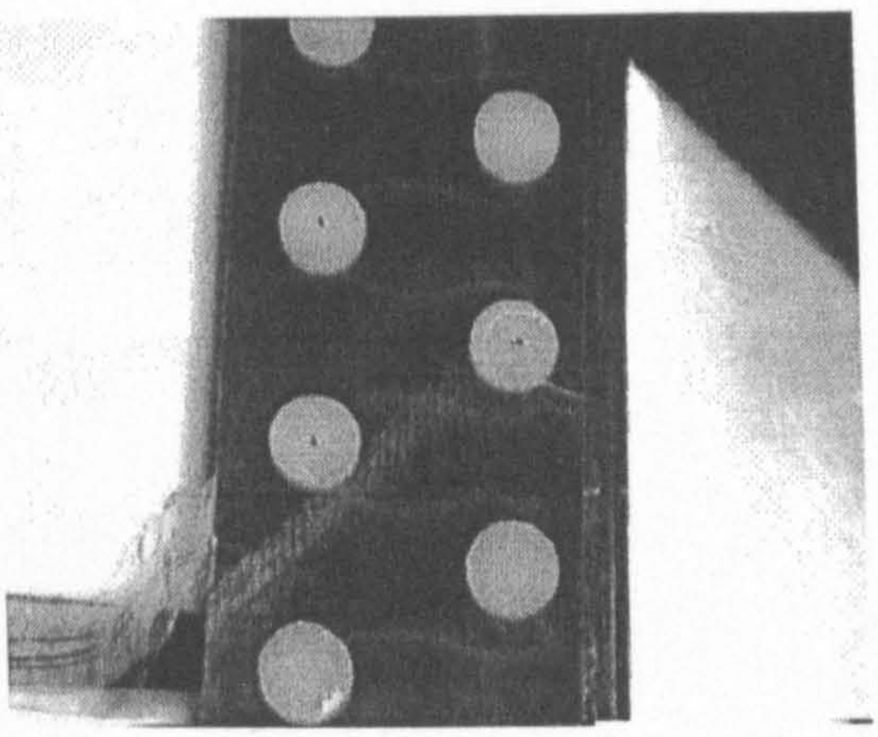

c: $\dot{q}$ = 565.8 W/m^2

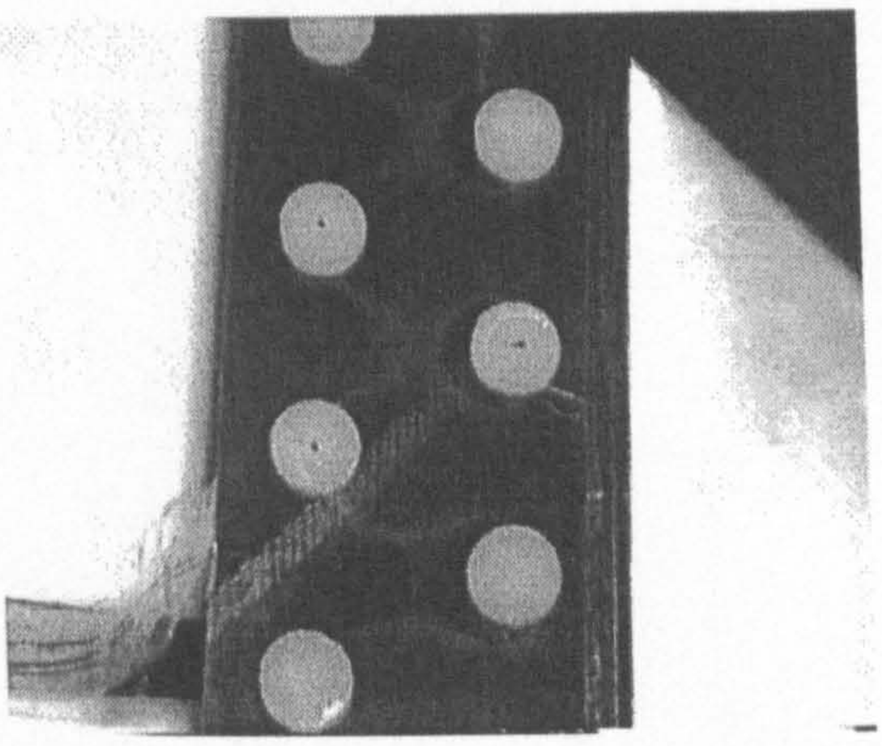

d: $\dot{q}$ = 605.4 W/m^2

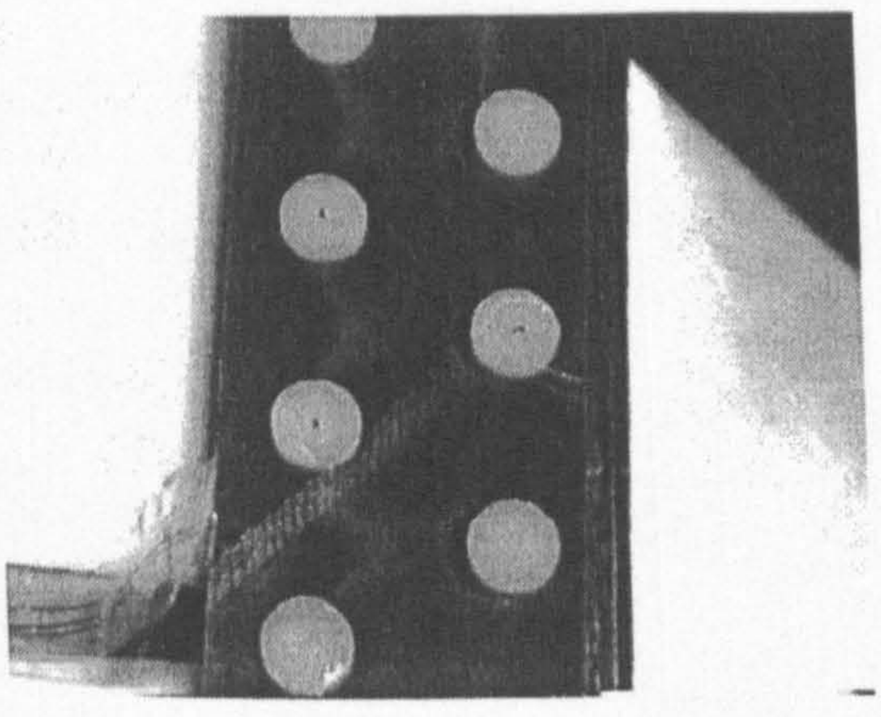

e: $\dot{q}$ = 680.8 W/m^2

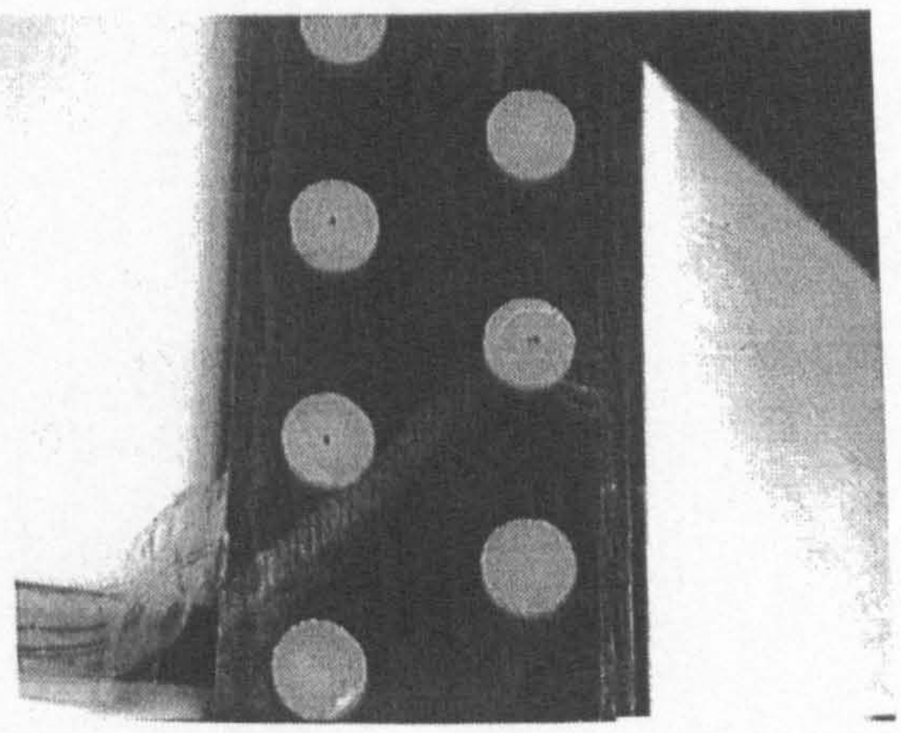

f: $\dot{q}$ = 958.4 W/m^2

Figure 6.1: Isotherm position for increasing heat flux input

A 3-D view showing the local heat transfer coefficient is shown in Figure 6.2. The

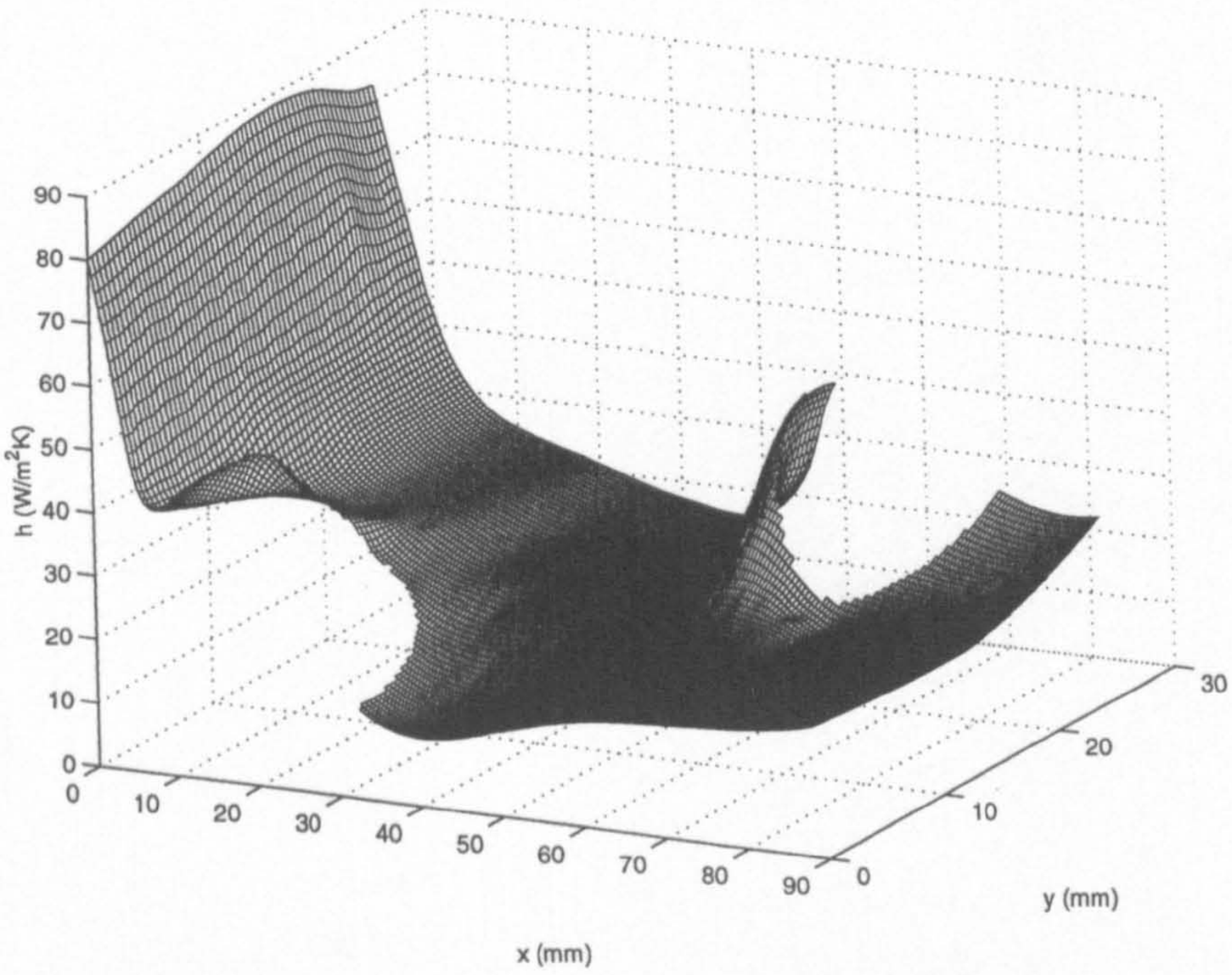

Figure 6.2: Local heat transfer coefficients for the staggered tube heat exchanger section for Re = 263

major features to be noted from this plot are: entry flow with developing boundary layers near the entrance resulting in decreasing heat transfer coefficient, horseshoe vortices in front of and on both sides of the tube resulting in increased heat transfer and flow separation with a 'dead water zone' behind the tubes resulting in low heat transfer. For a Reynolds number of 263, the average heat transfer coefficient was 26.6 W/m^2K with a pressure drop of 4.2 Pa through the test section.

6.1.2 Numerical results

The numerically predicted heat transfer coefficients for the staggered tube heat exchanger section are presented in Figures 6.3 and 6.4 along with the experimental

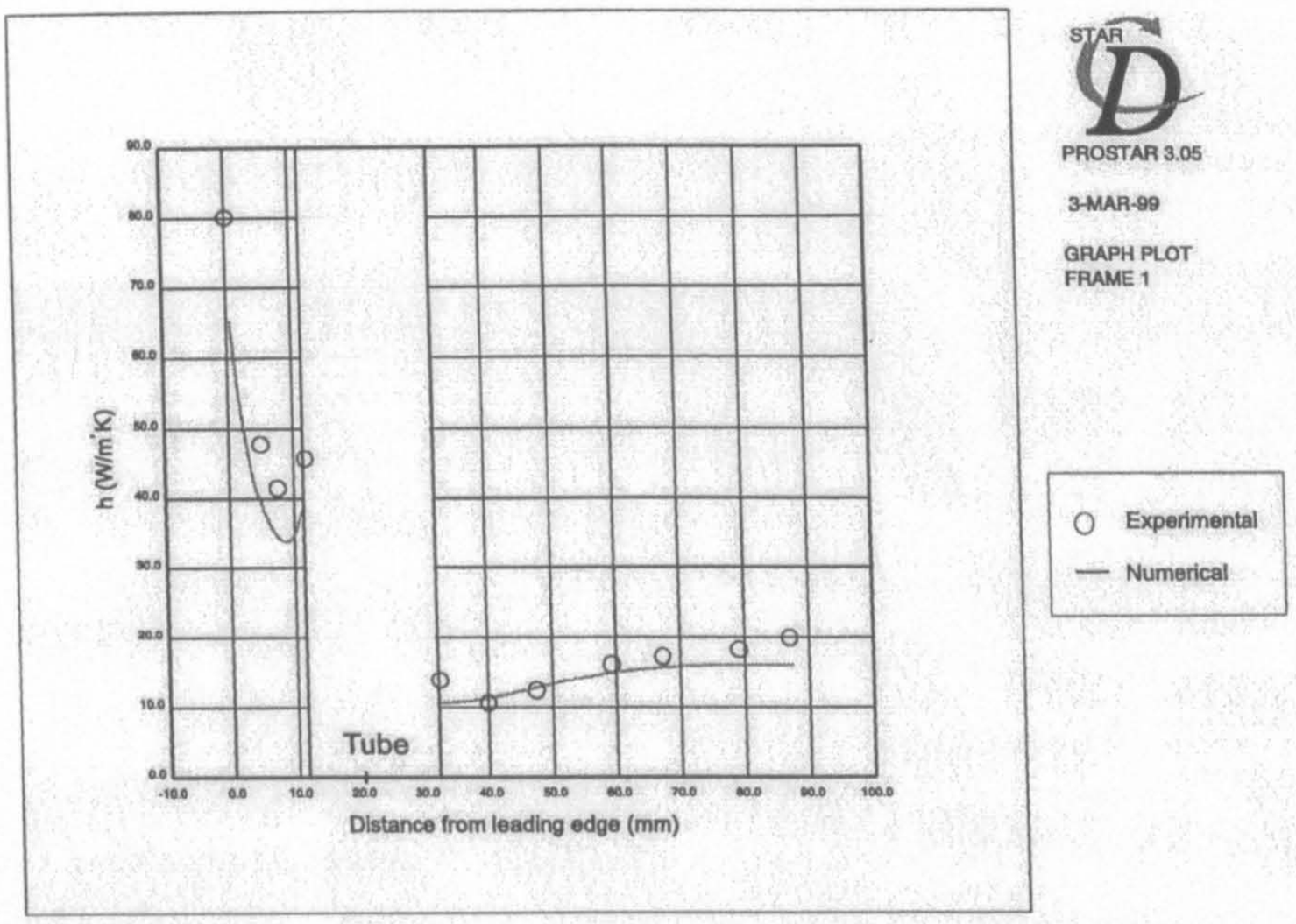

Figure 6.3: Comparison of experimental and numerically predicted heat transfer coefficients for the staggered tube heat exchanger section, taken through the upstream tube

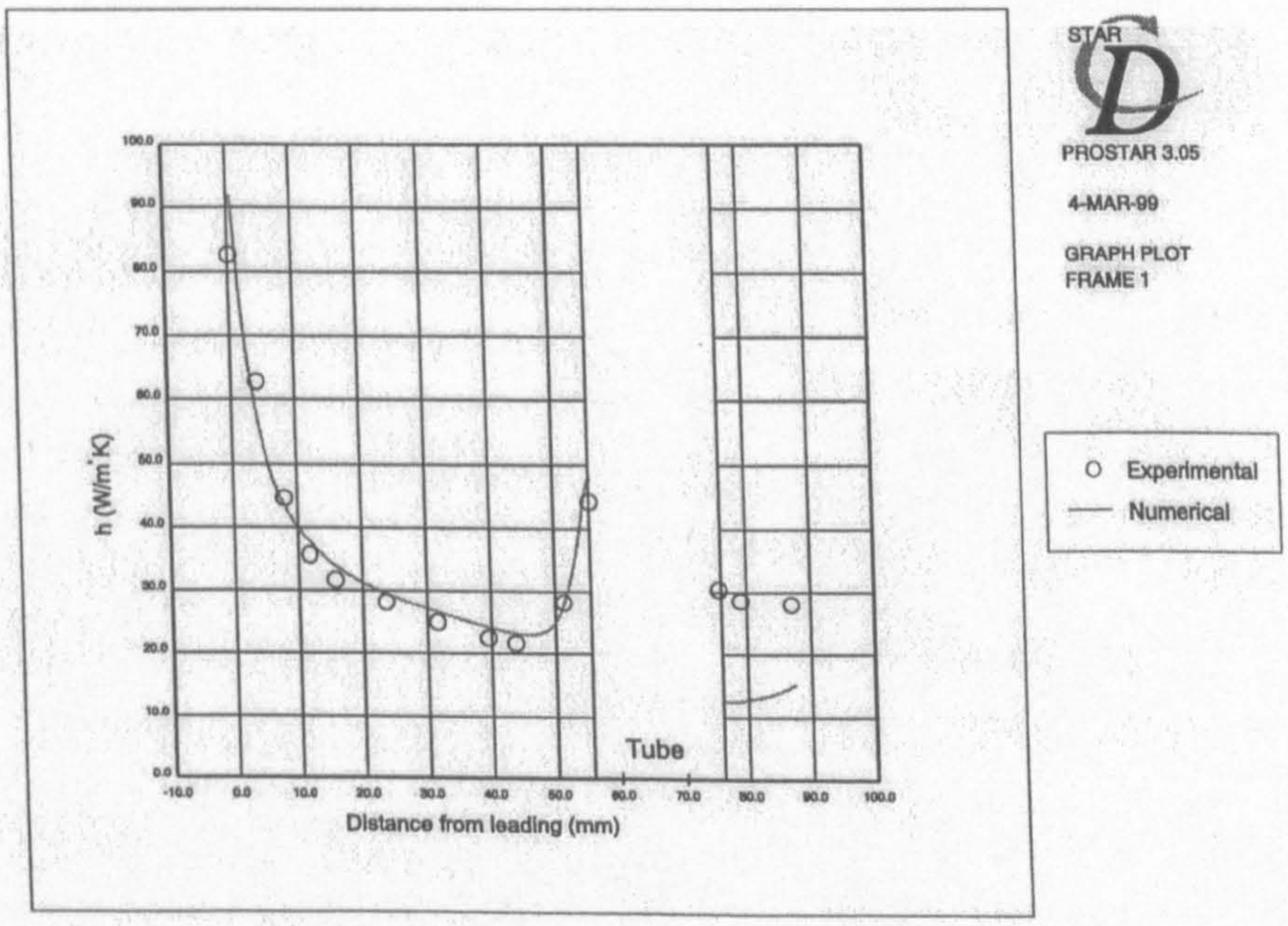

Figure 6.4: Comparison of the experimental and numerically predicted heat transfer coefficients for the staggered tube heat exchanger section, taken through the the downstream tube

data. These plots are section slices through the centre lines of the tube on each side of the test section. From these two plots the major flow features mentioned above can be seen to have been predicted reasonably accurately. The heat transfer is high at the leading edge and reduces because of boundary layer development. Increases in the heat transfer can be seen in-front of the tubes and low heat transfer can be seen behind the tubes.

The major discrepancies between the experimental and numerical results are the region in front of the first tube row and in the wake regions of both tubes. The numerical model offers a more diffuse flow field in-front of the first tube row that has resulted in an under-prediction of the horseshoe vortex strength. This could also be due to the inlet velocity profile not being known. In the wake region behind the first tube row the numerical model has predicted the lowest heat transfer coefficient directly behind the tube. In the experimental result the lowest heat transfer coefficient is measured in the centre of the wake region as would be expected. The application of symmetry boundary conditions on the sides of the domain has resulted in poor prediction of the velocity field directly next to the boundary from where the plot of heat transfer coefficient was taken. Moving away from the boundary the wake region has been predicted correctly. The large error between the experimental and numerical results behind the second tube row is due to lack of experimental data in this region. Unfortunately no isotherms were recorded in this area and the Matlab programme has interpolated to a higher value than if an isotherm had been recorded in this region. The numerical model slightly under-predicts the average

heat transfer coefficient at 24.7 W/m^2K and slightly over-predicts the pressure drop at 4.6 Pa.

From the numerical model, velocity vector plots show the reasons for the large increases in the heat transfer in the horseshoe vortex region and the reduced heat transfer in the wake region. At the interface between the tube and the fin a horseshoe vortex systems forms by the interaction between the crossflow over the tubes and the boundary layer. A horseshoe vortex is caused by the difference in static pressure as it approaches the stagnation point on the tube. The higher static pressure in the stagnation region, due to the higher velocity in the centre of the channel stagnating between the fins, is transmitted through the boundary layer and reverses the flow near the fin. This is shown in figure 6.5, where two horseshoe vortices can be seen to have formed on the top and bottom of the channel. Rotational motion is formed by the combination of the flow moving towards the tube and backwards along the fin. The increase in the heat transfer in the regions where the horseshoe vortices sit is due to a combination of increased velocity of the fluid particles and the increase in local shear rates due to the rapid movement of the fluid from the centre of the passage between the fins.

It is noticeable from Figure 6.4 is the comparably larger effect in the increase of heat transfer played by the horseshoe vortex sitting in-front of the second row tubes. The flow approaching the second row tubes is higher than approaching the first row tubes because of the channelling effect of the first tube-row. This leads to stronger horse-

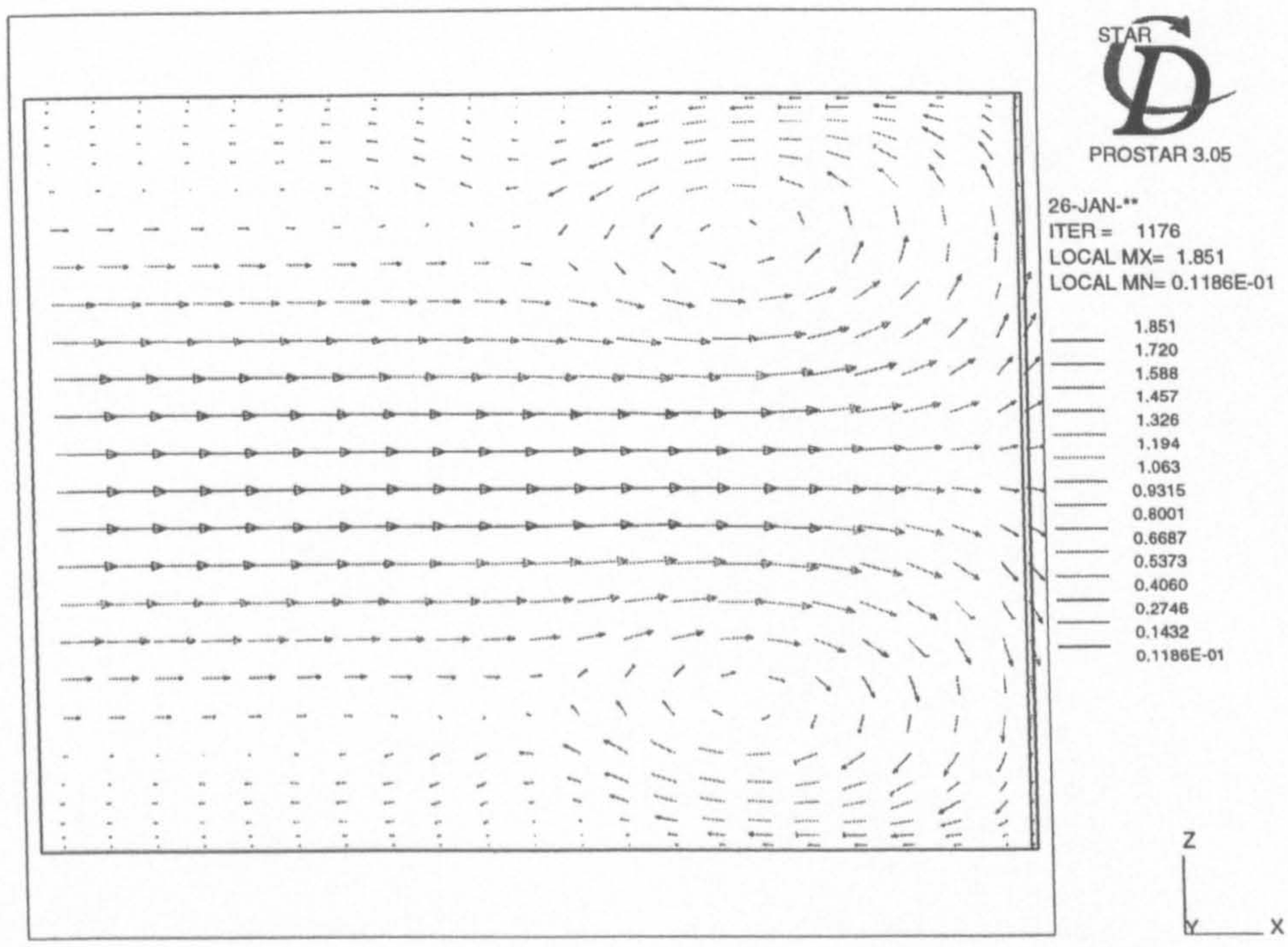

Figure 6.5: Horseshoe vortex system forming on the top and bottom of the fin in-front of the tube

shoe vortices being formed and the possibility of further smaller horseshoe vortices being formed in-front of the tubes, Baker (1979). Saboya and Sparrow (1974) who used the napthalene mass transfer technique to evaluate local heat transfer coefficients reported that the increase in heat transfer in-front of the second row tubes increased with Reynolds number and could eventually have a higher heat transfer coefficient than the leading edge.

The low heat transfer coefficients seen behind the tubes is due to the flow separation of the fluid around the tube. This occurs shortly after 90°. Due to viscous forces present between the free stream and the wake region a slow moving steady vortex is caused. The fluid velocities are very low in this region resulting in poor heat

transfer. The wake region behind the second row tubes extends further downstream than the trailing edge of the test section. This allows fluid to be entrained back into the test section, resulting in a smaller recirculation and thus slightly improved heat transfer. This effect was also noted by Romero-Mendez et al. (2000). Also note the the second row of tubes compresses the wake of the first tube-row before it expands towards the trailing edge.

6.1.3 Experimental results at different flow velocities

The second of the staggered tube heat exchanger cores which had a larger tube diameter (32 mm) and a larger transverse pitch (32 mm) was experimentally tested at three different flow velocities, $u = 0.25$, 1.25 and 2.5 m/s. These flow velocities corresponded to Reynolds numbers of 65, 326, 653 based on channel height. A numerical model was also tested at Re = 326.

The increase in average heat transfer coefficient and pressure drop over this range is shown in figure 6.6. The increase in the average heat transfer coefficient over the Reynolds number range investigated is non-linear. This non-linear increase can be explained by Figures 6.7 and 6.8. These figures show the local heat transfer coefficient, at section slices through the centre lines of the tubes, at the Reynolds number range investigated. For the lowest Reynolds number the majority of heat transfer takes place in the leading edge region where the boundary layer is still thin. As the Reynolds number is increased more heat is transferred in the horseshoe vortex region around the second row tube. This shows the importance of

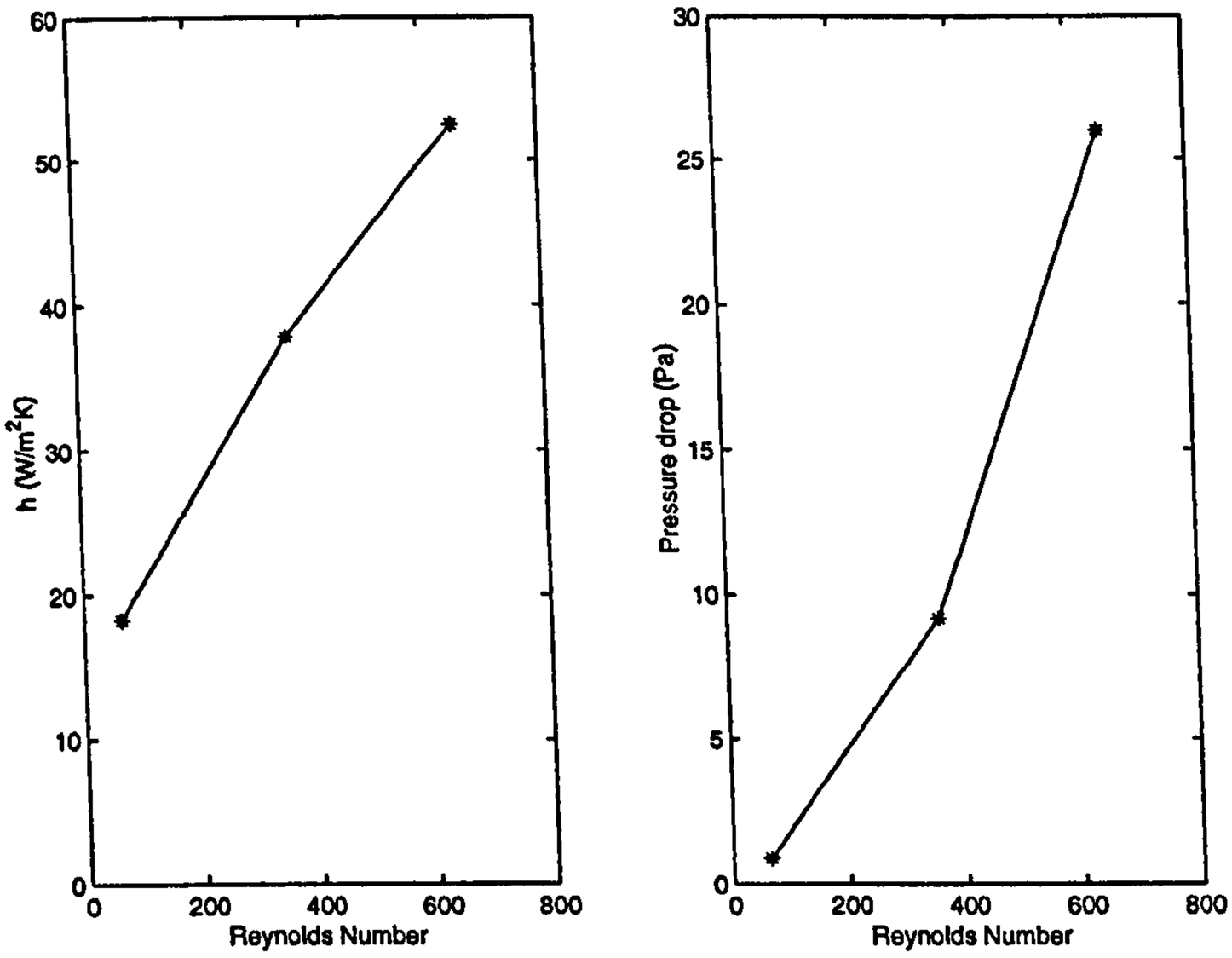

Figure 6.6: Average heat transfer coefficient and pressure increase with Reynolds number

the horseshoe vortices in increasing heat transfer. According to Saboya and Sparrow (1974) at a Reynolds number of 1089 (based on hydraulic diameter) there is nearly parity in the heat transfered between the upstream half and downstream half of the fin. The changing amounts of heat transfered from each half of the fin would explain the non-linearity in the increase of heat transfer coefficient.

In addition to the above points, it can also be seen from Figure 6.8 that the increase in the heat transfer coefficient in-front of the second tube-row, for Reynolds numbers above 300, are bigger than the increase seen in Figure 6.4 at a slightly lower Reynolds number. The stagnation point in-front of the second tube-row is also further upstream. Although these increases can be directly attributed to the increased velocity, inspection of the numerically predicted velocity vector plots show that a

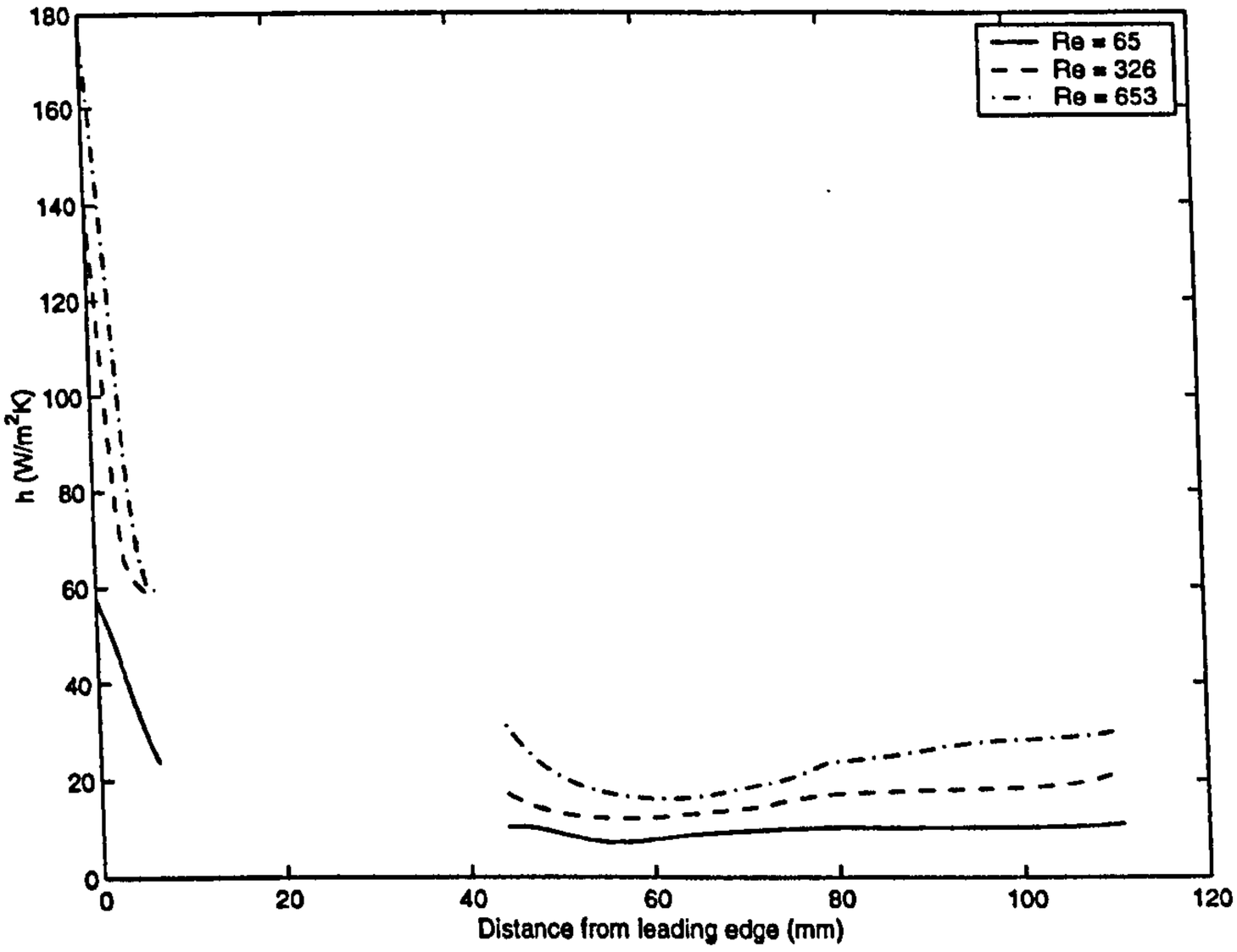

Figure 6.7: Section slice of experimentally measured heat transfer coefficient for different Reynolds numbers, taken through the upstream tube

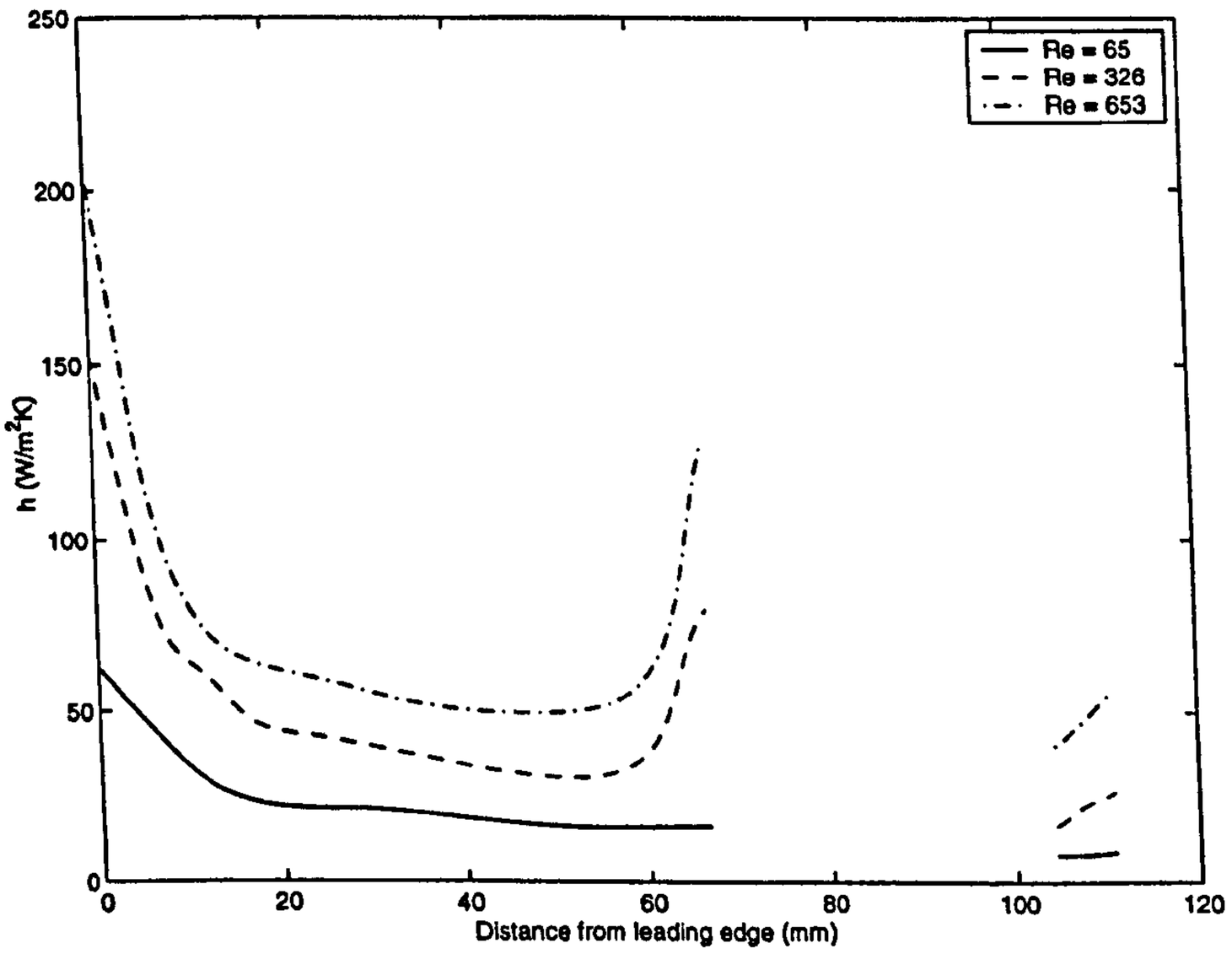

Figure 6.8: Section slice of experimentally measured heat transfer coefficient for different Reynolds numbers, taken through the downstream tube

double horse vortex has formed, Figure 6.9. Secondary horseshoe vortices can

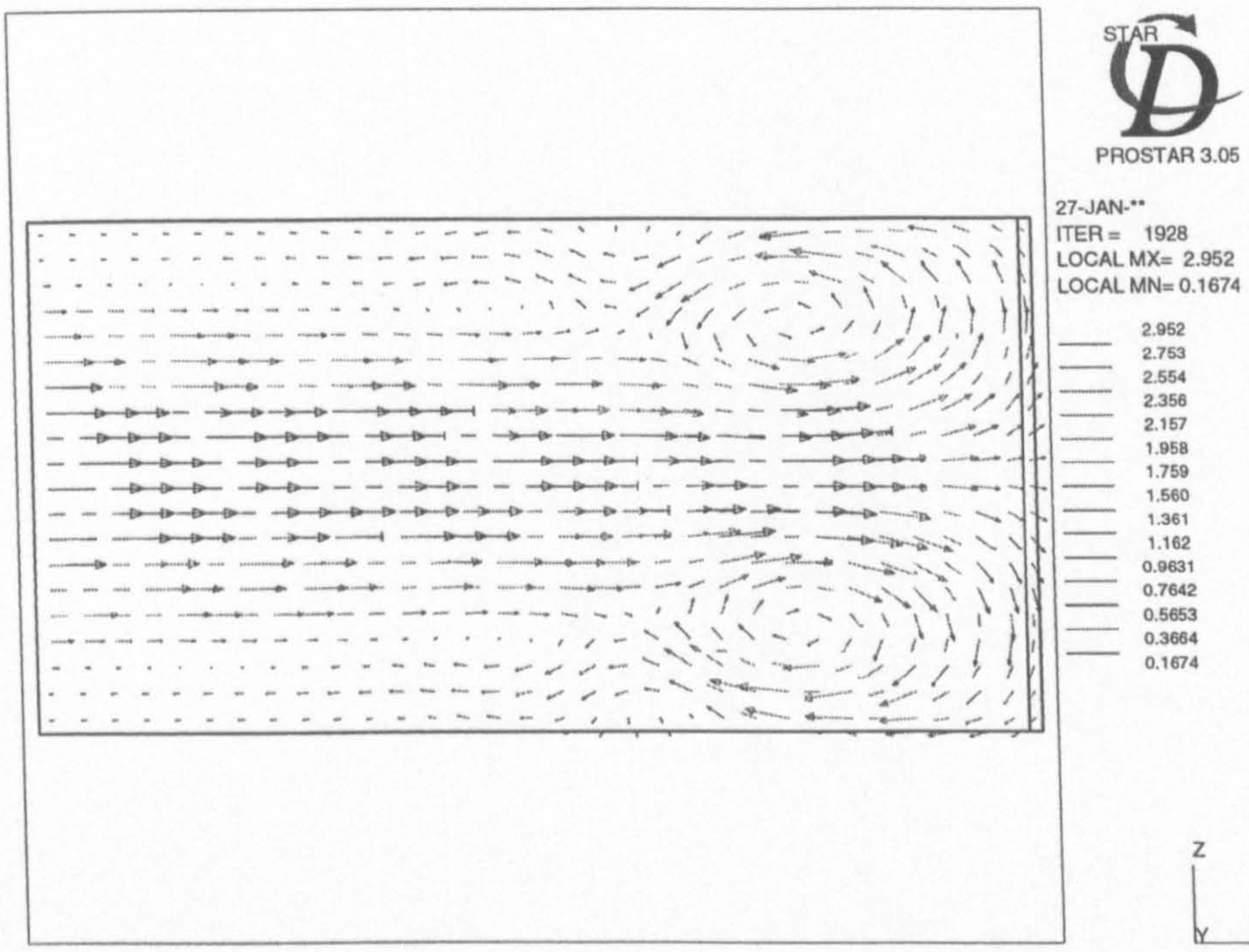

Figure 6.9: Double horseshoe vortex system forming on the top and bottom of the fin in-front of the tube

form upstream of a major horseshoe vortex as the first vortex appears effectively to be a solid body. Baldwin (1989) noted that complex horseshoe vortex systems could form around the second tube-row with many smaller upstream horseshoe vortices, as the Reynolds number and thus flow velocity was increased.

The comparison between the experimentally measured and numerically predicted heat transfer coefficients is shown in Figures 6.10 and 6.11 It is noticeable that for this geometry the discrepancies between the two sets of data are similar to those in Figures 6.3 and 6.4 which had a smaller tube size and transverse pitch. The numerical model under-predicts the average heat transfer coefficient by 21.9% at

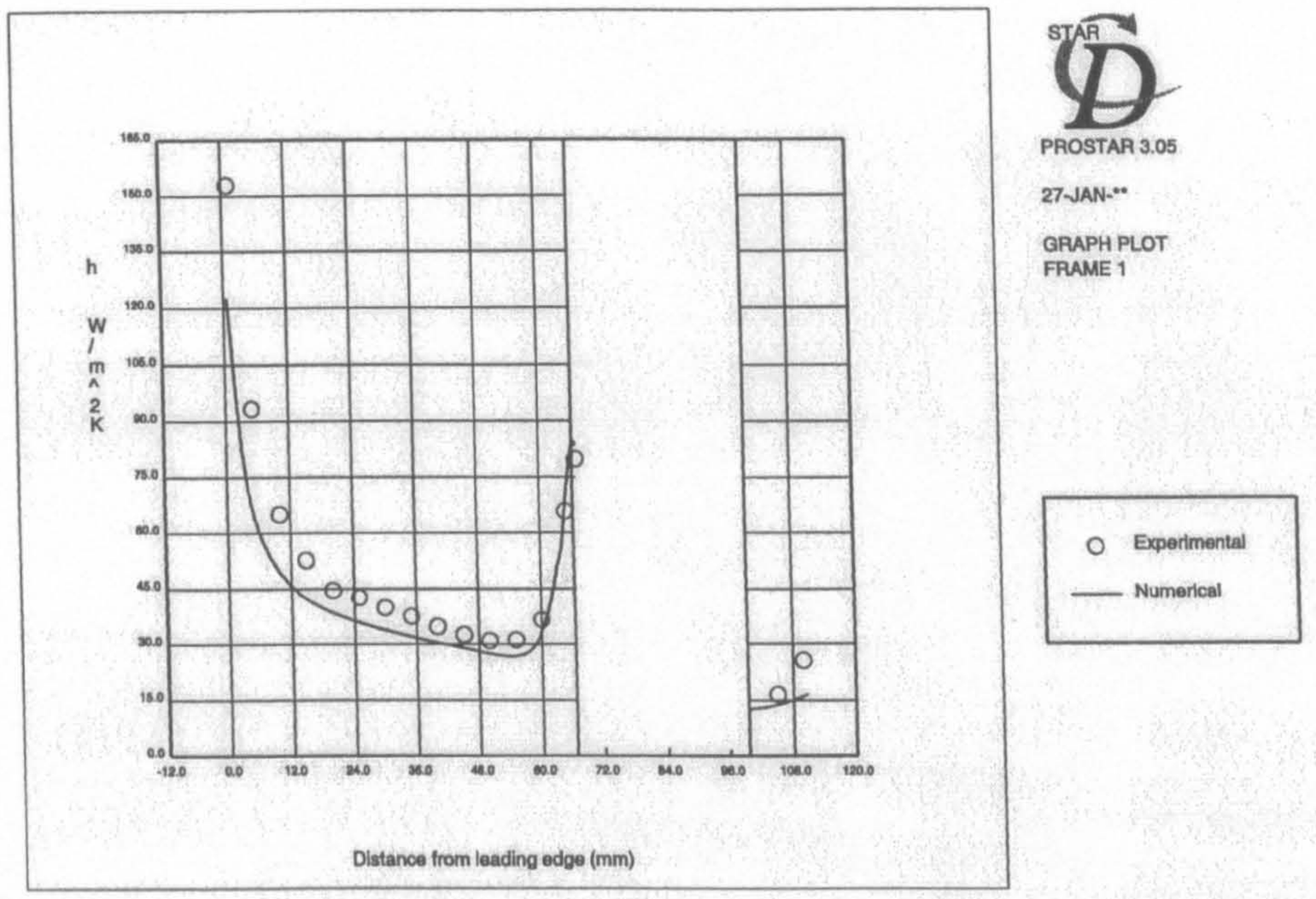

Figure 6.10: Comparison of experimental and numerically predicted heat transfer coefficients for the staggered tube heat exchanger section, taken through the downstream tube

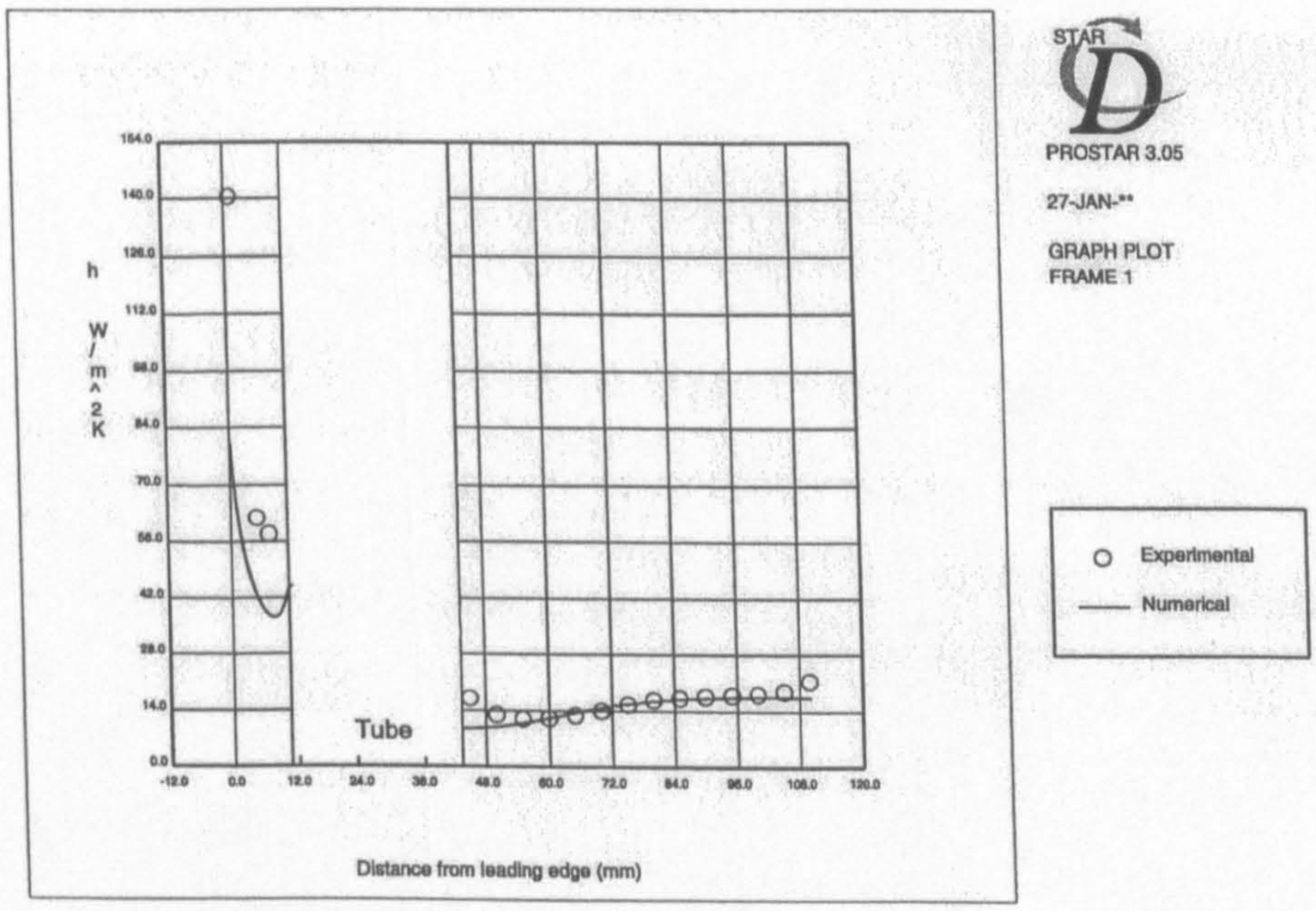

Figure 6.11: Comparison of the experimental and numerically predicted heat transfer coefficients for the staggered tube heat exchanger section, taken through the upstream tube

28.9 W/m^{2}K. This under-prediction arises because the numerical model predicts the isotherm position closer to the leading edge when compared to the experimental results, see Figure 4.18. This effect also shows in Figure 6.10 where in the leading edge region the local heat transfer coefficients are lower than the experimental values. Also noticeable from Figure 6.11 is the lack of a horseshoe vortex region in-front of the first tube-row from the measured local heat transfer coefficients. This is possibly due to some form of destruction of the boundary layer in the experimental case. As Fisher and Eibeck (1990) reported the horseshoe vortex size is dependent on the boundary layer thickness. The smaller the boundary layer thickness, the smaller the resulting horseshoe vortex will be. The numerical model over-predicted the pressure drop through the heat exchanger core by 25.3% at 12.2 Pa. It would be expected that the experimental model would give a higher pressure drop value due the fins not being perfectly aligned and other manufacturing inaccuracies.

6.2 In-line heat exchanger sections

6.2.1 Experimental results

The isotherm positions for various increasing heat flux levels is shown in Figure 6.12. The first change of the liquid crystal colour is behind the first tube-row, Figure 6.12a, in a nearly square shape. As the heat flux level increases the isotherms grow in length, until they reach the back of the first tube-row in the upstream direction and the front of the second tube-row in the downstream direction. As this is happening the liquid crystals also change colour behind the second tube-row, Figure 6.12b.

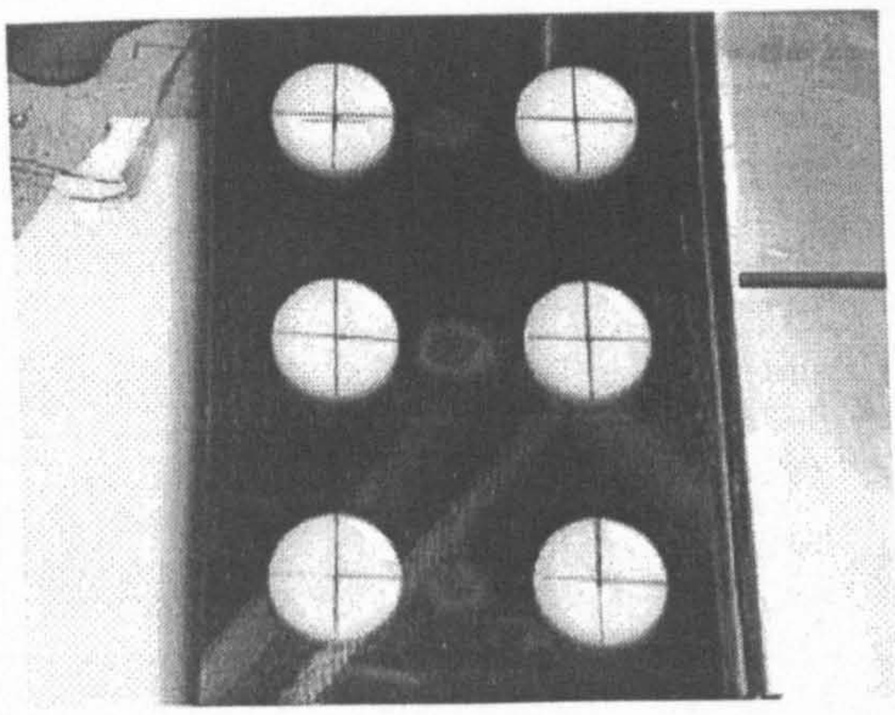

a: $\dot{q}$ = 247.0 W/m^2

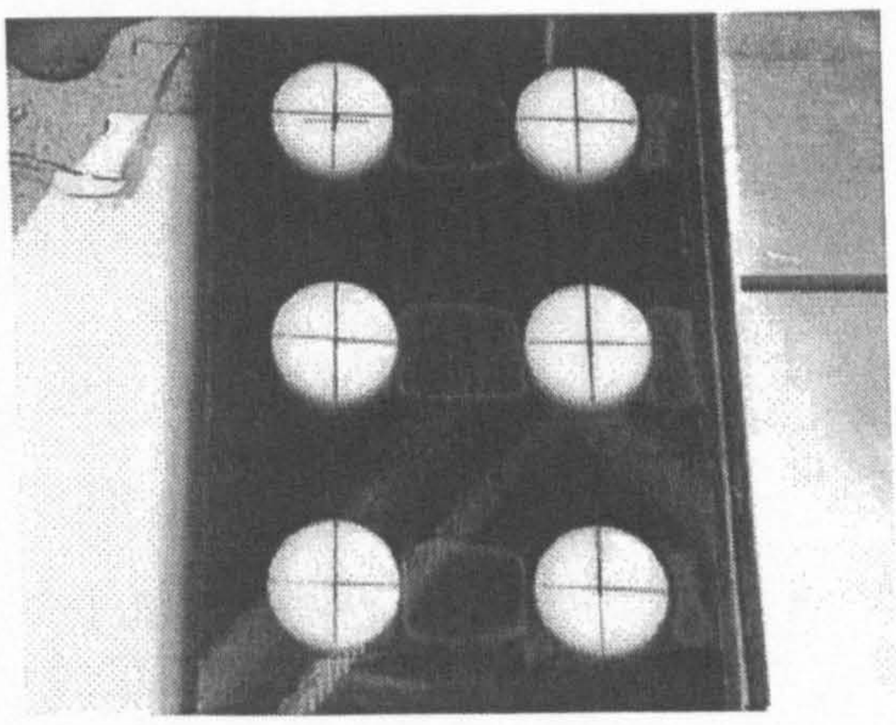

b: $\dot{q}$ = 305.0 W/m^2

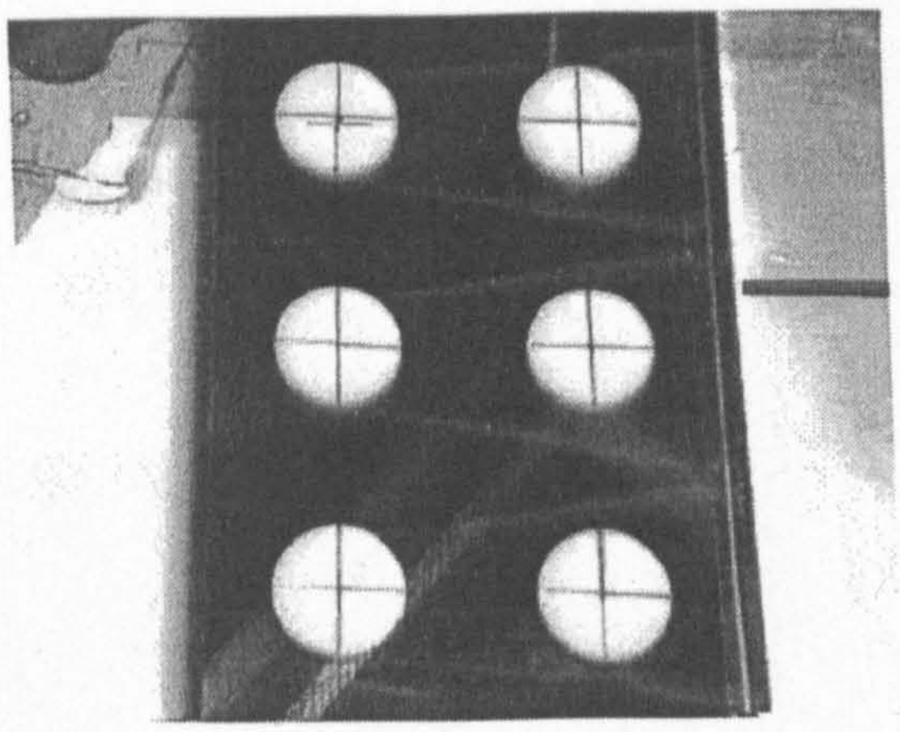

c: $\dot{q}$ = 479.9 W/m^2

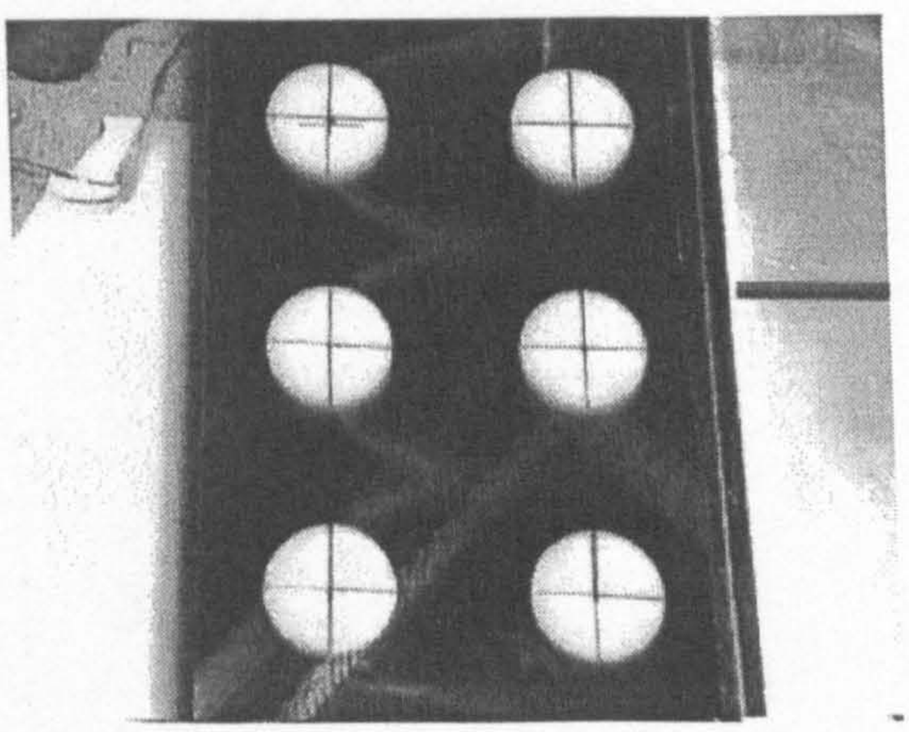

d: $\dot{q}$ = 592.2 W/m^2

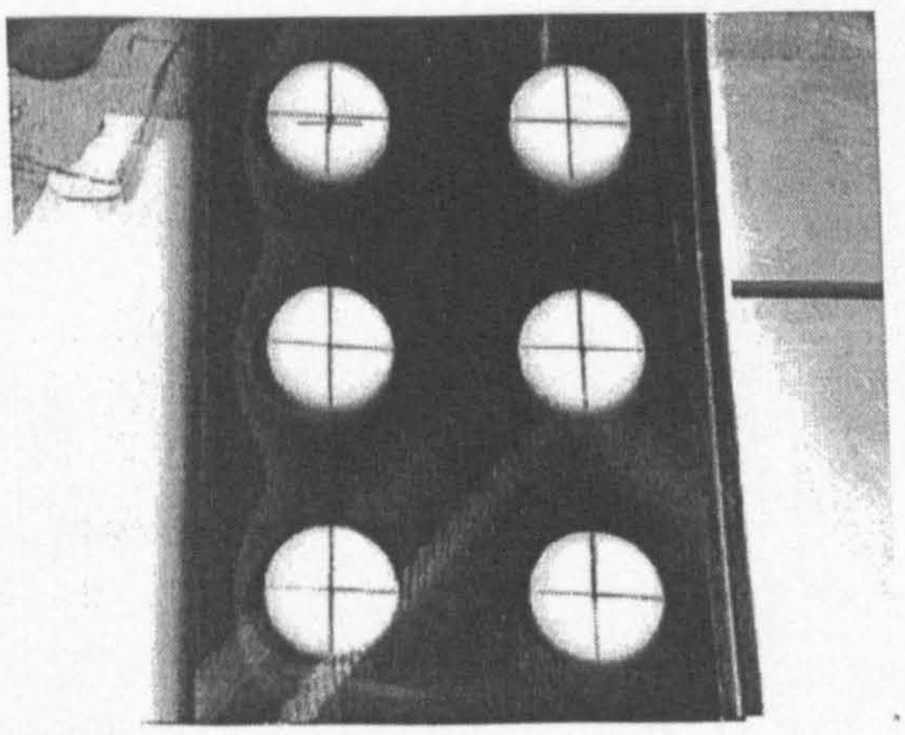

e: $\dot{q}$ = 768.2 W/m^2

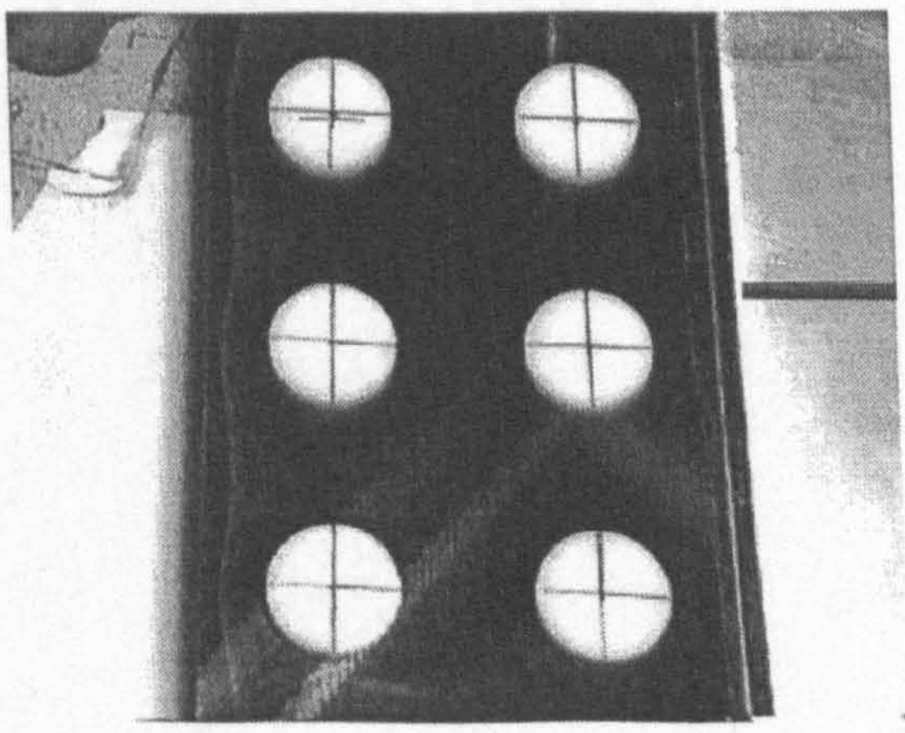

f: $\dot{q}$ = 988.5 W/m^2

Figure 6.12: Isotherm positions for various increasing heat flux input levels

The isotherms continue to get wider behind the first and second tube-rows until they meet at the trailing edge, Figure 6.12c, leaving a V-shape of unchanged colour where the flow velocity is highest. This V-shape is reduced in size and length as the heat flux is increased, Figure 6.12d. As the liquid crystal isotherms move toward the leading edge, they move in-front of the first tube-row leaving an unchanged colour region in-front of the first tube-row where the horseshoe vortex sits, Figure 6.12e. At the highest heat flux levels the isotherms continue to move toward the leading edge and they get thinner, indicating higher heat transfer with increasing temperature gradient. The experimentally measured average heat transfer coefficient was 26 W/m^2K with a pressure drop through the test section of 7.42 Pa.

6.2.2 Numerical results

Comparisons between the experimentally measured local heat transfer coefficient and the numerically predicted values are shown in Figure 6.13 which is taken from a section slice through the centre line of the tubes and Figure 6.14 which is taken from a section slice half-way between the tubes. In common with the other comparisons the local heat transfer coefficient is under-predicted by the numerical model near the leading edge due to tangential conduction occurring in the experimental model. The wake region behind the first tube row is also poorly predicted due to the application of symmetry boundary conditions.

From Figure 6.13 it is seen that the horseshoe vortex region in-front of the second tube-row is non-existent due to the recirculation region behind the first tube-row.

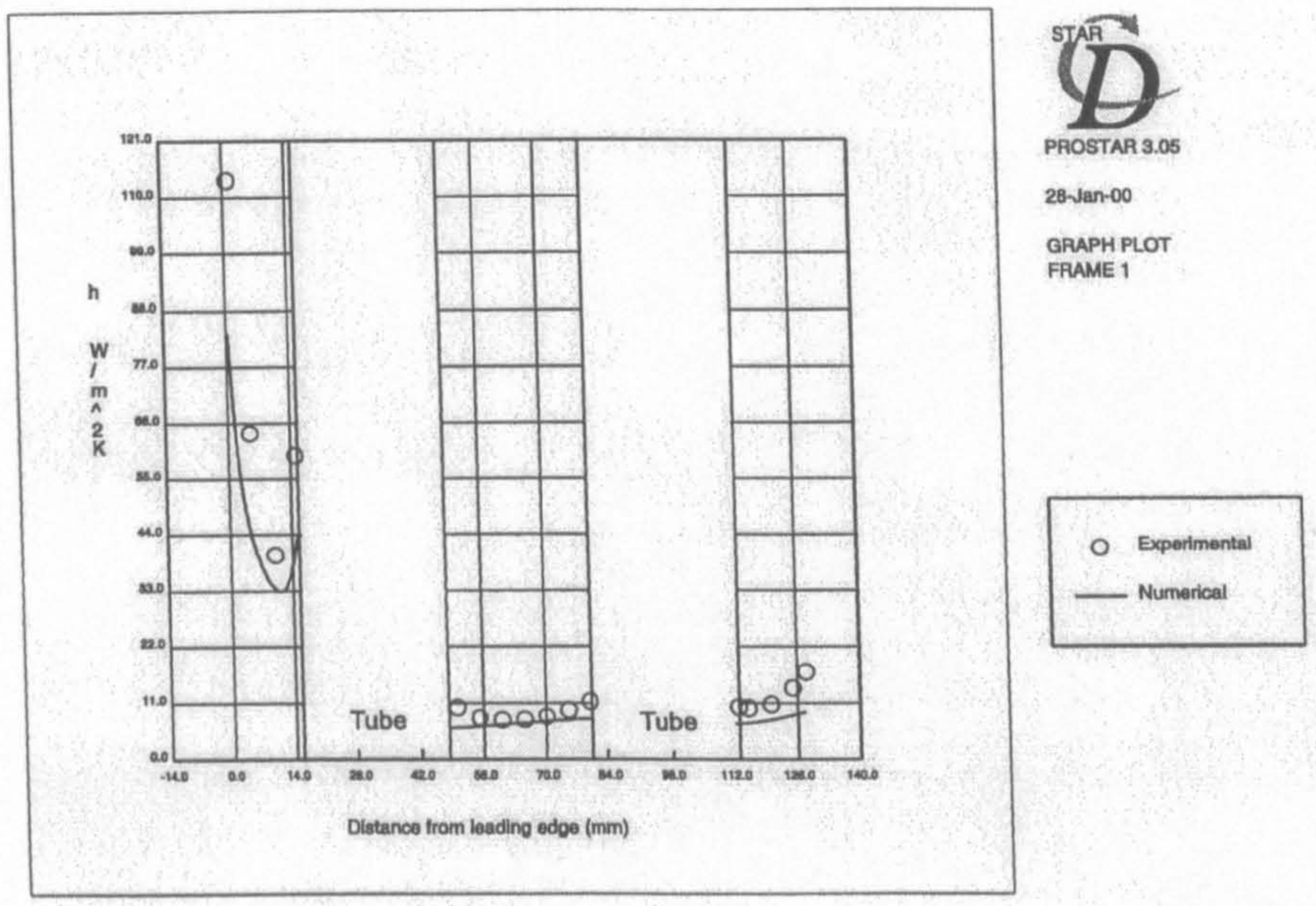

Figure 6.13: Comparison of experimental and numerically predicted heat transfer coefficients for the in-line tube heat exchanger section, taken through the tubes

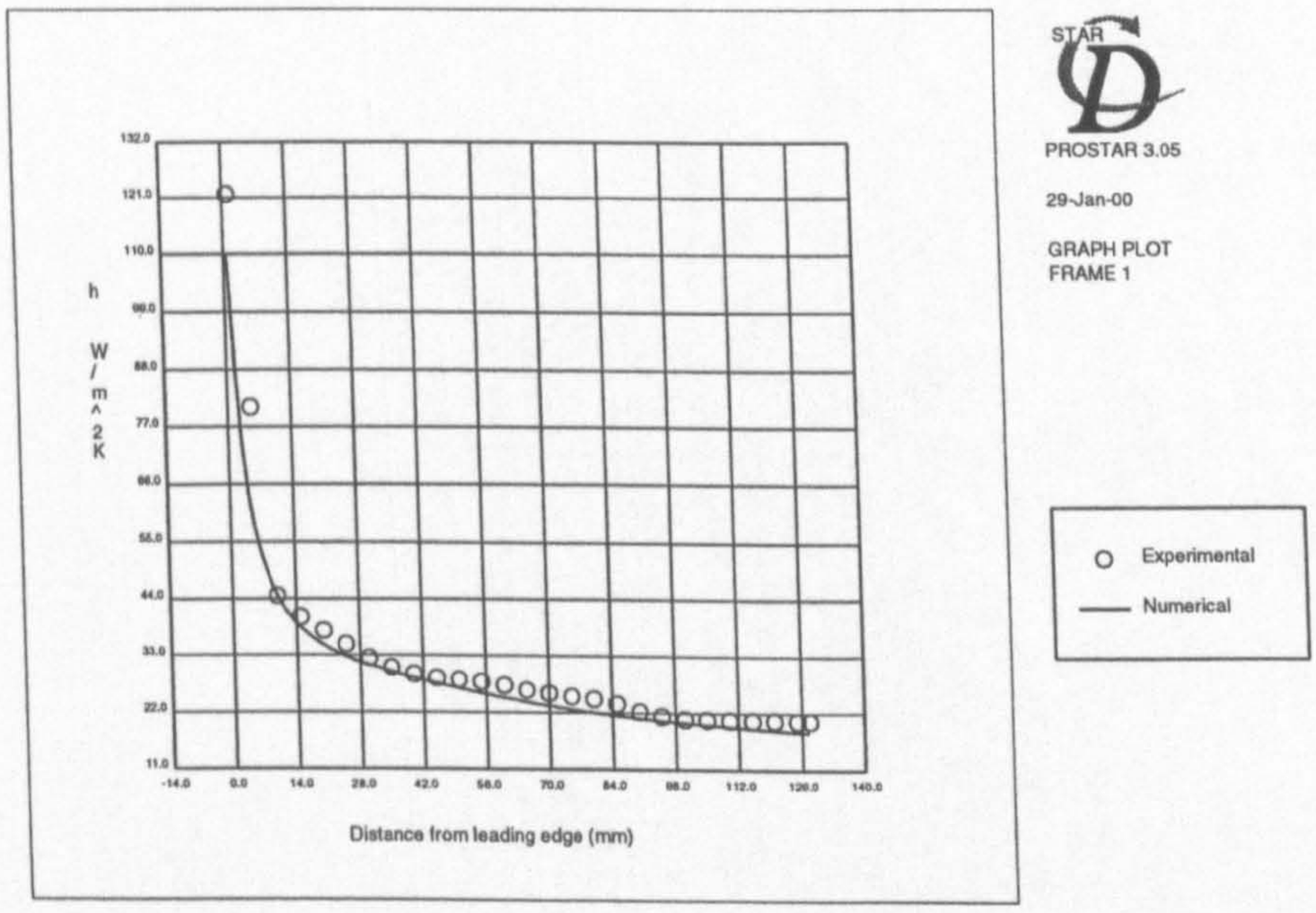

Figure 6.14: Comparison of the experimental and numerically predicted heat transfer coefficients for the in-line tube heat exchanger section, taken at a point midway between the tubes

The flow separates behind the first tube-row and re-attaches at the front of the second tube-row to form a closed recirculation region with low fluid velocities and thus low heat transfer coefficient. The tubes and the closed recirculation region causes a blockage effect that results in the main flow between the channels having a higher velocity and thus higher heat transfer coefficients. These higher values of heat transfer coefficient can be seen in Figure 6.14 which is taken at a point half-way between the tubes. The numerically predicted average heat transfer coefficient was 21.8 W/m^2K and the pressure drop 8.8 Pa.

6.2.3 Experimental results at different flow velocities

The in-line heat exchanger core was tested at three different Reynolds numbers, Re = 65, 326 and 653. The average heat transfer coefficient increase and pressure drop increase can be seen in Figure 6.15. As the Reynolds number is increased from 65 to 653 the average heat transfer coefficient increases from 14.3 W/m^2K to 35.7 W/m^2K. The pressure drop increases from 0.68 Pa to 19.7 Pa over the same range. From Figure 6.16 it can be seen that the increase in Reynolds number has a large effect on the size and strength of the horseshoe vortex that forms in front of the first tube-row. As the Reynolds number increases the stagnation point moves towards the leading edge indicating the formation of a larger horseshoe vortex. By the highest Reynolds number the heat transfer coefficient is almost equal to that attained at the leading edge.

It is interesting to note that with the increase in Reynolds number there is very

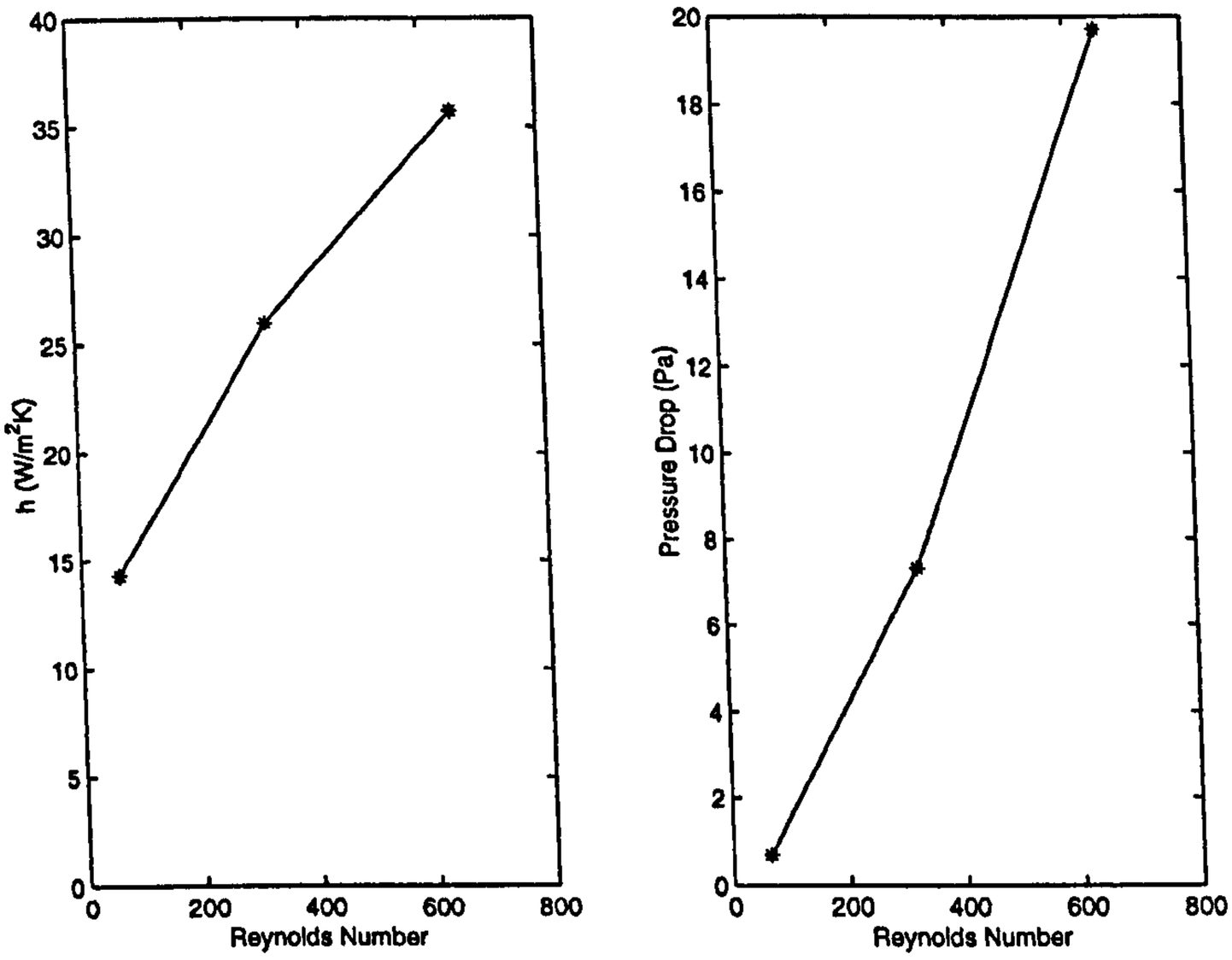

Figure 6.15: Average heat transfer coefficient and pressure drop increase with Reynolds number

little change in the heat transfer coefficient in the recirculation region behind the first tube-row. Although the strength of the recirculation eddy must increases due to the increase in fluid velocity in the channel between the tubes, it appears to have very little effect. The increase in the local heat transfer coefficient behind the second tube-row is more noticeable as the Reynolds number is increased. This can be expected as more fluid at a higher velocity is entrained back into the test section causing an increase in the local heat transfer coefficient.

Comparing the average heat transfer coefficients and pressure drop values for the in-line and staggered tube arrays it can be seen that the staggered tube heat exchanger gives a higher average heat transfer coefficient with a higher pressure drop over the Reynolds number range investigated. The higher values of pressure drop in the

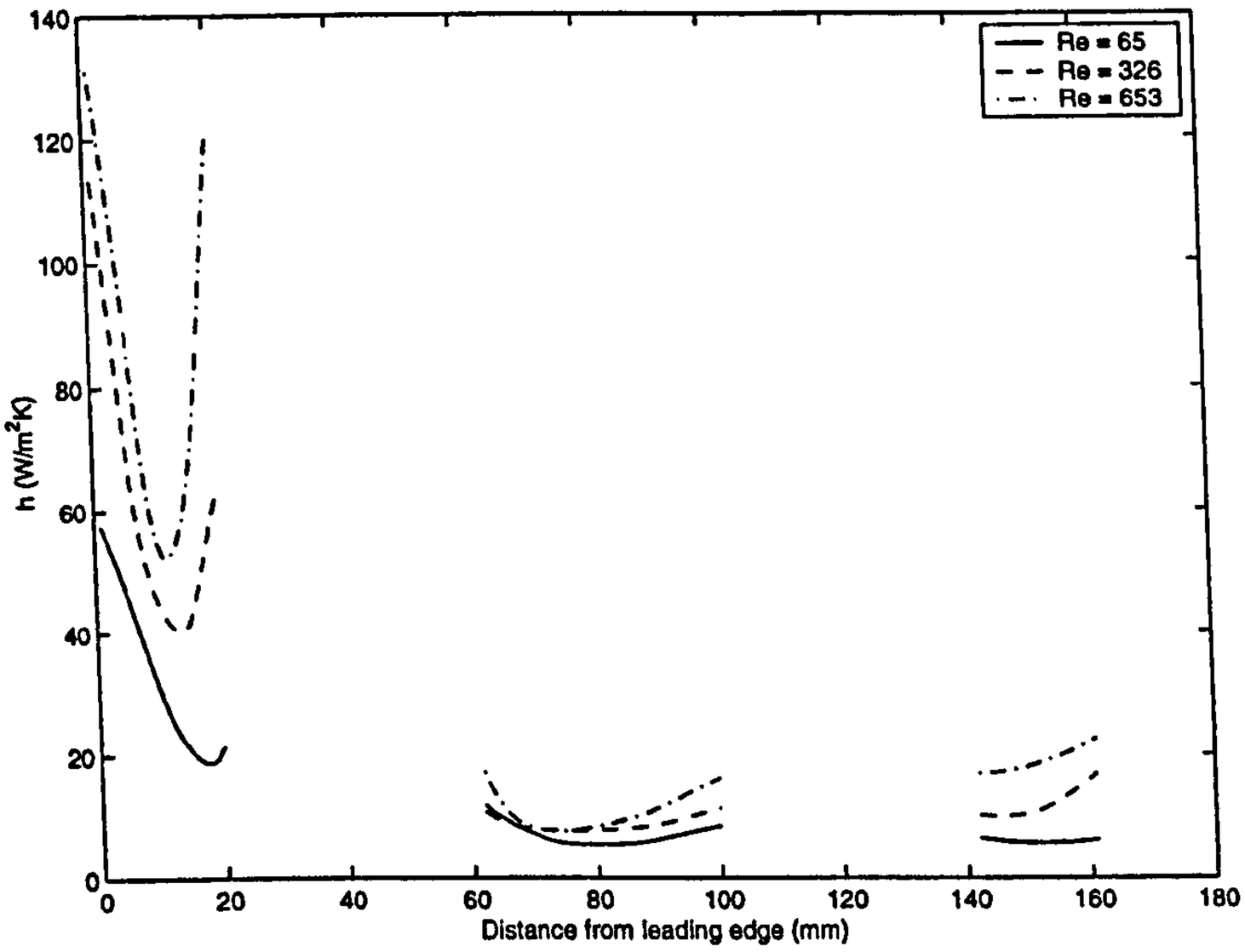

Figure 6.16: Section slice of experimentally measured heat transfer coefficient for different Reynolds numbers

staggered tube heat exchanger core occurs due the form drag of the tubes. In the case of the in-line heat exchanger section the form drag of the tubes is much lower as only the first tube-row is present to the fluid. The other tubes are hidden by the wake region of the first tube-row. However, in the staggered case the flow alters its flow direction to move around the tubes and thus repeatedly meets the blockage of the tubes in the downstream direction. This does however increase the heat transfer as the recirculation regions are smaller and horseshoe vortices formed in front of each tube. It should be noted here however, that the staggered and in-line tube arrays are not geometrically similar. Although they share a common tube diameter, and the transverse pitch for the in-line case is twice that for the staggered case, the tube pitch in the flow direction is not similar. This precludes direct comparisons between the two different types of heat exchanger sections.

6.3 Staggered tubes with vortex generators

6.3.1 Experimental results

Liquid crystal isotherm positions for various increasing heat flux input levels are shown in Figure 6.17. At low heat flux inputs, Figure 6.17a, the isotherm shapes are similar to those without vortex generators. However, as the heat flux input is increased, Figures 6.17b and 6.17c, it is noticeable that the vortex generators pinch the wake region behind the first tube-row. By a heat flux input of 432.0 W/m^2, the area downstream of the vortex generator has not yet changed colour. The area upstream, particularly in the area between the vortex generators where the fluid has reached the stagnation point in-front of the second tube-row, the liquid crystals have already changed colour. Figure 6.17d can be compared to Figure 6.1d, which is a similar isotherm position without vortex generators on the fin. The increase in unchanged colour, and thus improved heat transfer coefficient can be clearly seen. With increasing heat flux levels, the isotherms move round the back of the vortex generator and move towards the second tube-row, leaving the horseshoe vortex region and the wake region of the vortex generators unchanged in colour. As the heat flux is increased further, the isotherms continue to move towards the second tube-row, and toward the leading edge, Figure 6.17e, leaving a small bubble of unchanged colour in-front of the vortex generator. This area is due to the formation of corner vortices on the vortex generator. By the highest heat flux level, the isotherms continue to move towards the leading edge and towards the second tube-row. The measured average heat transfer coefficient was found to be 39.1 W/m^2K for a Reynolds number of 326, with a pressure drop through the core

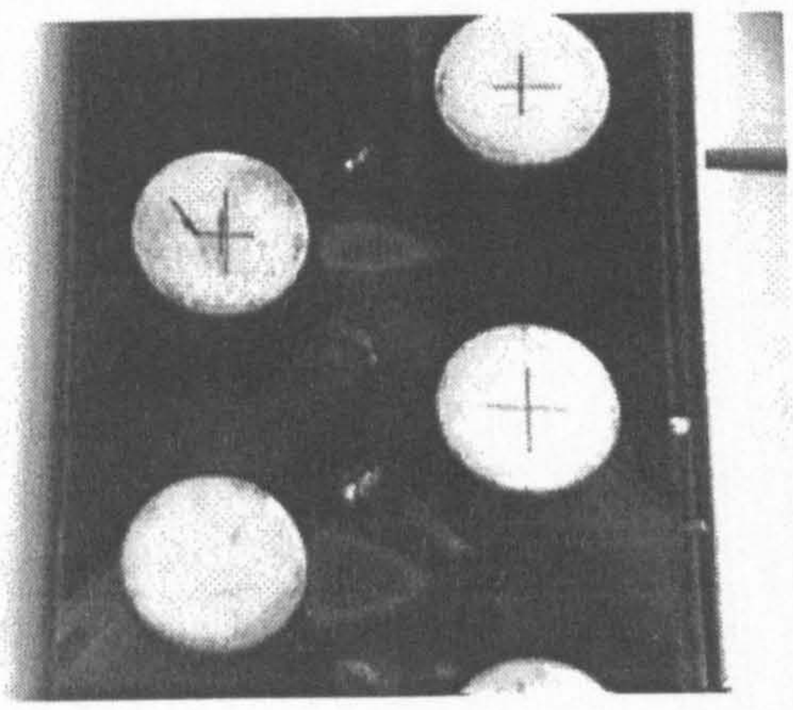

a: $\dot{q}$ = 279.3 W/m^2

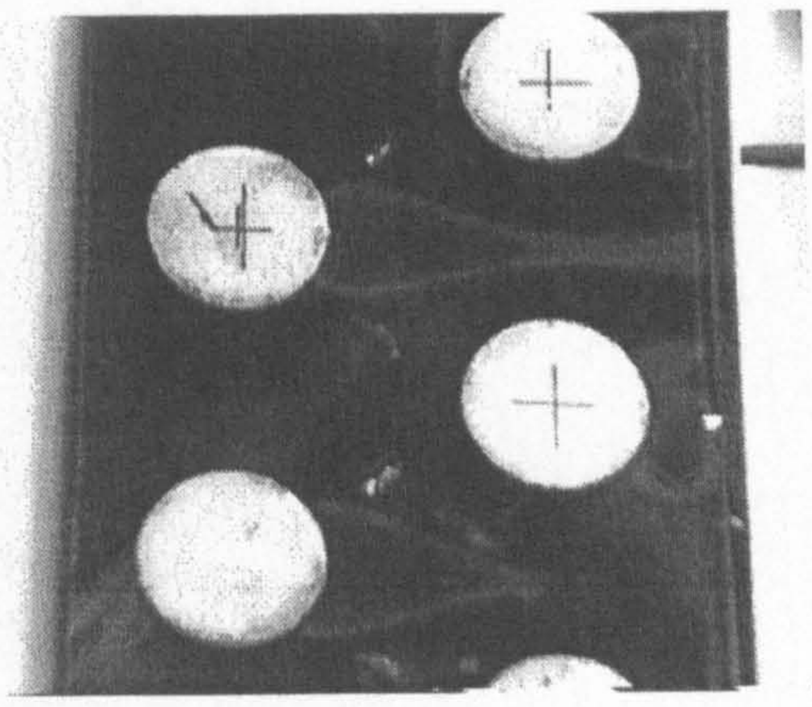

b: $\dot{q}$ = 321.3 W/m^2

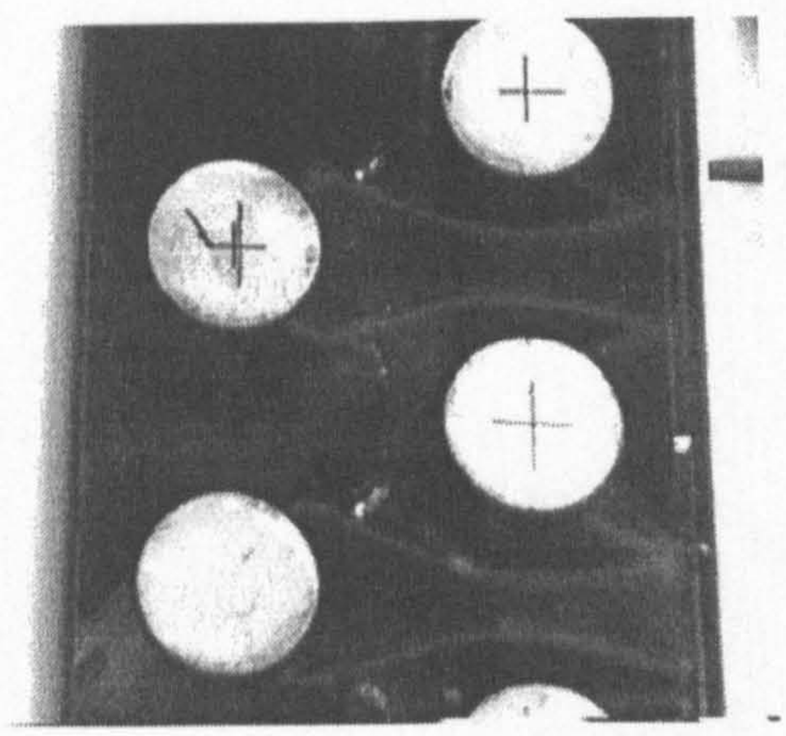

c: $\dot{q}$ = 386.6 W/m^2

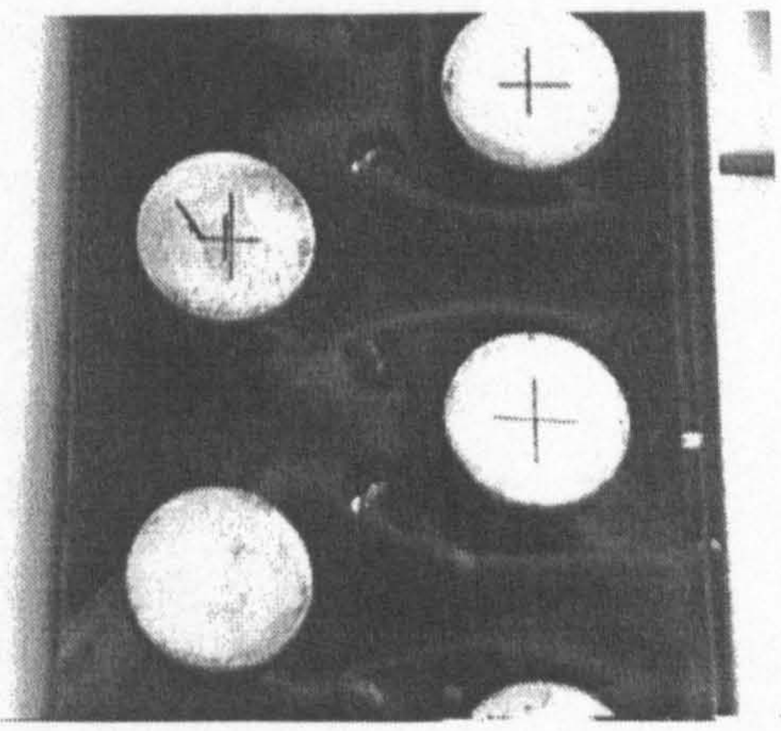

d: $\dot{q}$ = 432.0 W/m^2

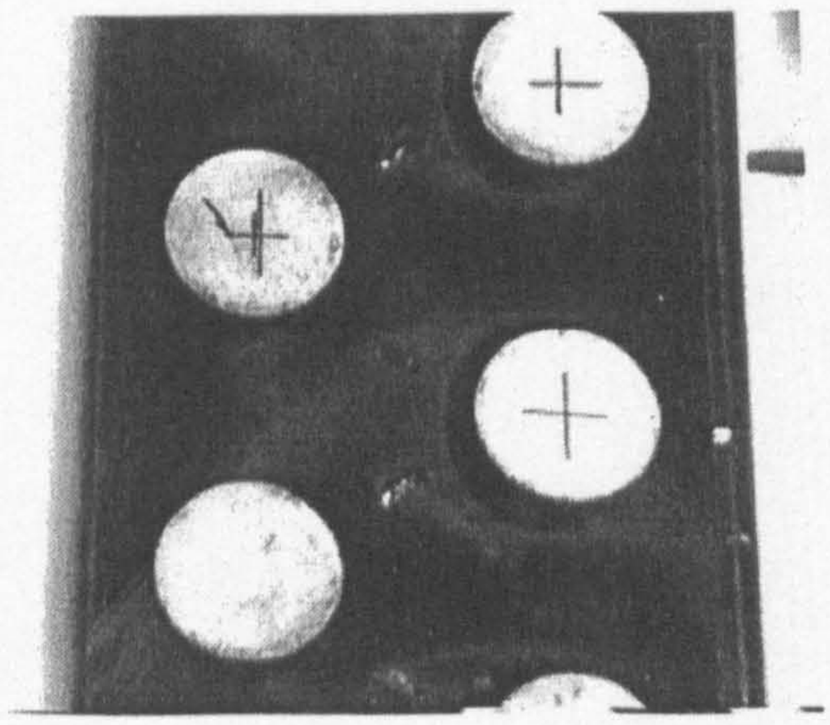

e: $\dot{q}$ = 470.4 W/m^2

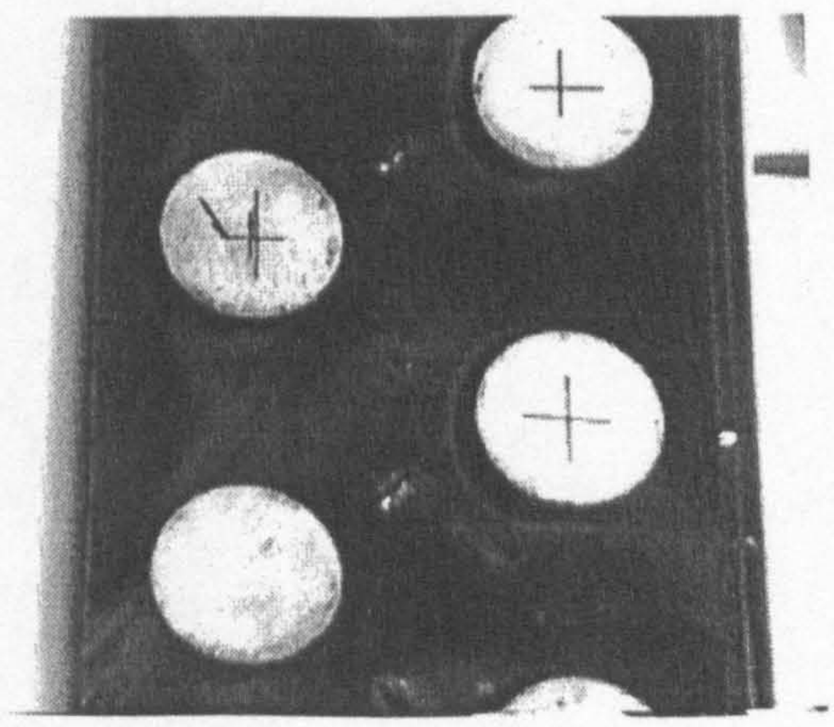

f: $\dot{q}$ = 616.6 W/m^2

Figure 6.17: Isotherm positions for various increasing heat flux input levels

of 9.9 Pa.

A three-dimensional plot of the measured local heat transfer coefficient in the staggered heat exchanger core with vortex generators is shown in Figure 6.18. In front of the horseshoe vortex region of the second tube-row, where high heat transfer coefficients are found, there is a distinct peak in the local heat transfer coefficient. This is due fluid moving over the vortex generator and causing high mixing of the warm air near the plate with the cooler bilk air temperature fluid. It is also noticeable how the increase in heat transfer coefficient continues in a ridge round the outside of the tube where the spiral motion of the vortex continues to provide high levels of mixing. This increase in the heat transfer coefficient eventually dies away near the trailing edge due to viscous dissipation of the vortex.

In addition to the benefit of the vortex providing increased levels of heat transfer due to higher levels of mixing, the vortex issued from the vortex generator also has the effect of reducing the size of the wake region. A small reduction in wake region size can be seen by comparing Figure 6.19, which is the same geometry without vortex generators and at the same Reynolds number with Figure 6.18. The distinct peak and ridge in the local heat transfer coefficient can not be seen in the case without vortex generators.

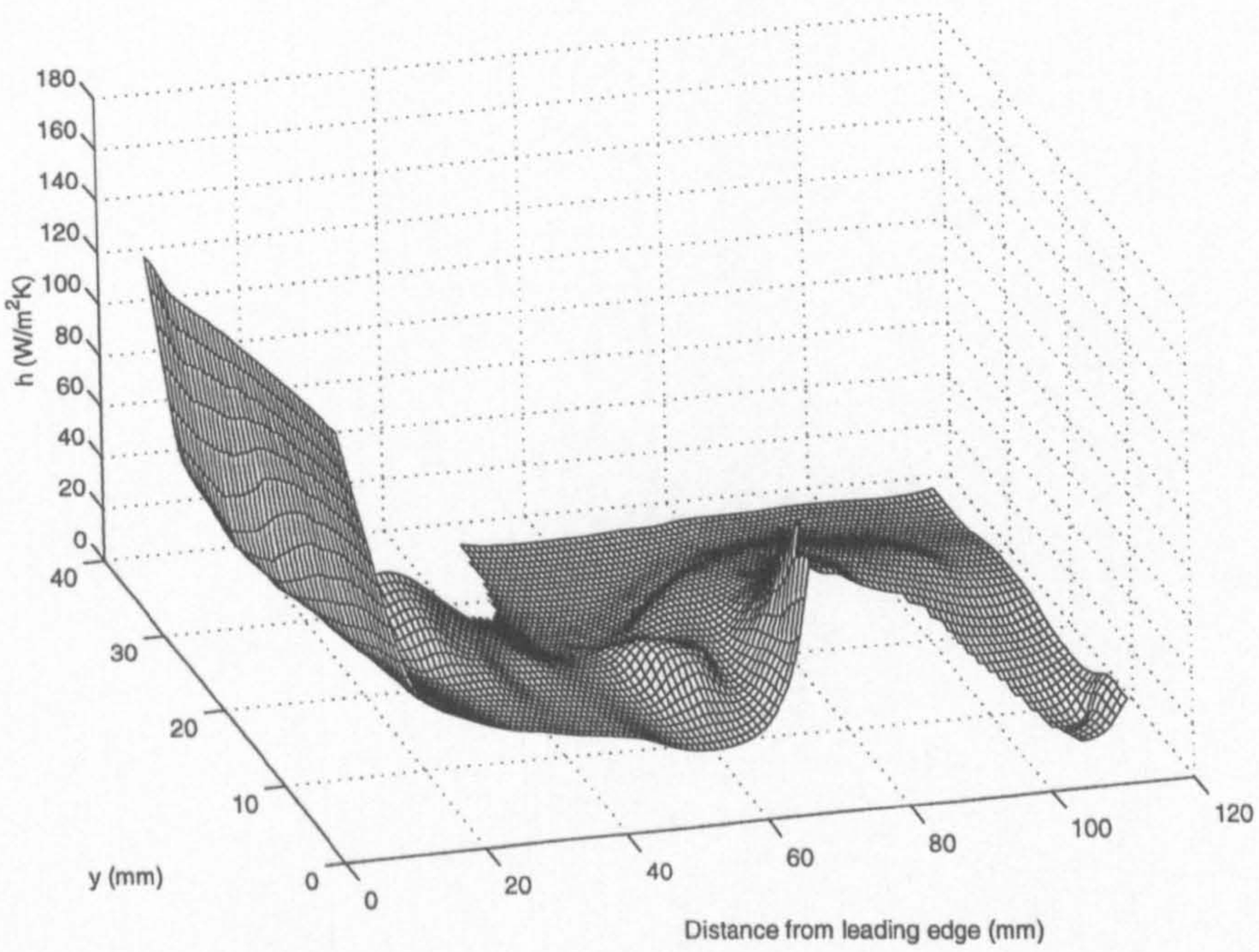

Figure 6.18: Local heat transfer coefficients for the staggered tube heat exchanger section with vortex generators at Re = 326

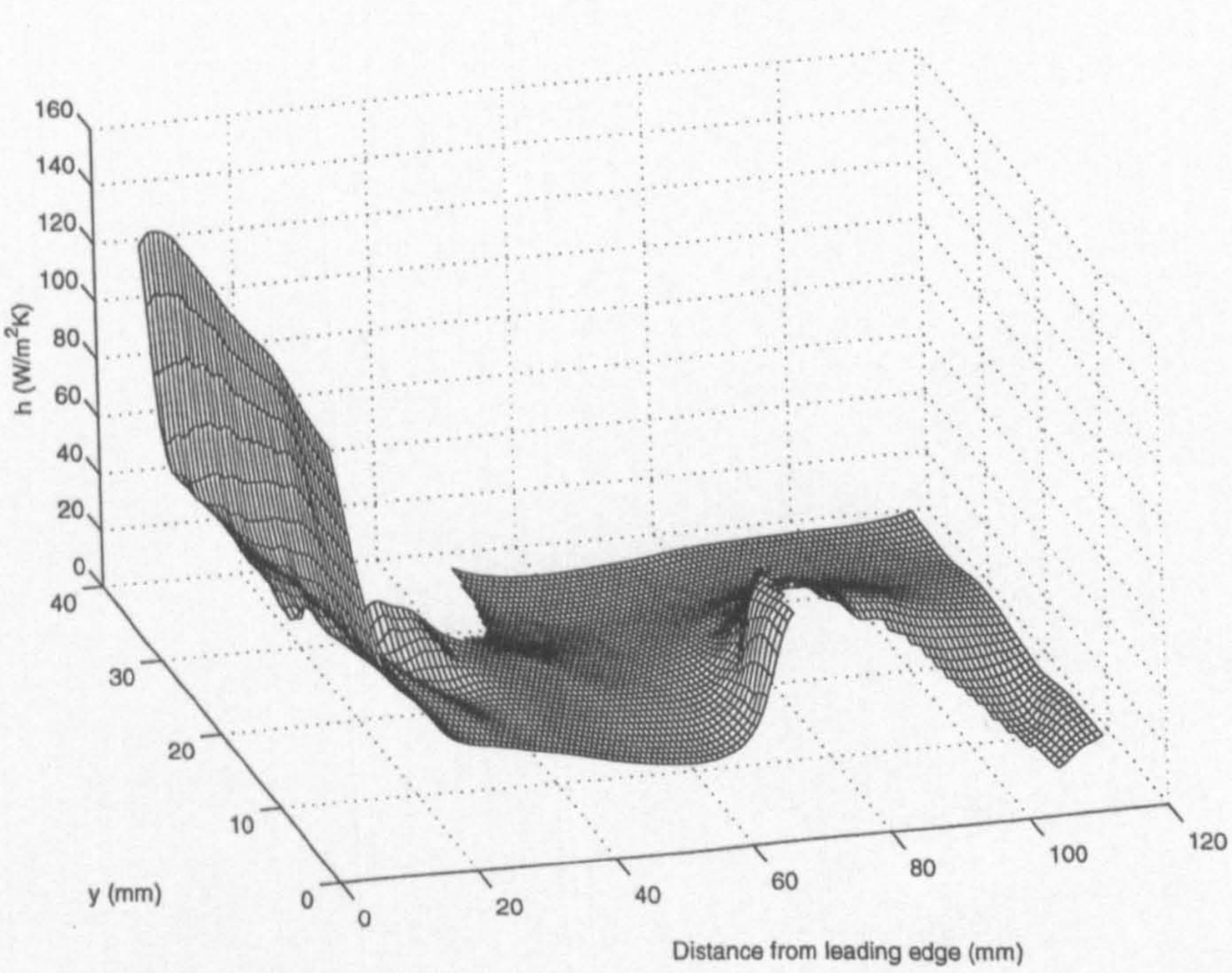

Figure 6.19: Local heat transfer coefficients for the staggered tube heat exchanger section without vortex generators at Re = 326

6.3.2 Numerical results

A comparison of the measured local heat transfer coefficient and the numerically predicted values is shown in Figure 6.20. This shows a section slice of the heat

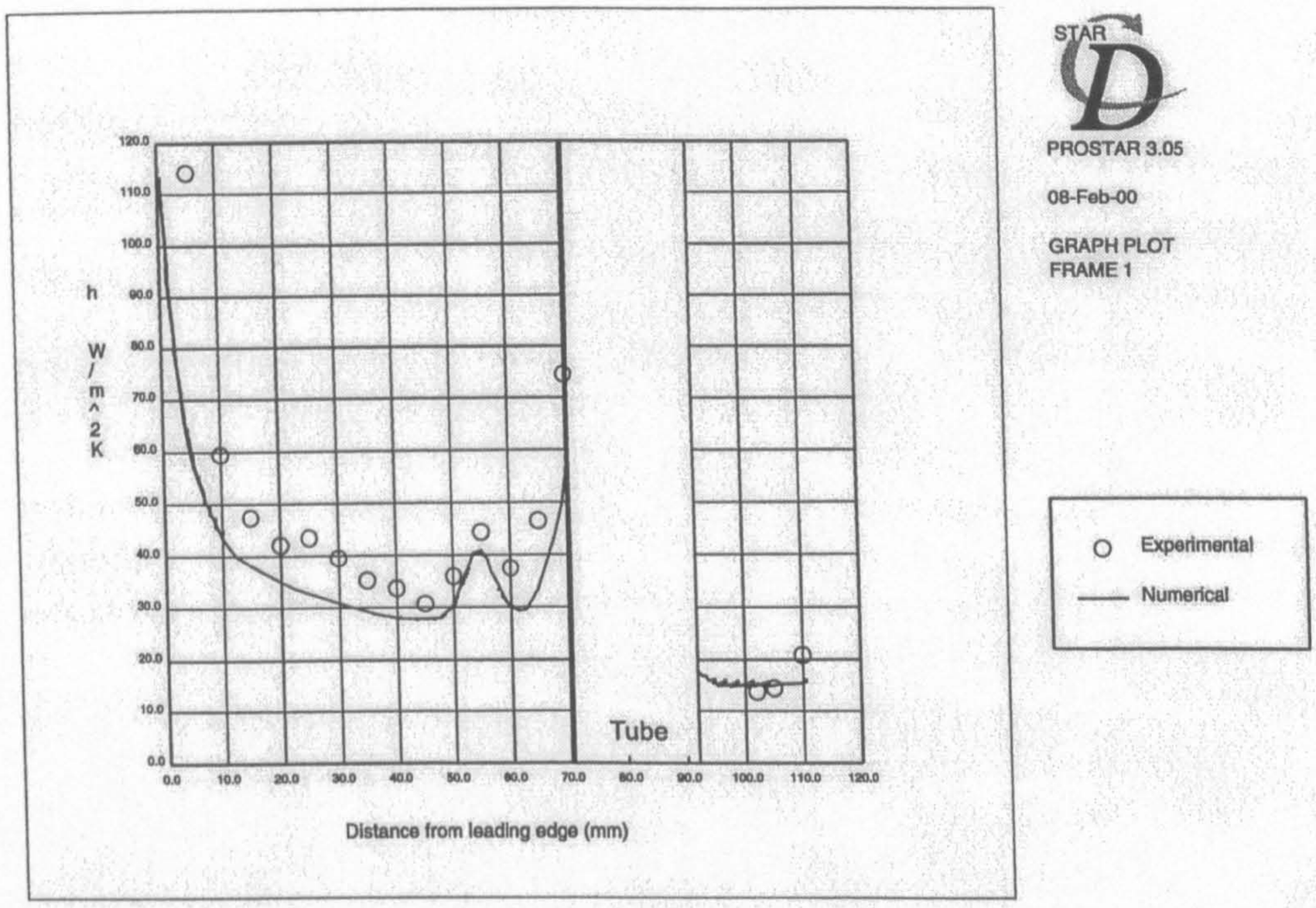

Figure 6.20: Section slice of experimentally measured heat transfer coefficient for different Reynolds numbers

transfer coefficient 12.5 mm into the test section from the left hand edge of the section, cutting through the vortex generator behind the first tube-row. The general trends of the heat transfer coefficient are well predicted, especially in the region before the second tube row, where the heat transfer coefficients are enhanced due to the vortex generator. Again with the other cases, the experimentally measured heat transfer coefficient is over predicted toward the leading edge due to tangential conduction. The numerically predicted average heat transfer coefficient was 30 W/m^2K and the pressure drop 11.86 Pa. This is an over- and under-prediction of 23.5% and

12.7% respectively.

From the velocity vector plots, Figure 6.21 and Figure 6.23, the actual enhancement mechanism of heat transfer can be explained. The fluid approaches the vortex generator at almost 90°, Figure 6.21, unlike the case of the plain channel model

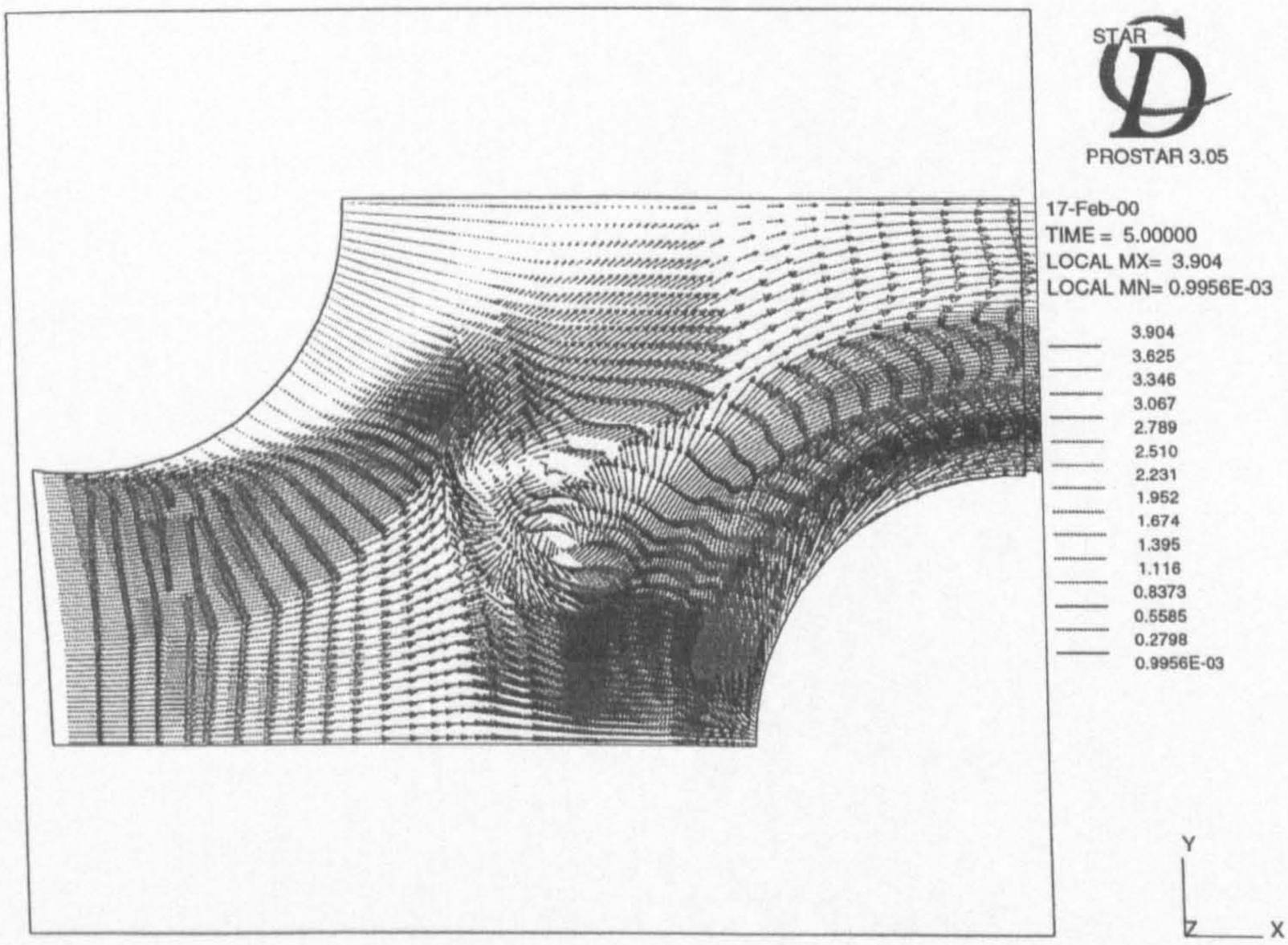

Figure 6.21: Velocity vectors approaching vortex generator in staggered tube heat exchanger section with vortex generators

with vortex generators, where the fluid approaches the vortex generator in the usual direction. The fluid approach at 90° causes the fluid to stagnate on the vortex generator, separating the fluid flow about half-way along the vortex generator, with the flow moving towards the first tube-row wake region and toward the horseshoe vortex region of the second tube-row. The fluid is also locally accelerated between the vortex generator and horseshoe vortex forming on the second tube-row. As

a result two distinct recirculation regions are set up behind the vortex generator, with the larger recirculation zone behind the tall end of the vortex generator. Also noticeable from Figure 6.21 is the fluid appearing to be travelling in the opposite direction to the main flow, in front of the vortex generator. This is the formation of a small corner vortex forming in the upstream side of the vortex generator and is the cause of the high heat transfer coefficients seen on the upstream side of the vortex generator in Figure 6.17e.

Cross-stream velocity vectors at positions indicted in Figure 6.22 are presented

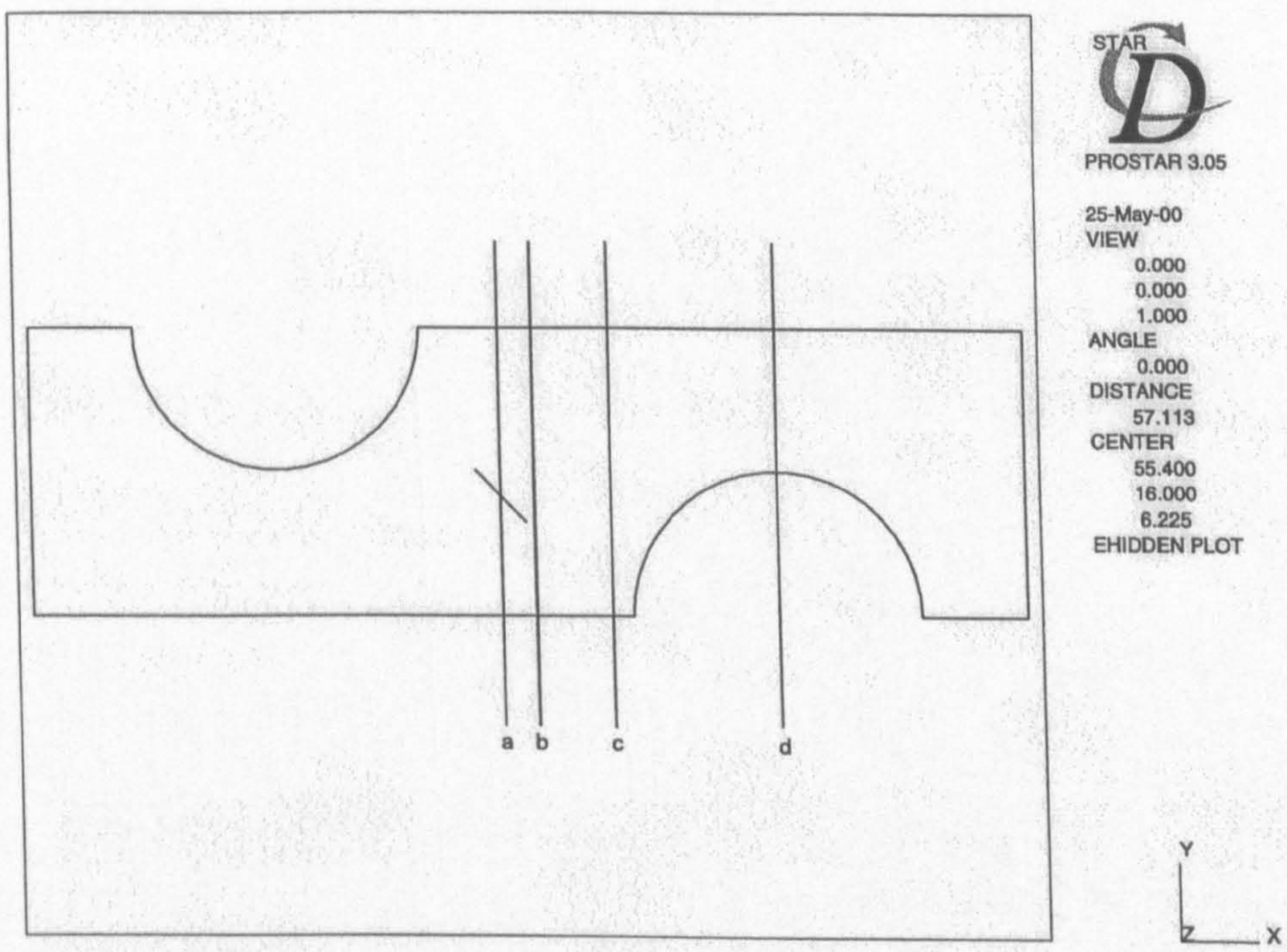

Figure 6.22: Positions of the numerically predicted cross-stream velocity vectors in the downstream direction

in Figure 6.23. The formation of the main vortex from the vortex generator is shown in Figure 6.23a. In the plot, which is taken half-way through the vortex

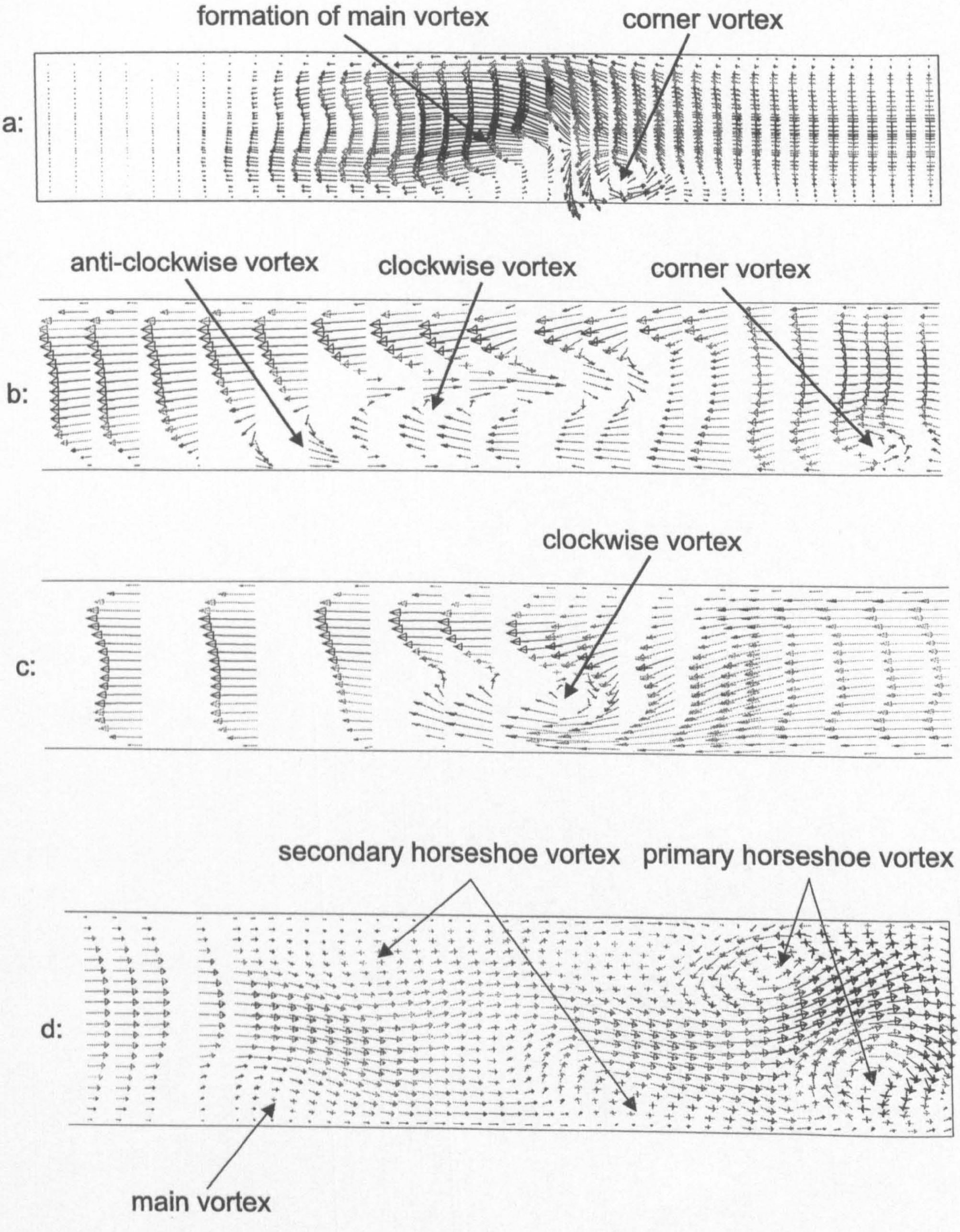

Figure 6.23: Velocity vectors in the downstream direction

generator in the downstream direction, the fluid is seen to accelerate over the vortex generator, before moving into the low pressure area behind. The corner vortex can also be clearly seen slightly to the right of the vortex generator. The formation of the main longitudinal vortex is shown, along with the corner vortex in Figure 6.23b. The main vortex is circulating in an anti-clockwise direction as would be expected. However, in the centre of the main vortex is another vortex that has fluid motion in a clockwise direction. This second vortex is formed from the larger of the two recirculation regions. As the fluid is drawn around the vortex generator, it moves towards the low pressure region where it picks up a clockwise rotational motion. This clockwise rotational motion is eventually transported downstream causing a clockwise longitudinal vortex to form. The second clockwise vortex continues to grow in size and strength and eventually kills the first anti-clockwise vortex, Figure6.23c. The second clockwise vortex moves in the downstream direction, where its path is deflected by flow around the tube. This causes a slight reduction in the size of the wake region behind the first tube-row.

As the second clockwise rotating vortex moves around the second tube-row region, it has the effect of severely distorting the shape and size of the primary and secondary horseshoe vortices, Figure 6.23d. It can be seen that due to viscous forces of the vortex issuing from the vortex generator the the primary and secondary horseshoe vortices have been pulled away from the tube wall and elongated towards the centre of the channel. This has the effect of increasing the area over which high rates of mixing between the cooler bulk air temperature and the warmer temperatures of the

fin and tube occur. This increases the heat transfer coefficient in this region and is the reason for the distinct ridge around the tube in Figure 6.18. As the main vortex passes the centre line of the second tube-row it continues to distort the horseshoe vortices around the tube, but due to viscous dissipation the vortex issued from the vortex generator decreases in size and strength until it no longer has any effect on the heat transfer near the trailing edge.

From the previous discussion, it is clear that although the vortex generator does have some effect on the heat transfer, the vortex generator position is hardly optimal, especially in terms of pressure drop increase. The vortex generator position for this study was decided with the research group at Bochum under an European sponsored project (JOE3-CT97-0056). For a single tube with vortex generators, Fiebig et al. (1990) and Fiebig (1993) suggested an optimum position for a delta winglet pair where the sharp end of the vortex generator was immediately behind the tube, one tube diameter apart and an angle of attack of 45°. However, this position is based on a Reynolds numbers of around 6000. For the much lower Reynolds numbers used in this study the vortex generator position was moved toward the trailing edge so that the vortex generator was in a position to magnify the horseshoe vortices coming of the tube. In the higher Reynolds number cases, the horseshoe vortex does not travel that far down-stream due to higher levels of dissipation.

When delta winglet pairs are placed in the position suggested by Fiebig et al. (1990) and Fiebig (1993), the vortex generator generates a longitudinal vortex with a low

pressure region in its core. Fluid from the main stream is sucked into the vortex, increasing levels of mixing. In addition, fluid is drawn between the vortex generator tip and the tube, delaying flow separation round the tube. This forces fluid into the wake region, strongly reducing its area and thus increasing the overall heat transfer from the fin. The position of the vortex generators used in this study don't exhibit the 'ideal' fluid flow behaviour discussed above. However, with inspection of the velocity vector plots from the plain staggered tube case, it's unlikely that the optimum position suggested by Fiebig et al. (1990) and Fiebig (1993) will extend to multi-row staggered tube heat exchangers where the fluid patterns are quite different from row-to-row.

6.3.3 Experimental results at different flow velocities and vortex generator angles of attack

The staggered tube heat exchanger section with vortex generators was tested with a flow velocity of 1.25 m/s at three angles of attack, $\beta = 15°$, 45° and 60° and two further flow velocities, 0.25 m/s and 2.5 m/s with $\beta = 45°$. Figure 6.24 presents the average heat transfer coefficient and pressure drop through the staggered tube heat exchanger section with and with out vortex generators at an angle of attack of 45°. At the lowest Reynolds number both the average heat transfer coefficient and pressure drop are less than the case without vortex generators by 22.8% and 9.6% respectively. By a Reynolds number of 339 positive increases were measured with values of 3.3% and 12.1% respectively. At the highest flow velocity further gains were measured with the increase in average heat transfer coefficient rising to 19.2%

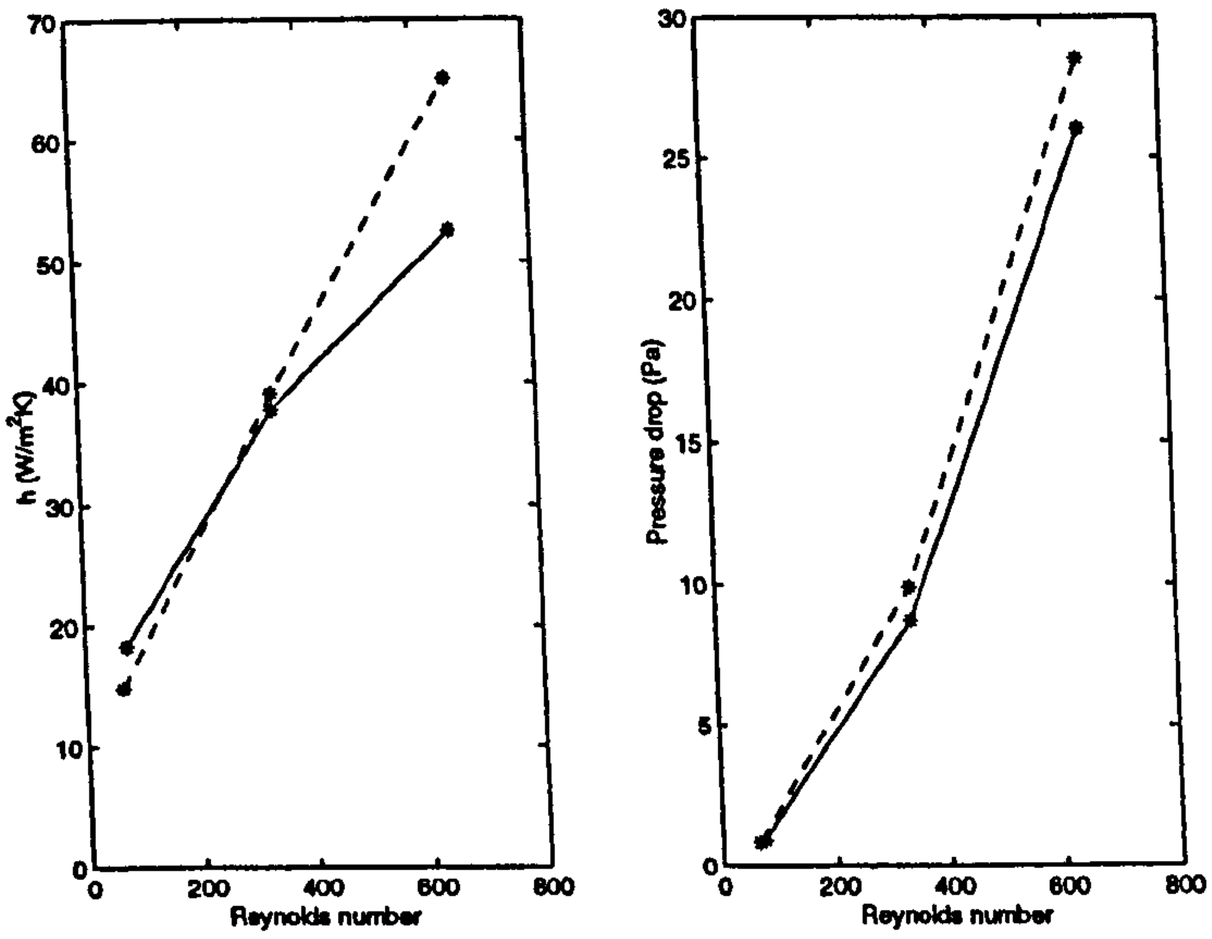

Figure 6.24: Average heat transfer coefficient and pressure drop for the staggered tube heat exchanger section with delta winglet pairs at $\beta = 45°$ (dashed line with vortex generators, solid line without vortex generators)

over the base case and pressure drop increase of 8.8%.

For a three tube-row staggered heat exchanger section with delta winglet pair vortex generators, Fiebig et al. (1993) measured the average heat transfer coefficient and pressure drop for the Reynolds number range 600 – 2700. The geometry of Fiebig et al. (1993) is broadly similar to the geometry used in this study, the two differences being that $H/D = 0.4$ and that the tips of the vortex generators were 19.2 mm downstream of the centre line of the tube in the Fiebig at al. (1993) study. At Reynolds numbers of around 600 Fiebig et al. (1993) reported an increase on the Nusselt number of 7% with an increase in friction factor of around 3%. The heat transfer coefficient enhancement increased with Reynolds number to about 9% at $\mathrm{Re} = 2700$ while the pressure drop enhancement remains constant at around 3%. It is also interesting to note that the average heat transfer coefficient is 21% and 32%

higher for a two-row staggered tube heat exchanger section with and without vortex generators when compared to a three-row configuration with and without vortex generators.

The average heat transfer coefficient and pressure drop for a Reynolds number of 339 is shown in Figure 6.25 where the angle of attack has been increased from

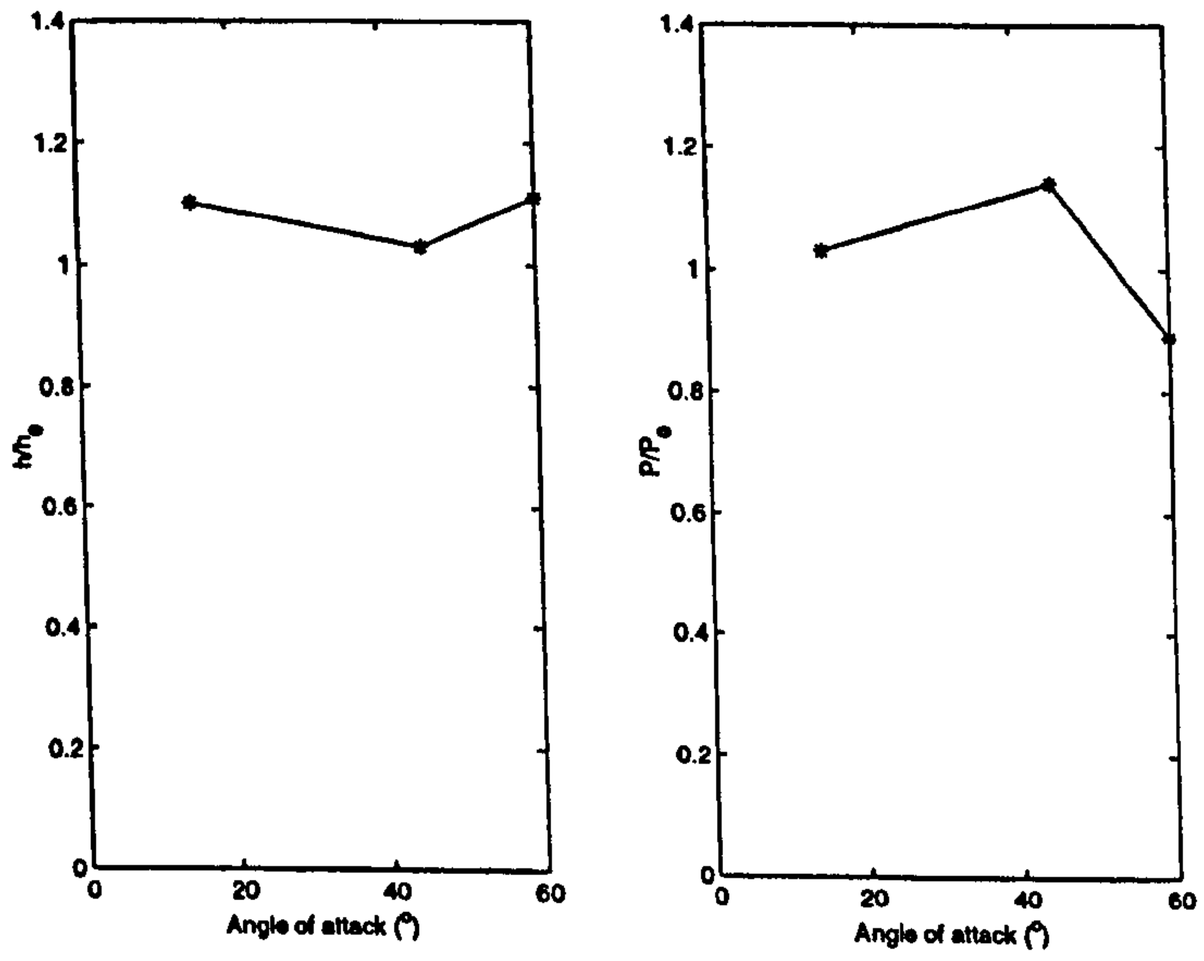

Figure 6.25: Average heat transfer coefficient and pressure drop for the staggered tube heat exchanger section with delta winglet pairs at for Re = 339 and increasing vortex generator angle of attack.

15° to 60°. Both the average heat transfer coefficient and pressure drop values have been non-dimensionalised against the plain staggered tube section without vortex generators. What is apparent is that the heat transfer coefficient increase remains reasonably constant at around 9% regardless of the angle of attack of the vortex generator. However, the pressure drop increases from 3.3% at $\beta = 15°$ to 12.1% at $\beta = 45°$ and then reduces significantly by 13.0% at $\beta = 60°$. The increase in pressure drop with increasing angle of attack can be expected due to the increase in

projected area and thus form drag. The reduction in pressure drop at $\beta = 60°$ was however unexpected.

A close inspection of the test piece manufactured for $\beta = 60°$ showed that the vortex generator had been rotated around the tall end and this tall end was now one tube diameter apart. From Figure 3.9 it can be seen that the vortex generator should be rotated around the sharp end and the sharp ends should be one tube diameter apart. Figure 6.26 shows the liquid crystal isotherm positions for increasing heat flux input levels for $\beta = 60°$ and can be compared with Figures 6.1 and 6.17 which are the staggered tube case without vortex generators and with vortex generators at $\beta = 45°$. From Figure 6.26 it can be seen that very different shapes and positions of isotherms are recorded. The vortex generators greatly reduce the size of the wake region, thus increasing the heat transfer and reducing the pressure drop. The vortex generators position used shows more of the 'ideal' flow behaviour that can be expected when vortex generators are mounted on a fin. Delayed separation is seen around the tube and cooler bulk air temperature is mixed in the wake region reducing its size. It is however, noticeable that the vortex issued from the vortex generator is not particularly strong, Figures 6.17c and 6.17d. For the $\beta = 60°$ case any enhancement effect ends at heat transfer coefficient values of around 30 W/m^2K where as for the $\beta = 45°$ case any enhancement effects persist up to values of around 40 W/m^2K. From Figure 6.21, it can be seen that the vortex generator in the $\beta = 60°$ case is placed in a region of lower velocity when compared to the mainstream and thus a weaker vortex can be expected. A direct comparison of a

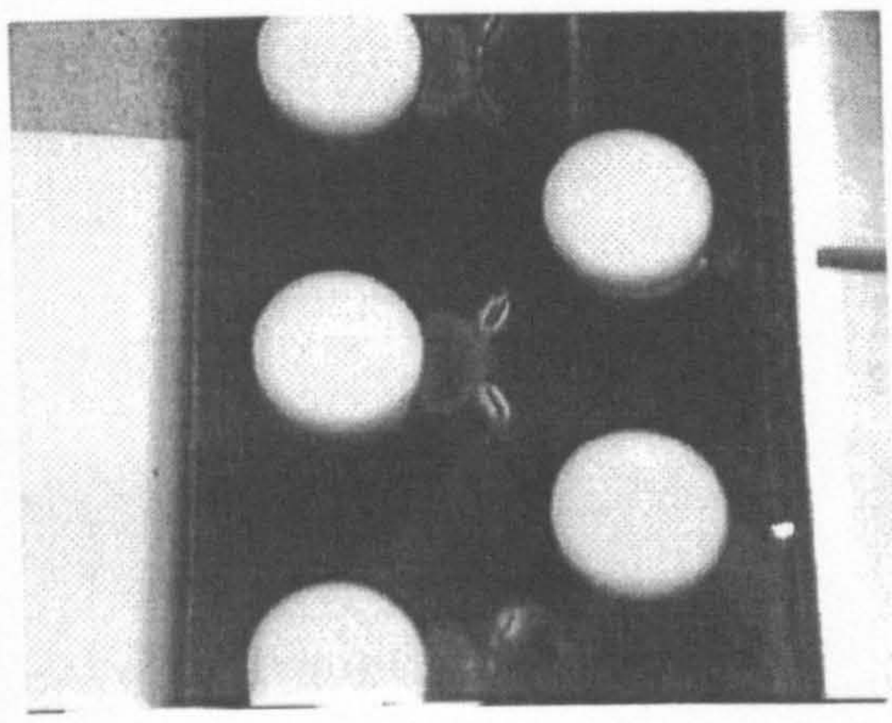

a: $\dot{q}$ = 226.6 W/m^2

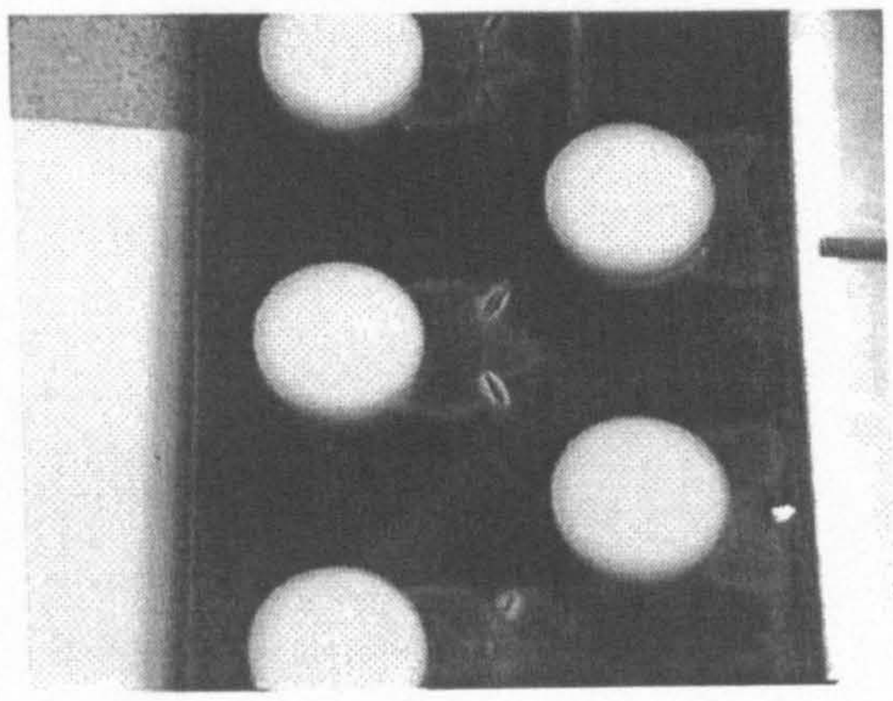

b: $\dot{q}$ = 260.0 W/m^2

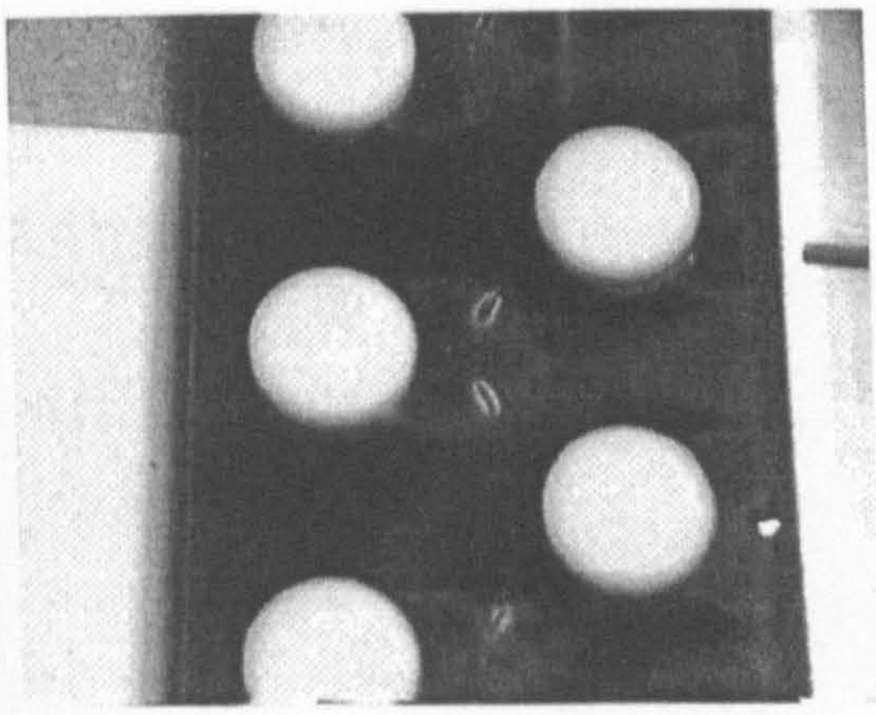

c: $\dot{q}$ = 267.6 W/m^2

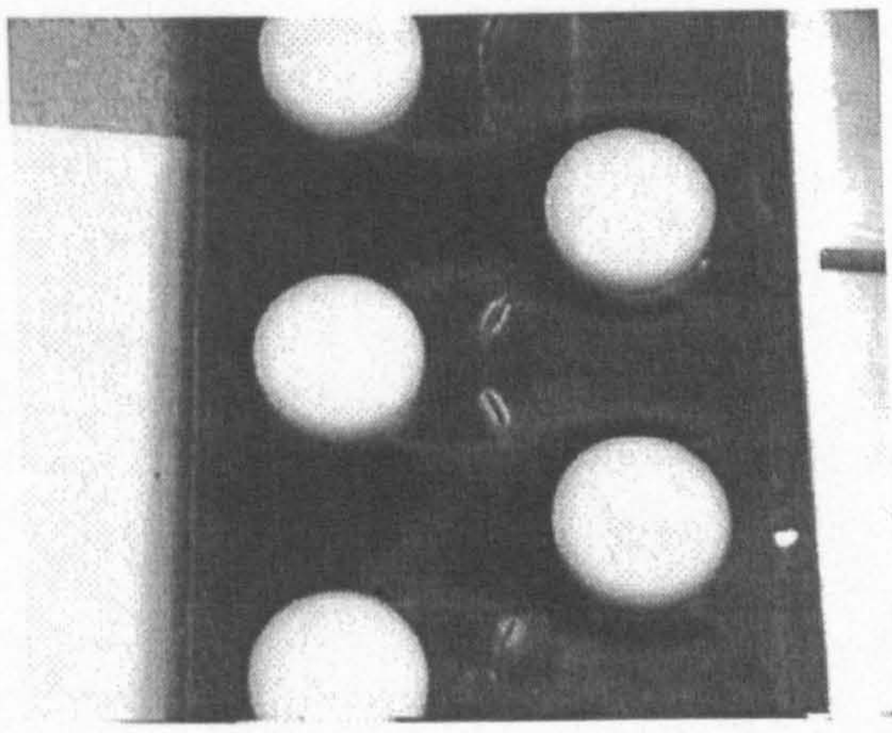

d: $\dot{q}$ = 288.8 W/m^2

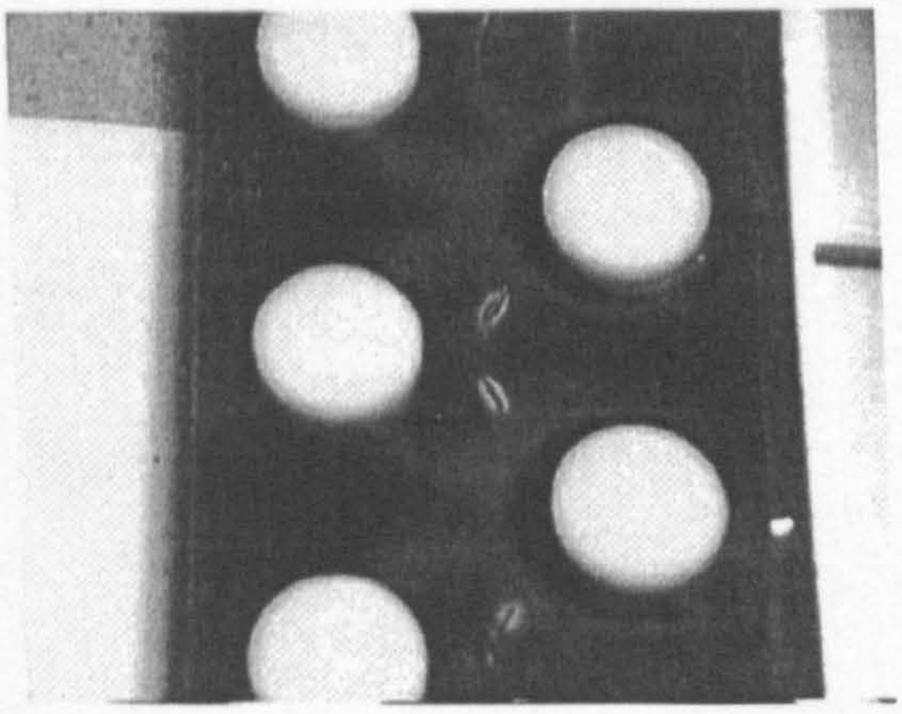

e: $\dot{q}$ = 308.6 W/m^2

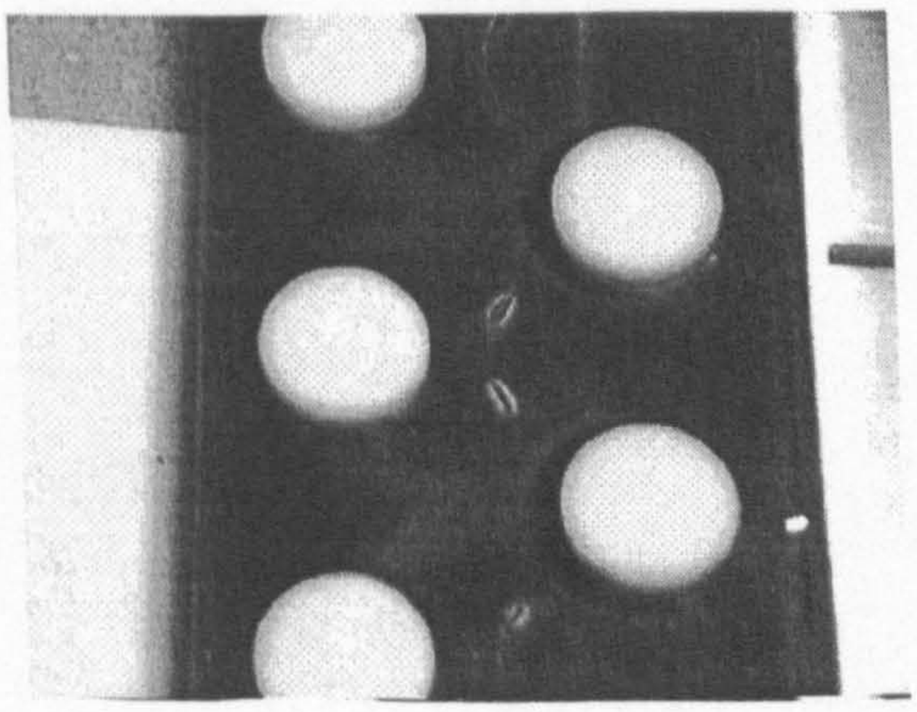

f: $\dot{q}$ = 317.8 W/m^2

Figure 6.26: Isotherm positions for various increasing heat flux input levels

line of constant heat transfer coefficient ($h = 19$ W/m^{2}K) is shown in Figure 6.27. As with the the isotherm positions it shows a much reduced wake area.

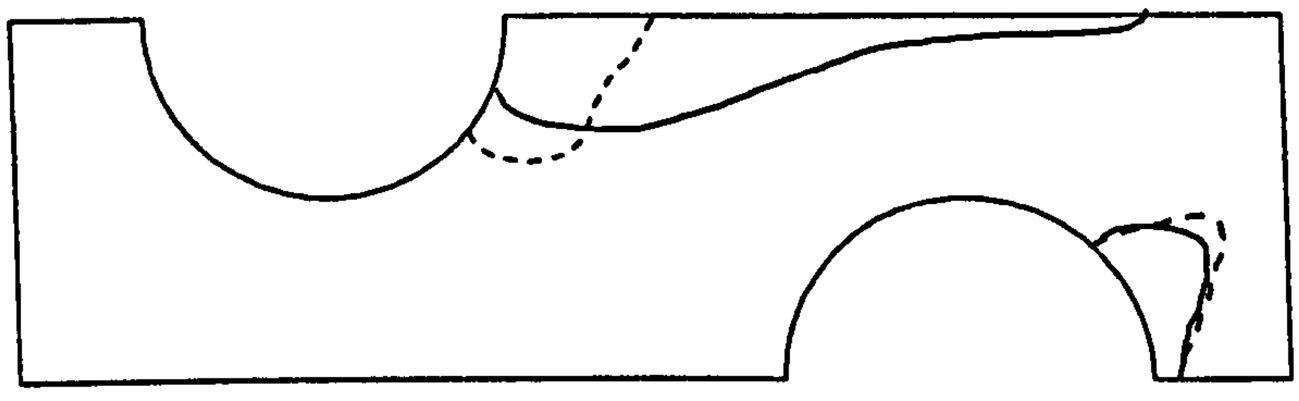

Figure 6.27: Lines of constant heat transfer coefficient, $h = 19\,\mathrm{W/m^2K}$, plain line without vortex generators, dotted line with vortex generators at $\beta = 60°$.

6.4 In-line tubes with vortex generators

6.4.1 Experimental results

The isotherm positions for the in-line heat exchanger section with vortex generators are shown in Figure 6.28, for increasing heat flux input levels. As with the staggered tube heat exchanger section with vortex generators, at low heat flux inputs, the vortex generators have very little effect on the size and shape of the isotherms. As the heat flux input is increased and the isotherms widen into the distinct ship shape wake (shown in Figure 6.12c, without vortex generators), the effect of the vortex generator is to reduce the widening of the isotherms. This is shown in Figure 6.28c, where the wake region has been slightly pinched and in Figure 6.28d, where the isotherm position in the wake region are nearly parallel until the second tube-row. At the second tube-row there is a U-shape in the isotherm due to a small horseshoe vortex forming around the second tube-row, going in the downstream direction,

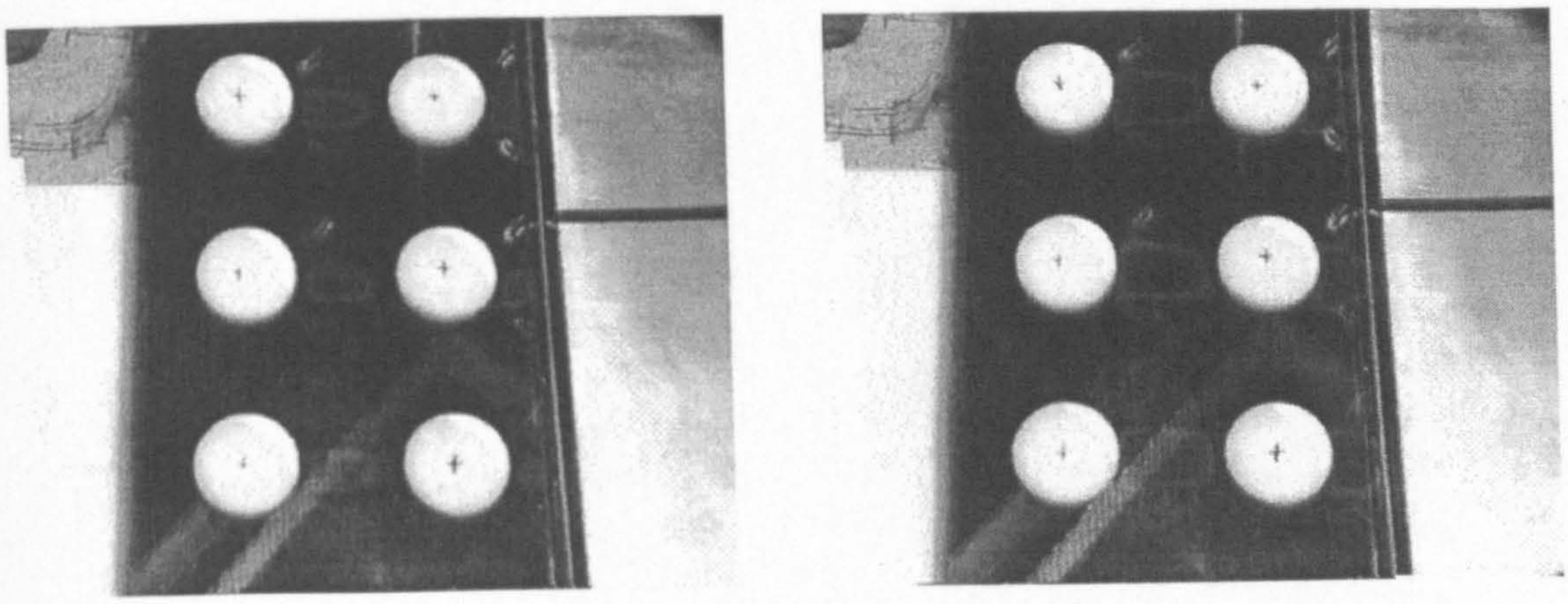

a: $\dot{q}$ = 188.1 W/m^2

b: $\dot{q}$ = 202.6 W/m^2

c: $\dot{q}$ = 248.8 W/m^2

d: $\dot{q}$ = 268.3 W/m^2

e: $\dot{q}$ = 287.1 W/m^2

f: $\dot{q}$ = 306.8 W/m^2

Figure 6.28: Isotherm positions for increasing heat flux input levels

meeting the isotherm from the other side. As the heat flux is increased further, the isotherms move upstream leaving an area of enhanced heat transfer behind the vortex generators, Figure 6.28e and 6.28f.

6.4.2 Numerical results

The numerically predicted heat transfer coefficient for the in-line heat exchanger core with vortex generators is shown in Figure 6.29 along with the experimental

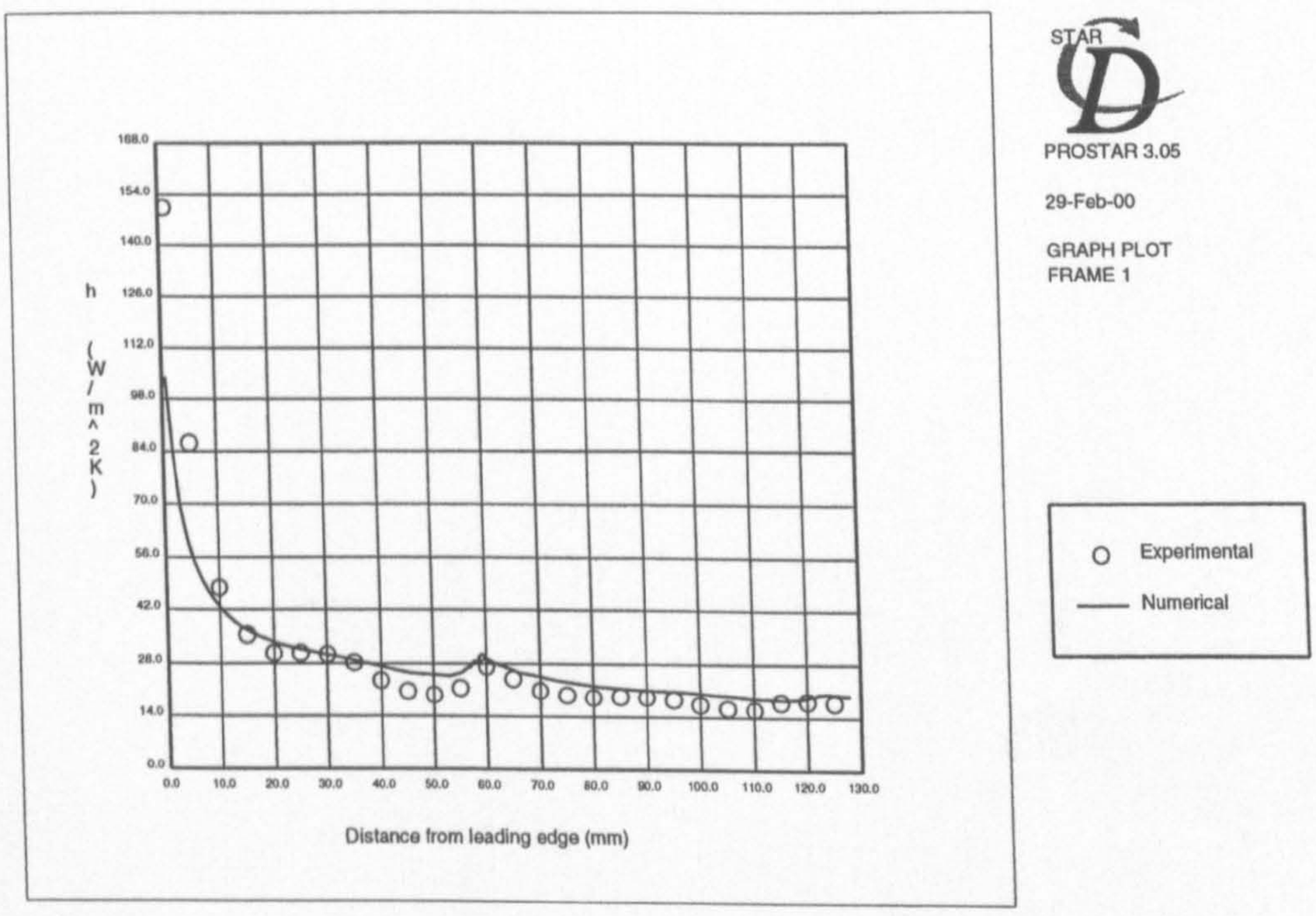

Figure 6.29: Comparison of numerically predicted and experimentally measured heat transfer coefficients for the in-line heat exchanger case with vortex generators

data. The heat transfer data is taken from a section slice in the flow direction, 20.2 mm from the edge of the domain. Apart from the leading edge, where tangential conduction has resulted in an over-prediction of the experimental data the heat

transfer coefficient has been reasonably predicted. This is also true at around $x =$ 60 mm from the leading edge where an increase in heat transfer coefficient can be observed due to the presence of the vortex generators. For the overall results, the predicted value of average heat transfer coefficient was under-estimated by 11.4% and the value of pressure drop over-estimated by 25.4%.

Figure 6.30, shows the velocity vectors 0.4 mm from the bottom of the fin, between

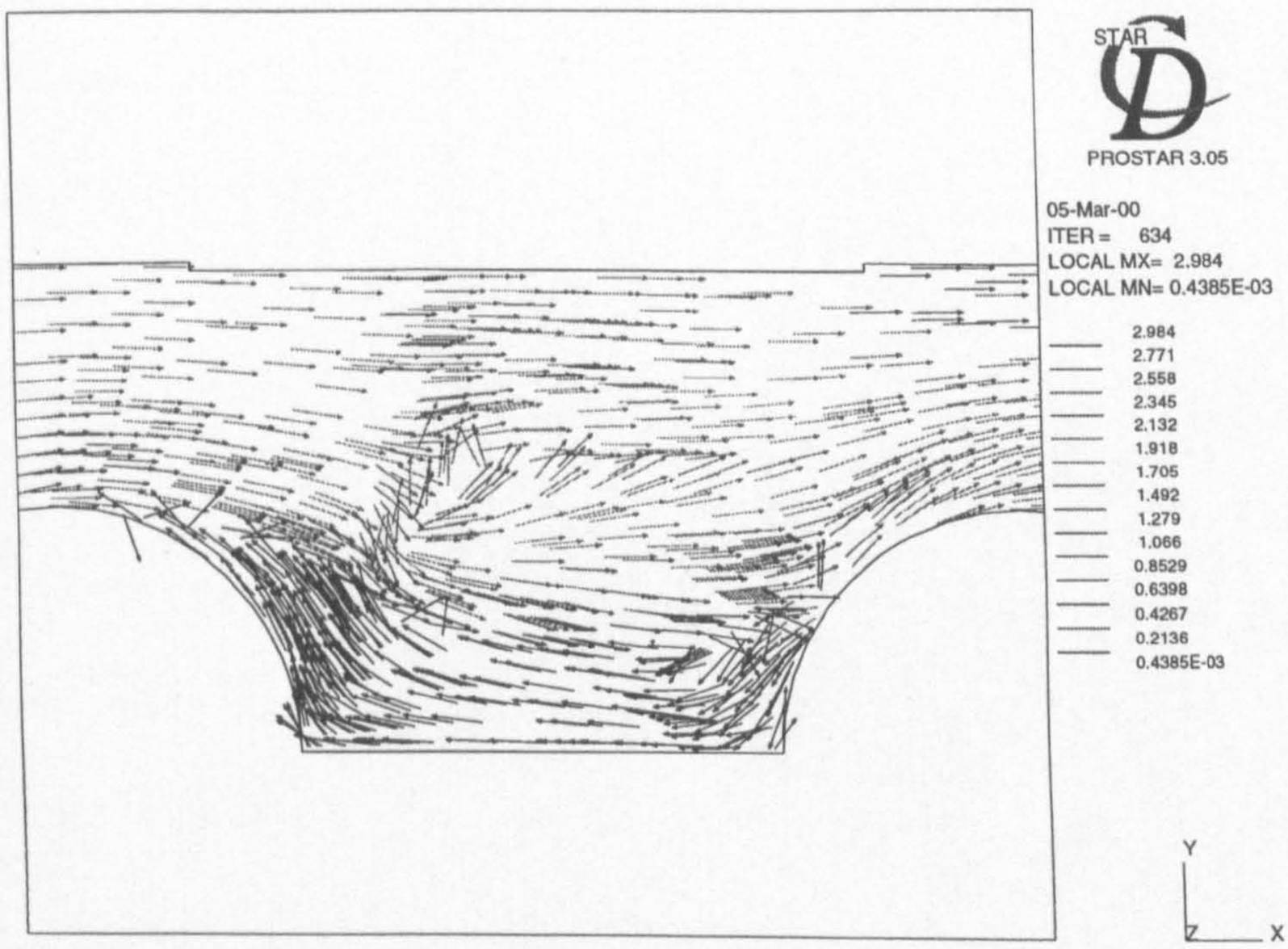

Figure 6.30: Velocity vectors 0.4 mm from the bottom of the fin in the in-line heat exchanger case with vortex generators

the two tubes. From the leading edge, the flow is constricted between the tubes in the first tube-row and is accelerated through the channel between the tubes. The flow around the tubes separates and mets the vortex generator at an angle of 45°. The vortex generator slightly delays the position of separation from 3° past the

midpoint of the tube to 13°. A vortex is issued from the vortex generator which is carried in the downstream direction. The effect of the vortex and the movement of the fluid towards the low pressure region of the vortex has the effect of reducing the size of the recirculation region behind the tubes.

In addition to increasing the heat transfer due to a reduced vortex size, it is interesting to note that a small horseshoe vortex has formed around the second tube-row. In the case without vortex generators, the horseshoe vortex around the second tube-row is completely absent. The effect of the vortex generator position and the issuing vortex has moved the re-attachment points of the wake region on the second tube-row closer together. This draws fluid towards the low pressure region of the recirculation zone where it enables a horseshoe vortex to form on the second tube-row.

The cross-stream velocity vectors at different axial locations in the channel, indicated in Figure 6.31, are shown in Figure 6.32. In Figure 6.32a, which is directly behind the vortex generators, the main vortex can be seen that has formed in the anti-clockwise direction. A smaller horseshoe vortex which has formed on the winglet can be seen to the right of the main vortex. As a result of the anti-clockwise vortex, clockwise motion of the fluid is induced which impinges into the wake region behind the tube. This has the effect of reducing the wake region size and increases mixing of the colder bulk temperature air with the warm air in the wake region, all of which has the effect of increasing the heat transfer. Moving in the down-stream direction, Figure 6.32b, which is taken half way between the tubes, shows a similar type of

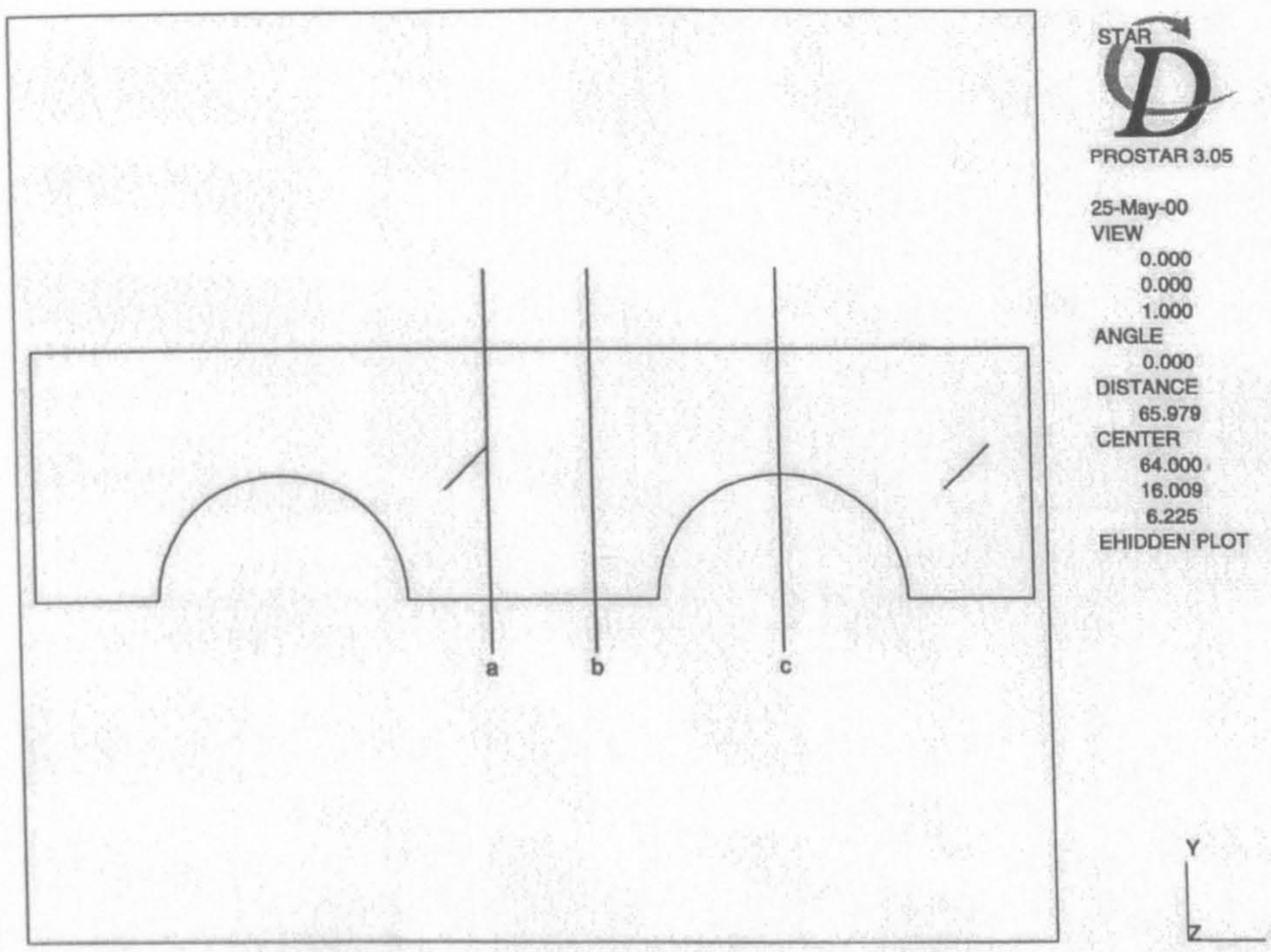

Figure 6.31: Location of the cross-stream velocty vector plots

flow pattern. The horseshoe vortex that had formed on the vortex generator has reduced in size due to viscous dissipation. The main vortex has continued to induce clockwise motion fluid that reduces the wake region size, and also a smaller clockwise vortex has been induced between the two. In Figure 6.32c, which is taken on the midway point of the second tube-row, the small horseshoe vortices that have formed due to the pinching of the wake region can be seen.

In a numerical study of Bastani et al. (1999) for a similar case of a two tube-row in-line heat exchanger core with vortex generators, similar flow patterns were observed. The effect of the vortex generators was however, more pronounced as the optimal vortex generator spacing suggested by Fiebig (1993) was used along with a higher Reynolds number. In the study by Bastani et al. (1999) the secondary cross stream velocity vectors were seen to induce flow all the way through the wake

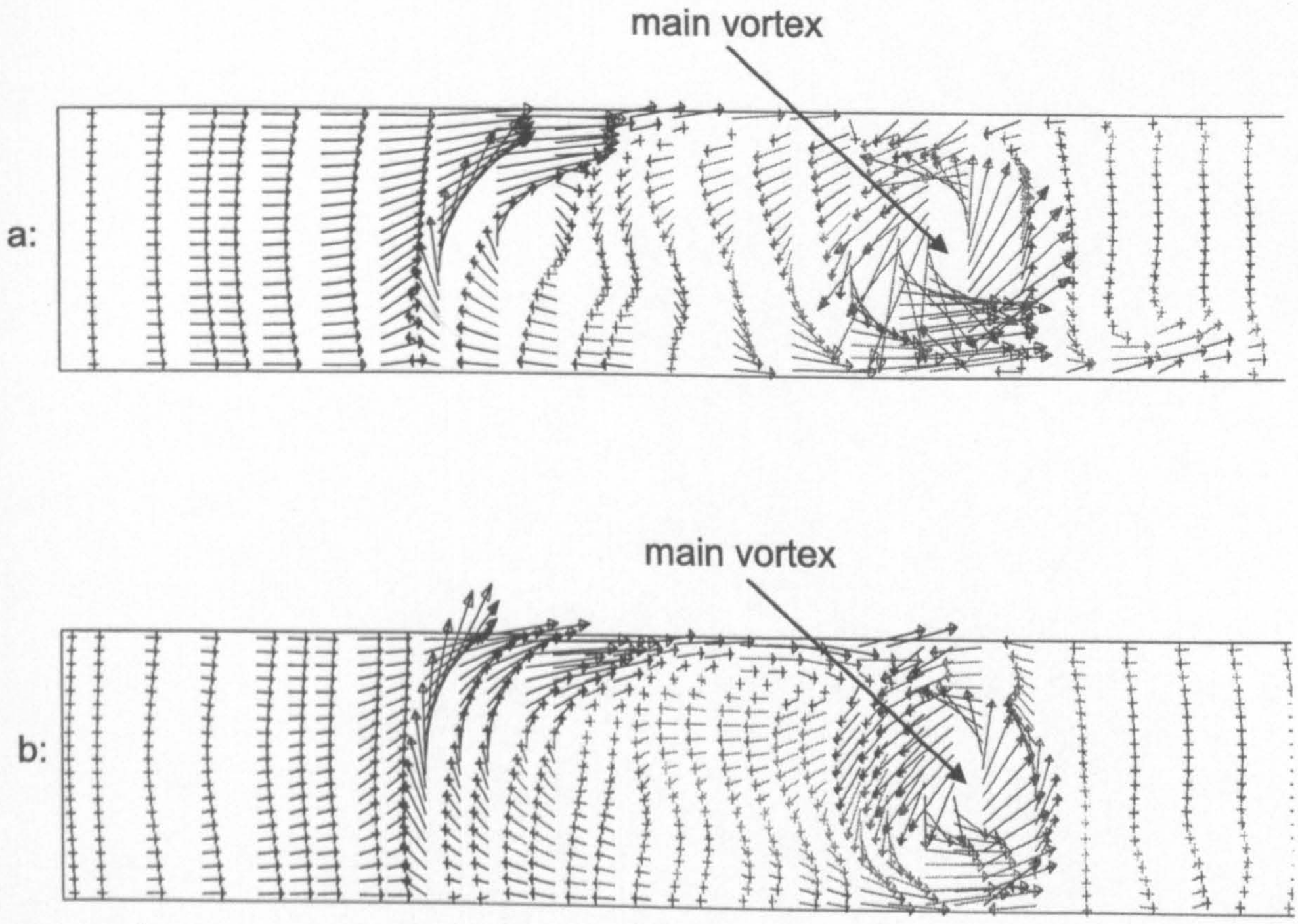

Figure 6.32: Velocity vectors in the downstream direction for the in-line case with vortex generators.

region. Although no cross stream velocity vector plots were shown for the midway point of the second tube-row, it appeared from vector plots in the same plane as the fin that horseshoe vortices were formed on the second tube-row.

6.4.3 Experimental results at different flow velocities

The in-line heat exchanger test section with vortex generators was tested at three different Reynolds numbers, Re = 65, 326 and 653, for one angle of attack, $\beta = 45°$. Figure 6.33, presents the average heat transfer coefficient and pressure drop for

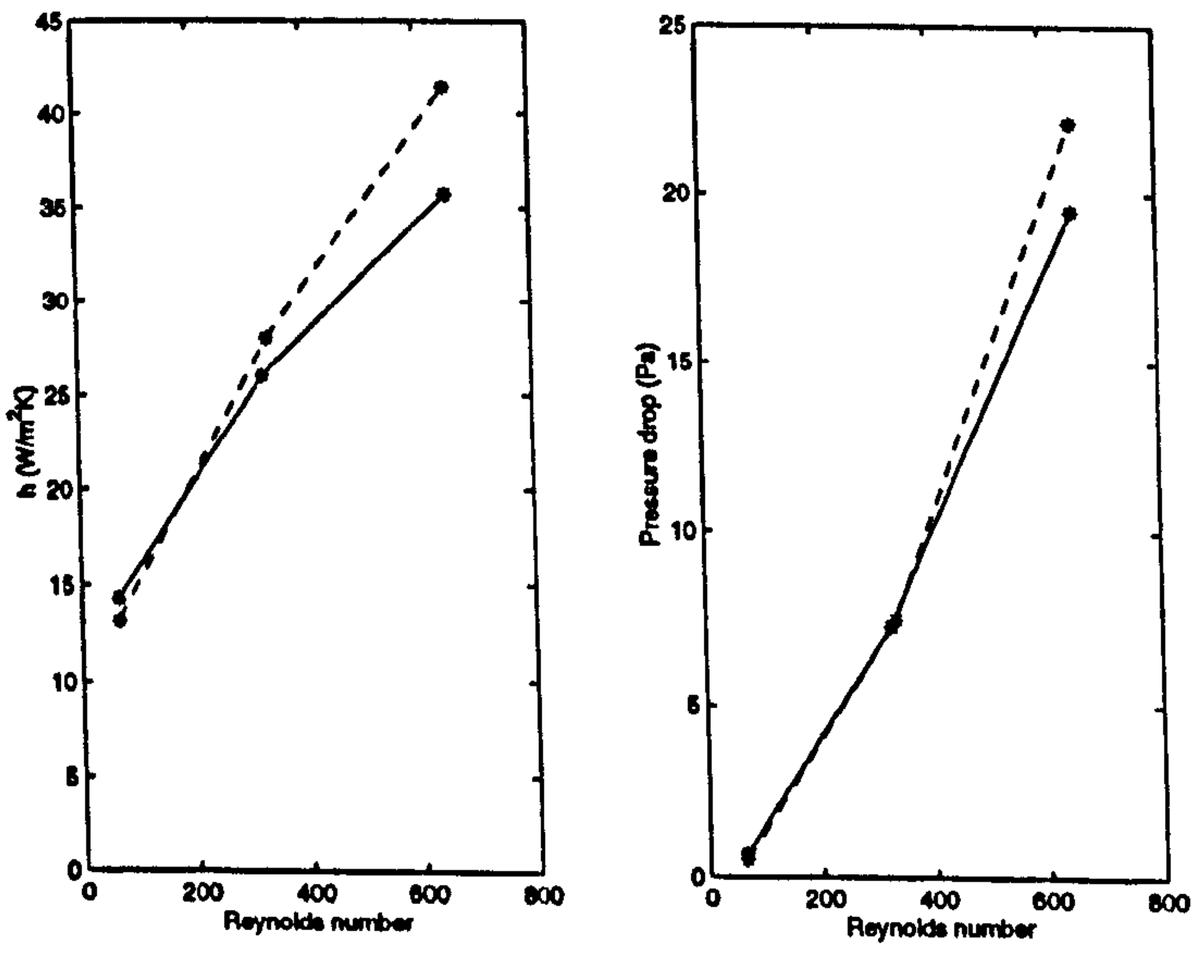

Figure 6.33: Average heat transfer coefficient and pressure drop for the in-line tube heat exchanger section with delta winglet pairs at $\beta = 45°$ (dashed line with vortex generators, solid line without vortex generators)

the three Reynolds numbers investigated at an angle of attack $\beta = 45°$. At the lowest Reynolds number, Re = 65, the effect of the vortex generators has reduced the average heat transfer coefficient and pressure drop by 8.3% and 33.3% respectively. This is similar to what occurred in the staggered tube heat exchanger case

with vortex generators. When the Reynolds number was increased to 326, positive increases were recorded for both the average heat transfer coefficient and pressure drop at 7.1% and 2.7% respectively. For the highest Reynolds number investigated these positive increases had risen to 13.8% and 11.9% respectively.

In comparison to other workers, the results presented here are approximately half the values of Nusselt number observed by Bastani et al. (1999) for his numerical model with entry flow at a Reynolds number of 400. He recorded Nusselt number values of 7.71 and 9.24 for the in-line case with and without vortex generators. The values recorded here are 3.96 and 4.26 respectively for a Reynolds number of 326. For the three tube-row model tested experimentally with and without vortex generators by Fiebig et al. (1993), at a Reynolds number of 650, Nusselt values were recorded at approximately 4.5 and 7.2 with and without vortex generators. The values recorded in this study, for two tube-rows, with and without vortex generators at a Reynolds number of 650 were 5.4 and 6.3. Higher values should be expected for the two tube row configuration. This suggests that there might be some dependence on the number of tube-rows used for optimal heat transfer when vortex generators are used.

6.5 Comparison of round and oval tubes in staggered and in-line arrangements

In these comparative tests, an in-line heat exchanger with round tubes was compared against a staggered tube heat exchanger core with oval tubes at a Reynolds number of 1224. Both the average heat transfer coefficient and pressure drop were measured experimentally to test the relative effects of the tube arrangement and shape. A

further test was carried out experimentally at a Reynolds number of 1567.

The liquid crystal isotherm pictures for the in-line case at a Reynolds number of 1224 is shown in Figure 6.34. It is interesting to compare this to the case studied earlier with the two tube-rows, although direct comparison cannot be made as the ratios of the tube diameters to the channel height and the tube pitch in the flow direction to the channel height is different. As in the earlier case the liquid crystals change colour behind the tubes in the wake region, although it is noticeable in the four tube-row case that there is a smaller area of reduced heat transfer behind the second and fourth tube-rows. At the rear of the channel the liquid crystals also change colour between the tube-rows. As the heat fluxes increased the liquid crystals changed colour over a bigger area in the wake region and also move up the centre between the tube-rows. It is apparent that horseshoe vortices are formed in front of all four tubes although they reduce in size in the flow direction. This was also noted by Wung and Chen (1989b) and Jang et al. (1996) in a numerical study.

A plot of the local heat transfer coefficient through the centre lines of the tubes is shown in Figure 6.35. A number of points are apparent from this plot. Firstly, it is obvious that horseshoe vortices are formed in front of all four tube-rows, causing large increases in the heat transfer coefficient. Larger increases in heat transfer coefficient are noted in front of the second and fourth tube-rows, than in front of the third tube-row. The increase in front of the first tube-row will always be larger than the others, due to the undisturbed flow reaching the first tube-row. The heat

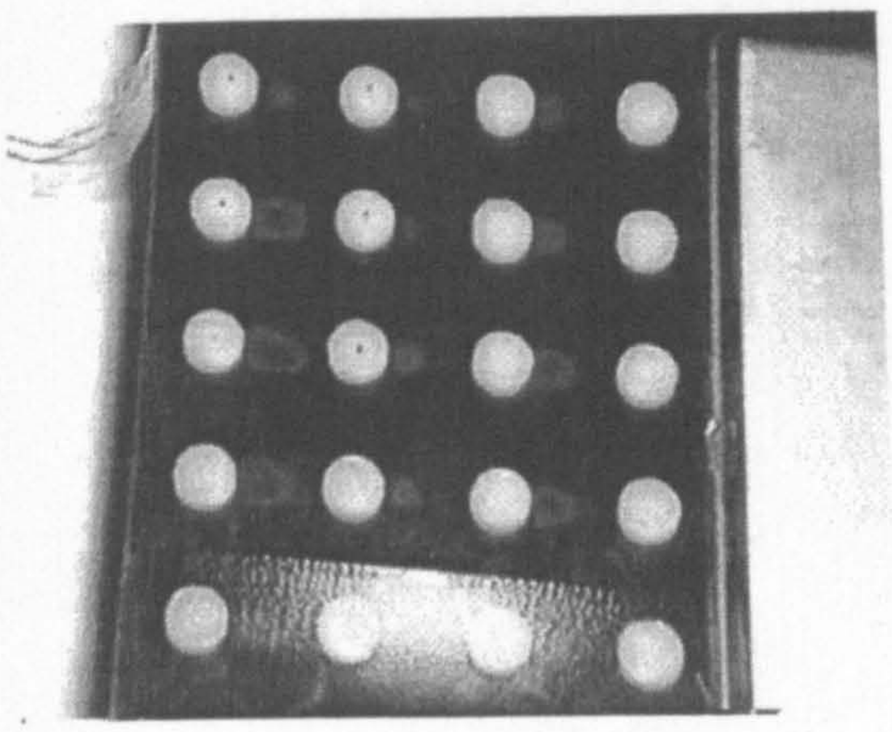

a: $\dot{q}$ = 633.4 W/m^2

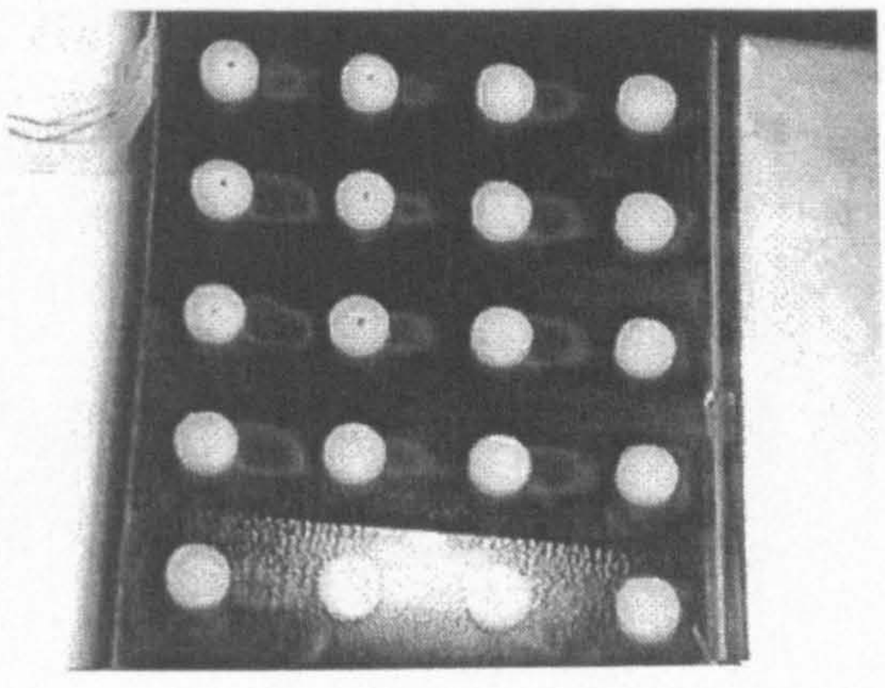

b: $\dot{q}$ = 649.2 W/m^2

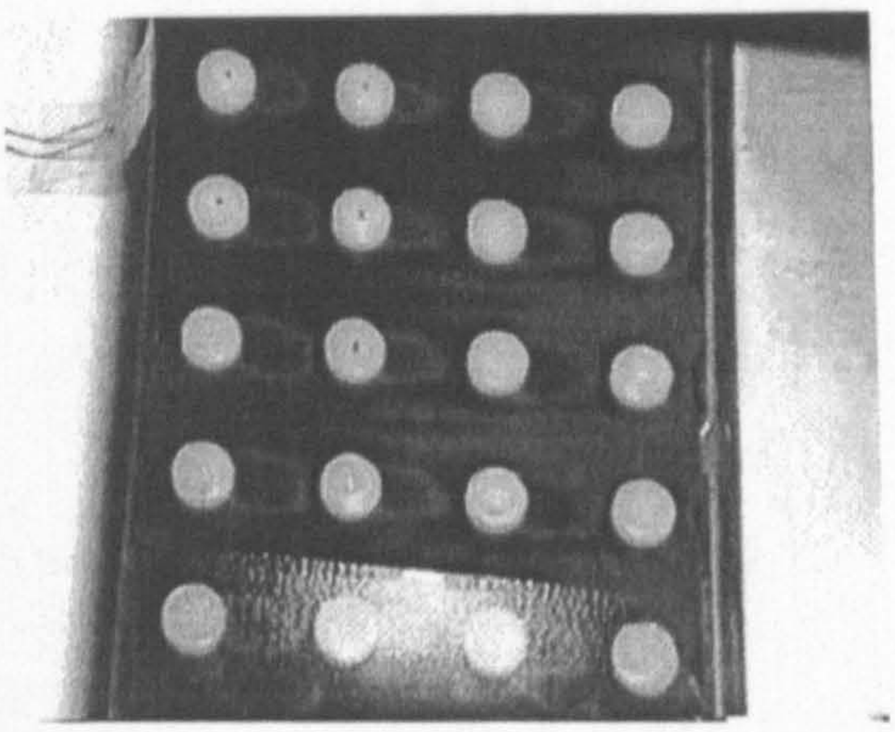

c: $\dot{q}$ = 676.9 W/m^2

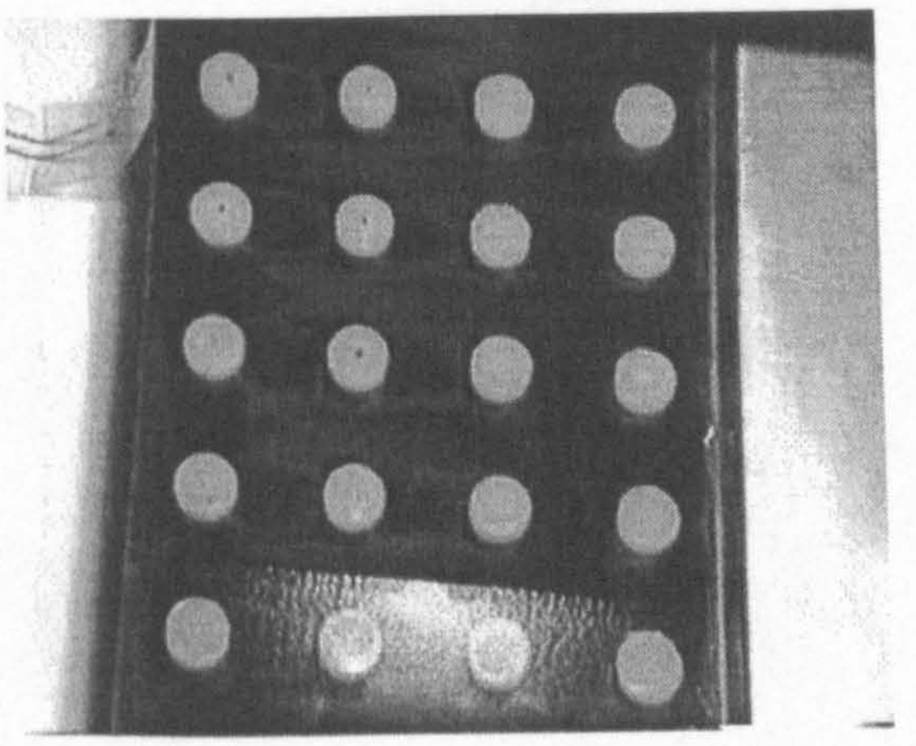

d: $\dot{q}$ = 766.5 W/m^2

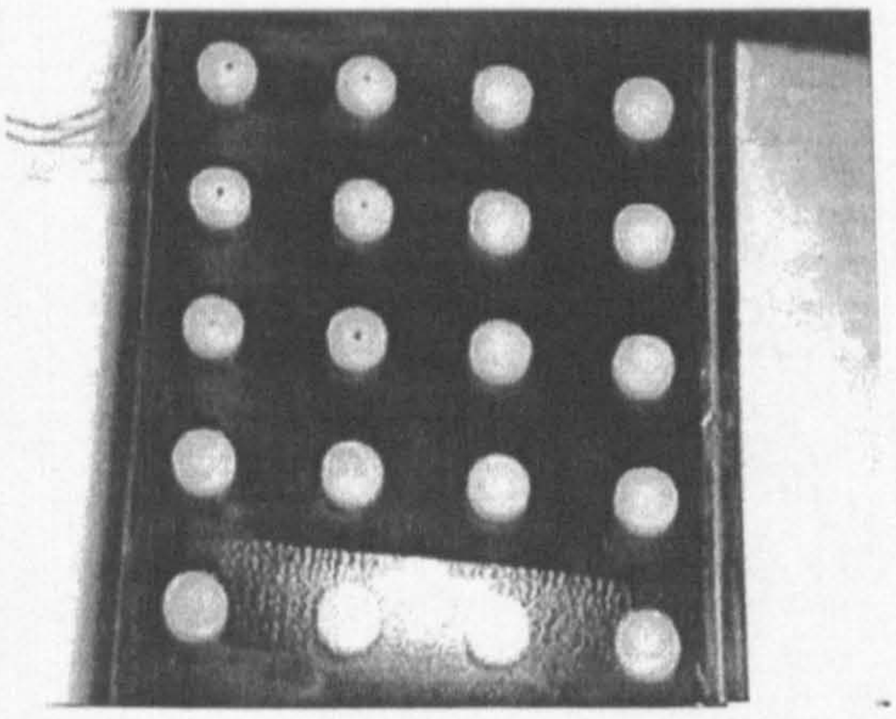

e: $\dot{q}$ = 908.8 W/m^2

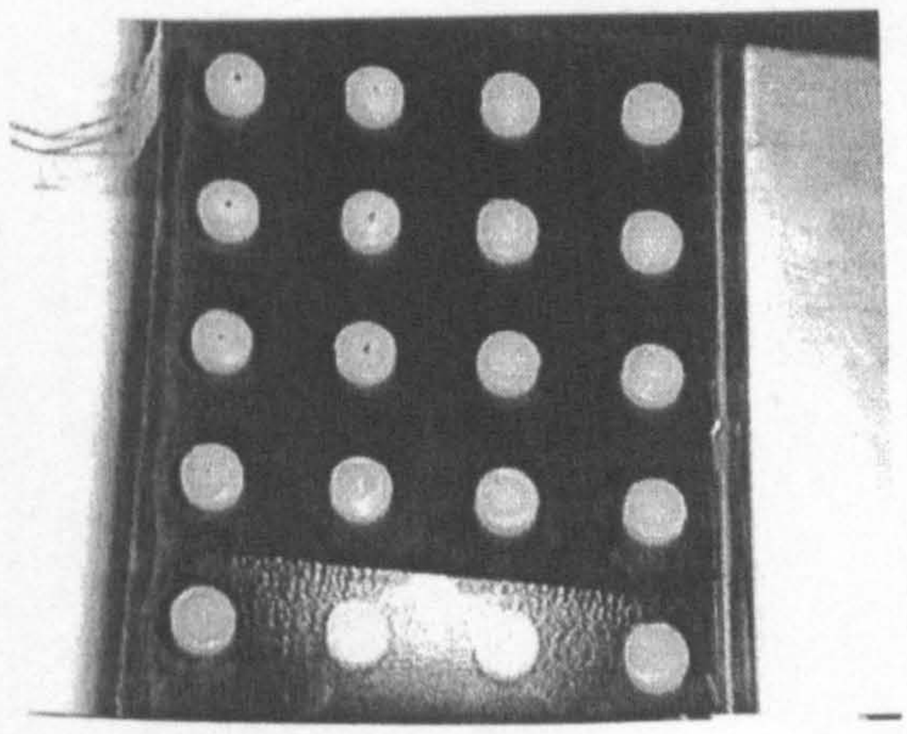

f: $\dot{q}$ = 993.1 W/m^2

Figure 6.34: Isotherm position for increasing heat flux input

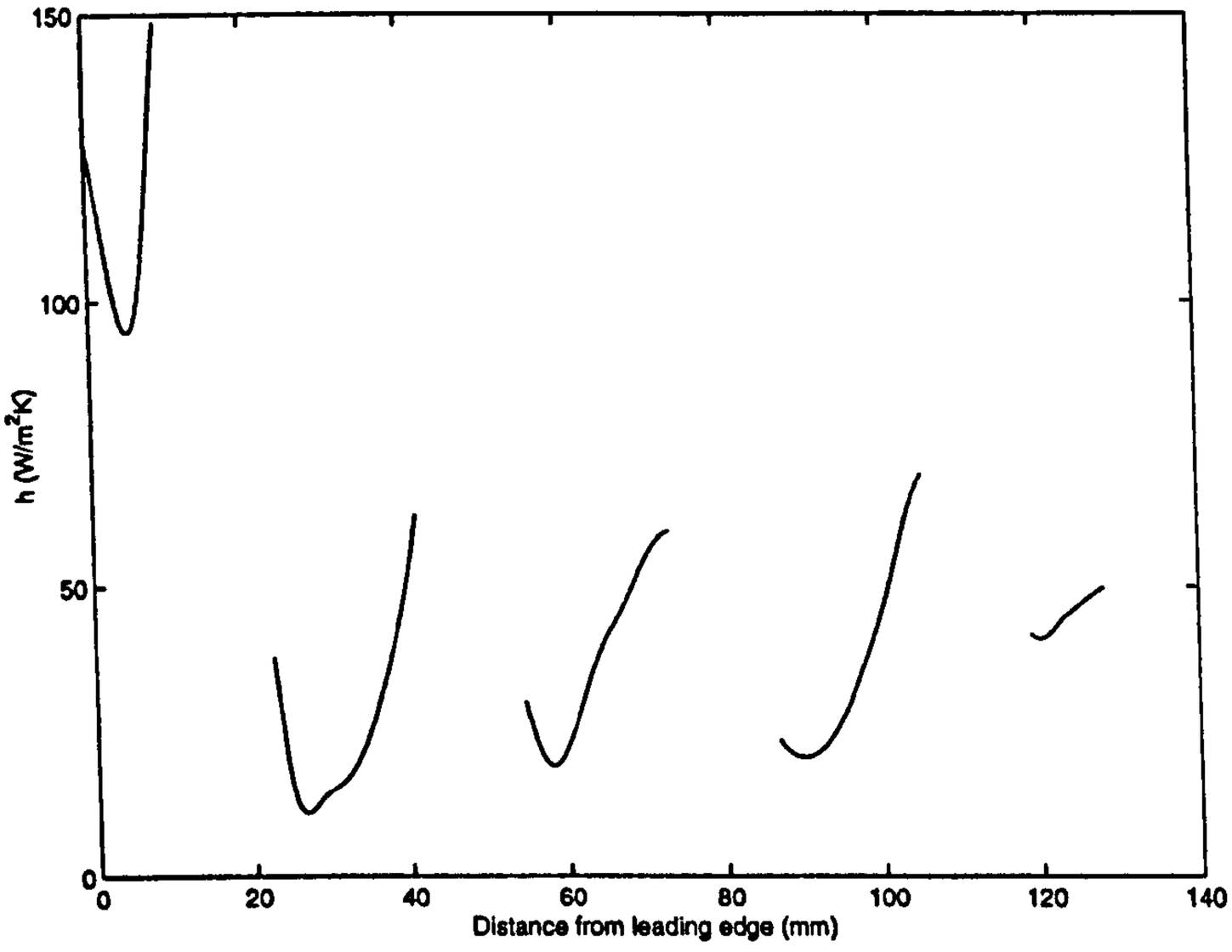

Figure 6.35: Heat transfer coefficient through the centre line of tubes in the in-line case with round tubes. Blank space is where tube is positioned

transfer coefficient in the wake regions increases with tube-row number, although the wake region of the second tube-row is slightly higher than that of the third tube-row. The increase in heat transfer is due to more active mixing between the free stream and the wake regions. This type of behaviour was noted by Baldwin (1989) although it was for a staggered tube heat exchanger section. The heat transfer coefficient in the wake region of the fourth tube-row is the highest observed of any wake region. This is due to entrainment back into the test section of the colder fluid air from the plenum.

The isotherm plots for the oval tube in the staggered arrangement is shown in Figure 6.36. At low heat flux input levels the isotherm plots are qualitatively similar to those seen for the round tubes, where the liquid crystals first change colour in the

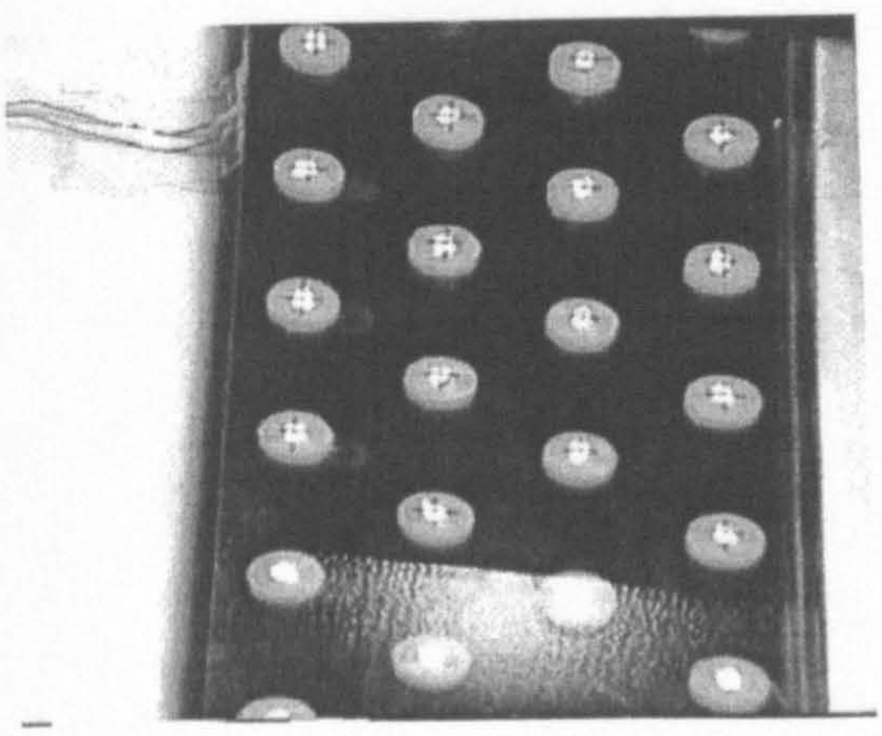

a: $\dot{q}$ = 655.8 W/m^2

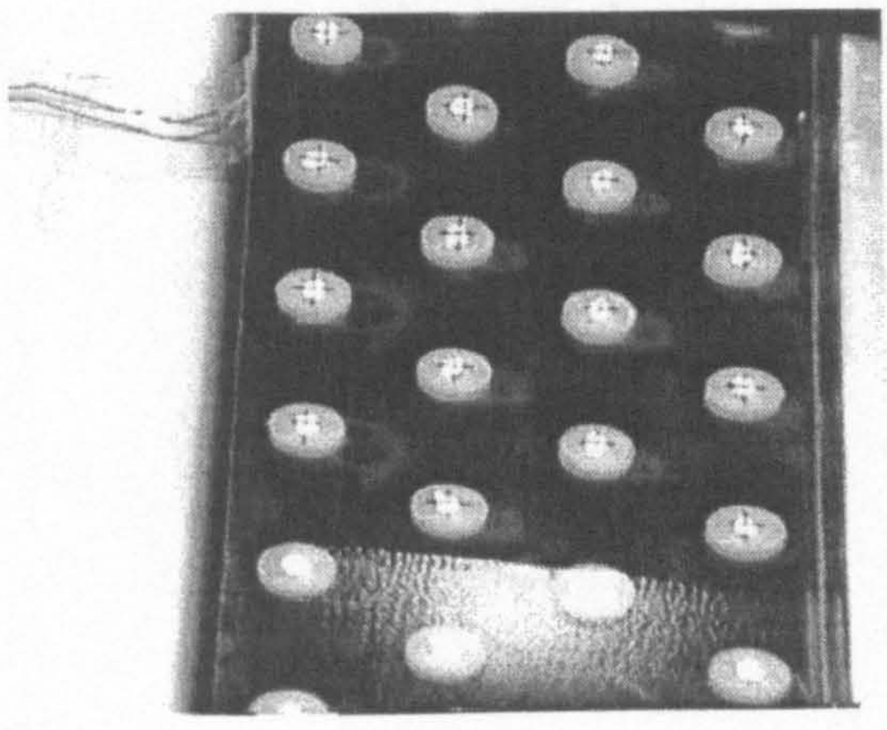

b: $\dot{q}$ = 733.5 W/m^2

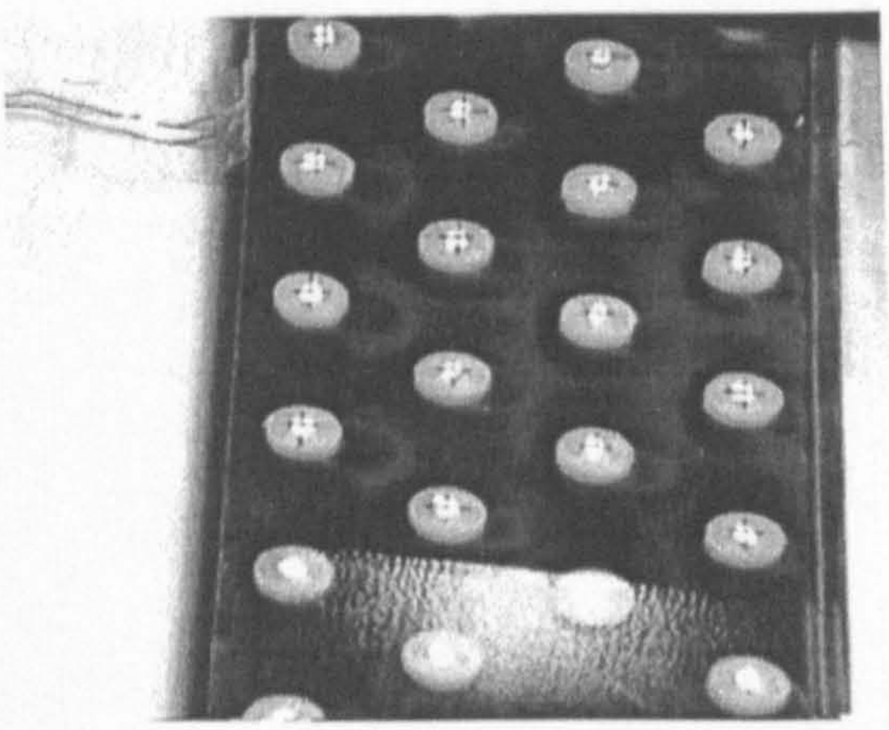

c: $\dot{q}$ = 775.7 W/m^2

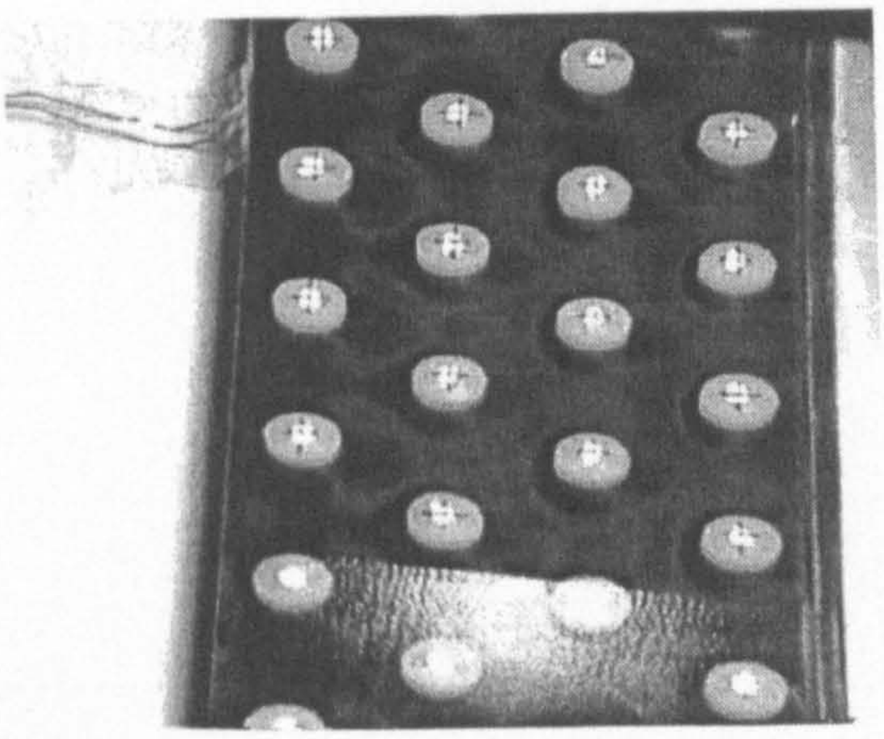

d: $\dot{q}$ = 819.2 W/m^2

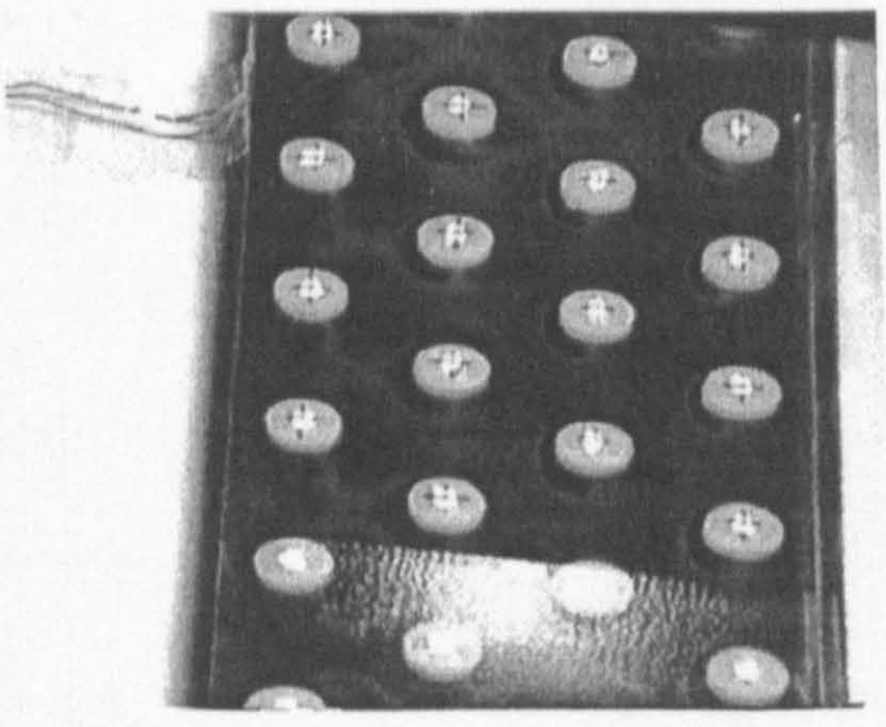

e: $\dot{q}$ = 960.1 W/m^2

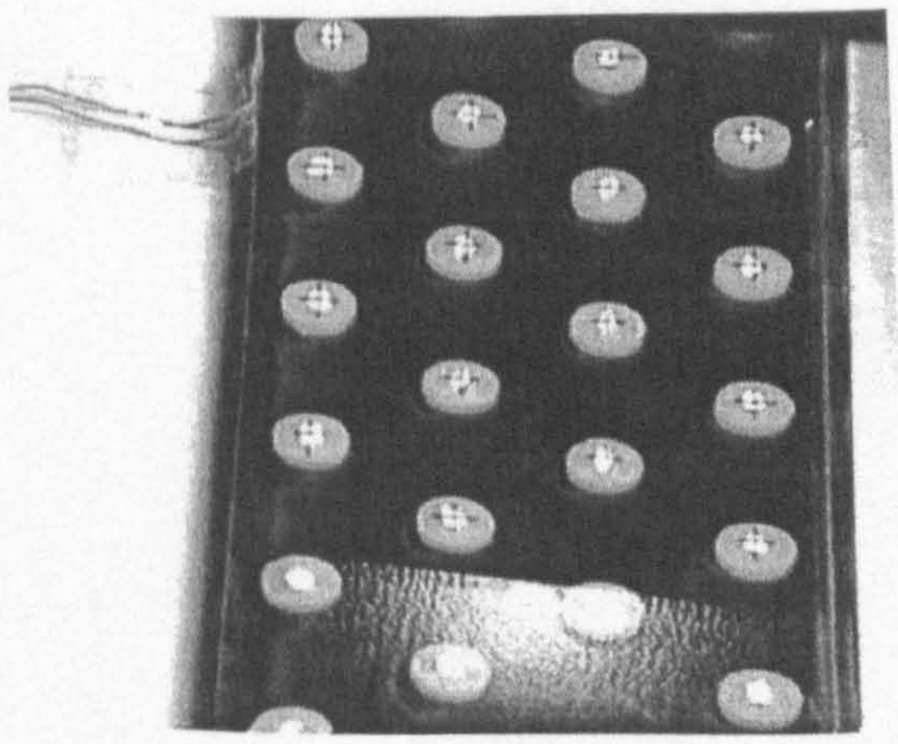

f: $\dot{q}$ = 1095.8 W/m^2

Figure 6.36: Isotherm position for increasing heat flux input

wake region. As the heat flux levels are increased, horseshoe vortices are observed in front of the oval tubes and stagnating flow is seen in front of the horseshoe vortices, reducing heat transfer. As the heat flux is increased still further, the isotherm patterns once again look qualitatively like those seen for round tubes in a staggered pitch.

The local heat transfer coefficient on the centre lines of the oval tubes are seen in Figures 6.37 and 6.38. In front of the first tube-row a horseshoe vortex is formed which results in an increase of heat transfer. Immediately behind the first tube-row a wake region is formed by the separating fluid. This wake region is, however, much smaller than what would be observed in the round tube case. This is due to later separation occurring on the more shallow curved oval tube and was also noted by Chen et al. (1998a), who numerically studied flow and heat transfer around a single oval tube. After the wake region there is an area of increased heat transfer due to the acceleration of the fluid between the second tube-rows. As this flow stagnates on the third tube-row, there is a local decrease in the heat transfer coefficient before increased heat transfer coefficients are seen, due to the horseshoe vortex. After the third tube-row there is once again a wake region and heat transfer recovery due to accelerated flow. On the opposite of the domain, Figure 6.38, the same flow features are observed with the horseshoe vortex being larger in-front of the second tube-row because of increased boundary layer thickness.

The average heat transfer coefficient and pressure drop values for the in-line case

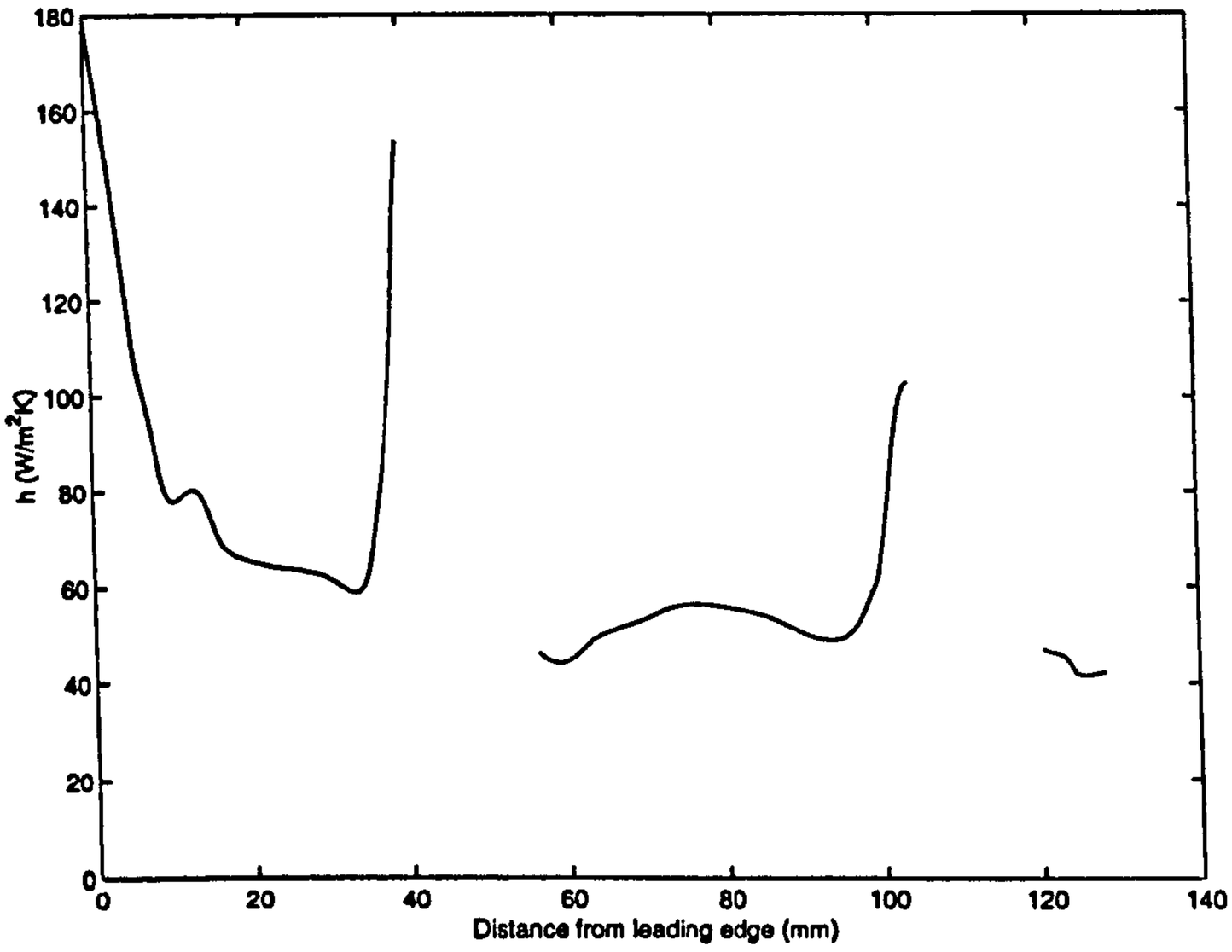

Figure 6.37: Heat transfer coefficient in the staggered case with oval tubes, taken through the centre line of the second and fourth tube rows. Blank space is where tube is positioned

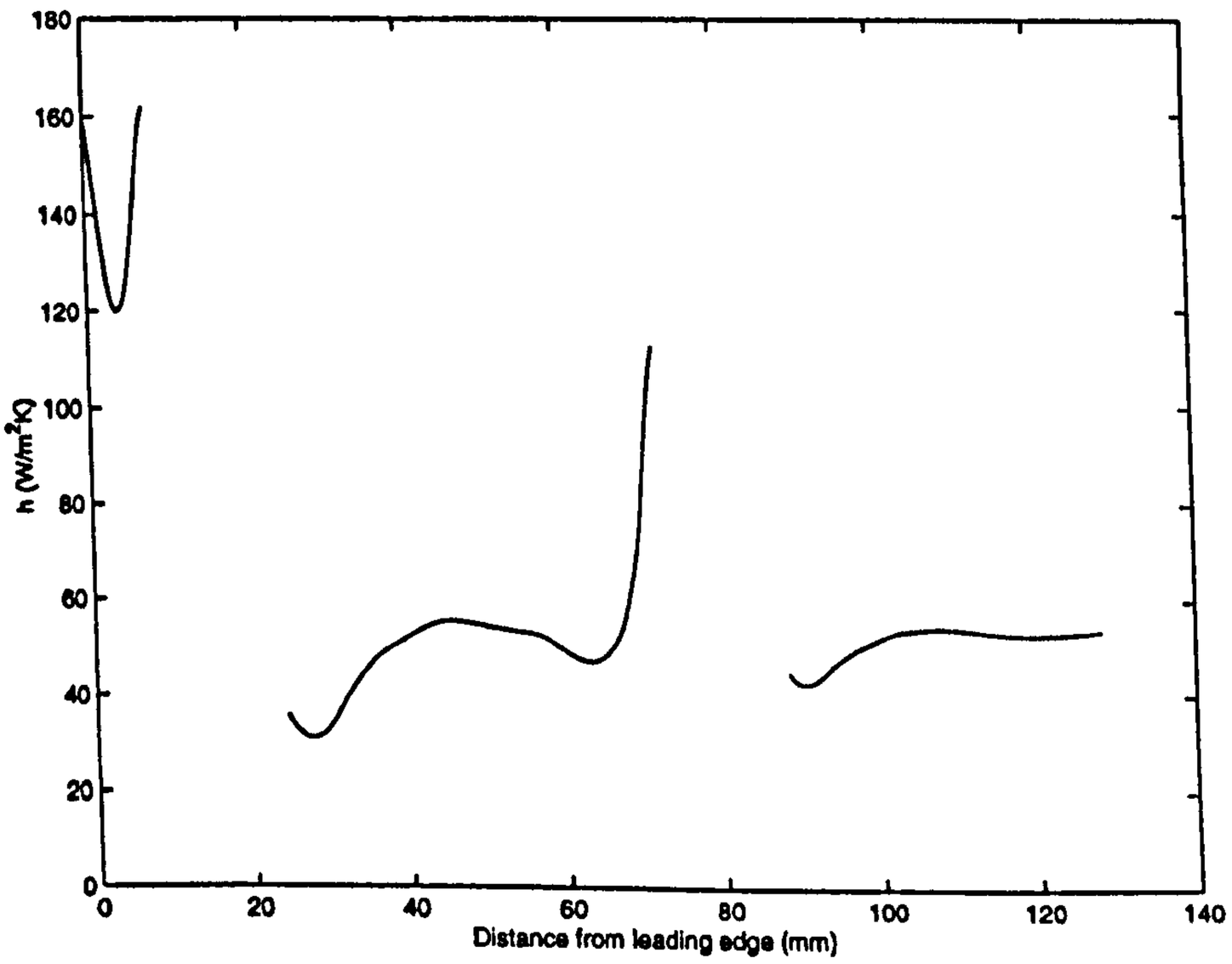

Figure 6.38: Heat transfer coefficient in the staggered case with oval tubes, taken through the centre line of the first and third tube rows. Blank space is where tube is positioned

with round tubes at a Reynolds number of 1224 was 49.6 W/m^{2}K and 64.9 Pa respectively. When this was compared to the oval tubes in the staggered arrangement the values were 62.9 W/m^{2}K and 59.8 Pa respectively. This is an increase of 20.1% in the average heat transfer coefficient and a reduction of 8.5% in the pressure drop. In the case of round tubes, by replacing an in-line arrangement with a staggered arrangement generally results in an increase in the heat transfer but also the pressure drop, Brauer (1964). These increases result from smaller wake regions and the increase in form drag of the tubes in the staggered arrangement. However, the replacement of circular tubes can substantially reduce the pressure drop without effecting the heat transfer characteristics, Saboya and Saboya (1981). For the case considered here the heat transfer has been enhanced due to the staggered arrangement being used, although smaller horseshoe vortices are formed in front of the tubes. In the oval case, it was reported by Chen et al. (1998a) that the form drag of the oval tubes causes only a small part of the total pressure drop through the section. The majority of the pressure drop results from skin friction. In the round tube case, the form drag of the tubes causes the majority of the pressure drop, Fiebig et al. (1995a) and (1995b). Even though it would be expected that their would be a pressure drop increase as the staggered arrangement was used, due to the better aerodynamic configuration of the oval tube, the pressure drop through the core was reduced. For the oval tube test section, by increasing the Reynolds number to 1567, the resulting values of average heat transfer coefficient and pressure drop increased to 73.7 W/m^{2}K and 86.0 Pa respectively. These are increases of 15.7% and 30.5% respectively.

6.6 Summary

In this chapter the experimental and numerical results for the cases investigated have been presented. The cases were: staggered tube heat exchanger cores with and without vortex generators, in-line heat exchanger cores with and without vortex generators and the comparison of round and oval tubes.

Due to the slightly better performance of the delta winglet pairs, this type of vortex generator was placed in both the staggered and in-line heat exchanger sections. When delta winglet pairs were placed in the staggered tube heat exchanger core at $\beta = 45°$, a large recirculation region was formed behind the vortex generator. This destroyed the main vortex but caused a vortex in the opposite direction to form. The vortex slightly reduced the area of the wake region behind the first tube-row and also distorted and moved the horseshoe vortices that had formed around the second tube-row away from the tube. This had the effect of increasing the heat transfer over a greater area around the second tube-row region.

Although the vortex generators had not been placed in an optimised position, especially in the case where $\beta = 45°$, increases in the heat transfer coefficient were noted for all three Reynolds numbers investigated. For these conditions the increases in the average heat transfer coefficient were -22.8%, +3.3% and 19.2%. The corresponding pressure drop values were -9.6%, +12.1% and +8.8%. When the Reynolds number was held constant at 326 and the angle of attack was increased from 15° to 60° the average heat transfer coefficient increases were +8.9%, +3.3% and +9.8%. Although the increase in the average heat transfer coefficients were reasonably constant large

changes in the pressure drop were recorded. The pressure drop values increased to +3.3% and +12.1% over the plain case for $\beta = 15°$ and 45° respectively. For the $\beta = 60°$ the vortex generator had been moved closer to the centre line of the tube. This had the effect of reducing the wake region size and thus pressure drop. The recorded value of pressure drop was 13.0% lower than the plain case. It should be noted that for $\beta = 60°$ case the vortex generator is somewhat closer to an optimised position than the other cases studied.

The numerical prediction of heat transfer coefficients once again showed the correct trends that were observed in the measured experimental results. As in the other cases the biggest discrepancies between the predicted results and measured results were near the leading edge, where tangential conduction had caused a higher value of heat transfer coefficient to be recorded than that observed in the numerical model.

The final heat exchanger core investigated with vortex generators was the in-line case. With the application of vortex generators into the core, a vortex was found to be issued from the vortex generator and carried into the downstream direction. The vortex had the effect of delaying separation around the tube and also diverting fluid into the wake region reducing its size. The re-attachment point of the wake on the second tube-row was closer to the centre line of the tube which resulted in a small horseshoe vortex forming on the second tube-row. This was completely absent when the vortex generator was not used.

For an angle of attack $\beta = 45°$ the increases in the heat transfer coefficient over the

Reynolds number range 65 – 653 were -8.3%, +7.1% and +13.8%. The respective pressure drop enhancements were -33.3%, +2.7% and +11.9%. The numerical model under-predicted the average heat transfer coefficient by 11.4% and over predicted the pressure drop through the core by +25.4%. The under-prediction in the average heat transfer coefficient is due to tangential conduction occurring in the experimental model. The general trends in the heat transfer coefficient were well predicted.

The final investigation carried out was into the relative effects of round and oval tubes in staggered and in-line heat exchanger cores. When compared at the same Reynolds number of 1224, an oval heat exchanger section in a staggered arrangement offered both a higher average heat transfer coefficient and a lower pressure drop when compared to a round tube heat exchanger in the in-line arrangement. The values for these enhancements are 20.1% and 5.5% respectively. The increase in the heat transfer is due to a staggered arrangement being used and the decrease in the pressure drop is due to the better aerodynamic properties of the oval tube. For an oval tube, separation occurs very late which reduces the wake region size and thus pressure drop. By increasing the Reynolds number to 1567 for the oval tube in the staggered arrangement the values of average heat transfer coefficient and pressure drop are increased by 15.7% and 30.5% respectively.

Using an oval tube in heat exchanger sections can reduce the pressure drop through the core but can result in slightly reduce heat transfer when compared to round tubes. Using vortex generators with oval tubes can increase the heat transfer to

levels above that achieved in round tube heat exchanger sections but also keep the lower pressure drop values. This situation could be beneficial in most heat exchanger applications.

Chapter 7

Conclusions

A combination of experimental and numerical methods has been shown to successfully measure and predict the local heat transfer characteristics in fin-tube heat exchangers with and without vortex generators. Both these methods accurately predicted areas of poor heat transfer and the relative effects of vortex generators on the average heat transfer coefficient and pressure drop.

The use of liquid crystals for the measurement of surface temperature and thus heat transfer coefficient was found to give results that compared well to standard correlations for plain channels when a constant heat flux boundary condition was used in the steady state. When the constant heat flux boundary condition was used in the transient method unrealistic heat transfer coefficient distributions were obtained due to the rise in bulk air temperature. By basing the heat transfer coefficient on the bulk air temperature the transient technique can be made to give compatible results with standard correlations for a plain channel. The steady state technique with a constant heat flux boundary conditions was used on all further tests which included heat exchanger sections with and without vortex generators.

A commercial computational fluid dynamics code was successfully used to simulate the use of the liquid crystals in the steady state. The application of a heat flux boundary between the top of the middle fin and the fluid replicated the experimental conditions of a constant heat flux boundary. The application of the same boundary condition types to the numerical model, that were used in the experimental set-up, allowed validation of the model and thus successfully tested the numerical models ability to predict local and average heat transfer coefficients and pressure drops.

The numerical model accurately predicted local fin surface temperatures and thus heat transfer coefficients for all the models of heat exchangers with and without vortex generators. Slight discrepancies were seen between the numerically predicted and measured heat transfer coefficients in the leading edge region and wake regions. These were due to tangential conduction occurring in the fin in the experiments. This can be avoided by using a thin fin with very low thermal conductivity so that the thermal resistance is negligible across its thickness compared with conduction within its plain. The application of symmetry boundary conditions were found to distort the flow field directly next to the boundary and thus move the point of lowest temperature to directly behind the tube. Periodic boundary conditions will provide better prediction of the flow velocities directly next to the boundary. Over prediction of the pressure drop through the core was recorded for some of the heat exchanger geometries.

The use of vortex generators in heat exchanger sections at low Reynolds numbers

has been shown to increase the average heat transfer coefficient and in most cases the pressure drop through the core. The increase in heat transfer coefficient arises from localised thinning of the boundary layer and increased mixing of the bulk air with the near wall fluid. Due to form drag and higher shear stress levels at the wall the pressure drop is increased. With increasing Reynolds number both the average heat transfer coefficient and pressure drop increased. With increasing angle of attack of the vortex generators the average heat transfer coefficient and pressure drop increased. After $\beta = 60°$ the value of heat transfer continued to increase but the pressure drop through the core decreased. This was due to delayed separation of the fluid around the tube and a reduction in wake region size.

Comparing the different types of vortex generator that were tested in plain channels, delta winglet pairs were judge to give the best performance. Although the enhancement in average heat transfer coefficient was similar between delta and rectangular winglet pairs, delta winglet pairs always offered a lower pressure drop penalty. When using delta winglet pairs in plain channels or heat exchanger sections the angle of attack of the vortex generator must be greater than 15° for there to be any benefit in terms of enhancement of heat transfer. Below this angle of attack no noticeable increases in heat transfer or pressure are noted. The local flow direction of the fluid before the vortex generator is very important for vortex generators to have any beneficial effect. The fluid should hit the vortex generator at an angle of greater than than 15° but less than 90°. Above 90° a recirculation region is formed behind the vortex generator and the vortex that is issued is either very weak or non-existent.

When vortex generators are placed in heat exchanger sections, the positioning of the vortex generator is also important. The tall ends of the delta winglet pair vortex generators behind each tube should not be more than one tube diameter apart. This allows the vortex that is issued to delay separation and increase mixing in the wake region.

Although vortex generators in plain channels are reasonably well understood, the effect in multi-row heat exchangers still needs further investigation. Optimal positioning of vortex generators for one tube-row is unlikely to be extended to multi-rows due to changing flow patterns in the core until periodic flow conditions exist. However, with modern computational and experimental methods, large numbers of geometries can be tested and the optimal positions found.

7.1 Recommendations and suggestions for further work

1. The use of an 'invariant' description for the heat transfer coefficient would eliminate the problems of different heat transfer coefficients being measured when they are referred to either the inlet temperature or bulk temperature. The use of an adiabatic heat transfer coefficient ($h_{adiabatic}$) bases the heat transfer coefficient on the adiabatic wall temperature and is thus independent of the thermal boundary conditions used.

2. The use of a low Reynolds number k-ϵ model should be investigated. From the research at low Reynolds numbers on plain channels with vortex generators it was

found that the transition to turbulent flow occurs at much lower Reynolds numbers than for the corresponding plain channel case. Although a low Reynolds number k-ϵ model was built and run for the delta winglet pair in a plain channel with no noticeable changes, larger effects might be noted on different geometries.

3. The use of vortices with 'common flow up' type flow could be of benefit when the fin pitch is increased due to the application of vortex generators in the heat exchanger core. No relevant literature was found in the area of the effects of fin pitch on vortex generators.

4. When using the steady state technique with radiant heating provided by a lamp, a dedicated power supply would be beneficial. This would avoid the problems of the heat flux changing due to fluctuations in the mains voltage.

5. The positioning of the vortex generator in the downstream direction still needs further investigation. The spacing in the transverse direction should not be more than one tube diameter. However, the effect of distance between the rear of the tube and the vortex generator pair still needs investigating.

References

Abbott M R and Basco D R, 1989. Computational fluid dynamics – An introduction for engineers. Longman

Akino H, Kunugi T, Ichimiya K and Ueda M, 1989. Improved liquid crystal thermography excluding human colour sensation. ASME Journal of Heat Transfer, Vol. 111, pp. 558—565

Anon, 1994. ETSU Guide to Compact Heat Exchangers, No. 89

Anon. 1998. STAR-CD Users Guide

Ashforth-Frost S A, Edwards R J, Greham D P, Lowesmith B J, Jambunathan K and Rhine J M, 1992. Measurements of convective heat transfer coefficients on the ligaments of a steel shell boiler plate, using liquid crystal thermography. Proc 3 rd UK National Conference Incorporating 1 st European Conference on Thermal Sciences, Birmingham, I. Chem E. Symposium Series, No. 129, pp. 351—359

Ashforth-Frost S A, 1994. Flow visualisation of semi-confined jet impingment. PhD Thesis, The Nottingham Trent University

Atkinson K N, Drakulic R, Heikal M R and Cowell T A, 1998. Two- and three-dimensional numerical models of flow and heat transfer over louvered fin arrays

in compact heat exchangers. Int. J. Heat Mass Transfer, Vol. 41, No. 24, pp. 4063—4080

Baker C J, 1979. The laminar horseshoe vortex. J. Fluid Mech., Vol. 95, pp. 347—367

Baldwin S, 1989. A study of heat and fluid flow phenomena on the gas side of circular-tube plate-fin heat exchangers. PhD Thesis, Coventry Lanchester Polytechnic

Baldwin S, White P R S and Al-Daini A J, 1986. Investigation of the gas side flow field in a circular tube-plate fin heat exchanger. Proc. 1st PHOENICS User Conf.: Numerical Simulation of Fluid Flow and Heat/Mass Transfer Processes, Markatos, Tatchell, Cross, Rhodes (eds), Springer-Verlag, Berlin, pp. 364—374

Baldwin B S and Lomax H, 1978. Thin layer approximation and algebraic model for separated turbulent flow. AIAA Paper 78—257

Barakat H Z and Clark J A, 1966. Analytical and experimental study of transient laminar natural convection flows in partially filled containers. Proc. 3rd Int. Heat Transfer Conf., Chicago, Vol. II, paper 57, p. 152

Barrozi G S and Pagliarini G, 1985. A method to solve conjugate heat transfer problems: the case of fully developed laminar flow in a pipe. ASME Journal of Heat Transfer, Vol. 107, pp. 77—83

Bastani A, Fiebig M and Mitra N K, 1991. Numerical studies of a compact fin-tube heat exchanger. Proc. EUROTHERM seminar No. 18, Design and Operation of Heat Exchangers, 27 Feb–1 March, Hamburg, Germany, pp. 154—163

Bastani A, Mitra N K and Biswas G, 1999. Numerical investigations on enhancement of heat transfer in a compact fin-and-tube heat exchanger using delta winglet type vortex generators. Enhanced Heat Transfer, Vol. 6, pp. 1—11

Baughn J W, Takahashi R K, Hoffman M A and McKillop A A, 1985. Local heat transfer coefficient measurements using an electrically heated thin gold-coated sheet. ASME Journal of Heat Transfer, Vol. 107, pp. 953—959

Baughn J W, Hoffman M A and Makel, 1986. Improvements in a new technique for measuring local heat transfer coefficients. Review of Scientific Instruments, Vol. 57, pp. 650—654

Baughn J W, Ireland P T, Jones T V and Saniei N, 1989. A comparison of the transient and heated-coating methods for the measurements of local heat transfer coefficients on a pin fin. ASME Journal of Heat Transfer, Vol. 111, pp. 877—881

Baughn J W and Yan X, 1991a. Liquid crystal methods in experimental heat transfer. Proc. 32 nd Heat Transfer and Fluid Mechanics Institute, pp. 15—36

Baughn J W and Yan X, 1991b. Liquid crystal methods in experimental heat transfer. Proc. 32 nd Heat Transfer Fluid Mech. Inst., California, State Univ.,

Sacramento, 6—7 June, pp. 15—40

Behle M, Schulz K, Leiner W and Fiebig M, 1996. Colour-based image processing to measure local temperature distributions by wide-band liquid crystal thermography. Applied Scientific Research, Vol. 56, pp. 113—143

Bergelin O P, Davies E S and Hull H L, 1949. A study of three tube arrangements in unbaffled tubular heat exchangers. Trans. ASME, Vol. 71, pp. 369—374

Bergelin O P, Brown G Aand Doberstein S C, 1952. Heat transfer and fluid friction during flow across banks of tubes–IV. Trans. ASME, Vol. 74, pp. 953—960

Bergles A E, 1997. Heat transfer enhancement – The encouragement and accommodation of high heat fluxes. 1995 Max Jakob Memorial Award Lecture. ASME Journal of Heat Transfer, Vol. 119, pp. 8—19

Biswas G and Chattopadhyay H, 1992. Heat transfer in a channel with built-in wing-type vortex generators. Int. J. Heat Mass Transfer, Vol. 35, No. 4, pp. 803—814

Biswas G, Deb P and Biswas S, 1994. Generation of longitudinal streamwise vortices – A device for for improving heat exchanger design. ASME Journal of Heat Transfer, Vol. 116, pp. 588—597

Biswas G, Mitra N K and Fiebig M, 1988. Computation of laminar mixed convection

flow in a rectangular duct with wing-type built-in obstacles. AIAA Paper No. 88-2647, AIAA Thermophysics, Plasmadynamics and Lasers Conference, San Antonio

Biswas G, Mitra N K and Fiebig M, 1989. Computation of laminar mixed convection flow in a channel with wing-type built-in obstacles. J. Thermophys. Heat Transfer (AIAA), Vol. 3, pp. 447—453

Biswas G, Mitra N K and Fiebig M, 1994. Heat transfer enhancement in fin-tube heat exchangers by winglet type vortex generators. Int. J. Heat Mass Transfer, Vol. 37, pp. 283—291

Biswas G, Torii K, Fujii D and Nishino K, 1996. Numerical and experimental determination of the flow structure and heat transfer effects of the longitudinal vortices in a channel flow. Int. J. Heat Mass Transfer, Vol. 39, No. 16, pp. 3441—3451

Bordalo S N and Saboya F E M, 1995. Experimental determination of the pressure drop coefficients in circular and elliptical tubes and plate fin heat exchangers. Proc. 13th COBEM, Brazilian Conference on Mechanical Engineering, Belo Horizonte, Brazil

Bradshaw P, 1971. An introduction to turbulence and its measurement. Pergamon, Oxford

Brauer H, 1964. Compact heat exchangers. Chem. Process Eng., pp. 451—460

Brockmeier U, Guëntermann Th and Fiebig M, 1993. Performance evaluation of a vortex generator heat transfer and comparison with different high performance surfaces. Int. J. Heat Mass Transfer, Vol. 36, No. 10, pp. 2575—2587

Campo A and Schuler C, 1988. Heat transfer in laminar flow through circular tubes accounting for two-dimensional wall conduction. Int. J. Heat Mass Transfer, Vol. 31, pp. 2251—2259

Cebeci T and Smith A M O, 1974. Analysis of turbulent boundary layers. Applied Mathematics and Mechanics, Vol. 15, Academic Press, New York

Celik I and Zhang W-M, 1993. Application of Richardson extrapolation to some turbulent flow calculations. Symposium on Quantification of the uncertainty in computational fluid dynamics, ASME Fluid Engineering Division Summer Meeting, Washington, D.C., FED-Vol. 158, pp. 29—38

Chapman A J, 1984. Fundamentals of heat transfer, Mcmillan

Chen Y, 1993. Numerische Untersuchung Von Lamellen-Rohr-Wärmeübertragor-elementen Unter Berücksichtigung der Wärmeleitung den Lamellen. Master Thesis, IFTB, RUB

Chen Y, Fiebig M and Mitra N K, 1998a. Conjugate heat transfer of a finned oval tube with a punched longitudinal vortex generator in the form of a delta winglet–parametric investigations of the winglet. Int. J. Heat Mass Transfer, Vol. 41, pp.

3961—3978

Chen Y, Fiebig M and Mitra N K, 1998b. Heat transfer enhancement of a finned oval tube with punched longitudinal vortex generators in-line. Int. J. Heat Mass Transfer, Vol. 41, pp. 4151—4166

Chen Z Q and Ren J X, 1988. Effect of the fin spacing on the heat transfer and pressure drop of a two-row plate fin and tube heat exchanger. Int. J. Refrig., Vol. 11, pp. 356—360

Clifford R J, Jones, T V and Dunne S T, 1983. Techniques for obtaining detailed heat transfer coefficients measurements within gas turbine blade and vane cooling passages. ASME Paper 83-GT-58

Coleman H W and Steele W G, 1989. Experimentation and uncertainty analysis for engineers. Wiley, New York

Cooper T E, Field R J and Meyer J F, 1975. Liquid crystal thermography and its application to the study of convective heat transfer. Transactions of the ASME, pp. 442—450

Courant R, Isaacson E and Rees M, 1952. On the solution of non-linear hyperbolic differential equations by finite differences. Comm. Pure Appl. Math., Vol. 5, p. 243

Critoph R E and Holland M K, 1996. A study of local heat transfer coefficients in a plate fin-tube heat exchanger using a steady state liquid crystal technique. In: Optical Methods and Data Processing in Heat and Fluid Flow, 18—19 April, City University, London, pp. 39—46

Critoph R E and Fisher M J, 1998. A study of local heat transfer coefficients in plate fin-tube heat exchangers using the steady state and transient liquid crystal techniques. In: Optical Methods and Data Processing in Heat and Fluid Flow, 16—17 April, City University, London, pp. 201—210

Critoph R E, Holland M K and Fisher M J, 1999. Comparison of the steady state and transient methods for measurement of local heat transfer in plate fin-tube heat exchangers using liquid crystal thermography with radiant heating. Int. J. Heat Mass Transfer, Vol. 42, pp. 1—12

Croft D R and Stone J A R, 1977. Heat transfer calculations using finite difference equations. Applied Science Publishers Ltd.

Demuren A O and Wilson R V, 1993. Estimating uncertainty in computations of two-dimensional separated flows. Symposium on Quantification of the uncertainty in computational fluid dynamics, ASME Fluid Engineering Division Summer Meeting, Washington, D.C., FED-Vol. 158, pp. 9—18

Edwards F J and Alker C R J, 1974. The improvement of forced convection surface heat transfer using surface protrusions in the form of (a) cubes and (b) vortex

generators. Heat Transfer, Proc. Fifth Int. Heat Transfer Conf., Vol. 2, pp. 244—248 (JSME Tokyo)

Eibeck P A and Eaton J K, 1985. An experimental investigation of the heat transfer effects of a longitudinal vortex embedded in a turbulent boundary layer. Rept. MD-48, Thermosciences Div., (Dept. Mech. Eng., Stanford Univ., Stanford, CA)

Eibeck P A and Eaton J K, 1986. The effects of longitudinal vortices embedded in a turbulent boundary layer on momentum and thermal transport. Proc. 8th Int. Heat Transfer Conf., San Francisco, CA, 3

Eibeck P A and Eaton J K, 1987. Heat transfer effects of a longitudinal vortex embedded in a turbulent boundary layer. ASME Journal of Heat Transfer, Vol. 109, pp. 16—24

Elmahdy P E and Briggs, 1979. Finned tube heat exchangers:correlation of dry surface heat transfer data. ASHRAE Trans., Vol. 85, No. 2, pp. 262—273

Faghri M and Rao N, 1987. Numerical computation of flow and heat transfer in finned and unfinned tube banks. Int. J. Heat Mass Transfer, Vol. 30, No. 2, pp. 363—372

Fergason J L, 1968. Liquid crystals in non-destructive testing. Applied Optics, Vol. 7, No. 9, pp. 1729—1737

Ferziger J H, 1988. A note on numerical accuracy. Int. J. Num. Meth. Fluids, Vol. 8, pp. 995—996

Ferziger J H, 1993. Estimation and reduction of numerical error. Symposium on Quantification of the uncertainty in computational fluid dynamics, ASME Fluid Engineering Division Summer Meeting, Washington, D.C., FED-Vol. 158, pp. 1—7

Fiebig M, 1993. Vortex generators for compact heat exchangers. 1993 ICHMT International Symposium on New Developments in Heat Exchangers, 6—9 September, Lisbon, Portugal

Fiebig M, 1995. Embedded vortices in internal flow: heat transfer and pressure loss enhancement. Int. J. Heat Fluid Flow, Vol. 16, No. 5, pp. 376—388

Fiebig M, 1997. Vortices and heat transfer. ZAAM Z angew Math. Mech., Vol. 77, No. 1, pp. 3—18

Fiebig M, 1998. Vortices, generators and heat transfer. Trans. IChemE, Vol. 76, Part A, pp. 108—123

Fiebig M, Kallweit P and Mitra N K, 1986. Wing type vortex generators for heat transfer enhancement. Proc. 8th Int. Heat Transfer Conf., San Francisco, Vol. 6, pp. 2909—2913

Fiebig M, Brockmeier U, Mitra N K and Güntermann Th, 1989. Structure of velocity

and temperature fields in laminar channel flows with longitudinal vortex generators. Num. Heat Transfer, Part A, Vol. 15, pp. 281—301

Fiebig M, Grosse-Gorgemann A, Chen Y and Mitra N K, 1995a. Conjugate heat transfer fir a finned tube part A: Heat transfer behaviour and the occurrence of heat transfer reversal. Numer. Heat Transfer, Part A, Vol. 28, pp. 133—146

Fiebig M, Grosse-Gorgemann A, Chen Y and Mitra N K, 1995b. Conjugate heat transfer fir a finned tube part B: Heat transfer augmentation and avoidance of heat transfer reversal by longitudinal vortex generators. Numer. Heat Transfer, Part A, Vol. 28, pp. 147—155

Fiebig M, Mitra N K and Dong Y, 1990. Simultaneous heat transfer enhancement and flow loss reduction of fin-tubes. Heat Transfer 1990, Proc. 9th Int. Heat Transfer Conf., Vol. 4, Hemisphere, New York, pp. 51—56

Fiebig M, Valencia A and Mitra N K, 1993. Wing-type vortex generators for fin-and-tube heat exchangers. Exp. Thermal Fluid Sci., Vol. 7, pp. 287—295

Fiebig M, Valencia A and Mitra N K, 1994. Local heat transfer and flow losses in fin-and-tube heat exchangers with vortex generators: A comparison of round and flat tubes. Exp. Thermal Fluid Sci., Vol. 8, pp. 35—45

Fiebig M and Sanchez M A, 1992. Enhancement of heat transfer and pressure loss by winglet vortex generators in a fin-tube element. HTD-Vol. 201, ASME, New

York, pp. 7—14

Fisher M J, 1996. An investigation into local heat transfer coefficients in a plate-fin-tube heat exchanger using liquid crystal thermography. MRes Thesis, The University of Warwick

Fisher E M and Eibeck P A, 1990. The influence of a horseshoe vortex on local convective heat transfer. ASME Journal of Heat Transfer, Vol. 112, pp. 329—335

Fisher E H and Rhodes N, 1996. Uncertainty in computational fluid dynamics. Proc. Instn. Mech. Eng., Vol. 210, pp. 91—94

Fraas A P and Özişik M N, 1965. Heat Exchanger Design, Wiley, New York

Freitas C J, 1995. Perspective: Selected benchmarks from commercial CFD codes. ASME Journal of Fluids Engineering, Vol. 117, pp. 208—218

Fujii M, Fujii T and Nagata T, 1984. A numerical analysis of laminar flow and heat transfer of air in an in-line tube bank. Numer. Heat Transfer, Vol. 7, pp. 89—102

Gentry R A, Martin R E and Daly B J, 1966. An Eulerian differencing method for unsteady compressible flow problems. J. Comp. Phys., Vol. 1, p. 87

Gillespie D R H, Byerley A R, Ireland P T and Kohler S T, 1994. Detailed measurement of local heat transfer coefficients in the entrance to normal and inclined film cooling holes. ASME Paper No. 94-GT-1

Graetz L, 1883. Über die Wärmeleitungsfähigkeit Von Flüssigkeiten, Part 1. Ann. Phys. Chem, Vol. 18, pp. 79—94

Grosse-Gorgemann A, 1996. Numerische Untersuchung der laminaren oszillierenden Strömung und des Wärmeüberganges in Kanälan mit rippenförmigen Einbauten. VDI-Fortschrittsberichte, Reihe, Wärmetechnik/Kältetechnik, Nr 87, ISBN 3-18-308719-7

Harten A, 1983. High resolution schemes for hyperbolic conservation laws. Journal of Computational Physics, Vol. 49, pp. 357—93

Harten A, 1984. On a class of high resolution total variation stable finite difference schemes. SIAM Journal of Numerical Analysis, Vol. 21, pp. 1—23

Hatton A P and Wooley, 1972. Heat transfer in two-dimensional turbulent confined flows. Proceedings of the Institute of Mechanical Engineers, Vol. 186, pp. 625—633

Hinze J O, 1975. Turbulence. 2nd edn, McGraw-Hill

Hippensteele S A, Russell L M and Stepka F S, 1983. Evaluation of a method for heat transfer measurements and thermal visualisation using a composite heater and liquid crystals. ASME Journal of Heat Transfer, vol. 105, No. 1, pp. 184—189

Hippensteele S A, Russell L M and Torres F J, 1985. Local heat transfer measurements on a large scale-model turbine blade airfoil using a composite of a heater

element and liquid crystals. Journal of Engineering for Gas Turbines and Power, Vol. 107, No. 4, pp. 953—960

Hippensteele S A, Russell L M and Torres F J, 1986. Use of a liquid crystal and heater-element composite for quantitative, high-resolution heat-transfer coefficients on a turbine airfoil including turbulence and surface-roughness effects. International Symposium on Pressure and Temperature Measurements, Anaheim, CA, ASME FED Vol. 58, pp. 105—120

Hirsch C, 1990. Numerical computation of internal and external flows – Vol. II: Computational methods for inviscid and viscous flows. John Wiley & Sons, New York

Holland M K, Fisher M, Critoph R E and Shaw C T, 1997. Prediction of the flow and heat-transfer characteristics in fin-tube heat exchangers. Proc. 10th Int. Conf. on Numerical Methods in Laminar and Turbulent Flow, Swansea, 21–25 July, pp. 1013—1023

Hwang C L and Fan L T, 1964. Finite difference analysis of forced-convection heat transfer in the entrance region of a flat rectangular duct. Appl. Sci. Res., Sect. A 13, pp. 401—422

Hwang K S, Sung H J and Hyun J M, 1996. Mass transfer measurements from a blunt-faced flat plate in a uniform flow. Int. J. Heat and Fluid Flow, Vol. 17, pp. 179—182

Igarashi T and Iida Y, 1988. Fluid flow and heat transfer around a circular cylinder with vortex generators. JSME International Journal, Series II, Vol. 31, pp. 701—708

Ireland P T and Jones T V, 1985. The measurement of local heat transfer coefficients in blade cooling geometries. AGARD Conference Proceedings No. 390, Paper No. 28

Ireland P T and Jones T V, 1986. Detailed measurements of heat transfer on and around a pedestal in fully developed passage flow. Proc. 8th Int. Heat Transfer Conf., Tien C L et al. (eds), Hemisphere Publishing Corp., Washington, DC, Vol. 3, pp. 795—980

Issa R I, 1986. Solution of the implicitly discretised fluid flow equations by operator-splitting. J. Comp. Phys., Vol. 62, pp. 40—65

Issa R I, Gosman A D and Watkins A P, 1986. The computation of compressible and incompressible recirculating flows by a non-iterative implicit scheme. J. Comp. Phys., Vol. 62, pp. 66—82

Issa R I, Ahmadi Befrui B, Beshay K and Gosman A D, 1991. Solution of the implicitly discretised reacting flow equations by operator-splitting. J. Comp. Phys., Vol. 93, pp. 388—410

Jacobi A M and Shah R K, 1995. Heat transfer surface enhancement through the

use of longitudinal vortices: A review of recent progress. Experimental Thermal and Fluid Science, Vol. 11, pp. 295—309

Jambunathan K, Ashforth-Frost S A and Whitney C, 1994. Design of surface heaters for liquid crystal thermography. In: Optical Methods and Data Processing in Heat and Fluid Flow, 14—15 April, City University, London, pp. 43—47

Jameson A and Lax P D, 1984. Conditions for the construction of multi-point total variation diminishing schemes. Department of Mechanical and Aerospace Engineering, University of Princeton, MAE Report 1650

Jang D S, Jetli R and Acharya S, 1986. Comparison of the PISO, SIMPLER and SIMPLEC algorithms for the treatment of the pressure velocity coupling in steady flow problems. Numer. Heat Transfer, Vol. 19, pp. 209—228

Jang J-Y, Wu M-C and Chang W-j, 1996. Numerical and experimental studies of three-dimensional plate-fin and tube heat exchangers. Int. J. Heat Mass Transfer, Vol. 39, No. 14, pp. 3057—3066

Jang J-Y, Lai J-T, Liu L-C, 1998. The thermal-hydraulic characteristics of staggered circular finned-tube heat exchangers under dry and dehumidifying conditions. Int. J. Heat Mass Transfer, Vol. 41, pp. 3321—3337

Johnson T R and Joubert P N, 1969. The influence of vortex generators on drag and heat transfer from a circular cylinder normal to an airstream. J. Heat Transfer,

Vol. 91, pp. 91—99

Jones T V, 1991. Definition of heat transfer coefficient in the turbine situation. Proceedings of the IMechE, Paper C423/046

Jones T V and Russell C M B, 1981. Heat transfer coefficients on finned tubes. ASME HTD, Vol. 20, pp. 17—25

Jones T V and Hippensteele S A, 1987. High-resolution heat-transfer-coefficient maps applicable to compound surfaces using liquid crystals in transient wind tunnels. 24 th ASME/AIchE National Heat Transfer Conference, ASME HTD-Vol. 71

Kakaç S, 1982. Introduction to low Reynolds number flow heat exchangers. In: Low Reynolds Number Flow Heat Exchangers, Kakaç S, Shah R K and Bergles A E, (eds), Hemisphere, pp. 3—8

Kakaç S and Yener Y, 1982. Laminar force convection in the combined entrance region of ducts. In: Low Reynolds Number Flow Heat Exchangers, Kakaç S, Shah R K and Bergles A E, (eds), Hemisphere, pp. 165—227

Kasagi N, Moffat R J and Hirata M, 1989. Liquid crystals. In: Handbook of flow visualisation, Wen Jel Yang, ed, Ch., 8, Hemisphere, New York

Kayansayan N, 1994. Heat transfer characterisation of plate fin-tube heat exchangers. Int. J. Refrig., Vol. 17, pp. 49—57

Kays W M and Crawford M E, 1980. Convection Heat and Mass Transfer. 2 nd ed., McGraw-Hill, New York

Kays W M and London A L, 1955, reprinted 1964, 1984. Compact Heat exchangers. McGraw-Hill

Kottke V, Blenke H and Schmidt K G, 1977. Eine remissionsfotometrische Meßmethode zur Bestimmung örtlicher Stoffübergangskoeffizienten bei Zwangskonvektion in Luft, Heat and Mass Transfer, Vol. 10, pp. 9—21

Kreith F and Black W Z, 1980. Basic Heat Transfer. Harper and Row

Kline S J and McClintock F A, 1953. Estimation of the uncertainty in single sample experiments. Mechanical Engineering, Jan. 1953

Krückels W and Kottke V, 1970. Untersuchung uber die verteilung des warmeubergangs an rippen und rippenrohr-modellen. Chemie. Ing. Tech., Vol. 42, pp. 355—362

Kundu D, Haji-Sheikh A and Lou D Y S, 1991a. Pressure and heat transfer in cross flow over cylinders between two parallel plates. Numer. Heat Transfer, A, Vol. 19, pp. 345—360

Kundu D, Haji-Sheikh A and Lou D Y S, 1991b. Heat transfer predictions in cross flow over cylinders between two parallel plates. Numer, Heat Transfer, A, Vol. 19,

pp. 361—377

Kurosaki Y, Kashiwagi T, Kobayashi H, Uzunhashi H and Tang S, 1988. Experimental study on heat transfer from parallel louvered fins by laser holographic interferometry. Experimental Thermal and Fluid Science, Vol. 1, pp. 59—67

Lai K Y M, 1983. Numerical analysis of fluid transport phenomena. PhD Thesis, The University of London

Launder B E and Massey T H, 1978. The numerical prediction of viscous flow and heat transfer in tube banks. ASME Journal of Heat Transfer, Vol. 100, pp. 565—571

Launder B E, Reece G J and Rodi W, 1975. Progress in the development of a Reynolds-stress turbulence closure. J. Fluid Mech., Vol. 68, Pt. 3, pp. 537—566

Launder B E and Spalding D B, 1974. The numerical computation of turbulent flows. Comput. Methods Appl. Mech. Eng., Vol. 3, pp. 269—289

Le Feuvre R F, 1973. Laminar and turbulent forced convection processes through in-line tube banks. HTS/74/5, Mechanical Engineering Department, Imperial College, London

Lee S H, Ryou H S and Choi Y K, 1999. Heat transfer in a three-dimensional turbulent boundary layer with longitudinal vortices. Int. J. Heat Mass Transfer,

Vol. 42, pp. 1521—1534

Leiner W, Schulz K, Behle M and Lorenz S, 1996. Imaging techniques to measure local heat and mass transfer. In: Optical Methods and Data Processing in Heat and Fluid Flow, 18—19 April, City University, London, pp. 1—13

Leonard B P, 1979. A stable and accurate convective modelling procedure based on quadratic upstream interpolation. Comput. Methods Appl. Mech. Eng., Vol. 19, pp. 59—98

Leschinziner M A, 1980. Practical evaluation of three finite difference schemes for the computation of steady-state recirculating flows. Comp. Meth. in Appl. Mech. & Eng., Vol. 23, pp. 293—312

Lewis R W, Morgan K, Thomas H R and Seetharamu, 1996. The finite element method in heat transfer analysis. Wiley

Lorenz S, Mukomilow D and Leiner W, 1995. Distribution of the heat transfer coefficient in a channel with periodic transverse groves. Experimental Thermal Fluid Science, Vol. 11, No. 3, pp. 234—242

Luikov A V, Aleksashenko V A and Aleksashenko A A, 1971. Analytical methods of solution of conjugated problems in convective heat transfer. Int. J. Heat Mass Transfer, Vol. 14, pp. 1047—1056

McMahon B and Murray D B, 1996. Local heat transfer measurements in a tube array using the transient method and liquid crystal thermography. In: Optical Methods and Data Processing in Heat and Fluid Flow, 18—19 April, City University, London, pp. 47—56

McQuiston F C, 1978. Heat mass and momentum data for five plate-fin-tube heat transfer surfaces. Trans. ASHRAE, Vol. 84, pp. 266—293

McQuiston F C and Tree D R, 1971. Heat transfer and flow friction data for two fin-tube surfaces. J. of Heat Transfer, Vol. 93 pp. 249—250

Mehta R D and Bradshaw P, 1988. Longitudinal vortices embedded in turbulent boundary layers. Part 2, Vortex pair with 'common flow' upwards. J. Fluid Mech., Vol. 188, pp. 529—546

Merker G P and Hanke H, 1986. Heat transfer and pressure drop on the shell-side of tube-banks having oval-shaped tubes. Int. J. Heat Mass Transfer, Vol. 29, No. 12, pp. 1903—1909

Metzger D E, Bunker R S and Bosch G, 1991. Transient liquid crystal measurement of local heat transfer on a rotating disk with jet impingment. J. Turbomachinery, Vol. 113, pp. 52—59

Metzger D E and Larson E E, 1986. Use of melting point surface coatings for local convective heat transfer measurements in rectangular channel flows with 90-degree

turns. ASME Journal of Heat Transfer, Vol. 108, pp. 48—54

Mitra N K 1999. Development, production and testing of optimised designs of compact heat exchangers containing heat transfer surfaces with implanted vortex generators (VEHE). Mid-term assessment report, Contract JOE3-CT97-0056, JOULE III

Mitra N K, Bastani A A and Fiebig M, 1991. Numerical simulation of 3D periodically fully developed flow between fins of a compact heat fin-tube heat exchanger. HTD-Vol 182, ASME-WAM, pp. 37—42

Moffat R J, 1985. Using uncertainty analysis in the planning of an experiment. Journal of Fluids Engineering, Transactions of the ASME, Vol. 107, No. 2, pp. 173—178

Moffat R J, 1988. Describing the uncertainties in experimental results. Exp. Thermal Fluid Sci. Vol. 1, pp. 3—17

Moffat R J, 1990. Experimental heat transfer. Proc. 9 th International Heat Transfer Conference, Jerusalem, Israel, Vol. 1, pp. 187—205

Mori S, Sakakibara M and Tanimoto A, 1976. Steady heat transfer to laminar flow between parallel-plates with conduction in the wall. Heat Transfer Jpn. Res. Vol. 5, pp. 17—25

Myrum T A, Qiu X and Acharya S, 1993. Heat transfer enhancement in a ribbed duct using vortex generators. Int. J. Heat Mass Transfer, Vol. 36, No. 14, pp. 3497—3508

Nguyen T V, 1992. laminar heat transfer for thermally developing flow in ducts. Int. J. Heat Mass Transfer, Vol. 35, No. 7, pp. 1733—1741

Nguyen T V and Maclaine-cross I L, 1988. Incremental pressure drop number in parallel-plate heat exchangers. ASME Journal of Fluid Engineering, Vol. 110, pp. 93—96

Nguyen T V and Maclaine-cross I L, 1991. Simultaneously developing, laminar flow, forced convection in the entrance region of parallel plates. ASME Journal of Heat Transfer, Vol. 113, pp. 837—842

Noack B R and Eckelmann H, 1994. A low-dimensional Galerkin method for the three-dimensional flow around a cylinder. Phys. Fluids, Vol. 6, No. 1, pp. 124—143

Norberg C, 1994. An experimental investigation of the flow around a circular cylinder: influence of aspect ratio. J. Fluid Mech., Vol. 258, pp. 287—316

O'Brien J E, Simoneau R J, LaGraff J E and Morehouse K A, 1986. Unsteady heat transfer and direct comparison for steady-state measurements in a rotor-wake experiment. 8th Int. Heat Transfer Conf., San Francisco, pp. 1243—1248

Oker E and Merte H, 1981. Semi-transparent golf film as simultaneous surface heater and resistance thermometer for nucleate boiling studies. ASME Journal of Heat Transfer, Vol. 103, pp. 65—85

Patankar S V and Spalding D B, 1972. A calculation procedure for heat, mass and momentum transfer in three-dimensional parabolic flows. Int. J. Heat Mass Transfer, Vol. 15, p. 1787

Patankar S V, 1980. Numerical heat transfer and fluid flow. Hemisphere Publishing Corporation, Taylor & Francis Group, New York

Patankar S V, 1982a. Numerical solution of forced convection. In: Low Reynolds Number Flow Heat Exchangers, Kakaç S, Shah R K and Bergles A E, (eds), Hemisphere, pp. 631—656

Patankar S V, 1982b. Computation of low-Reynolds-number turbulent flow. In: Low Reynolds Number Flow Heat Exchangers, Kakaç S, Shah R K and Bergles A E, (eds), Hemisphere, pp. 657—664

Patankar S V, Ivanović and Sparrow E M, 1979. Analysis of turbulent flow and heat transfer in internally finned tubes and Annuli. ASME Journal of Heat Transfer, Vol. 101, pp. 29—37

Pauley W R and Eaton J K, 1988a. The fluid dynamics and heat transfer effects of streamwise vortices embedded in a turbulent boundary layer. Stanford University

Pauley W R and Eaton J K, 1988b. Experiments on the development of longitudinal vortex pairs embedded in a turbulent boundary layer, AIAA J. Vol. 27, No. 7, pp. 816—823

Pauley W R and Eaton J K, 1994. The effect of embedded longitudinal vortex arrays on turbulent layer heat transfer. ASME Journal of Heat Transfer, Vol. 116, pp. 871—879

Plint M A and Böswirth L, 1978. Fluid mechanics: A laboratory course. Charles Griffin & and Company Limited, UK

Rahnema M, Yaghoubi M A and Kazeminejad H, 1997. A numerical study of convective heat transfer from an array of parallel blunt plates. Int. J. Heat and Fluid Flow, Vol. 18, pp. 430—436

Rich D G, 1973. The effect of fin spacing on the heat transfer and friction factors of multi-row, plate fin-and-tube heat exchangers. ASHRAE Trans. Vol. 79, No. 2, pp. 137—145

Rich D G, 1975. The effect of the number of tube rows on heat exchanger performance of smooth plate fin-and-tube heat exchangers. Trans. ASHRAE, Vol. 81, pp. 307—317

Richardson L F, 1910. The approximate arithmetical solution by finite differences of physical problems involving differential equations, with an application to the stresses in a masonry dam. Transactions of the Royal Society of London, Series A, Vol. 210, pp. 307—357

Richardson L F, 1927. The deferred approach to the limit. Transactions of the Royal Society of London, Series A, Vol. 226, pp. 299—361

Roache P J, Ghia K N and White F M, 1986. Editorial policy statement on the control of numerical accuracy. ASME Journal of Fluids Engineering, Vol. 108, p. 2

Roache P J, 1990. Need for control of numerical accuracy. J. Spacecraft and Rockets, Vol. 27, pp. 98—102

Roache P J, 1993. A method for the uniform reporting of grid refinement studies. Symposium on Quantification of the uncertainty in computational fluid dynamics, ASME Fluid Engineering Division Summer Meeting, Washington, D.C., FED-Vol. 158, pp. 109—120

Rocha L A O, Saboya F E M and Vargas J V C, 1997. A comparative study of elliptical and circular sections in one-and two-row tubes and plate fin heat exchangers. Int. J, Heat Fluid Flow, Vol. 18, pp. 247—252

Romero-Méndez R, Sen M, Yang K T and McClain R, 2000. Effect of fin spacing on convection in a plate fin and tube heat exchanger. Int. J. Heat Mass Transfer,

Vol. 43, pp. 39—51

Rosman E C, Carajilescov P and Saboya F E M, 1984. Performance of one and two-row tube and plate-fin heat exchangers. ASME Journal of Heat Transfer, Vol. 106, pp. 627—632

Rostami A A and Mortazavi S S, 1990. Analytical prediction of Nusselt number in a simultaneously developing laminar flow between parallel plates. Int. J. Heat and Fluid Flow, Vol. 11, No. 1, pp. 44—47

Runchal A K and Wolfshtein M, 1969. Numerical integration procedure for the steady state Navier-Stokes equations. J. Mech. Eng. Sci., Vol. 11, p. 445

Russell C M B, Jones T V and Lee G H, 1982. Heat transfer enhancement using vortex generators. Heat transfer 1982, Proc. Seventh Heat Transfer Conf, Vol. 3, pp. 283—288

Saboya S M and Saboya F E M, 1981. Transfer coefficients for plate fin and elliptical tube heat exchangers. Proc. COBEM, 5th Congresso Brasileiro de Engenharia Mecancia, Rio de Janeiro, 15-18 Dec., pp. 153—162

Saboya F E M and Sparrow E M, 1974. Local and average transfer coefficients for one-row plate fin and tube heat exchanger configurations. ASME Journal of Heat Transfer, Vol. 96, pp. 265—272

Saboya F E M and Sparrow E M, 1976a. Transfer characteristics of two-row plate fin and tube heat exchanger configurations. Int. J. Heat Mass Transfer, Vol. 19, pp. 41—49

Saboya F E M and Sparrow E M, 1976b. Experiments on a three-row fin and tube heat exchanger. ASME Journal of Heat Transfer, Vol. 98, pp. 521—523

Schlichting H, 1979. Boundary-layer theory. 7th edn., McGraw-Hill, New York

Schubauer G B and Spangenberg W G, 1960. Forced mixing in boundary layers. J. Fluid Mech., Vol. 8, pp. 10—31

Schulemberg F, 1966. Finned elliptical tubes and their applications in air-cooled heat exchangers. J. Eng. Ind., Vol. 88, pp. 179—190

Schultz D L and Jones T V, 1973. Heat transfer measurements in short-duration hypersonic facilities. NATO Advisory Group for Aeronautical Research and Development (AGARD), AG 165

Schulz T and Fiebig M, 1996. Accurate inexpensive local heat/mass transfer determination by digital image processing applied to the ammonia absorbption method. 2 nd European Thermal Science Conference, Rome

Schulz T, Behle M and Leiner W, 1996. High resolution measurements of heat transfer coefficients by liquid crystal thermography. In: Optical Methods and Data

Processing in Heat and Fluid Flow, 18—19 April, City University, London, pp. 57—69

Sedney R, 1973. A survey of the effects of small protuberances on boundary-layer flows. AIAA J., Vol. 11, pp. 782—792

Seshimo Y and Fujii M, 1991. An experimental study of the performance of plate fin and tube heat exchangers at low Reynolds numbers. 3rd ASME/JSME Thermal Engineering Joint Conf., Vol. 4, pp. 449—454

Shepherd D G and Ithaca N Y, 1956. Performance of one-row tube coils with thin-plates, low velocity forced convection. Heating Piping and Air Conditioning, Vol. 28, pp. 137—174

Shah R K, 1981. Classification of Heat Exchangers. In: Heat Exchangers, Kakaç S, Bergles A E and Mayinger F, (eds), Hemisphere, pp. 9—46

Shah R K, 1982a. Classification of heat exchangers. In: Low Reynolds Number Flow Heat Exchangers, Kakaç S, Shah R K and Bergles A E, (eds), Hemisphere, pp. 3—8

Shah R K, 1982b. Compact heat exchanger surface selection, optimisation, and computer-aided thermal design. In: Low Reynolds Number Flow Heat Exchangers, Kakaç S, Shah R K and Bergles A E, (eds), Hemisphere, pp. 845—874

Shah R K and London A L, 1978. Laminar flow forced convection in ducts. In: Advances in Heat Transfer, Academic Press, New York

Shah R K and Webb R L, 1983. Compact and enhanced heat exchangers. In: Heat Exchangers Theory and Practice, Taborek J, Hewett G R and Afgan N, (eds), Hemisphere, Washington, pp. 425—468

Shah R K and Bhatti M S, 1987. Laminar convective heat transfer in ducts. In: Handbook of single-phase convective heat transfer, Kakaç S, Shah R K and Aung W, (eds), John Wiley, New York

Shaw C T, 1992, Using computational fluid dynamics. Prentice Hall

Simonich J C and Moffat R J, 1982. A new technique for the measurement of heat transfer coefficient. Review of Scientific Instruments, Vol. 53, pp. 678—683

Smith G D, 1985. Numerical solution of partial differential equations: Finite difference methods. 3rd edn, Oxford University Press, Oxford

Soliman H M, Chau T S and Trupp A C, 1980. Analysis of laminar heat transfer in internally finned tubes with uniform outside wall temperature. ASME Journal of Heat Transfer, Vol. 102, pp. 598—604

Spalding D B, 1972. A novel finite-difference formulation for differential expressions involving both the first and second derivatives. Int. J. Num. Methods Eng., Vol.

Spalding D B, 1982a. Methods of calculating heat transfer within the passages of heat exchangers. In: Low Reynolds Number Flow Heat Exchangers, Kakaç S, Shah R K and Bergles A E, (eds), Hemisphere, pp. 665—676

Spalding D B, 1982b. The calculation of heat-exchanger performance. In: Low Reynolds Number Flow Heat Exchangers, Kakaç S, Shah R K and Bergles A E, (eds), Hemisphere, pp. 677—691

Sparrow E M, 1955. Analysis of laminar forced-convection heat transfer in the entrance region of flat rectangular ducts. NACA Tech. Notes TN 3331

Sparrow E M, Baliga B R and Patankar S V, 1978. Forced convection heat transfer from a shrouded fin array with and without tip clearance. ASME Journal of Heat Transfer, Vol. 100, pp. 572—579

Sparrow E M, Stahl T J and Traub P, 1984. Heat transfer adjacent to the attached end of a cylinder in crossflow. Int. J. Heat Mass Transfer, Vol. 27, No. 2, pp. 233—242

Thom A and Apelt C J, 1961. Field computation in engineering and physics. Van Nostrand, London

Thoman D C and Szewcyzk A A, 1969. Time-dependent viscous flow over a circular

cylinder. Physics of Fluids, Supplement II, pp. 76—86

Throckmorton D A and Stone D R, 1974. Model wall and recovery temperature effects on experimental heat transfer data analysis. AIAA Journal, Vol. 12, No. 9, pp. 169—170

Tiggelbeck S, Mitra N K and Fiebig M, 1993. Experimental investigations of heat transfer enhancement and flow losses in a channel with double rows of longitudinal vortex generators. Int. J. Heat Mass Transfer, Vol. 36, No. 9, pp. 2327—2337

Tiggelbeck S, Mitra N K and Fiebig M, 1994. Comparison of wing type vortex generators for heat transfer in channel flows. ASME Journal of Heat Transfer, Vol. 116, pp. 880—885

Torii K and Yanagihara J I, 1989. The effects of longitudinal vortices on heat transfer of laminar boundary. JSME International Journal, Series II, Vol, 32, pp. 359—402

Torii K and Yanagihara J I, 1991. Heat transfer enhancement by vortex generators. Proc. 3rd ASME/JSME Thermal Engineering Joint Conf., Lloyd J R and Kurosaka Y, (eds), pp. 77—83, ASME Book No. I0309C

Turaga M, Lin S and Fazio P P, 1988. Performance of direct expansion plate finned tube coils for air cooling and dehumidifaction. Int. J. Refrig., Vol. 11, pp. 78—86

Valencia A, Fiebig M and Mitra N K, 1995. Influence of the heat conduction on the determination of heat transfer coefficient by liquid crystal thermography. Experimental Heat Transfer, Vol. 8, No. 4, pp. 271—279

Valencia A, Fiebig M and Mitra N K, 1996. Heat transfer enhancement by longitudinal vortices in a fin-tube heat exchanger element with flat tubes. ASME Journal of Heat Transfer, Vol. 118, pp. 209—211

Valencia A, Fiebig M, Mitra N K and Leiner W, 1992. Heat transfer and flow loss in a fin-tube heat exchanger element with wing-type vortex generators. Inst. Chem. Eng. Symp. Ser., Vol. 129, No. 1, pp. 327—333

Van Treuren K W, Wang Z, Ireland P T, Jones T V and Kohler S T, 1994. Local heat transfer coefficient and adiabatic wall temperature measurement beneath arrays of staggered and in-line impinging jets. ASME Paper No. 94-Gt-181

Versteeg H K and Malalasekera W, 1995. An introduction to computational fluid dynamics, The finite volume method. Longman

Walker G, 1982. Heat Exchanger Design Handbook, Hemisphere, Washington

Wang C-C, Chang Y-J, Hsieh Y-C and Lin Y-T, 1996. Sensible heat and friction characteristics of plate fin-and-tube heat exchangers having plain fins. Int. J. Refrig. Vol. 19, No. 4, pp. 223—230

Wang Z, Ireland P, Jones T V and Kohler S, 1994. Measurements of local heat transfer coefficient over the full surface of a bank of pedestals with fillet radii. ASME Paper 94-GT-307

Wilkes N S and Thompson, 1983. An evaluation of higher-order upwind differencing for elliptic flow problems. CSS 137, AERE, Harwell

Wroblewski D E and Eibeck P A, 1991. Measurement of turbulent heat transport in a boundary layer with an embedded streamwise vortex. Int. J. Heat Mass Transfer, Vol. 34, No. 7, pp. 1617—1631

Wung T S and Chen C J, 1989a. Finite analytic solution of convective heat transfer for tube arrays in crossflow–I Flow field analysis. ASME Journal of Heat Transfer, Vol. 111, pp. 633—640

Wung T S and Chen C J, 1989b. Finite analytic solution of convective heat transfer for tube arrays in crossflow–II Heat transfer analysis. ASME Journal of Heat Transfer, Vol. 111, pp. 641—648

Xi G and Torikoshi K, 1996. Computation and visualisation of flow and heat transfer in finned tube heat exchangers. Int. Symp. Heat Transfer, Beijing, China, pp. 632—637

Ximenes M P, 1981. Heat and mass transfer in elliptical tubes and plate fin heat exchangers. PhD Thesis, Mechanical Engineering Division, Air Force Institute of

Technology, Sao Jose dos Campos, Brazil

Yamashita H, Kushida G and Izumi R, 1986a. Fluid flow and heat transfer in a plate-fin and tube heat exchanger (Analysis of fluid flow around a square cylinder situated between parallel plates). Bull. JSME, Vol. 29, pp. 2562—2569

Yamashita H, Kushida G and Izumi R, 1986b. Fluid flow and heat transfer in a plate-fin and tube heat exchanger (Analysis of fluid flow around a square cylinder situated between parallel plates). Bull. JSME, Vol. 29, pp. 4185—4191

Yan X, Baughn J W and Mesbah M, 1992. The effect of Reynolds number on the heat transfer distribution from a flat plate to an impinging jet. ASME HTD Vol. 226, pp. 1—7

Yanagihara J I and Torii K, 1990. Heat transfer characteristics of laminar boundary layers in the presence of vortex generators. Heat Transfer–1990, Hetsroni G, (ed), Hemisphere, Wasighton, D.C, Vol. 6, pp. 323—328

Yanagihara J I and Torii K, 1991. Enhancement of laminar boundary layer heat transfer in the presence of vortex generators. Proc. 4th Int. Symp. of Transport Phenomena in Heat and Mass Transfer, Davies G V, (ed), Hemisphere, Washington, D.C, pp. 942—953

Yanagihara J I and Torii K, 1992. Enhancement of laminar boundary layer heat transfer by a vortex generator. JSME Int. J. Series II, Vol. 35, pp. 400—405

Yanagihara J I and Torii K, 1993. Heat transfer enhancement by longitudinal vortices rows. Experimental Heat Transfer, Fluid Mechanics and Thermodynamics, pp. 560—567

Yianneskis M, 1986. Thermal monitoring by liquid crystals. Int. Conf. Condition Monitoring, Brighton, England, 21—23 May, pp. 131—141

Zhang X and Collins W C, 1993. Flow and heat transfer in a turbulent boundary layer through skewed and pitched jets. AIAA J., Vol. 30, pp. 49—55

Zhang Z J, Fiebig M and Mitra N K, 1991. Vortex breakdown and its effect on heat transfer enhancement in flows between parallel plates. ENTROPIE, Creteil, France, pp. 29—32

Zhu J X, Fiebig M and Mitra N K, 1993. Comparison of the numerical and experimental results for a turbulent field with a longitudinal vortex pair. J. Fluids Engng., Vol. 115, pp. 270—274

Zienkiewicz M A and Taylor R L, 1989. The finite element method, 4th edn, Volume 1: Basic formulation and linear problems. McGraw-Hill, New York

Bibliography

Hewitt G F (Co-ord. ed.), 1990. Hemisphere handbook of heat exchamger design. Hemisphere

Appendix A

The temperature equation for the transient heating of a glass sheet is given by:

$$\dot{q} = 2h(T_w - T_\infty) + kz\left(\frac{\partial^2 T}{\partial x^2} + \frac{\partial^2 T}{\partial y^2} + \frac{\partial^2 T}{\partial z^2}\right) + \rho c_p z \frac{\partial T}{\partial t} + \dot{q}_{rad} \qquad (1)$$

Assuming steady, incompressible flow, negligible heat conduction through the glass sheet (i.e. negligible temperature gradient in the z direction), and that the tangential conduction and the radiation losses are ignored (see Section 3.4), equation 1 reduces to:

$$\rho c_p z \frac{\partial T}{\partial t} = \dot{q} - 2h(T_w - T_\infty) \qquad (2)$$

$$\frac{\partial T}{\dot{q} - 2h(T_w - T_\infty)} = \frac{\partial t}{\rho c_p z} \qquad (3)$$

Integrating between the limits of the known temperatures, i.e. T_w and T_∞:

$$\left[-\frac{1}{2h}\ln(\dot{q} - 2h(T_w - T_\infty))\right]_{T_\infty}^{T_w} = \frac{t}{\rho c_p z} \qquad (4)$$

$$\frac{1}{2h}\ln\left[\frac{\dot{q} - 2h(T_\infty - T_\infty)}{\dot{q} - 2h(T_w - T_\infty)}\right] = \frac{t}{\rho c_p z} \qquad (5)$$

$$\ln\left[\frac{\dot{q}}{\dot{q} - 2h(T_w - T_\infty)}\right] = \frac{2ht}{\rho c_p z} \qquad (6)$$

On rearranging, the heat heat transfer coefficient, locally averaged for the upper and lower sides at any point (x, y) or along any isotherm is given by:

$$h = \frac{-\rho c_p z}{2t} ln \left[1 - \frac{2h}{\dot{q}}(T_w - T_\infty)\right] \tag{7}$$

This equation can be solved iteratively.

Appendix B

Matlab programme to determine the heat transfer coefficient at any point (x, y) using the Newton Raphson iterative technique.

```
q = input('enter heat flux input ');
t = input('enter time ');
am = input('enter ambient temperature ');
lc = input('enter liquid crystal event temperature ');


a = 0.1
b = 0.2
g = 0.001

while g > 0

        c = ((2*a)/q) * (lc - am);
        d = ((2*a*t)/1568) + ln(1 - c);
        e = ((2*b)/q) * (lc - am);
        f = ((2*b*t)/1568) + ln(1 - e);


        g = (d*f);
        a = b:
        b = b + 0.1;

end

        a = a - 0.1;
        b = b - 0.1;
```

```
x = ((a*f) - (b*d))/(f - d);
x0 = 0.10;

while abs(x - x0) > 0.00001

    h = ((2*(x0 + 0.001))/q) * (lc - am);
    i = ((2*(x0 + 0.001)*t)/1568) + ln(1 - h);
    j = ((2*(x0 - 0.001))/q) * (lc - am);
    k = ((2*(x0 - 0.001)*t)/1568) + ln(1 - j);
    dx = (i - k)/0.002;
    l = ((2*x0)/q) * (lc - am);
    m = ((2*x0*t)/1568) + ln(1 - j);
    x0 = x;
    x = x0 - (m/dx);

end

x
```

Appendix C

Matlab programme to calculate solid and gas temperatures in a channel with transient heating.

```
tamb = input('enter ambient temperature ');
u = input('enter air temperature ');
t = input('enter total time ');
c = input('enter number of time steps ');


delt = (t/c);
l = 45;


for r = 1:l

        h(r,1) = 84.9078 - (4.0082*r) + (0.1116*r^2) - (0.0010*r^3);          % HTC
        a(r,1) = (t/c)/1.6464;                                  % (delta t)/(m cp) solid
        b(r,1) = (4.8441)/(h(r,1) * 0.001);                       % (m cp)/(h a) gas


end


% set up initial solid temperatures


for r = 1:l

        ts(r,1) = tamb;

end


% set up initial gas temperatures at inlet


for s = 1:c
```

```
        tg(1,s) = tamb;

end

% set up initial gas temperatures in channel

for r = 2:l
        tg(r,1) = tamb;
end

% calculate temperatures


for s = 2:c          % scan through time
        tg(1,s) = u;

for r = 2:l          % scan through length

% calculate gas temperatures


        d = 2 * ts(r-1,s-1);
        e = tg(r,s-1) * ((a(r,1) * 4.8441) + 0.5 + b(r,1));
        f = tg(r-1,s-1) * ((a(r,1) * 4.8441) - 0.5 + b(r,1));
        g = tg(r-1,s) * ((a(r,1) * 4.8441) - 0.5 + b(r,1));
        j = b(r,1) + (a(r,1) * 4.8441) + 0.5;
        tg(r,s) = (d - e + f + g)/j;


% calculate wall temperatures
```

```
            m = tg(r,s-1) - tg(r-1,s-1) + tg(r,s) - tg(r-1,s);
            n = 4.8441;
            p = delt/1.6464;
            ts(r-1,s) = ts(r-1,s-1) - (p * (n * m));


end
end
```

Appendix D

Three Matlab programmes that reads in the contours of the heat transfer coefficient and interpolates between them to obtain a mesh of heat transfer coefficient over the whole test domain.

crysplot.m

```
% Reads in contours, displays them and then interpolates and shows mesh.

global X Y del R C r c n x y z

n=0;                                    % No. of points read in from all contours.
setxy                                   % create X,Y with NaN's where the tubes are.
d='y'


while d=='y' — d=='Y'

        cont                            % inputs a contour and generates x,y,z triplets from it
        ' Number of points is now ',n
        d = input(' Another contour ? [y or n]','s');

 end

plot3(x,y,z,'o')
hold on
Z=griddata(x(1:5:n),y(1:5:n),z(1:5:n),X,Y);
mesh(X,Y,Z)
view(20,60)
```

```
countr=0;countc=0;countz=0;sumz=0;


for countr=1:64

        for countc=1:221
        if isnan(Z(countr,countc)) ,sumz=sumz;
        else sumz=sumz+Z(countr,countc);countz=countz+1;
        end
end

end,

' average heat transfer co-efficient = ',sumz/countz
```

cont.m

```
% Creates x,y,z triplets for one contour and adds them to previous triplets

global X Y del R C r c n x y z

name=input('Name of contour gif-file ( without .gif extension ) ','s');

h=input('Watts / m^2 deg C ')


[fred,mapp]=gifread(name);
cont=fred;
```

```
[r, c]=size(cont);
cont(1,1:c)=0*cont(1,1:c);
cont(r,1:c)=0*cont(1,1:c);
cont(1:r,1)=0*cont(1:r,1);
cont(1:r,c)=0*cont(1:r,1);                                  % Set edges to zero


for a=1:r
for b=1:c

        if cont(a,b)==1;                                    % test for line present
        n=n+1;                                  % n'th point of full set inc. other contours
        x(n)=(b-1)*44/c;                                    % x in mm from leading edge
        y(n)=(a-1)*12.7/r;                                  % y in mm 'up'
        z(n)=h;                                             % notional heat transfer coeff.
        end

end
end
```

setxy.m

```
% Creates co-ordinate arrays for plotting fin heat transfer.
% Pairs of elements from X and Y are used by GRIDDATA. Parts of X
% are NaN's. These are the tubes, which will not be plotted.
% Grid spacing = del (mm)

global X Y del R C r c n x y z

del=input('Grid spacing required im mm ?')
R=floor(12.7/del + 1);                                  % Number of rows for 1/2 inch width
C=floor(44/del + 1);                                    % Number of columns for 44mm depth
```

```
for r=1:R
for c=1:C

        x=del*(c-1);                                    % x-coord of point
        y=del*(r-1);                                    % y coord of point
        X(r,c)=x;
        Y(r,c)=y;
        if(((y - 0)^2+(x - 11)^2)<=5.0^2) — ( (y - 12.7)^2+(x - 33)^2 <= 5.0^2)
        X(r,c)=NaN;
        Y(r,c)=NaN;
        end

end
end


plot(X,Y,'.')


d=input('Flip top to bottom ? [Y or N]','s');


if d=='y' — d=='Y'

        Y=Y(:,C:-1:1);
        X=X(R:-1:1,:);
        plot(X,Y,'.')

end
```

Appendix E

User coded Fortan programme to specify the heat flux in the numerical models.

```
C*************************************************************************
      SUBROUTINE SORENT(S1P,S2P)

C       Source-term for enthalpy
C*************************************************************************
C-------------------------------------------------------------*
C       STAR VERSION 2.300 *
C-------------------------------------------------------------*

      INCLUDE 'comdb.inc'
      COMMON/USR001/INTFLG(100)

      INCLUDE 'usrdat.inc'
      DIMENSION SCALAR(50)
      EQUIVALENCE( UDAT12(001), ICTID )
      EQUIVALENCE( UDAT03(001), CON )
      EQUIVALENCE( UDAT03(019), VOLP )
      EQUIVALENCE( UDAT04(001), CP )
      EQUIVALENCE( UDAT04(002), DEN )
      EQUIVALENCE( UDAT04(003), ED )
      EQUIVALENCE( UDAT04(004), HP )
      EQUIVALENCE( UDAT04(006), P )
      EQUIVALENCE( UDAT04(008), TE )
      EQUIVALENCE( UDAT04(009), SCALAR(01) )
      EQUIVALENCE( UDAT04(059), U )
      EQUIVALENCE( UDAT04(060), V )
```

```
      EQUIVALENCE( UDAT04(061), W )
      EQUIVALENCE( UDAT04(062), VISM )
      EQUIVALENCE( UDAT04(063), VIST )
      EQUIVALENCE( UDAT04(007), T )
      EQUIVALENCE( UDAT04(067), X )
      EQUIVALENCE( UDAT04(068), Y )
      EQUIVALENCE( UDAT04(069), Z )
C-----------------------------------------------------------------
C
C     This subroutine enables the user to specify a source term (per unit
C     volume) for enthalpy in linearized form:
C
C     Source = S1P-S2P*T, (W/m3)
C
C     in an arbitrary manner.
C
C     If temperature is to be fixed to a given value T, then the
C     following may be used:
C
C     S1P=GREAT*T
C      S2P=GREAT,
C
C     where T can be a constant or an arbitrary function of the
C     parameters in the parameter list.
C
C     ** Parameters to be returned to STAR: S1P,S2P
C
C-----------------------------------------------------------------
C
C     Sample coding: Fix temperature to the value of 300 K in solid
C     No 3 (IMAT=-3)
C

      IF(IMAT.EQ.-3) THEN
```

```
    S1P=650.7/1E-6                    % Specify heat flux here
    S2P=0
ENDIF


RETURN
END
```